eman ta zabal zazu

Universidad del País Vasco

Euskal Herriko Unibertsitatea

Design, synthesis and characterization of multifunctional materials based on carboxylate ligands. Screening of applications.

Applied Chemistry Department-Coordination Chemistry Group

Doctoral dissertation presented by:

Estitxu Echenique Errandonea

To qualify for the degree of

Doctor from Universidad del País Vasco/ Euskal Herriko Unibertsitatea

Supervisors: José Manuel Seco Botana and Antonio Rodríguez Diéguez

Euskal Herriko Unibertsitatea UPV-EHU

Donostia (Gipuzkoa), 2022

Glossary of Abbreviations and Acronyms

Abbreviations and Acronyms

1-BT	1-benzothiophene	**DMAB**	Dimethylamine-borane
4- MDBT	4-methyldibenzothiophene	**DMF**	Dimethylformamide
4,4'-azopy	4,4'-azopyridine	**DMF**	N,N'-dimethylformamide
4,6-DMDBT	4,6-dimehtyldibenzothiophene	**DMSO**	Dimethyl sulfoxide
ac	Alternating current	**DVS**	Dynamic vapour sorption
ACN	Acetonitrile	***E. coli***	*Escherichia coli*
[BMIM]PF_6	1- butyl-3-methylimidazolium hexafluorophosphate	**ECODS**	Extraction and Catalytic Oxidative Desulfurization
BPY	Bipyridine	**EtOH**	Ethanol
CA	Contrast agent	**FT-IR**	Infrared spectroscopy
CD	Circular Dichroism	**iPrOH**	Isopropanol
CEST	Chemical Exchange Saturation Transfer	**ISC**	Intersystem crossing
CP	Coordination Polymer	**IUPAC**	International Union of Pure and Applied Chemistry
CPL	Circularly Polarised Luminescence	**M'MOFs**	Mixed-Metal-Organic Frameworks
CT	Computed tomography	**MBC**	Minimum bactericidal concetration
DBT	Dibenzothiophene	**MeOH**	Methanol
dc	Direct current	**MIC**	Minimum inhibitory concentration

MMM	Mixed matrix membrane	**SBU**	Secondary Building Unit
MMMs	Multifunctional molecular materials	**SD**	Standard deviation
MOF	Metal-Organic Framework	**SEM**	Secondary Electron Microscopy
MRI	Magnetic resonance imaging	**SIM**	Single Ion Magnet
NSAID	Non-Steroidal Anti-Inflammatory Drug	**THF**	Tetrahydrofuran
ODS	Oxidative desulfuration		
OM	Oil model		
PMMA	Polymethyl methacrylate		
POM	Polyoxometalate		
PSF	Polysulphone		
PSM	Post-synthetic modification		
PSMO	Post-synthetic metathesis and oxidation		
PXRD	Powder X-Ray Diffraction		
RH	Relative humidity		
RT	Room temperature		
S. aureus	*Staphylococcus Aureus*		

Summary

Summary

In recent decades, coordination chemistry has been among the most widely investigated field in the scientific community. The interest in these compounds derives from the wide range of properties they can exhibit. The diversity of these possible properties enables them becoming of great interest to be applied in many fields such as magnetism, luminescence, catalysis, separation and storage of gases and biomedicine, among others.

Consequently, understanding the molecular structure of these systems enable setting the basis for designing and synthesising novel materials with modulated properties.

Nonetheless, the most appealing feature of these materials is the possibility to combine several of these unique characteristics to simultaneously obtain a multifunctional coordination compound. In this sense, the versatility and multifunctionality of these materials has encourage the scientific community to continue developing and improving this family of materials.

Starting from this premise, this thesis pursues the objective to develop novel coordination compounds and metal-organic frameworks by the self-assembly of lanthanides or d block metals and carboxylate based organic ligands. First of all, the ideal synthetic conditions have been set and various synthetic approaches have allowed to prepare a bunch of materials. Hydrothermal routes have permitted to isolate single-crystals; while microwave assisted synthesis was set as an ideal method not only to scale up the reaction but also to significantly reduce the required reaction-time.

For the characterization of the presented materials the combination of several techniques has been needed; among them can be mention, infrared spectroscopy (FTIR), elemental analysis (EA), thermogravimetry (TG), electron microscopy (SEM and EDS) and powder X-ray diffraction (PXRD). The crystal structures were unveiled using single crystal X-ray diffraction analysis.

Subsequently, learning from the material final features a shaped and fine-tuned application has been explored. Consequently, this doctoral thesis includes the synthesis and characterization of novel coordination compounds and MOFs based on carboxylate ligands of diverse nature for their subsequent multifunctional applications in fields broaden from catalysis to gas storage.

To conclude, with the aim of implementing prepared materials in industrial processes shaping techniques have been explored along with stability-assays performed in processed materials to evaluate such processing.

Regarding the organization of this thesis, the content is structured in six individual chapters. This configuration has been set in accordance with the organic ligand employed for the synthesis of each family of materials. Consequently, each section will contain a general introduction framing the work and explored applications followed by the most important results and discussion to end with obtained conclusions. Part of the work presented in this thesis has already been published in scientific journals while some other sections are expected to be in a close future. A more detailed information can be found in the section of list of publications.

Table of contents

Introduction

Coordination polymers and Metal-Organic Frameworks: origin and terminology

In 2009, the International Union of Pure and Applied Chemistry (IUPAC), presented a guideline entitled *Coordination Polymers and Metal-Organic Frameworks: Terminology and Nomenclature* with the aim of unifying nomenclature within the scientific community. In the latest recommendations published in 2013, IUPAC defined the aforementioned terms as:[1]

Coordination polymer: *A coordination compound with repeating coordination entities extending in 1, 2, or 3 dimensions.*

Metal-organic frameworks: *A metal-organic framework, abbreviated to MOF, is a coordination network with organic ligands containing potential voids. This wording accounts for the fact that many systems are dynamic, and changes in structure and thus corresponding changes in potential porosity or solvent and/ or guest filled voids may occur depending on temperature, pressure or other external stimuli.*

A vast number of structures can be addressed by these definitions. Consequently, for the sake of clarity, in this thesis, Coordination Compounds or Polymers will refer to discrete molecules or compounds with 1 or 2 dimensions, meanwhile, the Metal-Organic Framework will be considered structures presenting a 3-dimensional network, leaving aside the emphasis on the porosity. Concretely, in this thesis, chapters 2-4 and 6 will be related to 3D-MOFs while chapters 1 and 5 to coordination compounds with lower dimensionality.

Metal-organic frameworks are coordination networks composed of a metal ion or node and an organic linker that permit the rational structural design of functional materials. Consequently, structure-property relationships are established enabling fine-tuning of their functionalities for tailored applications.[2]

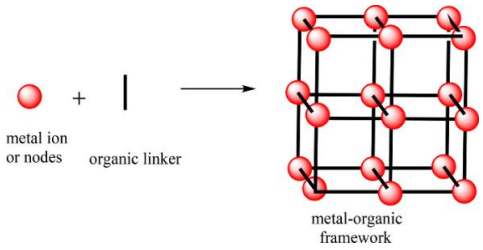

Figure I.1. Illustration of MOF's building blocks and resulting porous, crystalline structure.[3]

The history of MOF began in the 1990s. Concretely, the work developed by B. F. Hoskins and R. Robson laid the foundations.[4,5] However, the importance of the porous MOFs is derived from O. Yaghi's group, who published the MOF-5 structure in 1995: the first three-dimensional porous MOF known today.[6] Nonetheless, the contribution of several researchers among which S. Kitagawa,[7–9] G. Férey,[10–12] and J. R. Long,[13] should be highlighted. Being relatively young materials, during the last years, the chemistry of MOFs has undergone a relatively rapid evolution motivated by their intrinsic characteristics which make them ideal candidates to be applicable in many fields.[14,15]

Among the unique features of MOFs their high surface area, design flexibility, tuneable porosity and ease of chemical functionalization can be mentioned.[3] By playing with the size of the organic linker, tailorable pore morphologies can be acquired as can be appreciated in Figure I.2. Nonetheless, generally, porous structures tend to be unstable and can easily degrade under high pressure or extreme temperature conditions.[16]

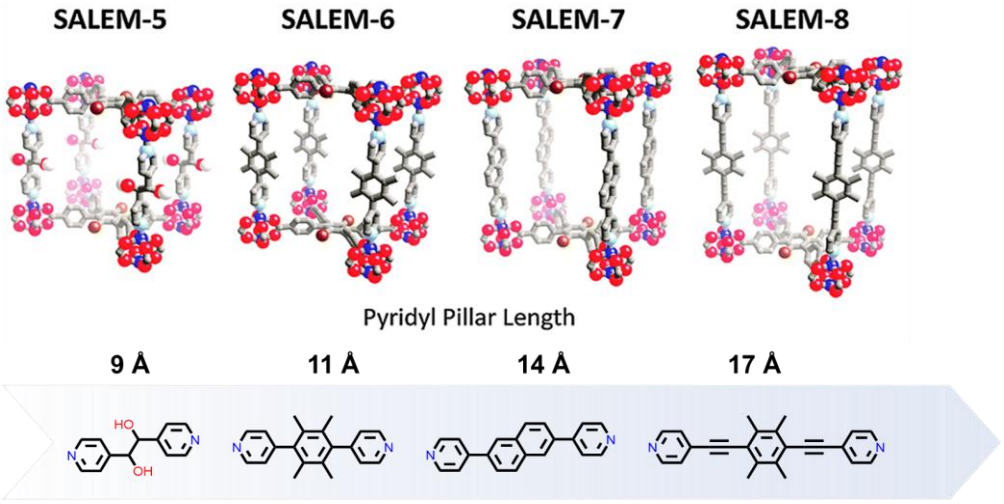

Figure I.2. Increasing pore size in an isoreticular series of paddlewheel MOFs.[17,18]

Synthetic methodologies

Traditionally, CPs and MOFs have been synthesised through direct self-assembly of metal ions and organic linkers under solvothermal conditions.[19] However, many synthetic strategies allow the preparation of MOFs. Those methods developed in recent years are electrochemical, sonochemical, and microwave, among others. Generally, these novel methods yield in most cases low cost, faster and yield cleaner products.[16] A summarized overview of the available synthetic methods is depicted in Figure I.3.

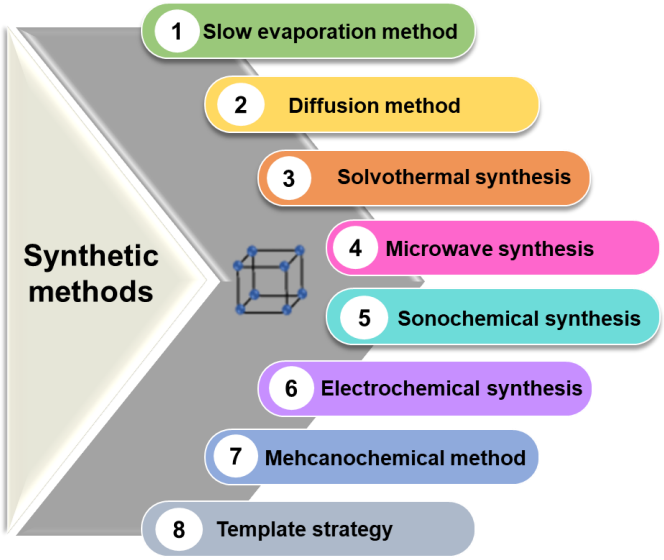

Figure I.3. Several synthetic methods for MOFs preparation.[20]

Additionally, several factors determine the synthesis of MOFs: reaction time and temperature selected, solvent and the nature of the metal ions and organic linkers. The combination of the aforementioned factors and the selected synthetic method would lead to the production of final materials with particular characteristics (particle sizes, distributions and morphologies). Consequently, a fine-tuning must be carried out taking into consideration the strengths and weaknesses that a particular synthetic method can offer trying to find an equilibrium for the selection of the most suitable method that would provide a solution to a particular application.[21]

Accordingly, and taking into consideration the infrastructure and disponible equipment, for the development of this thesis, the employed synthetic routes have been: slow evaporation, diffusion method, hydrothermal synthesis and microwave synthesis. Scale up and structural transformations.

When a process originally developed in a laboratory is going to be transferred into an industrial stage, several considerations must be taken. A key factor to consider is *Materials Tetrahedron*, a concept established by Materials Science and Engineering for the large-scale production of any material in the industry.[22] This tetrahedron correlates the structure, composition, synthetic procedure and performance of the material produced at a large scale with its production cost and final applicability.[23]

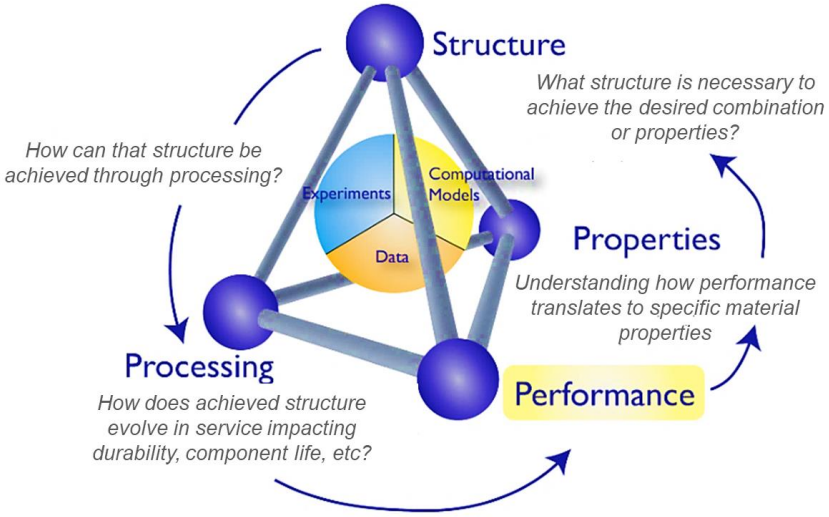

Figure I.4. The material tetrahedron is to be considered in the selection of materials in the industry.[22]

If *Materials Tetrahedron* is applied to large-scale production of MOFs, it is essential to first select the appropriate reagents (metal ion or node and organic linker). As metal ions or nodes, metal oxides and sulphates are the most commonly used raw materials.[24] Like organic linkers, the most widespread precursors are carboxylic acid derivatives such as terephthalic, isophthalic and formic acid. At the industry level, structures with higher complexity are often discarded because of poor accessibility and incremented production costs.[23,25]

In terms of solvent selection, water is presented as the best environmentally sustainable and “greener” option.[26] However, the use of other organic solvents is often required in MOF syntheses, such as DMF, DMSO or EtOH. The industry seeks to reduce and minimise the use of the latter, which are generally far more polluting and costly. As an interesting approach, solvent-free synthesis has been investigated in recent years; not only for offering the possibility to save solvent costs but also for the environmental

compromise.[27] In addition, it is necessary to consider the post-synthesis procedures of the material, as they largely determine the cost-effectiveness of a reaction. Filtration, cleaning, drying and activation processes are often time-consuming and affect the cost of the final product.[20,28]

On another level, MOFs offer the possibility to be modified either during the synthetic procedure (*in situ*) or post-synthetically. The first option refers to the introduction of ions, molecules, or polymers into the MOF pores while crystallization and generally procedures homogeneous materials; while the second procedure allows the addition of different species that are not compatible with the reaction media *a posteriori*, being in principle, easy to obtain heterogenous modified materials. Several post-synthetic modifications are summarized in Scheme I.1.[29]

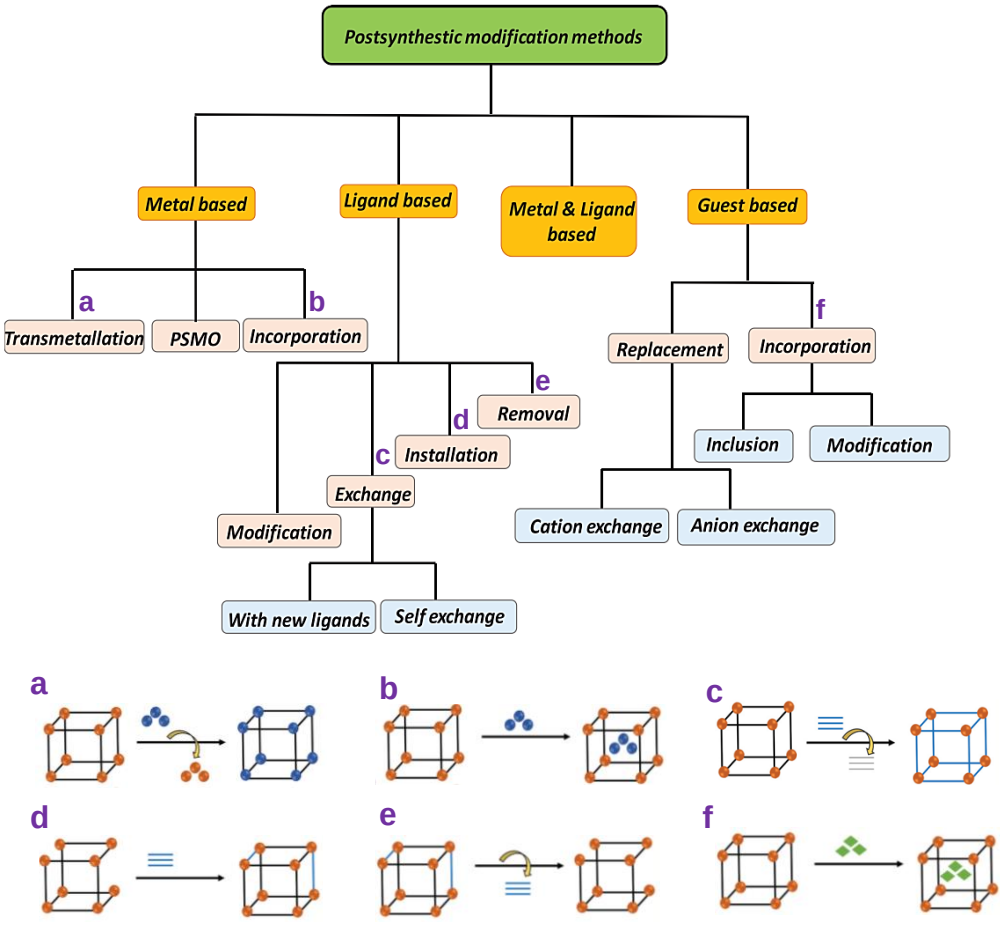

Scheme I.1. Scheme of possible PSM in MOFs synthesis and representation of a-e modifications.[29]

Relevant applications

The possibility of developing intriguing structures with unique properties has led MOFs to find application in many fields that broadens from heterogeneous catalysis,[30–32] magnetism,[33] chemical separation,[34–36] and luminescence[37–39] to energy storage.[3,19,40] An overview of possible applications is depicted in Figure I.5.[41]

In this thesis, several of these applications have been explored taking into consideration the suitability of the final material for its potential application in a determinate area. Consequently, we opt for presenting a summarized overview in the introduction and dedicate a focused and detailed explanation to the particular application selected for each family of compounds studied in Chapters 1-6.

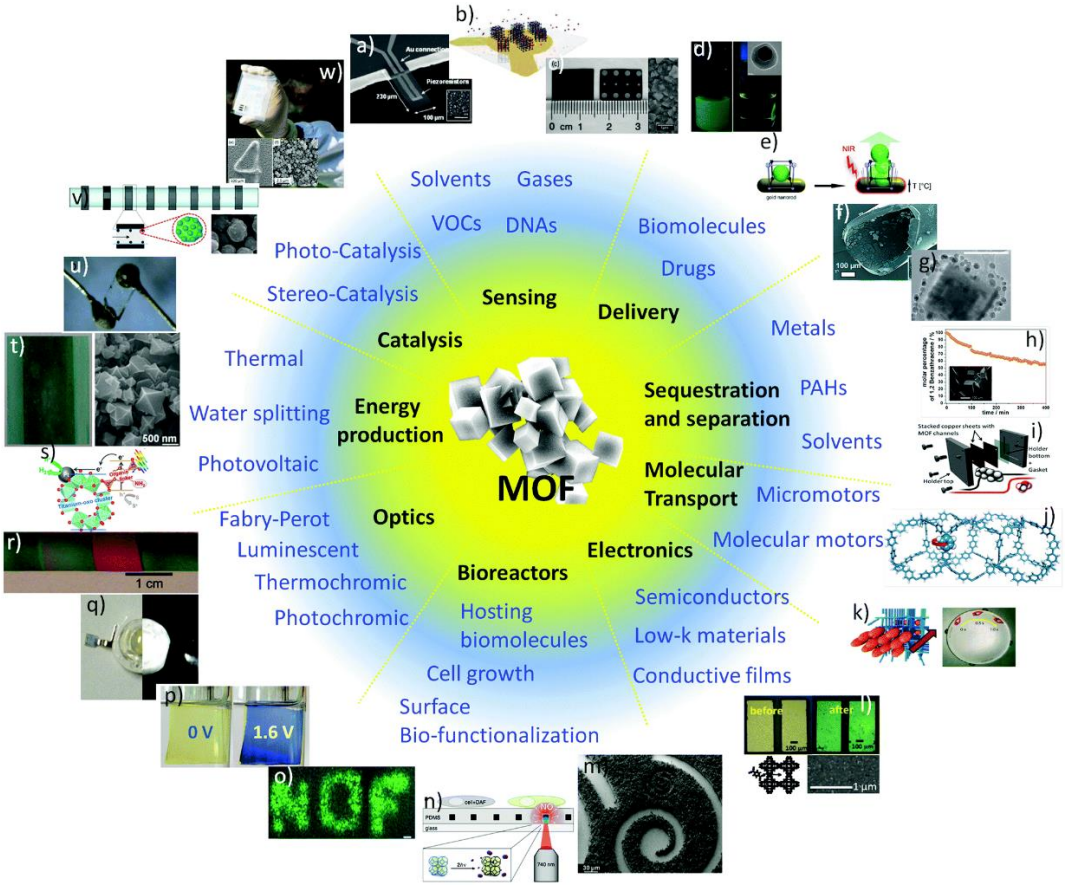

Figure I.5. Multidiscipline application of MOFs.[41]

Shaping of materials

Regardless of the presented exceptional properties of metal-organic frameworks, MOFs need to be adapted before being implemented into devices for a specific final application. In general, MOF synthesis yields insoluble loose powders with low packing density that are difficult to handle. Therefore, the shaping of MOFs is a prerequisite and adequate optimization is required.[28,42–44]

One of the easiest ways to shape MOFs is through mechanical compression. However, this procedure has some limitations. Under high-pressure conditions, the porous material can be amorphized. Also, due to the tight packing, the material may have a lower permeability to host molecules. In that case, the use of other substances called binders, such as sucrose, is employed by mixing with MOF to ease the formation of the composite.[44,45] The shaped MOFs structures with high mechanical stabilities are presented as beads, pellets or monoliths which afford to pack uniformly and maximize bulk density.[46]

Among the processing techniques for MOFs shaping mechanical pressure application, surface coating, template synthesis, or extrusion can be mentioned among others.[43] The optimal processing technique is selected by taking into consideration the MOF properties, the followed synthetic route and the final application to which is addressed. Figure I.6 exhibits several MOF processing techniques.[47,48]

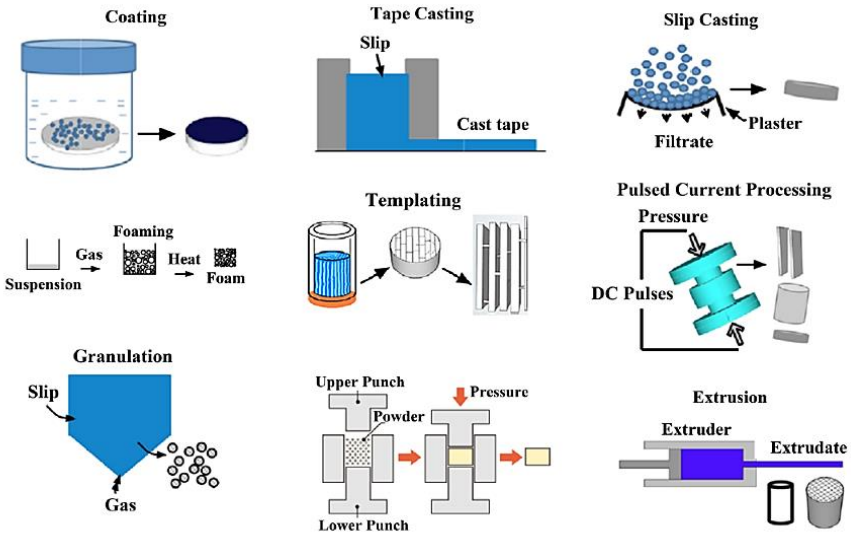

Figure I.6. Several MOFs shaping techniques.[42]

For the development of this thesis, we focused our attention on two of the mentioned shaping techniques, concretely, pelletization and immobilization into polymeric membranes have been performed.

Objectives

Having in mind the versatility of MOFs and CPs and the broad applications they offer; the present work is focused on the synthesis and structural characterization of multifunctional materials for various applications. The report on this doctoral thesis is divided into five main chapters and a complimentary sixth one which includes annexes. As aforementioned, the proposed distribution was performed in accordance with the organic ligand employed for the synthesis of each family of compounds. In each chapter, a summary will highlight the most representative information about the work. A general introduction will include the current state of the art of the research area in which the work is framed focusing on the particular applications that are explored. Afterwards, the most relevant findings will be explained along with a general discussion. To end, conclusions will be outlined.

References

1. Stuart R. Batten, Neil R. Champness, Xiao-Ming Chen, Javier Garcia-Martinez, Susumu Kitagawa, Lars Öhrström, Michael O'Keeffe, Myunghyun Paik Suh, and J.R. Terminology of metal–organic frameworks and coordination polymers (IUPAC Recommendations 2013)*. *Pure Appl. Chem.* **2013**, *85*, 1715–1724, doi:10.1007/978-1-4684-0904-8_6.

2. Wang, C.; Liu, D.; Lin, W. Metal-organic frameworks as a tunable platform for designing functional molecular materials. *J. Am. Chem. Soc.* **2013**, *135*, 13222–13234, doi:10.1021/JA308229P/ASSET/IMAGES/LARGE/JA-2012-08229P_0011.JPEG.

3. Singh, C.; Mukhopadhyay, S.; Hod, I. Metal–organic framework derived nanomaterials for electrocatalysis: recent developments for CO2 and N2 reduction. *Nano Converg.* **2021**, *8*, 1–10, doi:10.1186/S40580-020-00251-6/TABLES/2.

4. Hoskins, B.F.; Robson, R. Infinite Polymeric Frameworks Consisting of Three Dimensionally Linked Rod-like Segments. *J. Am. Chem. Soc.* **1989**, *111*, 5962–5964, doi:10.1021/JA00197A079/SUPPL_FILE/JA00197A079_SI_001.PDF.

5. Robson, R. Design and its limitations in the construction of bi- and poly-nuclear coordination complexes and coordination polymers (aka MOFs): A personal view. *Dalton Trans.* **2008**, 5113–5131, doi:10.1039/b805617j.

6. 0. M. Yaghi, G.L.& H.L. Selective binding and removal of guests in a microporous metal-organic framework. *Lett. to Nat.* **1995**, *378*, 703–706.

7. Kitagawa, S.; Kitaura, R.; Noro, S.I. Functional porous coordination polymers. *Angew. Chemie - Int. Ed.* **2004**, *43*, 2334–2375, doi:10.1002/anie.200300610.

8. Batten, S.R.; Champness, N.R.; Chen, X.M.; Garcia-Martinez, J.; Kitagawa, S.; Öhrström, L.; O'Keeffe, M.; Suh, M.P.; Reedijk, J. Terminology of metal-organic frameworks and coordination polymers (IUPAC recommendations 2013). *Pure Appl. Chem.* **2013**, *85*, 1715–1724, doi:10.1351/PAC-REC-12-11-20/MACHINEREADABLECITATION/RIS.

9. Omagari, S.; Nakanishi, T.; Seki, T.; Kitagawa, Y.; Takahata, Y.; Fushimi, K.; Ito, H.; Hasegawa, Y. Effective Photosensitized Energy Transfer of Nonanuclear Terbium Clusters Using Methyl Salicylate Derivatives. *J. Phys. Chem. A* **2015**, *119*, 1943–1947, doi:10.1021/JP512892F.

10. Férey, G. Hybrid porous solids: Past, present, future. *Chem. Soc. Rev.* **2008**, *37*, 191–214, doi:10.1039/b618320b.

11. Volkringer, C.; Loiseau, T.; Guillou, N.; Fèrey, G.; Haouas, M.; Taulelle, F.; Audebrand, N.; Margiolaki, I.; Popov, D.; Burghammer, M.; et al. Structural transitions and flexibility during dehydration - Rehydration process in the MOF-type aluminum pyromellitate A12(OH)2[C1008H2](MIL-118). *Cryst. Growth Des.* **2009**, *9*, 2927–2936, doi:10.1021/cg900276g.

12. McKinlay, A.C.; Morris, R.E.; Horcajada, P.; Férey, G.; Gref, R.; Couvreur, P.; Serre, C. BioMOFs: Metal-organic frameworks for biological and medical applications. *Angew. Chemie - Int. Ed.* **2010**, *49*, 6260–6266, doi:10.1002/anie.201000048.

13. Long, J.R.; Yaghi, O.M. The pervasive chemistry of metal-organic frameworks. *Chem. Soc. Rev.* **2009**, *38*, 1213–1214, doi:10.1039/b903811f.

14. Moosavi, S.M.; Nandy, A.; Jablonka, K.M.; Ongari, D.; Janet, J.P.; Boyd, P.G.; Lee, Y.;

Smit, B.; Kulik, H.J. Understanding the diversity of the metal-organic framework ecosystem. *Nat. Commun. 2020 111* **2020**, *11*, 1–10, doi:10.1038/s41467-020-17755-8.

15. Kong, X.J.; Li, J.R. An Overview of Metal–Organic Frameworks for Green Chemical Engineering. *Engineering* **2021**, *7*, 1115–1139, doi:10.1016/J.ENG.2021.07.001.

16. Raptopoulou, C.P. Metal-Organic Frameworks: Synthetic Methods and Potential Applications. *Mater. 2021, Vol. 14, Page 310* **2021**, *14*, 310, doi:10.3390/MA14020310.

17. Kirchon, A.; Feng, L.; Drake, H.F.; Joseph, E.A.; Zhou, H.-C. From fundamentals to applications: a toolbox for robust and multifunctional MOF materials. *Chem. Soc. Rev.* **2018**, *47*, 8611–8638, doi:10.1039/C8CS00688A.

18. Deria, P.; Mondloch, J.E.; Karagiaridi, O.; Bury, W.; Hupp, J.T.; Farha, O.K. Beyond post-synthesis modification: evolution of metal–organic frameworks via building block replacement. *Chem. Soc. Rev.* **2014**, *43*, 5896–5912, doi:10.1039/C4CS00067F.

19. Annamalai, J.; Murugan, P.; Ganapathy, D.; Nallaswamy, D.; Atchudan, R.; Arya, S.; Khosla, A.; Barathi, S.; Sundramoorthy, A.K. Synthesis of various dimensional metal organic frameworks (MOFs) and their hybrid composites for emerging applications – A review. *Chemosphere* **2022**, *298*, 134184, doi:10.1016/J.CHEMOSPHERE.2022.134184.

20. Sharanyakanth, P.S.; Radhakrishnan, M. Synthesis of metal-organic frameworks (MOFs) and its application in food packaging: A critical review. *Trends Food Sci. Technol.* **2020**, *104*, 102–116, doi:10.1016/J.TIFS.2020.08.004.

21. Howarth, A.J.; Peters, A.W.; Vermeulen, N.A.; Wang, T.C.; Hupp, J.T.; Farha, O.K. Best practices for the synthesis, activation, and characterization of metal−organic frameworks. *Chem. Mater.* **2017**, *29*, 26–39, doi:10.1021/acs.chemmater.6b02626.

22. Donald R. Askeland, Pradeep P. Fulay, W.J.W. *The Science and Engineering of Materials*; Cengage Le.; USA, 2017; ISBN 9781351431545.

23. Ren, J.; Dyosiba, X.; Musyoka, N.M.; Langmi, H.W.; Mathe, M.; Liao, S. Review on the current practices and efforts towards pilot-scale production of metal-organic frameworks (MOFs). *Coord. Chem. Rev.* **2017**, *352*, 187–219, doi:10.1016/j.ccr.2017.09.005.

24. Silva, P.; Vilela, S.M.F.; Tomé, J.P.C.; Almeida Paz, F.A. Multifunctional metal-organic frameworks: From academia to industrial applications. *Chem. Soc. Rev.* **2015**, *44*, 6774–6803, doi:10.1039/c5cs00307e.

25. Rubio-Martinez, M.; Avci-Camur, C.; Thornton, A.W.; Imaz, I.; Maspoch, D.; Hill, M.R. New synthetic routes towards MOF production at scale. *Chem. Soc. Rev.* **2017**, *46*, 3453–3480, doi:10.1039/c7cs00109f.

26. An, H.-T.; Zhang, X.; Dong, C.; Lu, M.-Y.; Li, R.; Xie, Y.; Xie, L.-H.; Li, J.-R. Seed-aided green synthesis of metal-organic frameworks in water. *Green Chem. Eng.* **2022**, doi:10.1016/J.GCE.2022.04.004.

27. Chen, D.; Zhao, J.; Zhang, P.; Dai, S. Mechanochemical synthesis of metal–organic frameworks. *Polyhedron* **2019**, *162*, 59–64, doi:10.1016/J.POLY.2019.01.024.

28. Kong, X.-J.; Li, J.-R. An Overview of Metal–Organic Frameworks for Green Chemical Engineering. *Engineering* **2021**, *7*, 1115–1139, doi:10.1016/J.ENG.2021.07.001.

29. Mandal, S.; Natarajan, S.; Mani, P.; Pankajakshan, A.; Mandal, S.; Mani, P.; Pankajakshan, A.; Natarajan, S. Post-Synthetic Modification of Metal–Organic

Frameworks Toward Applications. *Adv. Funct. Mater.* **2021**, *31*, 2006291, doi:10.1002/ADFM.202006291.

30. Alzamly, A.; Bakiro, M.; Hussein Ahmed, S.; Alnaqbi, M.A.; Nguyen, H.L. Rare-earth metal–organic frameworks as advanced catalytic platforms for organic synthesis. *Coord. Chem. Rev.* **2020**, *425*, 213543, doi:10.1016/j.ccr.2020.213543.

31. A, B.; N, K.; IS, K.; JA, B.; A, R.; J, G. Metal-Organic Frameworks in Heterogeneous Catalysis: Recent Progress, New Trends, and Future Perspectives. *Chem. Rev.* **2020**, *120*, 8468–8535, doi:10.1021/ACS.CHEMREV.9B00685.

32. Yang, D.; Gates, B.C. Catalysis by Metal Organic Frameworks: Perspective and Suggestions for Future Research. *ACS Catal.* **2019**, *9*, 1779–1798, doi:10.1021/ACSCATAL.8B04515.

33. Fernández, B.; Oyarzabal, I.; Fischer-Fodor, E.; MacAvei, S.; Sánchez, I.; Seco, J.M.; Gómez-Ruiz, S.; Rodríguez-Diéguez, A. Multifunctional applications of a dysprosium-based metal–organic chain with single-ion magnet behaviour. *CrystEngComm* **2016**, *18*, 8718–8721, doi:10.1039/C6CE01810F.

34. García, H.; Navalon, S. *Metal-Organic Frameworks : Applications in Separations and Catalysis*; ISBN 978-3-527-80910-3.

35. Saha, S.; Chandra, S.; Garai, B.; Banerjee, R. Carbon dioxide capture by metal organic frameworks. *Indian J. Chem. - Sect. A Inorganic, Phys. Theor. Anal. Chem.* **2012**, *51*, 1223–1230.

36. Li, J.-R.; Kuppler, R.J.; Zhou, H.-C. Selective gas adsorption and separation in metal–organic frameworks. *Chem. Soc. Rev.* **2009**, *38*, 1477–1504, doi:10.1039/B802426J.

37. Haldar, R.; Bhattacharyya, S.; Maji, T.K. Luminescent metal–organic frameworks and their potential applications. *J. Chem. Sci.* **2020**, *132*, 1–25, doi:10.1007/s12039-020-01797-y.

38. Hasegawa, M.; Ohmagari, H.; Tanaka, H.; Machida, K. Luminescence of lanthanide complexes: From fundamental to prospective approaches related to water- and molecular-stimuli. *J. Photochem. Photobiol. C Photochem. Rev.* **2022**, *50*, 100484, doi:10.1016/J.JPHOTOCHEMREV.2022.100484.

39. Cui, Y.; Yue, Y.; Qian, G.; Chen, B. Luminescent functional metal-organic frameworks. *Chem. Rev.* **2012**, *112*, 1126–1162, doi:10.1021/cr200101d.

40. Zhang, X.; Chen, A.; Zhong, M.; Zhang, Z.; Zhang, X.; Zhou, Z.; Bu, X.H. Metal–Organic Frameworks (MOFs) and MOF-Derived Materials for Energy Storage and Conversion. *Electrochem. Energy Rev.* 2019, *2*, 29–104.

41. Falcaro, P.; Ricco, R.; Doherty, C.M.; Liang, K.; Hill, A.J.; Styles, M.J. MOF positioning technology and device fabrication. *Chem. Soc. Rev.* **2014**, *43*, 5513–5560, doi:10.1039/C4CS00089G.

42. Ren, J.; Langmi, H.W.; North, B.C.; Mathe, M. Review on processing of metal-organic framework (MOF) materials towards system integration for hydrogen storage. *Int. J. Energy Res.* 2015, *39*, 607–620.

43. Liu, X.M.; Xie, L.H.; Wu, Y. Recent advances in the shaping of metal–organic frameworks. *Inorg. Chem. Front.* **2020**, *7*, 2840–2866, doi:10.1039/C9QI01564G.

44. Ntouros, V.; Kousis, I.; Pisello, A.L.; Assimakopoulos, M.N. Binding Materials for MOF

Monolith Shaping Processes: A Review towards Real Life Application. *Energies* **2022**, *15*, doi:10.3390/en15041489.

45. Ahmed, I.; Jhung, S.H. Composites of metal-organic frameworks: Preparation and application in adsorption. *Mater. Today* **2014**, *17*, 136–146, doi:10.1016/j.mattod.2014.03.002.

46. Valizadeh, B.; Nguyen, T.N.; Stylianou, K.C. Shape engineering of metal–organic frameworks. *Polyhedron* **2018**, *145*, 1–15, doi:10.1016/J.POLY.2018.01.004.

47. Ma, Q.; Zhang, T.; Wang, B. Shaping of metal-organic frameworks, a critical step toward industrial applications. *Matter* **2022**, *5*, 1070–1091, doi:10.1016/J.MATT.2022.02.014.

48. Ren, J.; Langmi, H.W.; North, B.C.; Mathe, M.; Jianwei Ren, Henrietta W. Langmi, B.C.N. and M.M. Review on processing of metal-organic framework (MOF) materials towards system integration for hydrogen storage. *Int. J. Energy Res.* **2015**, *39*, 607–620, doi:10.1002/er.3255.

Chapter 1

Multidimensional (2-(1H-tetrazol-5-yl)ethyl)amino acid derivative coordination compounds

Summary

In this chapter a family of multidimensional (2-(1H-tetrazol-5-yl)ethyl) amino acid coordination compounds have been synthesised and thoroughly characterized. For this purpose, glycine, valine, phenylalanine and tyrosine have been selected as starting amino acids and Mn^{2+}, Zn^{2+} and Cd^{2+} as metallic nodes. Three main applications have been explored for this family of compounds:

- From one side, for Mn^{2+} based dimer magnetic resonance imaging studies have been conducted, prompted by the number and disposition of the coordinated water molecules and taking into consideration the promising future of manganese-based coordination compounds as bio-compatible substitutes to conventional Gd based contrast agents.
- From another side, d^{10} block metal-based complexes allowed exploring photoluminescence properties derived by *in situ* synthesised ligands.
- Finally, amino acid preserved structural chirality allowed us to examine chiroptical properties, particularly focusing on circularly polarized luminescence.

1.1 Introduction

In the synthesis of novel coordination compounds *in situ* metal/ligand reaction is presented as a very important approach for organic- and coordination chemistry; traditionally, pre-synthesised commercially obtained ligands and metal ions in the form of metallic salts have been the source for the synthesis of novel coordination complexes. Nonetheless, recently, *in situ* ligand synthesis appears as an appealing synthetic procedure, particularly for the crystal engineering field since it allows providing not only very stable materials, but also products with limited accessibility or not easily obtained through conventional methods. In this procedure, conventional ligands are substituted by precursors that undergo a transformation and coordinate to metals to produce single crystal of the desired product.[1,2]

Generally, for the synthesis of coordination compounds with extended dimensionality solvothermal routes have allowed featuring chemical reactions at high temperature and pressure conditions yielding crystalline coordination complexes. Among in situ synthesised ligands, Demko-Sharpeless [2+3] cycloaddition reaction [3–5] is presented as an easy-handling alternative for the synthesis of tetrazole derivate ligands by reaction of organonitriles with metal azides (Scheme 1.1).[6,7]

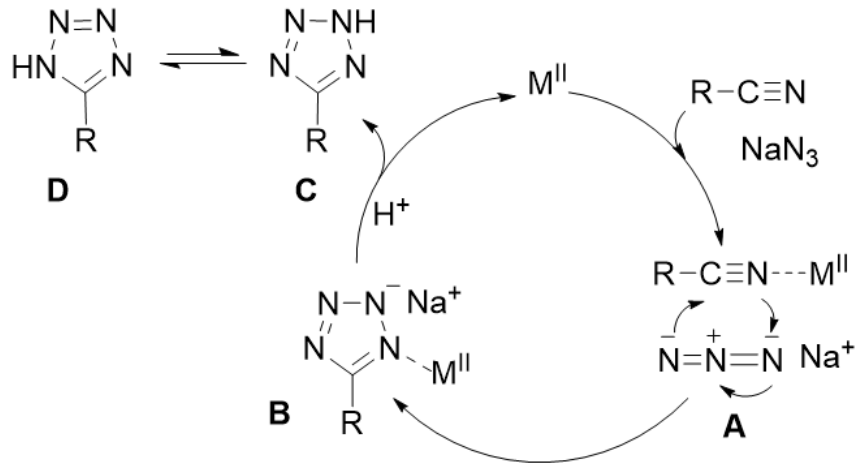

Scheme 1.1. A plausible mechanism for the formation of tetrazoles.[7]

In this chapter, our main goal will be the synthesis of novel luminescent chiral *in situ* generated tetrazole-derivative amino acid based coordination compounds as novel

imaging agents. *In situ* synthesised coordination compounds will derive by the cycloaddition of cyanoethylated amino acids with sodium azide according to the procedure described by Demko-Sharpeless.[5] For that, amino acids have been used as initial precursors and cyanoethyl functionalization has been previously carried out before tetrazolate transformation.[6,8–10] Amino acids are molecules that contain both amino and carboxylic functionalities and are the monomers in protein synthesis, in other words, the building blocks of life.[4] Tetrazoles are known to be precursors in multiple nitrogen containing heterocycles and are broadly investigated for many medical applications in diverse areas.[4,11–15] Because of their multifunctionality, many examples of several coordination compounds and MOFs have been reported in the literature so far.[16–19] In fact, the combination of amino acids with tetrazoles not only derives in ligands with multiple binding sites what promotes stable tridentate structures when coordinated to metal centres, but also tetrazole functionality enhances light absorption promoting better emissive capacity of the synthesised materials.

In diagnosis, when conditions, animalities, injuries or abnormalities such as damaged cellular tissue, tumours, organ injuries, among others need to be locally detected, magnetic resonance imaging (MRI) and fluorescence imaging are a powerful non-invasive techniques that allows focalised and temporal resolution and offers unique diagnostic information avoiding the need for harmful invasive interventions such as biopsies.[20]

Concretely, MRI is based on nuclear spins magnetization and makes use of energies in the radio frequency range to alter the alignment of the magnetization of nuclear spin, most commonly belonging to water molecules, thus causing these hydrogen nuclei to produce a detectable rotational magnetic field.[21]

In the absence of an external magnetic field protons spin in randomly oriented directions. However, when an external field is applied a small overall alignment of the nuclear spin will occur in the direction of the applied field. In MRI a uniform external magnetic field is employed to align protons of the water nuclei of the tissue being examined (Figure 1.1).[22]

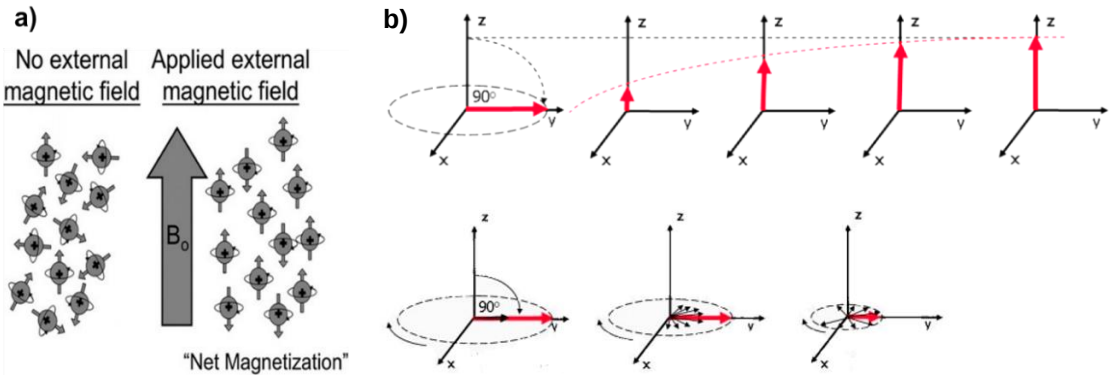

Figure 1.1. **a)** Alignment of protons with the B_0 field. In the absence of an external magnetic field, protons are oriented randomly. When the protons are placed in a strong magnetic field (B_0), a net magnetization will be produced parallel to the main magnetic field. **b)** T_1 (up) and T_2 (bottom) relaxation process gradual recovery to equilibrium after a 90º radio frequency pulse was applied to the system.[22,23]

This uniform alignment is disrupted by an external perpendicular magnetic field with a radio frequency pulse inducing perturbation in nuclei. On the removal of this field, nuclear spin suffers a recovery and precession period to come back to the initial field-aligned situation. This recovery occurs in both the x-y plane (transverse) and z axis (longitudinal) direction producing an NMR signal (Figure 1.2).

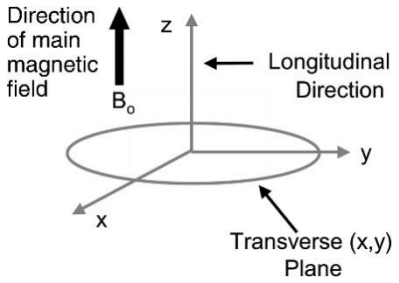

Figure 1.2. Coordination system in which transverse plane (x,y) and longitudinal direction (z) are represented.[22]

MRI, compared to NMR, offers spatial information which is obtained by the conjunction of NMR signal along with magnetic field gradients. Different pulse sequences and acquisition parameters allow for recording images emphasizing one type of contrast or another. In general, the density of the tissue to be analysed, and T_1 and T_2 values along with the specific pulse sequence define the contrast of a tissue in an MRI image.

The contrast of an image obtained will depend on the density of the nuclei to be observed presently in a voxel (volumetric unit of an image, analogous to a two-dimensional pixel) and to T_1 and T_2 relaxation times, longitudinal and transverse relaxation times respectively, which are related to the medium and are characteristic for each type of tissue.

In MRI, contrast agents (CA) are employed to enhance the detection of the anatomical information (contrast) obtained. Contrast agents are molecules, external to a body, that are used to emphasize the observation of a pathology operating by modifying relaxation times of water present in tissues. These agents are broadly used in clinical research (not only in MRI, nuclear imaging and computed tomography (CT) are also using this CA) and function by modifying with its presence the T_1 and T_2 relaxation time of the water molecules. Generally, the modification is a shortening of the relaxation times, with a modification in T_1 yields positive contrast or brightening and T_2 relaxation darkening of the affected tissue.

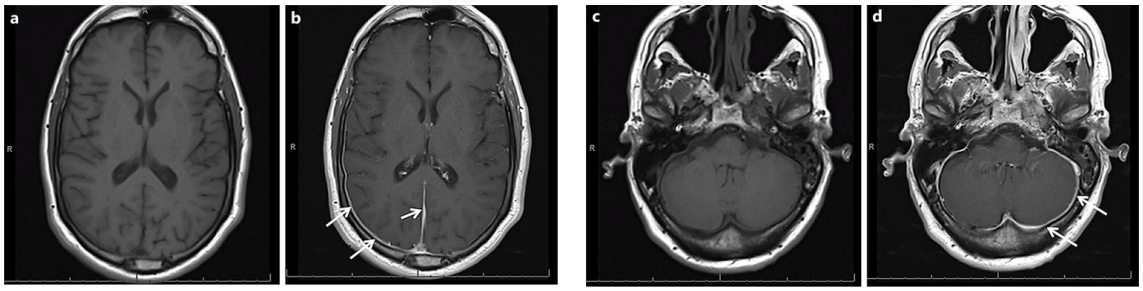

Figure 1.3. T_1-weighted pre- and post-contrast sequences showing contrast enhancement of pachymeninges (arrows). a, c Axial T_1 pre-contrast. b, d Axial T_1 post-contrast.[24]

Contrast agents can be classified regarding the mechanism of contrast generation. Four major subgroups are differentiated in function depending on their behaviour under the effect of a magnetic field (1) Paramagnetic (Gd^{3+} and Mn^{2+}), (2) superparamagnetic (Fe NPs), (3) ferromagnetic (Fe_3O_4) and (4) diamagnetic ($BaSO_4$).[25]

Contrast agents that shorten both longitudinal and transverse relaxation times to approximately the same degree are called T_1-contrast agents. Agents that shorten transverse relaxation times to a much greater extent than longitudinal relaxation times are called T_2-contrast agents.[26]

The parameter that measures the effect of contrast agents is relaxativity and it is commonly measured in mM^{-1} s^{-1} units. The final value of the relaxativity is a complex mixture of effects, including the molecular structure of the CA and/or kinetics of the complex with the water molecules. As a general strategy, a signal enhancement is obtained by maximizing the number of unpaired electrons of CA; in addition to, increasing the number of accessible water molecules in the inner sphere of the complex and minimizing the distance between metal ion and water protons enables signal increment.[27]

Several key elements must be taken into consideration for a successful design of a MRI CA: relaxativity, toxicity, stability, biodistribution and pharmacokinetics are among them. Because the potential *in vivo* use of the CAs, they should have minimal risk of toxicity and be stable in application media. This is why it is relatively common that CAs generally are presented as chelated metal complexes since they allow masking of the potential toxicity of free metal ions. Another key element is CAs' pharmacokinetic; which involves absorption, distribution, metabolism and excretion, this last step is described as the removal process of MRI CAs from the body. Although absorption and metabolism have relatively low influence along the aforementioned process, distribution is fundamental as it rules the scope of in vivo application of MRI. The pursued objective is to obtain a specific accumulation in the site of interest.[28,29]

In this work, we will focus on paramagnetic contrast agents. They are characterized by having unpaired electrons in the metal orbitals that act as T_1 shortening relaxation pathways in the protons of the water molecules present in the medium. Paramagnetic contrast agents or positive contrast agents are by far the clinically most employed CAs, that increase the MRI signal coming from the region where the CA is distributed to. In the literature, several examples can be found; Figure 1.4 summarizes some commercially approved T_1 contrast agents.[29]

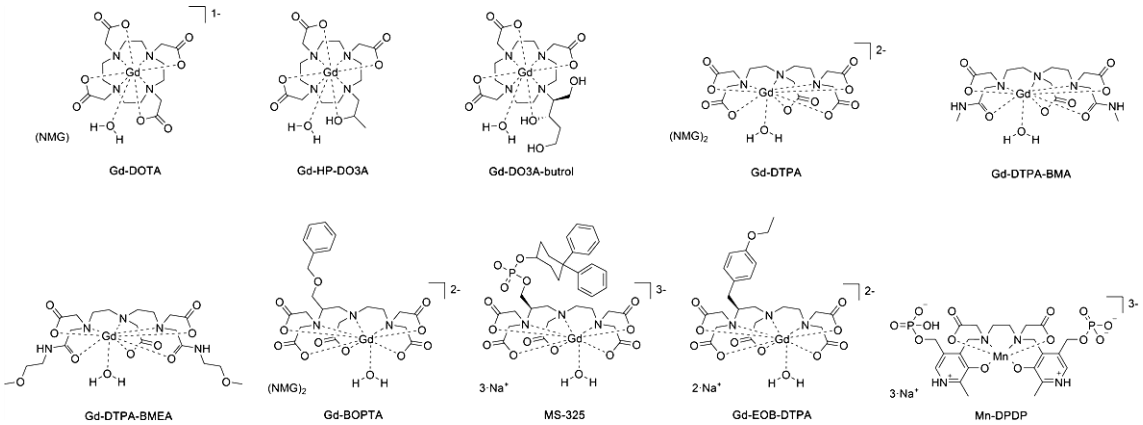

Figure 1.4. Commercially approved T_1 contrast agents. (NMG = meglumine).[29]

Among T_1 shortening contrast agents, historically, Mn^{2+} has been selected as the first chemical species to demonstrate the paramagnetic contrast enhancement in MRI. The very first MR phantom image published in 1973 by Lauterbur[30] summarizes that $MnSO_4$ was used to create the contrast in the first MR phantom images. Concerning biocompatibility, Mn^{2+} is an essential micronutrient and a cofactor of various enzymes responsible for diverse cellular functions and controls oxidative stress.[28] Nonetheless, in practice, Gd-based MRI CAs have been more extendedly used in clinics and have been heavily relied upon radiologic diagnosis of tissue. However, long-term Gd retention concerns from the point of view of toxicity since it is known that after CA exposure some patients can develop fibrosis.[31] This problem is particularly disturbing to patients suffering from renal insufficiency as CA's eliminated via is the kidney. In the attempt to overcome this problem, Mn^{2+} based CAs (high spin d^5 with five unpaired electrons), are presented as suitable candidates as they exhibit lower toxicity in comparison to Gd^{3+}. Nevertheless, it must be mentioned that in high concentrations Mn^{2+} ion is known to cause neural and cardiovascular toxicity.[27]

In this chapter, we will *in situ* synthesise a novel Mn^{2+} based coordination compound and examine it as a possible MRI contrast agent. Additionally, to analyse the photoluminescent behaviour, tetrazole derivative amino acid ligands and biologically acceptable d^{10} block metals will be selected as metal sources and with them, a family of compounds will be synthesised. The closed-shell configuration of metals disables possible potential quenching processes derived from d-d transitions permitting luminescent emission, consequently, the lowest energy excited states of their complexes

are mainly for a ligand centred (LC) or/ and ligand to ligand charge transfer (LLCT) nature.[32–34]

Ligand centred emission processes are favoured by extended conjugated systems. Tetrazole derivative *in situ* synthesised amino acid ligands will display such aromaticity being adequate candidates for exhibiting long lasting luminescent properties.[35]

Finally, we further wanted to exploit another functionality of our materials and motivated by the preserved chirality of the amino acid precursors in synthesised compounds, in this chapter, we will investigate the ability of our materials to display differential absorption of right- and left-circularly polarized light (Figure 1.5).[36]

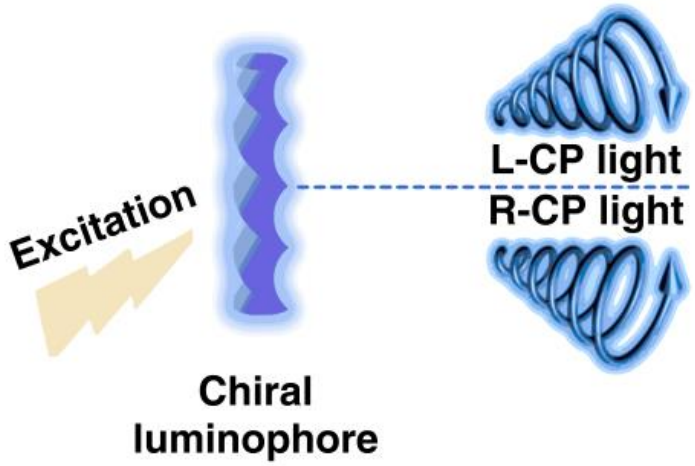

Figure 1.5. Circularly polarized luminescence.[37]

Chirality of a molecule refers to a geometrical property of an object not being superimposable to its mirror image. Chiral molecules exhibit unique photophysical properties such as circular dichroism (CD) and, interestingly, some examples have also been described to show circularly polarized luminescence (CPL).[38]

CPL is defined as the intensity difference of left and right circularly polarized radiation emitted by a chiral luminophore and is quantified by luminescence dissymmetry factor g_{lum}[39] and is calculated according to Equation 1.1.

$$g_{lum} = 2(I_L - I_R)/(I_L + I_R) \qquad \textbf{Equation 1.1}$$

Where I_L and I_R refer to the intensity of left- and right-CPL, respectively. The maximum value of 2 reached by the equation refers to a completely left- or right-polarized CPL while g_{lum} values of 0 correspond to unpolarized luminescence. In other words, the higher g_{lum} value refers to a better degree of polarization of the emitted light, referring to lower energy loss.[37]

Circularly polarized luminescence can be employed as the source of information about chiral substances (conformation information) and finds application in diverse areas from information processing,[40] OLED[37,41] to bioimaging.[42] Exploring new approaches to construct CPL active materials with maximum g_{lum} values is if of great importance.

Herein, a family of tetrazolyl amino acid derived coordination compounds will be synthesised and characterized for finding application in molecular imaging, photoluminescence and chiroptical applications.

1.2 Materials and methods

1.2.1 Compound synthesis

1.2.1.1 Synthesis of N-(2-cyanoethyl) amino acid derivative precursor.

The synthesis of the precursors was carried out according to the procedure described by McKinney et al.[10]

N-(2-Cyanoethyl)glycine: 3.76 g (0.05 mol) of glycine was suspended in 20 mL of deionized water in an Erlenmeyer flask. One equivalent of sodium hydroxide was dissolved in 10 mL of water and added dropwise to the amino acid solution. In this step, it is important to keep the temperature below 30 ºC. To the cold alkaline solution, 1.25 equivalents of acrylonitrile were added dropwise and kept stirring for 2 h until a colourless solution was obtained. It is important to notice that temperature may rise while acrylonitrile is being added. That is why acrylonitrile addition to the amino acid solution was done in an ice bath to avoid side reactions which would reduce the yield of the monocyanoethyl derivative. Subsequently, the solution had stood overnight in the fridge. Then, 2.86 mL (0.05 mol) of acetic acid was added to the reaction keeping magnetic stirring. Subsequently, reaction volume was reduced to 10 mL and 50 mL ethanol was added afterwards. After standing overnight in the fridge N-(2-Cyanoethyl)-glycine precipitates and is collected by filtration and washed with ethanol.

N-(2-Cyanolethyl)-L- or -D-valine: The same procedure was used for the cyanoethylation of L- or D-valine. In this case, 2 g (0.017 mol) of L- or D-valine were suspended in 10 mL of deionized water. The addition of one equivalent of NaOH dissolved in 4 mL of H_2O allowed the dissolution of the ligand. As previously described, this step was carried out in an ice bath. Finally, 1.67 mL (0.0255 mol) of acrylonitrile was added keeping the temperature below 30 ºC to avoid side reactions left reacting for 2 h. The resulting solution was stood in the fridge overnight before ligand acidification with an equivalent of acetic acid with 1 mL (0.017 mol). Finally, 50 mL of EtOH was added to promote ligand complete precipitation. After standing for an hour in the fridge crystals were collected by filtration and washed with ethanol. The product was recrystallized in hot water.

N-(2-Cyanoethyl)-L- or -D-phenylalanine: For the synthesis of these precursors the procedure followed in the cyanoethylation of glycine was pursued. In this case, 1.65 g (0.1 mol) of L- or D- phenylalanine, 0.6 g (0.015 mol) of NaOH and 1.1 mL (0.0165 mol)

of acrylonitrile were used. After the addition of acrylonitrile and standing in the fridge overnight it was necessary to reflux for 2 h to complete de reaction. The acidification process was performed by adding an equivalent of concentrated hydrochloric acid and precipitation occurred instantaneously. After standing in the fridge overnight the precipitate was collected by filtration and washed with water.

N-(2-Cyanoethyl)-L- or -D-tyrosine: It was followed exactly the procedure described for phenylalanine. 2 g (0.01 mol) of L- or D- tyrosine, 0.6 g (0.015 mol) NaOH and 1.1 mL (0.0165 mol) acrylonitrile were used to carry on the reaction.

1.2.1.2 Transition metal-based compound synthesis

In general, the synthesis of the complexes was performed by hydrothermal reaction of the appropriate metal chloride or nitrate (1 mmol) with the corresponding N-(2-cyanoethyl)amino acid derivative (1 mmol) and sodium azide (1.5 mmol), in water/methanol solvent mixture (5:5 mL) at 100 ºC for 12 h followed by cooling to room temperature over 3 h produced single crystals. Their crystal structures were determined using single crystal X-ray crystallography. In the succeeding lines a detailed procedure will be described for each compound:

Synthesis of single crystals of $[Mn_2L_2(H_2O)_4]\cdot H_2O$, in advance Mn_gly (1.1)

0.128 g (1 mmol) of N-(2-cyanoethyl)glycine (H_2L^1) were dissolved in 5 mL of an equal mixture of H_2O/MeOH, 0.065 g (1 mmol) of NaN_3 was added to the solution and 0.198 g (1 mmol) of $Mn(NO_3)_2\cdot 4H_2O$. The solution was placed in a Teflon liner vessel and heated at 100 ºC for 12 h. Single crystals were obtained after cooling down to room temperature.

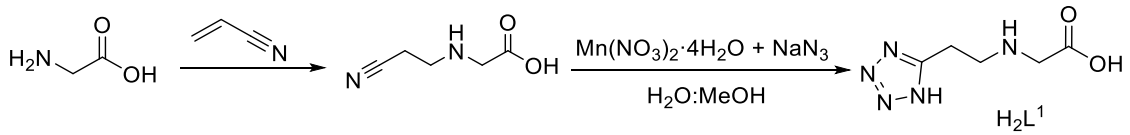

Scheme 1.2. *In situ* synthesis of (2-(1H-tetrazol-5-yl)ethyl)glycine ligand by hydrothermal routes.

Synthesis of single crystals of $[ZnL^2]_n$, in advance Zn-L/D_val (1.2/ 1.3)

0.26 g of (1.5 mmol) of N-(2-cyanoethyl)-L or D-valine (H_2L^2) were dissolved in 10 mL water/ 5 mL methanol mixture. To this solution, first 0.129 g (1.98 mmol) of NaN_3 were added and once dissolved, 0.45 g (1.5 mmol) of $Zn(NO_3)_2 \cdot 6H_2O$. Magnetic stirring was kept for 10 minutes and the colourless solution was placed in a capped vial and placed at 100 ºC for 12 h to get single crystals.

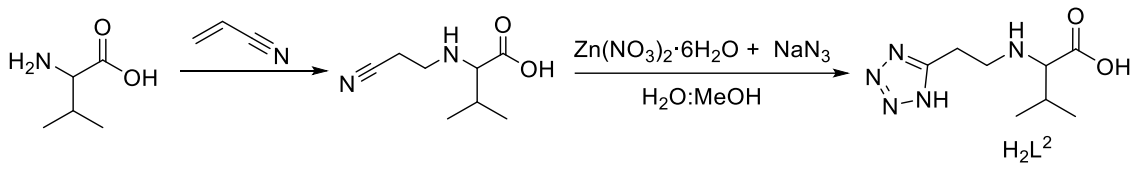

Scheme 1.3. *In situ* synthesis of (2-(1H-tetrazol-5-yl)ethyl)valine ligand by hydrothermal routes.

Synthesis of single crystals of $[ZnL^3]_n$, in advance Zn-L/D_phen (1.4/ 1.5)

0.22 g of (1 mmol) of N-(2-cyanoethyl)-L- or -D-phenylalanine (H_2L^3) were suspended in a mixture of 10 mL H_2O/ 5 mL MeOH. 0.04 g (1 mmol) of NaOH were added to the suspension to get a dissolution to which 0.065 g (1 mmol) of NaN_3 were added. Finally, 0.30 g (1 mmol) of $Zn(NO_3)_2 \cdot 6H_2O$ to the reaction and kept stirring for 10 minutes. The final solution was poured into a capped vial and placed in the oven for 12 h at 100 ºC. Single crystals were obtained after slowly cooling down to room temperature.

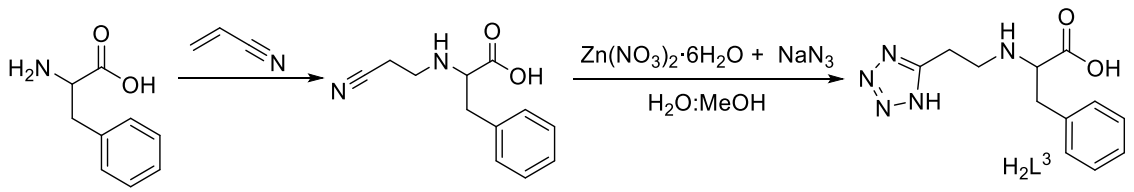

Scheme 1.4. *In situ* synthesis of (2-(1H-tetrazol-5-yl)ethyl)phenylalanine ligand by hydrothermal routes.

Synthesis of single crystals of {[ZnL^4]·H$_2$O}$_n$, in advance Zn-L/D_tyr (**1.6**/ **1.7**)

The same procedure was followed for the synthesis of Zn-L/D_phen (**1.4**/**1.5**), but in this case, 0.234 g (1 mmol) of N-(2-cyanoethyl)-L- or -D-tyrosine (H_2L^4) were used for the reaction.

Synthesis of {[CdL^4]·H$_2$O}$_n$, in advance Cd-L/D_tyr (**1.8**/ **1.9**)

0.117 g (0.5 mmol) of N-(2-cyanoethyl)-L- or -D-tyrosine (H_2L^4), 0.154 g (0.5 mmol) of $Cd(NO_3)_2{\cdot}4H_2O$ and 0.0325 g (0.5 mmol) of NaN_3 were weighted in a vial. 8 mL of water were added and placed in a Teflon liner vessel solvothermal reactor for 48 h at 140 ºC. After slow cooling to room temperature, the polycrystalline powder was obtained, which was collected by filtration and washed with water.

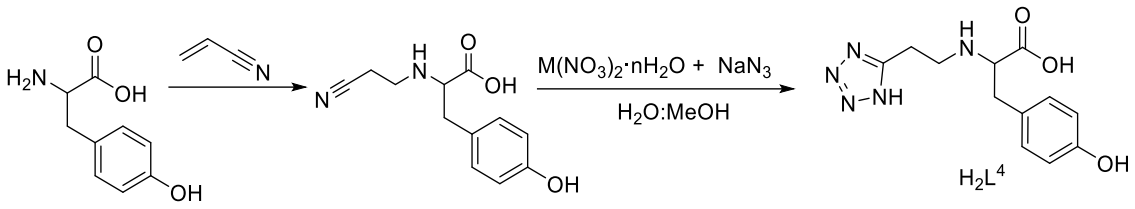

Scheme 1.5. *In situ* synthesis of (2-(1H-tetrazol-5-yl)ethyl)tyrosine ligand by hydrothermal routes, being M = Zn and Cd for compounds **1.6**, **1.7** and **1.8**, **1.9**, respectively.

The corresponding structural characterization (elemental analysis, FTIR spectra and PXRD) was performed for all compounds to confirm the purity of the samples. For more details consult Appendix 1 (Table A1.1, Figure A1.1-4 and Figure A.1.5-6.).

1.2.2 Relaxation time measurements

Relaxativity measurements were carried out in compound .**1.1** (Mn_gly). For that purpose, solutions of 1 mM, 0.5 mM and 0.1 mM concentration (relative to Mn^{2+}) were prepared in Milli-Q water and analysed. To ensure that the material was completely dissolved, they were sonicated over 30 minutes and filtered off by a 0.22 µm microfilter. Milli-Q water employed in dissolution preparation was used as blank or reference in relaxativity measurements. Three different measurements of T_1 and T_2 were performed for each sample and each concentration. Relaxivity values r_1 and r_2 were obtained from the slopes of the curves $1/T_1$ and $1/T_2$ vs. the concentration of Mn^{2+} expressed in mM.

1.2.3 Chiroptical properties

General procedure for circular dichroism experiments

Samples for CD measurements were prepared as follows: a precision weighted amount of material (2 mg) was suspended in Milli-Q H_2O (4 mL) and sonicated over 1 h.

General procedure for circularly polarized luminescence experiments

Samples for CPL measurements were prepared as follows: a precision weighted amount of well-grounded material (5 mg) was suspended in 4 mL H_2O and sonicated over 5 min. To prevent material decantation sample was manually shacked between spectra collection. For racemic mixture preparation, well-grounded 2.5 mg of L-enantiomer and 2.5 mg of D-enantiomer were weighed and suspended in 4 mL of H_2O. Next, fluorescence and CPL spectra were collected for pure enantiomers. The resulting CPL spectra were calculated as an average of recorded 100 scans.

For data collection, a set of 100 scans for each enantiomer and the racemic mixture have been recorded in suspension exciting the sample by 300 nm LED. Note that, the equipment possesses a negative correction.

As a proof of concept, and to ensure that the material remains stable in water, 5 mg of material were suspended in 4 mL of H_2O and sonicated for 5 minutes. Then, the decanted solution was filtered with the aid of a 45 µm syringe and fluorescence and CPL of the solution were collected giving in all enantiomeric pairs a negligible CPL and luminescence signal.

1.2.4 Statistical analysis of the chiroptical properties

F-test variance and t-test were conducted intending to conclude whether variances significantly differ among them and determine the veracity of the recorded CPL signals. In t-student statistical analysis, a comparison of L- and D- enantiomers data concerning racemic mixture was performed.

$$F = \frac{s_1^2}{s_2^2} \ (s_1 > s_2)$$ **Equation 1.2**

$H_0 \equiv \ s_1^2 = \ s_2^2$ ($F_{calc} < F_{tab}$) Variances are not significantly different

$H_1 \equiv s_1^2 \neq s_2^2$ ($F_{calc} \geq F_{tab}$) Variances are significantly different

Additionally, t-student statistical analysis was carried out as aforementioned to compare data obtained for each enantiomer concerning racemic mixture.

$$t = \frac{|\bar{x}_1 - \bar{x}_2|}{s_p\sqrt{\frac{1}{n_1} + \frac{1}{n_2}}}$$ **Equation 1.3**

$$s_p = \sqrt{\frac{(n_1 - 1)s_1^2 + (n_2 - 1)s_2^2}{n_1 + n_2 - 2}}$$ **Equation 1.4**

s_1 refers to each enantiomer and s_2 to racemic mixture.

$H_0 \equiv s_1 \leq s_2$ $(t_{calc} < t_{tab})$ Indicates are not significantly different

$H_0 \equiv s_1 > s_2$ $(t_{calc} \geq t_{tab})$ Indicates are significantly different with enantiomers giving a higher signal than the racemic mixture.

1.3 Results and discussion

1.3.1 Structural characterization

Single crystal studies revealed that compound **1.1** exhibits the following formula $[Mn_2L^1{}_2(H_2O)_4]\cdot H_2O$, where H_2L^1 = (2-(1H-tetrazol-5-yl)ethyl)glycine. It was *in situ* synthesised by [2+3] cycloaddition of sodium azide to N-(cyanoethyl)glycine and crystallizes in the monoclinic *P*21/*c* space group. The asymmetric unit of this dimeric entity is composed of a ligand molecule and a metallic centre (Figure 1.6a). The coordination environment is completed by the coordination of two water molecules, and a crystallization water molecule.

Mn1 atom presents a hexacoordinated MnN_3O_3 environment composed by the coordination of three nitrogen atoms belonging two of them to a tetrazolyl moiety (from two different ligands) and the remaining nitrogen corresponding to the amino group of the amino acid precursor. One oxygen atom corresponds to a monodentate carboxylate moiety of the organic ligand and the remaining two oxygens to two coordinated water molecules. Continuous shape measurements (CShMs)[43] reveal that Mn1 builds octahedral polyhedron (Table A1.5).

Growing the asymmetric unit, it can be seen that the dimeric structure presents hydrogen bonding governed by supramolecular interactions (Figure 1.6b).

a) **b)**

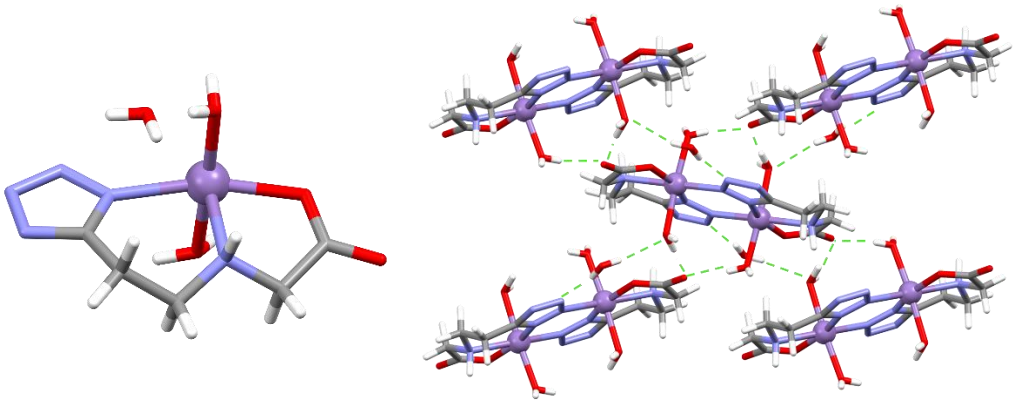

Figure 1.6. a) Excerpt of the asymmetric unit of compound Mn_gly (**1.1**) and **b)** perspective view of the packed dimeric structure where H bonding interactions are shown in dashed green lines.

Single-crystal X-ray crystallographic studies carried out on isostructural enantiomeric pairs with the formula $[ZnL^2]_n$ where H_2L^2 is 2-(1H-tetrazol-5-yl)ethyl)-L-valine or (2-(1H-tetrazol-5-yl)ethyl)-D-valine generated by [2+3] cycloaddition of sodium azide to the corresponding N-(cyanoethyl)-L or D-valine, yields respectively compounds Zn-L_val (**1.2**) and Zn-D_val (**1.3**). The enantiomeric pairs reveal three dimensional (3D) MOFs that crystalise in the orthorhombic $P2_12_12_1$ space group (Figure 1.7). The asymmetric unit of **1.2** and **1.3** is comprised of doubly deprotonated ligand (carboxylate and tetrazolate) molecule and a metallic centre. The organic linker, 2-(1H-tetrazol-5-yl)ethyl)valine coordinates to the Zn^{2+} from the oxygen atom of the carboxylate moiety as well as from two nitrogen atoms, one belonging to the amino group and the other belonging to the tetrazolate ring of the amino acid derivative.

Zn1 presents a $[ZnN_3O_2]$ coordination environment in compounds Zn-L_val (**1.2**) and Zn-D_val (**1.3**) (Figure 1.7) composed of the *syn-anti* monodentate coordination of two oxygen atoms belonging to the carboxylate moieties of two ligands molecules, two nitrogen atoms of a tetrazolate moiety again from adjacent ligands as well as from the coordination of the nitrogen atom belonging to the amino group of the amino acid derivative. Continuous shape measurements (CShMs) [43] reveal that Zn1 build a spherical square pyramid (SPY-5) polyhedron (Table A1.6).

The analysis of the topology through TOPOS Pro software[44] reveals that compounds Zn-L_val (**1.2**) and Zn-D_val (**1.3**) possess a 6-c unimodal net with $(3^3{\cdot}5^9{\cdot}6^3)$ point symbol and **lcy** topology. Although the structure expands in three dimensions the growth of the structure does not have solvent accessible volume according to the geometrical calculations performed with the PLATON-v1.18 program (Figure A1.8).

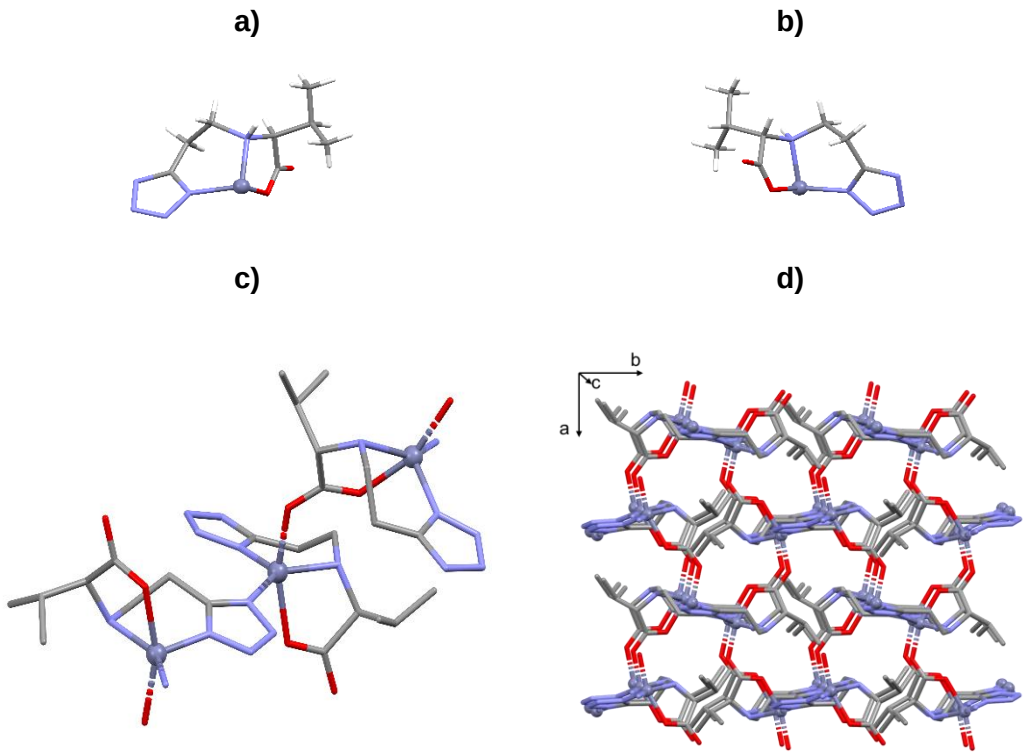

Figure 1.7. a) View of the asymmetric unit of Zn-L_val and **b)** Zn-D_val, compounds **1.2** and **1.3**, respectively, **c)** Perspective view of the ligand coordination modes in Zn-L_val and **d)** packed structure.

Single-crystal X-ray crystallographic studies undertaken on isostructural enantiomeric pairs with the formula $[ZnL^3]_n$ where H_2L^3 is 2-(1H-tetrazol-5-yl)ethyl)-L-phenylalanine or (2-(1H-tetrazol-5-yl)ethyl)-D-phenylalanine which was derived by *in situ* [2+3] cycloaddition of sodium azide with the corresponding N-(cyanoethyl)-L or D-phenylalanine, yields respectively compounds Zn-L_phen (**1.4**) and Zn-D_phen (**1.5**). Note that good quality single-crystals have been only obtained for compound **1.5** but due to the isostructural character of compound **1.4** in the following section compound **1.5** description will be performed in detail as a representative example of the enantiomeric pair. Compound Zn-L_phen (**1.4**) and Zn-D_phen (**1.5**) exhibit layered two-dimensional structure that crystallises in the monoclinic $P2_1$ space group. The asymmetric unit of **1.4** and **1.5** is composed of a doubly deprotonated ligand molecule and a Zn^{2+} metallic centre.

As for the previous examples, the organic ligand coordinates the metallic centre from the carboxylate moiety (in a monodentate way in *syn-anti* disposition to

neighbouring metallic centres) and the nitrogen's, one belonging to the tetrazolate moiety and the other to the amino group of the amino acid derivative (Figure 1.8).

Zn1 presents a [ZnN_3O_2] coordination environment in compounds Zn-L_phen (**1.4**) and Zn-D_phen (**1.5**) composed of the *syn-anti* monodentate coordination of the oxygens belonging to adjacent carboxylates, in addition to the coordination from the nitrogen of the amino group as well as to two nitrogen atoms from the tetrazolate moiety. Continuous shape measurements (CShMs)[43] reveal that Zn1 build a spherical square pyramid (SPY-5) polyhedron (Table A1.6).

Two-dimensional layered topology performed with TOPOS Pro software[44] exhibits that compounds Zn-L_phen (**1.4**) and Zn-D_phen (**1.5**) display a 3.5-c unimodal net with ($\{3\cdot5^2\}\{3^2\cdot5^3\cdot6^4\cdot7\}$) point symbol and **3,5L50** topology.

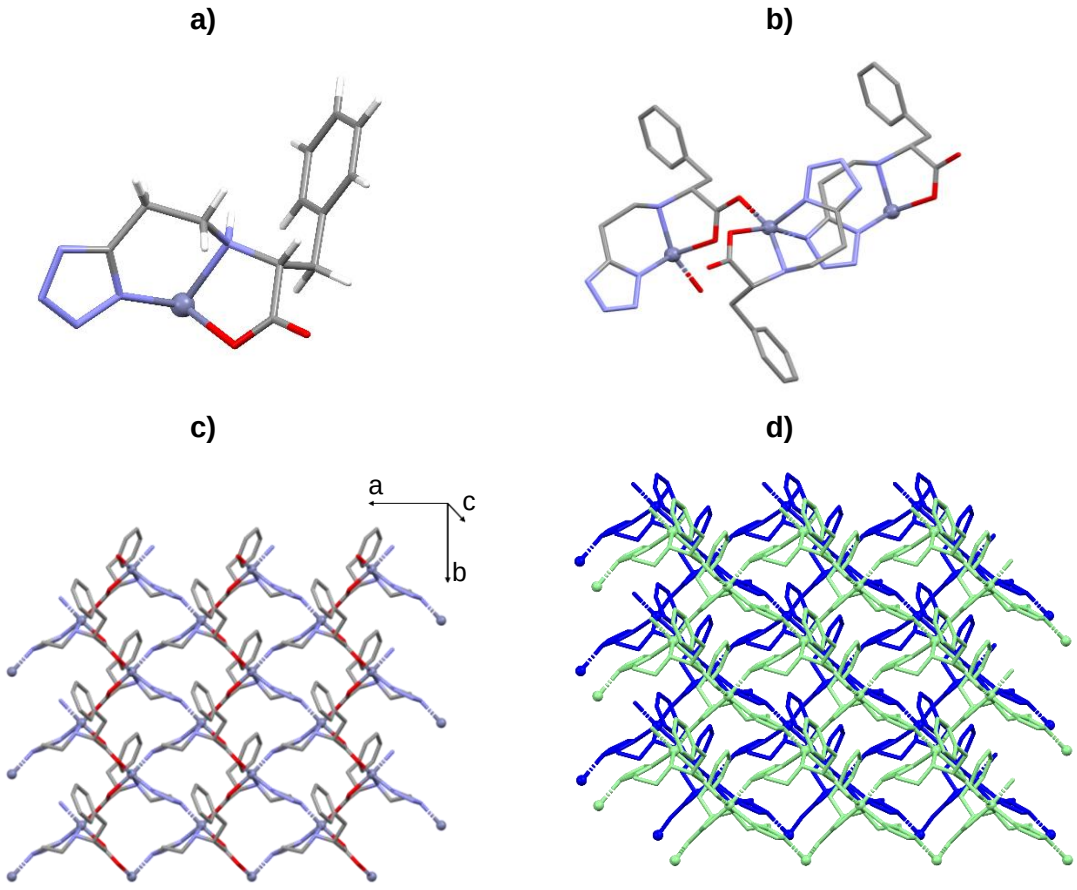

Figure 1.8. a) Asymmetric unit **b)** excerpt of the crystal structure of compound **1.5**$_{\text{Zn-D\_phen}}$ **c)** and **d)** perspective view and and packed structure

To conclude with structural description, single-crystal X-ray crystallographic studies performed on isostructural enantiomeric pairs with the formula $\{[ZnL^4]\cdot H_2O\}_n$ and $\{[CdL^4]\cdot H_2O\}_n$ where H_2L^4 is 2-(1H-tetrazol-5-yl)ethyl)-L-tyrosine or (2-(1H-tetrazol-5-yl)ethyl)-D-tyrosine *in situ* generated by [2+3] cycloaddition of sodium azide to the corresponding N-(cyanoethyl)-L- or -D-tyrosine, yields respectively two isostructural enantiomeric pairs, in advance, Zn-L_tyr (**1.6**) and Zn-D_tyr (**1.7**), Cd-L_tyr (**1.8**) and Cd-D_tyr (**1.9**), respectively. Good quality single-crystals have been obtained for Zn^{2+} counterparts, nonetheless, due to the isostructural nature of Cd^{2+} enantiomeric pairs, the crystal description of **1.6** will be held in advance as a representative example of the isostructural family.

Compounds **1.6**-**1.9** exhibit a two-dimensional structure that crystallises in the orthorhombic $P2_12_12_1$ space group. The asymmetric unit of **1.6**-**1.9** is composed of a doubly deprotonated (carboxylate and tetrazolate; note that the phenol group remains unaltered providing intermolecular hydrogen bonds) ligand molecule and a Zn^{2+} metallic centre in addition to a crystallization water molecule.

In resemblance to the previously described structures, 2-(1H-tetrazol-5-yl)ethyl) tyrosinate ligand coordinates the metallic centre from the carboxylate moiety (in a monodentate way in *syn-anti* disposition to adjacent metallic centres) and from the nitrogen's one, belonging to the tetrazolate moieties and the other to the amino group of the amino acid derivative (Figure 1.9).

Zn1 presents a $[ZnN_3O_2]$ coordination environment in compounds **1.6**-**1.9** composed of the *syn-anti* monodentate coordination of the oxygens belonging to adjacent carboxylates, in addition to the coordination from the nitrogen of the amino group as well as to two nitrogen atoms from the tetrazolate moiety. Continuous shape measurements (CShMs)[43] reveal that Zn1 build a spherical square pyramid (SPY-5) polyhedron (Table A1.6).

Two-dimensional layered topology performed with TOPOS Pro software[44] exhibits that compounds **1.6**-**1.9** display a 3.7-c unimodal net with $(\{3\cdot5^2\}\{3^2\cdot5^{11}\cdot6^7\cdot7\})$ point symbol. Growing the asymmetric unit, it can be seen that the layered structure presents remarkable supramolecular interactions which are governed by hydrogen bonding interactions.

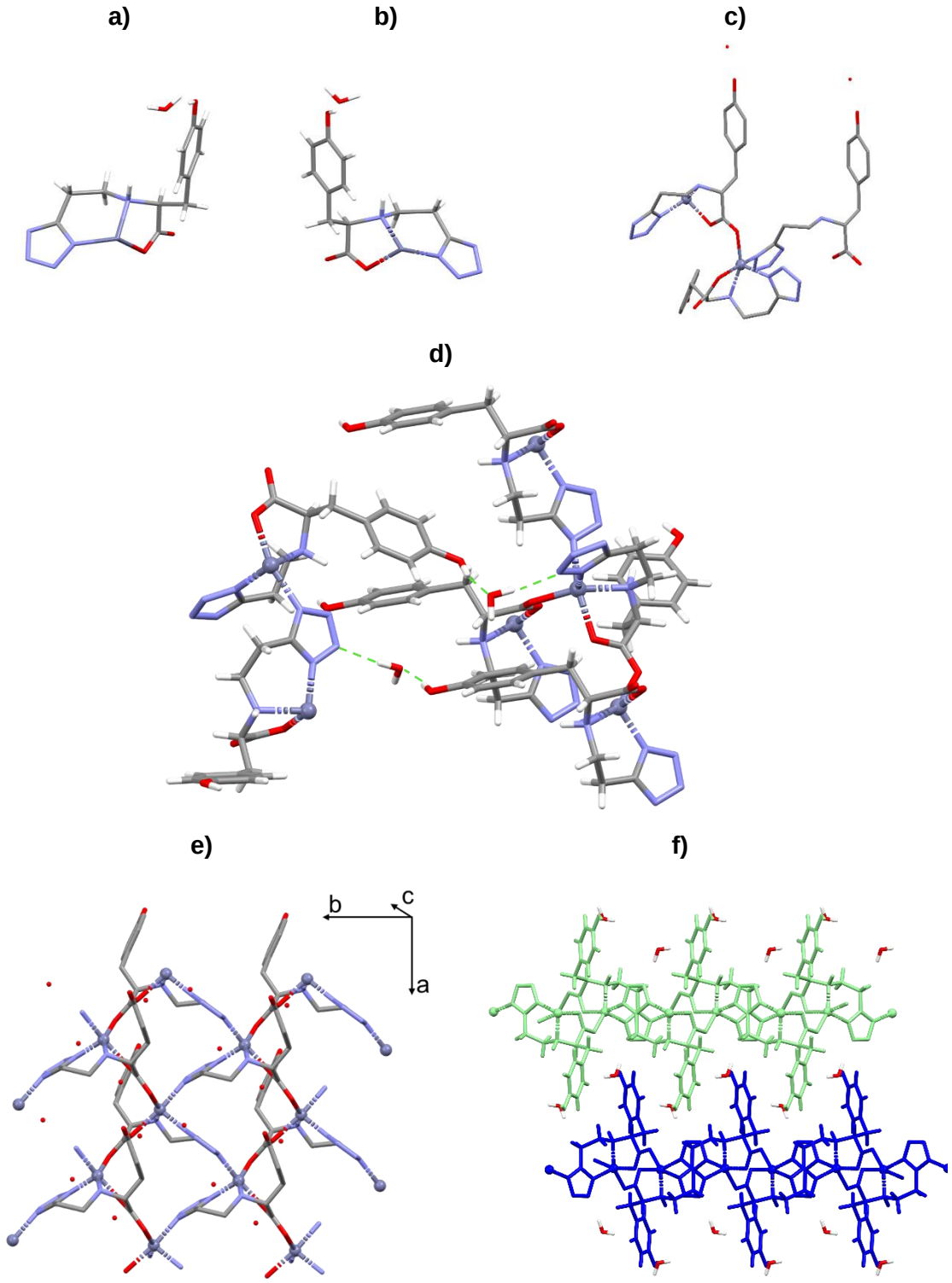

Figure 1.9. View of the asymmetric unit **a)** of Zn-L_tyr and **b)** Zn-D_tyr, compounds **1.5** and **1.7**, respectively, **c)** Perspective view of the ligand coordination modes in Zn-D_tyr **d)** most representative intermolecular hydrogen bonds **e)** perspective view and **f)** packed structure along *a* axis.

1.3.2 Relaxativity measurements

To understand how Mn_gly (**1.1**) performs as a potential contrast agent for MRI, we studied its relaxativity under 1.4 T scanner at Bruker Minispec mq60 working at 37 ºC and at 7 T by a Bruker Biospec 70/30 preclinical MRI spectrometer. The former equipment provides the relaxativity of a compound in the clinical field and at body temperature giving an idea of the performance as a potential contrast agent in clinical environments while the latter, provides relaxitivity values at a much higher magnetic field, typically used in preclinical research.

Relaxativity is dependent on external parameters among which applied field, temperature and hydration state of the molecule can be highlighted. Regarding applied field, it is known that r_1 relaxativity typically decreases with an increase of the external field while transverse relaxativity, r_2, is static or increases resulting in an increased r_2/r_1 ratio.[45]

This r_2/r_1 ratio classifies a substance working as a T_1 or T_2 contrast agent. Generally, contrast agents with a low r_2/r_1 ratio (<5) are classified as T_1 substances, while agents exhibiting larger ratios (> 10) are categorized as T_2 contrast media.[23]

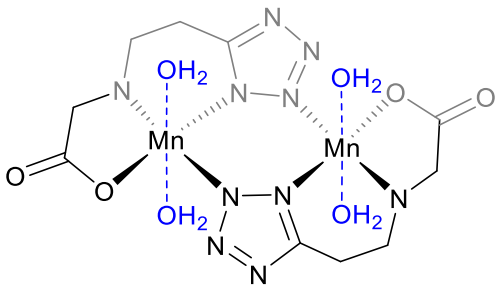

Scheme 1.6. Schematic representation of in situ synthesised Mn^{2+} based contrast agent displaying four coordinated water interchangeable molecules in the first coordination sphere.

Relaxativity measurements undertaken in compound **1.1** were carried out in ultrapure Milli-Q water media at three different concentrations (1.0 mM, 0.5 mM and 0.1 mM) for both fields (1.4 T and 7 T). The longitudinal (r_1) and transverse (r_2) relaxativity values were calculated from the slope of the plot of $1/T$ *vs.* [Mn] expressed in mM.

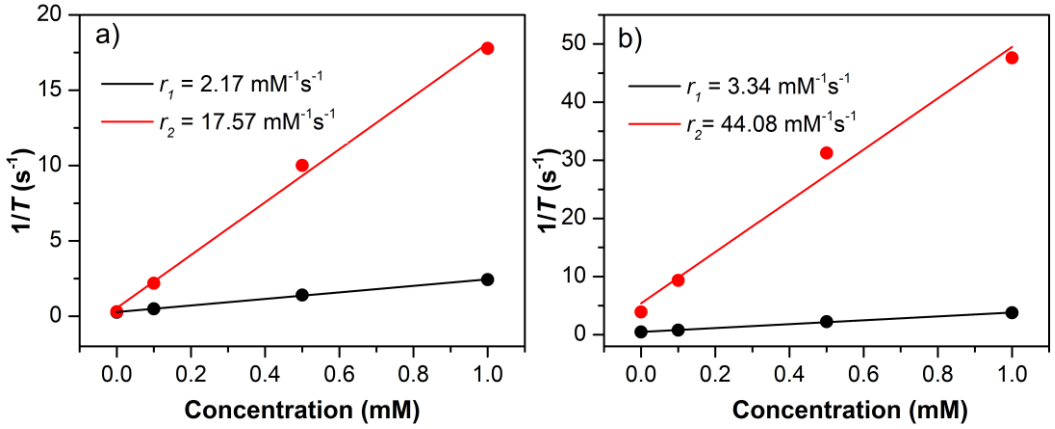

Figure 1.10. Longitudinal (r_1) and transverse (r_2) relaxativity rate of compound 1.1 Mn_gly as a function of Mn^{2+} concentration measured in **a)** Minispec at 1.4 T and **b)** in Bruker Biospec 70/30 at 7 T, respectively.

The r_1 value obtained for Mn^{2+} was 2.17 mM^{-1} s^{-1} and 3.34 mM^{-1} s^{-1} at 1.4 T and 7 T, respectively; little below relaxativities found for small Mn^{2+} complexes containing one inner-sphere water molecule which generally exhibit r_1 values of 2.4–3.7 mM^{-1} s^{-1} at 0.47 T and 25 ºC[46,47] and comparable to Mangafodipir trinatrium Mn-DPDP (r_1 = 2.1 mM^{-1} s^{-1}, 20 ºC, 1.5 T[48]), an intravenously administrated CA used to enhance the contrast of the liver and pancreas marketed under the name of Teslacan®.[49]

As previously stated, the r_2/r_1 ratio rules a contrast agent potentially working as a T_1 brightening or T_2 endarkening agent and ratios below 5 are categorized as T_1 substances, while agents exhibiting larger ratios (over 10) are classified as T_2 contrast substance.[23] In our studied Mn_gly (**1.1**) compound, the ratio r_2/r_1 was 8.1 for 1.4 T and 13.2 for 7 T, working potentially as a T_2 substance.

Subsequently, to evaluate the efficiency of compound **1.1** as a brightening or endarkening contrast agent, T_1 and T_2 weighted-phantom MR images of the complex at three concentrations have been collected.

A T_1-weighted image will expect to present water with a shorter relaxation time displaying a brighter image; while in *a* T_2-weighted image, the shorter T_2 signal, the faster will disappear and thus, the presence of the CA will contribute to destroying signal deriving in a darker image.

In principle, obtained relaxativity values both at 1.4 T and 7 T fields have demonstrated relatively high r_2/r_1 ratios considering **1.1** behaving as a potential T_2 contrast agent.

For the aforementioned measurements, again, analysis was carried out in ultrapure Milli-Q water media at three different concentrations for compound **1.1** and in 1 mM concentration for $MnCl_2$ which was used as a reference. It would be expected for $MnCl_2$ to display higher r_1 and r_2 values since possibly the number of accessible and interchangeable water molecules in the metal surrounding would be higher in number compared to compound **1.1**.

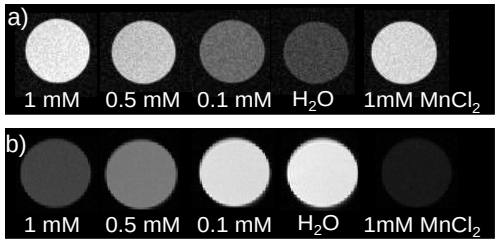

Figure 1.11. a) T_1-weighted (up) and **b)** T_2-weighted (bottom) phantom MR images of complex **1.1** and $MnCl_2$ at different concentrations at 7 T.

At a first sight, taking into consideration T_1 and T_2 weighted-phantom MR images we can appreciate that our contrast agent at 1 mM concentration possesses a slightly brighter contrast ability compared to 1 mM $MnCl_2$ dissolution mainly associated with the coordinated water molecules in the complex's inner-sphere, leading to the exchange of water molecules with the surrounding water.

Although, T_1-weighted images exhibit that intensity of the image was found to slightly increase with concentration increasing of complex **1.1** is detectable (see Figure 1.11, up), T_2-weighted images with increasing concentrations exhibit smaller signal coming in accordance with the behaviour expected for relatively high r_2 values, (concretely of 44 mM^{-1} s^{-1} at 7 T for **1.1**) as shown in Figure 1.11, bottom.

Given these results, it can be stated that synthesized Mn_gly (**1.1**), which under clinical conditions (1.4 T and 37 ºC), has demonstrated an r_1 value of 2.17 mM^{-1} s^{-1}, a relatively high r_2/r_1 ratio of 8.1 along with an efficient negative effect as evident from the T_2-weighted MR image could have potential applicability as a novel T_2 negative contrast agent.

1.3.3 Photoluminescence measurements

Solid-state photoluminescent studies were conducted in polycrystalline samples to assess emission characteristics and study the influence of the assembling ligands. Note that, due to the equivalent emission of enantiomers, the emission capacity of one enantiomer has been studied as representative of the pair.

Synthesised d^{10} metal complexes present extended aromaticity promoted by a poly-heterosubstituted penta-atomic ring; this feature made us think about the possibility of these entities being good candidates for displaying enhanced photoluminescent properties. In addition to that, ligand coordination to metals with fully-filled d orbitals promote structural rigidity, and in consequence, reduces the efficiency of non-radiative pathways yielding increased fluorescent emission. Because of that, d^{10} metal complexes have been broadly studied for applications ranging from fields of sensing to photochemistry, so far.[50–52]

To begin with, the excitation spectrum of Zn_val recorded at 15 K (Figure 1.12) monitoring at the ligand emission at 394 nm display a broad band ranging from 250-400 nm where a set of transitions are appreciable peaking at 289, 328, 336 and 340 nm, respectively.

15 K emission spectrum of Zn_val has been collected upon excitation at 289 nm. The emission profile consists of a main broad band, from 350 to ca. 650 nm, with the maximum intensity at 445 nm with a set of less intense shoulders peaking at 384, 416 and 463 nm, respectively. The emission of Zn_val stems from the ligand centred π-π* electronic transition suggesting that the conjugated ligand is the part contributing to the emission while the Zn^{2+} centre commits to structural rigidity enhancing ligand emissive properties.

Zn_Val decay curve recorded at ambient temperature while monitoring the strongest emission at 445 nm under direct excitation at 340 nm (inset of Figure 1.12), is only properly fitted by a second order exponential function yielding lifetimes of 5.82 ± 0.09 ns and 1.29 ± 0.02 ns with an averaged lifetime of 1.34 ns. It must be noted that the contribution of the longest decay time is significantly higher than the shortest one and that decays shorter than 1 ns can be assessed to lamp pulse.

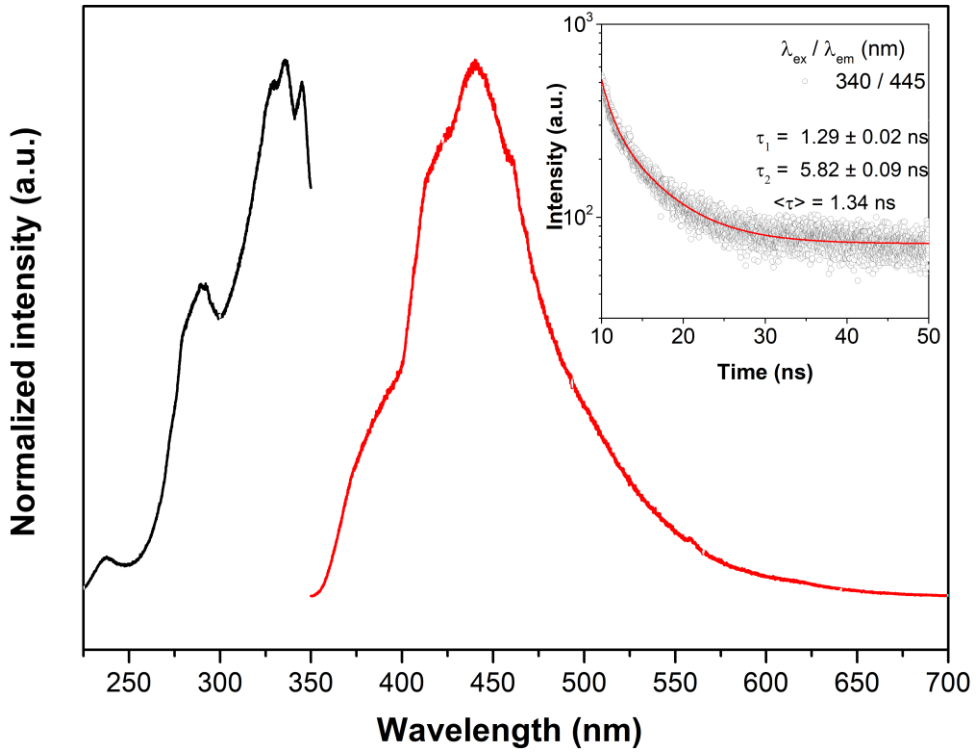

Figure 1.12. 15 K excitation spectra of Zn_val (black; $\lambda_{Exc.}$ = 394 nm) and emission spectra (red) with the excitation fixed at 289 nm. The inset shows the corresponding decay curve monitoring the emission at 445 nm with the excitation selected at 340 nm collected at room temperature; the solid red lines are the best fits using second-order decay functions, $y = y_0 + A_1 \cdot \exp(-x/\tau_1) + A_2 \cdot \exp(-x/\tau_2)$ ($r^2 > 0.999$). The average lifetimes were calculated according to the formula $<\tau> = (A_1\tau_1^2 + A_2\tau_2^2)/(A_1\tau_1 + A_2\tau_2)$.

Emission spectra of Zn_val were performed at different temperatures (15–300 K) selecting the excitation at 289 nm to study temperature induced changes in the emission spectrum. For that, the temperature dependence of the integrated intensity (I_{Zn_Val}) was determined by integrating emission spectra in the range of 350–575 nm. As shown in the thermal behaviour (Figure 1.13, inset) there is a linear relationship between temperature and emission intensity. As it was expected, temperature decrease diminishes the possibility of relaxation via non-radiative paths and thus increments emission intensity.

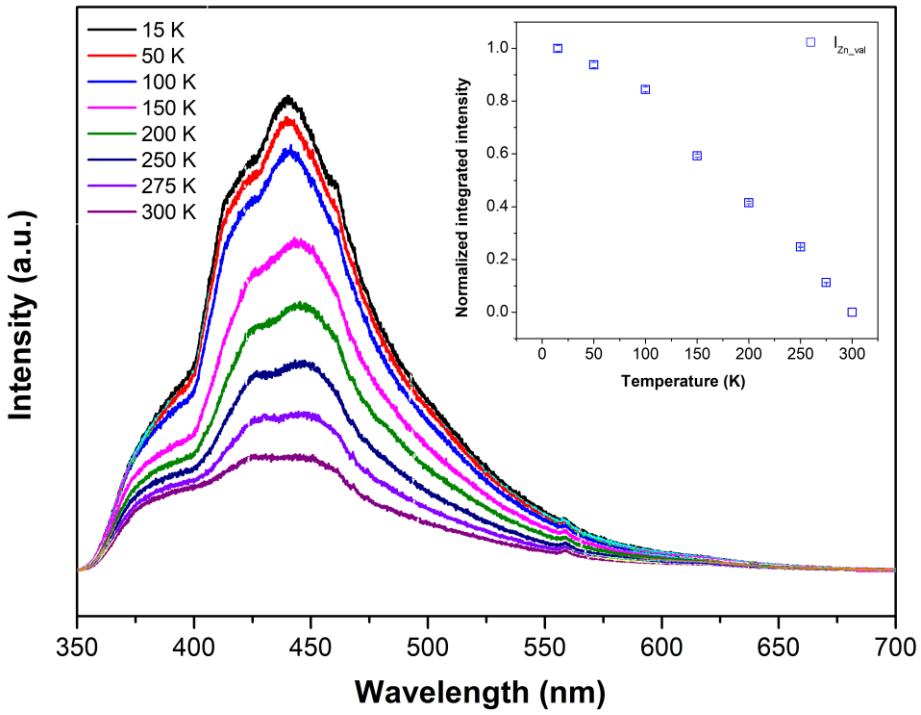

Figure 1.13. The emission spectra of Zn_val in the 15–300 K range with the excitation selected at 289 nm. Inset: Temperature dependence of $I_{Zn\text{-}val}$ in the same temperature range.

Subsequently, the 10 K excitation spectrum of Zn_phen monitoring at the maximum emission at 480 nm shows a broad band, from 275 to 400 nm, with the maximum at 388 nm with a shoulder at 309 nm (Figure 1.14).

The emission spectrum of Zn_phen, collected at 10 K and, excited at 325 nm presents a broad band, from 350 to ca. 750 nm, exhibiting the maximum intensities at 413 nm and 500 nm which is attributed, as for Zn_val analogue, to ligand aromatic π-π* electronic transition.

Zn_phen decay curve recorded at ambient temperature while monitoring the strongest emission at 480 nm under direct excitation at 370 nm (inset of Figure 1.14), is only properly fitted by a second order exponential function yielding lifetimes of 5.56 ± 0.18 ns and 1.23 ± 0.04 ns with an averaged lifetime of 1.29 ns. It must be noted that the contribution of the longest decay time is significantly larger than the shortest one and that decay times shorter than 1 ns can be assigned to the laser pulse.

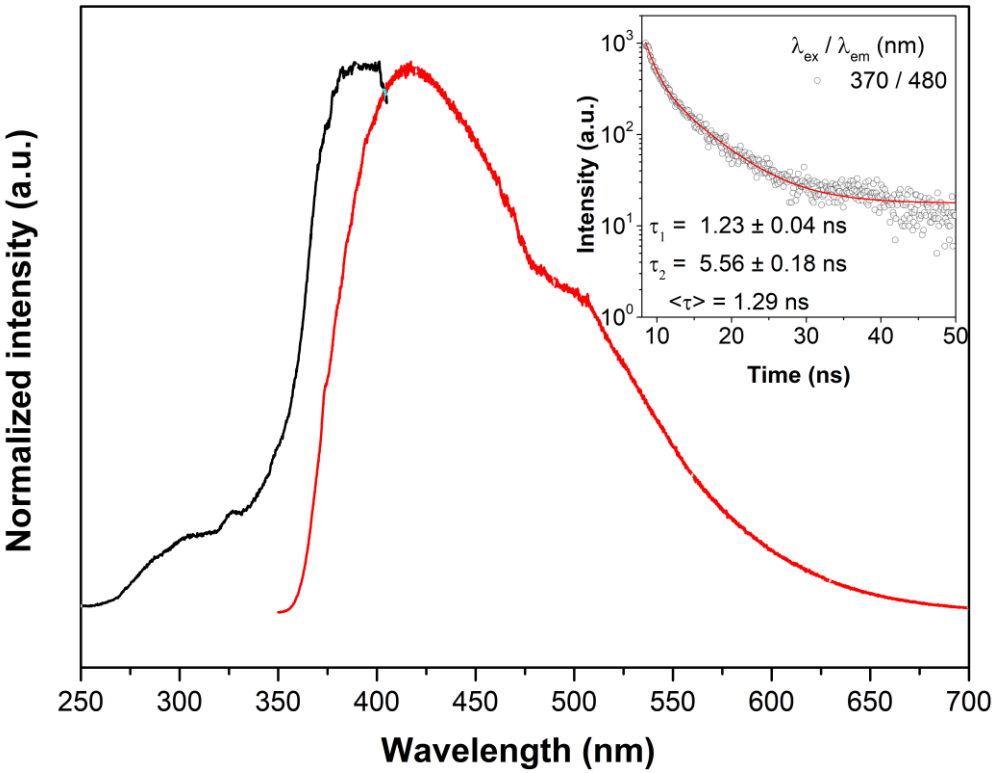

Figure 1.14. 10 K excitation spectrum of Zn_phen (black; $\lambda_{Exc.}$ = 552 nm) and emission spectrum (red) with the excitation fixed at 325 nm. The inset shows the corresponding decay curve monitoring the emission at 480 nm with the excitation selected at 370 nm collected at ambient temperature; the solid red lines are the best fits using second-order decay functions, $y = y_0 + A_1 \cdot \exp(-x/\tau_1) + A_2 \cdot \exp(-x/\tau_2)$ ($r^2 > 0.999$). The average lifetimes were calculated according to the formula $\langle \tau \rangle = (A_1\tau_1^2 + A_2\tau_2^2)/(A_1\tau_1 + A_2\tau_2)$.

To conclude, the emission capacity of isostructural Zn_tyr and Cd_tyr analogues has been studied in detail.

10 K excitation spectrum of Zn_tyr detecting at the maximum emission at 511 nm shows a broad band, from 275 to 400 nm, with the maximum at 377 nm with a shoulder at 313 nm. On its part, when isostructural Cd_tyr possess a highly resembling excitation spectrum displaying a broad band located in the range of 250–400 nm and with a well-defined shoulder peaking at 306 nm and 399 nm when excited at 520 nm.

The emission spectra of Zn_tyr and Cd_tyr, recorded at 10 K and, excited at 325 nm presents a broad band, from 350 to ca. 750 nm attributed, as for Zn_val analogue, to ligand aromatic π-π* electronic transition. Nonetheless, it must be noted that Zn_tyr analogue exhibits poorly defined shoulders peaking at 377 and 511 nm with the spectrum maximum located at 452 nm; while the Cd_tyr emission spectrum displays

a similar emission pattern with maxima located at the same position, but a higher relative intensity in 519 nm peak concerning 453 nm signal.

Cd_tyr decay curve recorded at ambient temperature while monitoring the strongest emission at 460 nm under direct excitation at 370 nm (inset of Figure 1.15 b), is only properly fitted by a second order exponential function yielding two lifetimes of 5.21 ± 0.46 ns and 1.29 ± 0.02 ns with an averaged lifetime of 0.66 ns.

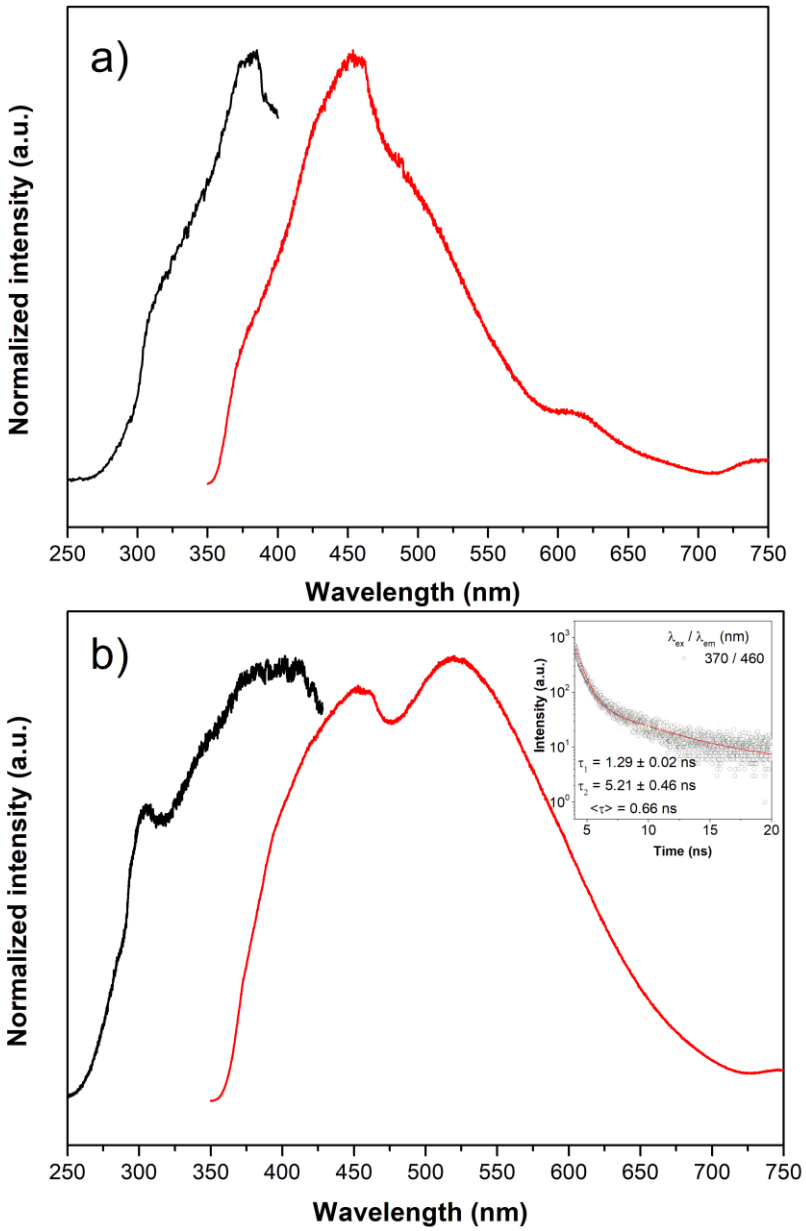

Figure 1.15. a) 10 K excitation spectrum of Zn_tyr (black; $\lambda_{Exc.}$ = 511 nm) and emission spectrum (red) with the excitation fixed at 325 nm. **b)** 10 K excitation spectrum of Cd_tyr (black; $\lambda_{Exc.}$ = 520 nm) and emission spectrum (red) with the excitation fixed at 325 nm The inset shows the corresponding decay curve monitoring the emission at 460 nm with the excitation selected at 370 nm collected at ambient temperature; the solid red lines are the best fits using second-order

decay functions, $y = y_0 + A_1 \cdot \exp(-x/\tau_1) + A_2 \cdot \exp(-x/\tau_2)$ ($r^2 > 0.999$). The average lifetimes were calculated according to the formula $\langle \tau \rangle = (A_1\tau_1^2 + A_2\tau_2^2)/(A_1\tau_1 + A_2\tau_2)$.

Variable temperature emission spectra were performed in Zn_tyr to explore temperature induced changes in the emission spectrum. By integrating the emission spectra in the range of 350–750 nm the corresponding temperature dependence of the integrated intensity (I_{Zn_tyr}) was calculated. Inset of Figure 1.16 exhibits a linear relationship dependency among emission intensity and temperature; as it was expected, since it is known that low temperature minimizes kinetic energy of molecules and thus, disables electrons being relaxed from excited states through non-emissive paths.

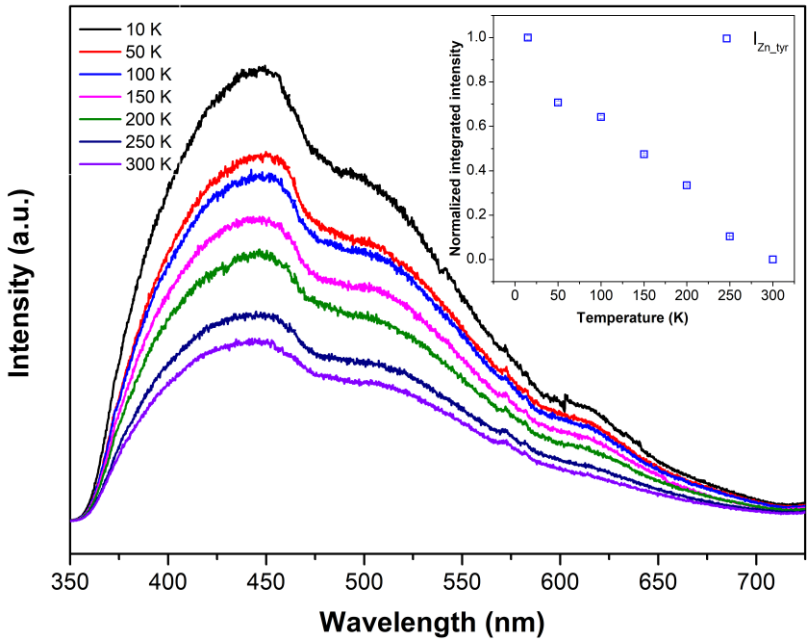

Figure 1.16. The emission spectra of Zn_tyr in the 15–300 K range with the excitation selected at 325 nm (laser). Inset Temperature dependence of I_{Zn_tyr} in the same temperature range.

1.3.4 Chiroptical properties of MOFs

1.3.4.1 Circular dichroism experiments

Given the chiral nature of the synthesised compounds (**1.2**-**1.9**), differential absorption of the right and left circularly polarized light (CD) was investigated as the absolute configuration of homochiral coordination compounds can be confirmed by positive or negative CD signals. For that, the corresponding water suspensions CD spectra were collected from each enantiomeric pair according to the procedure detailed in the 1.2.3 section. As observed in Figure 1.17, spectra of enantiomeric compounds are mirror-symmetric images indicating in all cases the formation of enantiopure samples.

When CD spectra of each pair are analysed in detail, Zn-L_val (**1.2**) and Zn-D_val (**1.3**) spectra exhibit several bands with maxima at 183, 196 and 213 nm with alternating Cotton effects. Compounds Zn-L_phen (**1.4**) and Zn-D_phen (**1.5**) peak at 194, 207, 217, 226 and 267 nm. Compounds Zn-L_tyr (**1.6**) and Zn-D_tyr (**1.7**) display a set of bands located at 180, 186, 191, 202, 236 and 287 nm. Finally, Compounds Cd-L_tyr (**1.8**) and Cd-D_tyr (**1.9**) exhibit three main bands at 183, 213 and 230 nm, with alternating Cotton effects for all previously described compounds (**1.4**-**1.9**). Note that, despite the isostructural nature of compounds Zn-L_tyr (**1.6**) and Zn-D_tyr (**1.7**) concerning Cd-L_tyr (**1.8**) and Cd-D_tyr (**1.9**) CD spectra exhibit slightly different shape which is due to the data collection parameters. Nonetheless, the maxima peak at a similar wavelength. In all cases, CD absorption bands are present in the corresponding UV-Vis spectra in compounds (**1.2**-**1.9**).

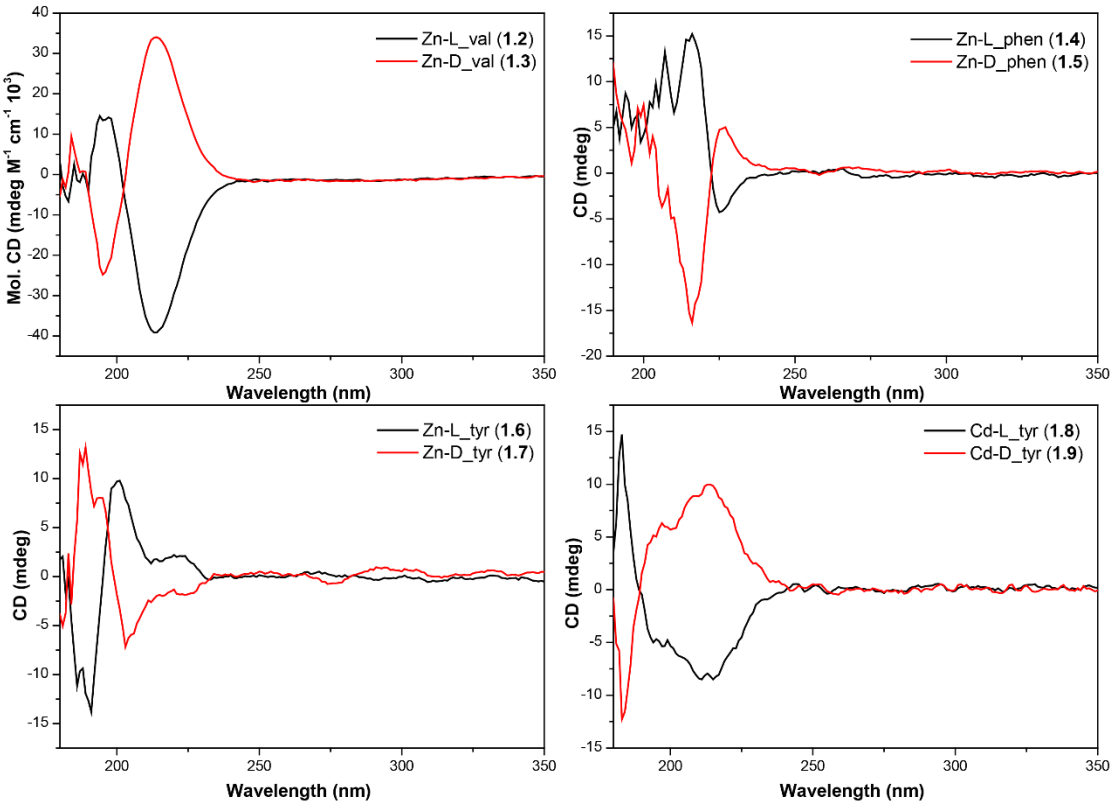

Figure 1.17. Circular dichroism spectra were recorded for compounds **1.2-1.9**.

1.3.4.2 Circularly polarized luminescence experiments

In the present work, circularly polarized luminescence spectra have been collected in suspension for left-handed and right-handed enantiomers of compounds Zn-L_phen (**1.4**) and Zn-D_phen (**1.5**) based on the emission of the ligand; the experiments run on the rest of the enantiomeric pairs did not yield measurable CPL signal.

To begin with, fluorescence spectra has been collected in the 350–750 nm region; nonetheless, the CPL signal was only clearly detectable at 560–610 nm. This is due to numerous transitions occurring below the fluorescence band and that the transition involved in CPL is only appreciable at high wavelengths and in consequence, low energetic range. Because of that reason, spectra have been recorded in the aforementioned region allowing multiple accumulations to reduce signal noise.

Recorded CPL spectra present weak but distinguished opposed signals (Figure 1.18). No maxima can be foreseen since the observed region corresponds to the tail of

the emission appreciated in the steady-state photoluminescent spectrum which stems from the ligand π–π* electronic transition.

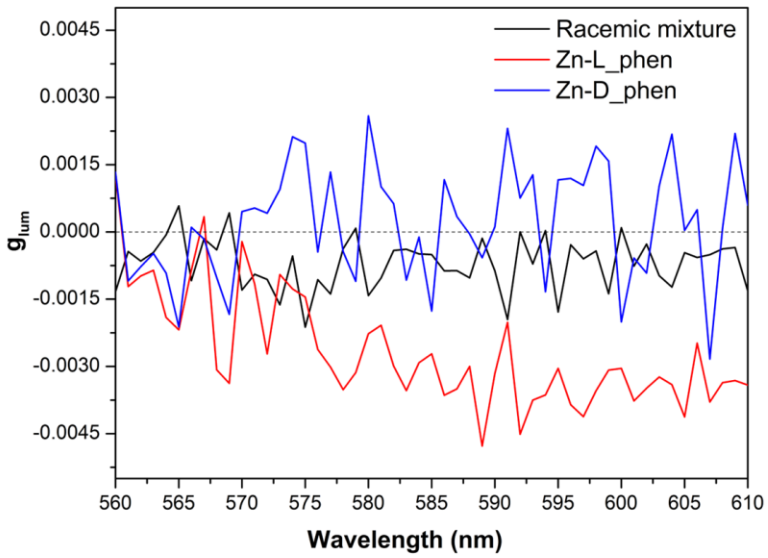

Figure 1.18. g_{lum} values of the CPL bands were found for the main emission bands of compounds Zn-L_phen **(1.4)** and Zn-D_phen **(1.5)**.

As observed, in Figure 1.18, Zn-L_phen (**1.4**) presents a negative signal meaning that it emits preferentially right-handed circularly polarized emission, while Zn-D_phen (**1.5**) exhibits major emission of left-handed CPL. As aforementioned, equipment correction error is slightly negative, which triggers g_{lum} values of racemic mixture values being slightly negative.

Acquired dissymmetry factor g_{lum} exhibit values around 1 x 10^{-3}; measuring g_{lum} values for L - 2.38 x 10^{-3} and D enantiomer 2.22 x 10^{-4}, respectively.

These results confirm that the compound can produce the searched luminescent phenomenon in suspension since the emitted light is similarly polarized in opposite directions by each enantiomer.

Nonetheless, to further confirm that obtained weak signals steam from the sample and were not derived from the data-collection procedure, a statistical study was performed according to the procedure described in the bibliography.[53] For this statistical analysis of CPL activity, collected 100 scans recorded for each enantiomer (L- and D-) along with a racemic mixture were divided into 10 sets of scans; then, the mean corresponding to the 10-scan subgroup was calculated and the corresponding

average area was determined for each data set. In all cases, to avoid any relationship between the compared sets of data those have been randomized. Figure 1.19 exhibits represented data, as it can be appreciable, the D-enantiomer displays only positive areas while L- the enantiomer exhibits negative values, which indicates that the net negative areas calculated for the spectra delimit in the negative part of the scale. Racemic mixture shows opposite signed areas.

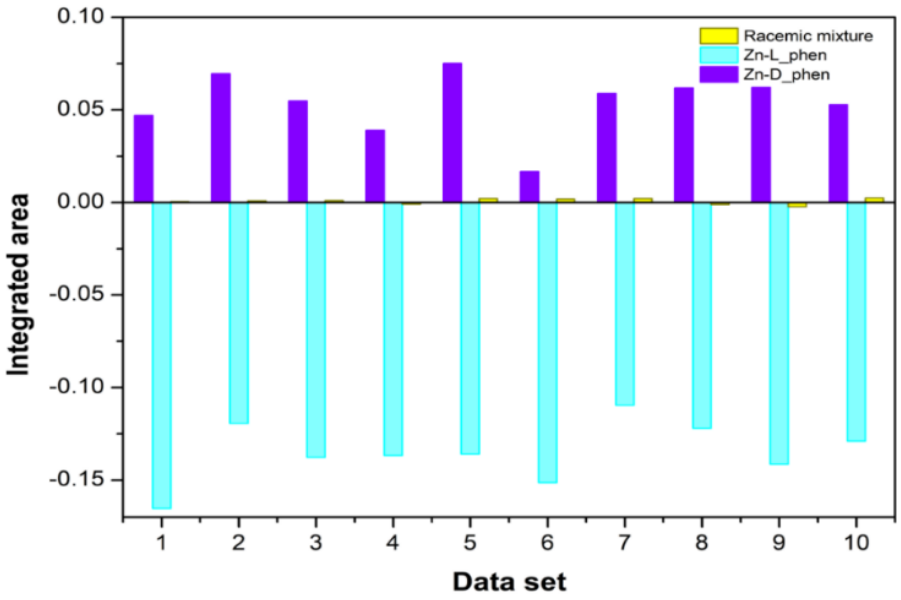

Figure 1.19. Areas of the differentiated data set were obtained from the CPL activity of compounds Zn-L_phen (**1.4**, blue) and Zn-D_phen (**1.5**, purple), and the racemic mixture (yellow).

Subsequently, the mean of the integrated area and its standard deviation were calculated for the spectra of each compound taking into consideration all data sets. With this information, F-test variance and t-test were conducted intending to conclude whether variances significantly differ among them and determine the veracity of the recorded CPL signals. In t-student statistical analysis, a comparison of L- and D- enantiomers data concerning racemic mixture was performed.

The F-test statistical analysis yielded results collected in Table 1.1. According to results, calculated F values are higher than tabulated ones which determines that according to F-test variances differ significantly in both cases.

Table 1.1. F-test for the area data

	F_{calc}	F_{tab}
Zn-L_phen (**1.4**)	100.41	3.18
Zn-D_phen (**1.5**)	107.99	3.18
$F_{calc} < F_{tab}$		

Additionally, t-student statistical analysis was carried out as aforementioned with the objective of comparing data obtained for each enantiomer with respect to racemic mixture. The t student analytical analysis results are summarized in Table 1.2.

Table 1.2. t-test for the area data of the CPL activity of the L and D enantiomers concerning the racemic mixture.

	t_{calc}	t_{tab}
Zn-L_phen (**1.4**)	26.48	2.10
Zn-D_phen (**1.5**)	10.02	2.10
$t_{calc} > t_{tab}$		

Taking into consideration the values of t-student statistical analysis, it was observed that calculated t-student value is higher than the tabulated one which indicates that at 95 % confidence signals observed for L- and D- enantiomer are significantly higher compared to racemic mixture signals. For more details consult Appendix 1.9. Chiroptical properties. Statistical analysis of the CPL data section.

Statistical analysis of the CPL data carried out in samples Zn-L_phen (**1.4**) and Zn-D_phen (**1.5**) and the racemic mixture allowed confirming that despite the signal weakness, the collected spectra are derived from the sample and that no error has been performed in the data collection which could detriment recorded data.

1.4 Conclusions

In this chapter, we have successfully synthesised and characterized a family of nine multifunctional coordination compounds based on (2-(1H-tetrazol-5-yl)ethyl)amino acid derivative (amino acid = glycine, valine, phenylalanine and tyrosine) ligands and d-block metals.

Concretely, relaxativity measurements have been carried out in Mn^{2+} based compound **1.1**, demonstrating **1.1** being a novel manganese-based contrast agent which could find potential application in magnetic resonance imaging as a T_2 contrast agent. The high r_2/r_1 ratio, along with observed signal intensity reduction and endarkening found in T_2-weighted images has prompted us to conclude compound **1.1** potential applicability as a T_2 contrast agent. Future research steps should be conducted in the direction of **1.1** being clinically applied. For that purpose, future analysis will address additional characteristics such as its cytotoxicity, aggregation of blood proteins and biodistribution and pharmacokinetics with *in vivo* experiments.

On another level, motivated by the extended aromaticity of *in situ* synthesised ligands, photoluminescent properties have been studied in d^{10} metal derived complexes. Compounds **1.6**-**1.9** display similar excitation and emission lines derived from ligand centred π→π* transition emission in all cases displaying relatively short decay times of around 5 ns.

Finally, amino acid precursor's preserved chirality prompted us to study the chiroptical properties of compounds **1.6**-**1.9**. Circular dichroism allowed us to conclude that in all cases enantiomeric pairs display opposite cotton effects being only Zn_phen enantiomeric pairs able to display circularly polarized luminescence. Obtained dissymmetry factor, g_{lum}, is in the range of 1×10^{-3} and line with values examples in the bibliography.[38] To conclude, we further confirmed by statistical study that the obtained weak CPL is a property intrinsic to the sample and does not derive from the data-collection procedure.

1.5 References

1. Chen, X.M.; Tong, M.L. Solvothermal in Situ Metal/Ligand Reactions: A New Bridge between Coordination Chemistry and Organic Synthetic Chemistry. *Acc. Chem. Res.* **2006**, *40*, 162–170, doi:10.1021/AR068084P.

2. Zhang, X.M. Hydro(solvo)thermal in situ ligand syntheses. *Coord. Chem. Rev.* **2005**, *249*, 1201–1219, doi:10.1016/J.CCR.2005.01.004.

3. Demko, Z.P.; Sharpless, K.B. Preparation of 5-substituted 1H-tetrazoles from nitriles in water. *J. Org. Chem.* **2001**, *66*, 7945–7950, doi:10.1021/jo010635w.

4. Demko, Z.P.; Sharpless, K.B. An expedient route to the tetrazole analogues of α-amino acids. *Org. Lett.* **2002**, *4*, 2525–2527, doi:10.1021/ol020096x.

5. Demko, Z.P.; Sharpless, K.B. An intramolecular [2 + 3] cycloaddition route to fused 5-heterosubstituted tetrazoles. *Org. Lett.* **2001**, *3*, 4091–4094, doi:10.1021/OL010220X/SUPPL_FILE/OL010220X_S.PDF.

6. Vorona, S.; Artamonova, T.; Zevatskii, Y.; Myznikov, L. An improved protocol for the preparation of 5-substituted tetrazoles from organic thiocyanates and nitriles. *Synth.* **2014**, *46*, 781–786, doi:10.1055/s-0033-1340616.

7. Cantillo, D.; Gutmann, B.; Kappe, C.O. Mechanistic insights on azide-nitrile cycloadditions: On the dialkyltin oxide-trimethylsilyl azide route and a new vilsmeier-haack-type organocatalyst. *J. Am. Chem. Soc.* **2011**, *133*, 4465–4475, doi:10.1021/JA109700B/SUPPL_FILE/JA109700B_SI_001.PDF.

8. Rickinney, B.Y.L.L.; Setzkorn, E.A.; Uhing, E.H. Cyanoethylation of a-Amino Acids . 111 . Hydrolysis of Cyanoethyl Derivatives The Influence of Sulfide , Sulfoxide and Sulfone Groups on the Saponification of Ethyl. **1945**, *876*, 3–4.

9. Finnegan, W.G.; Henry, R.A.; Lofquist, R. An Improved Synthesis of 5-Substituted Tetrazoles. *J. Am. Chem. Soc.* **1958**, *80*, 3908–3911, doi:10.1021/ja01548a028.

10. McKinney, L.L.; Uhing, E.H.; Setzkorn, E.A.; Cowan, J.C. Cyanoethylation of Alpha Amino Acids. I. Monocyanoethyl Derivatives. *J. Am. Chem. Soc.* **1950**, *72*, 2599–2603, doi:10.1021/ja01162a069.

11. Nasrollahzadeh, M.; Nezafat, Z.; Bidgoli, N.S.S.; Shafiei, N. Use of tetrazoles in catalysis and energetic applications: Recent developments. *Mol. Catal.* **2021**, *513*, 111788, doi:10.1016/J.MCAT.2021.111788.

12. Wei, C.X.; Bian, M.; Gong, G.H. Tetrazolium Compounds: Synthesis and Applications in Medicine. *Mol. 2015, Vol. 20, Pages 5528-5553* **2015**, *20*, 5528–5553, doi:10.3390/MOLECULES20045528.

13. Elewa, S.I.; Fatthallah, N.A.; Nessim, M.I.; El-Farargy, A.F. Synthesis and characterization of some tetrazoles and their prospective for aerobic micro-fouling mitigation. *Arab. J. Chem.* **2020**, *13*, 8750–8757, doi:10.1016/J.ARABJC.2020.10.005.

14. Ostrovskii, V.A.; Trifonov, R.E.; Popova, E.A. Medicinal chemistry of tetrazoles. *Izv. Akad. Nauk. Seriya Khimicheskaya* **2012**, *61*, 765–0777.

15. Popova, E.A.; Trifonov, R.E.; Ostrovskii, V.A. Tetrazoles for biomedicine. *Russ. Chem. Rev.* **2019**, *88*, 644–676, doi:10.1070/rcr4864.

16. Salinas-Castillo, A.; Calahorro, A.J.; Briones, D.; Fairen-Jiménez, D.; Gándara, F.; Mendicute-Fierro, C.; Seco, J.M.; Pérez-Mendoza, M.; Fernández, B.; Rodríguez-Diéguez, A. 2D-cadmium MOF and gismondine-like zinc coordination network based on the N-(2-tetrazolethyl)-4′-glycine linker. *New J. Chem.* **2015**, *39*, 3982–3986, doi:10.1039/c5nj00011d.

17. Xu, Y.; Liu, W.; Li, D.; Chen, H.; Lu, M. In situ synthesized 3D metal-organic frameworks (MOFs) constructed from transition metal cations and tetrazole derivatives: A family of insensitive energetic materials. *Dalton Trans.* **2017**, *46*, 11046–11052, doi:10.1039/c7dt02582c.

18. Wang, S.H.; Zheng, F.K.; Zhang, M.J.; Liu, Z.F.; Chen, J.; Xiao, Y.; Wu, A.Q.; Guo, G.C.; Huang, J.S. Homochiral zinc(II) coordination compounds based on in-situ-generated chiral amino acid-tetrazole ligands: Circular dichroism, excitation light-induced tunable photoluminescence, and energetic performance. *Inorg. Chem.* **2013**, *52*, 10096–10104.

19. Wang, S.-H.; Zheng, F.-K.; Wu, M.-F.; Liu, Z.-F.; Chen, J.; Guo, G.-C.; Wu, A.-Q. Hydrothermal syntheses, crystal structures and physical properties of a new family of energetic coordination polymers with nitrogen-rich ligand N-[2-(1H-tetrazol-5-yl)ethyl]glycine. *CrystEngComm* **2013**, *15*, 2616, doi:10.1039/c3ce27048c.

20. Lacerda, S. Targeted contrast agents for molecular MRI. *Inorganics* **2018**, *6*, 1–17, doi:10.3390/inorganics6040129.

21. Pan, D.; Schmieder, A.H.; Wickline, S.A.; Lanza, G.M. Manganese-based MRI contrast agents: Past, present, and future. *Tetrahedron* **2011**, *67*, 8431–8444, doi:10.1016/j.tet.2011.07.076.

22. Pooley, R.A. AAPM/RSNA physics tutorial for residents: fundamental physics of MR imaging. *Radiographics* **2005**, *25*, 1087–1099.

23. Caspani, S.; Magalhães, R.; Araújo, J.P.; Sousa, C.T. Magnetic Nanomaterials as Contrast Agents for MRI. *Mater. 2020, Vol. 13, Page 2586* **2020**, *13*, 2586, doi:10.3390/MA13112586.

24. Wyrostek, S.; Chakrabarti, S.; Baldwin, K.; David Avila, J. A Case of Hypertrophic Pachymeningitis Associated with Immunoglobulin-G4 and c-ANCA. *Case Rep Neurol* **2019**, *11*, 290–294, doi:10.1159/000502569.

25. Martínez-Banderas, A.I.; Aires, A.; Plaza-García, S.; Colás, L.; Moreno, J.A.; Ravasi, T.; Merzaban, J.S.; Ramos-Cabrer, P.; Cortajarena, A.L.; Kosel, J. Magnetic core-shell nanowires as MRI contrast agents for cell tracking. *J. Nanobiotechnology* **2020**, *18*, 1–12, doi:10.1186/S12951-020-00597-3/FIGURES/5.

26. Siriwardena-Mahanama, B.N.; Allen, M.J. Strategies for optimizing water-exchange rates of lanthanide-based contrast agents for magnetic resonance imaging. *Molecules* 2013, *18*, 9352–9381.

27. Wang, J.; Wang, H.; Ramsay, I.A.; Erstad, D.J.; Fuchs, B.C.; Tanabe, K.K.; Caravan, P.; Gale, E.M. Manganese-Based Contrast Agents for Magnetic Resonance Imaging of Liver Tumors: Structure-Activity Relationships and Lead Candidate Evaluation. *J. Med. Chem.* **2018**, *61*, 8811–8824, doi:10.1021/acs.jmedchem.8b00964.

28. Liu, H.; Zhang, X.-A. Manganese-Based Magnetic Resonance Imaging Contrast Agents. *Encycl. Inorg. Bioinorg. Chem.* **2018**, 1–16, doi:10.1002/9781119951438.eibc2626.

29. Wahsner, J.; Gale, E.M.; Rodríguez-Rodríguez, A.; Caravan, P. Chemistry of MRI contrast

agents: Current challenges and new frontiers. *Chem. Rev.* 2019, *119*, 957–1057.

30. Lauterbur, P.C. Image Formation by Induced Local Interactions: Examples Employing Nuclear Magnetic Resonance. *Nat. 1973 2425394* **1973**, *242*, 190–191, doi:10.1038/242190a0.

31. Leyba, K.; Wagner, B. Gadolinium-based contrast agents: why nephrologists need to be concerned. *Curr. Opin. Nephrol. Hypertens.* **2019**, *28*, 154, doi:10.1097/MNH.0000000000000475.

32. Barbieri, A.; Accorsi, G.; Armaroli, N. Luminescent complexes beyond the platinum group: The d^{10} avenue. *Chem. Commun.* **2008**, 2185–2193, doi:10.1039/b716650h.

33. San Sebastian, E.; Rodríguez-Diéguez, A.; Seco, J.M.; Cepeda, J. Coordination Polymers with Intriguing Photoluminescence Behavior: The Promising Avenue for Greatest Long-Lasting Phosphors. *Eur. J. Inorg. Chem.* **2018**, *2018*, 2155–2174, doi:10.1002/ejic.201800124.

34. Pamei, M.; Puzari, A. Luminescent transition metal–organic frameworks: An emerging sensor for detecting biologically essential metal ions. *Nano-Structures and Nano-Objects* **2019**, *19*, 100364, doi:10.1016/j.nanoso.2019.100364.

35. Cui, Y.; Yue, Y.; Qian, G.; Chen, B. Luminescent functional metal-organic frameworks. *Chem. Rev.* **2012**, *112*, 1126–1162, doi:10.1021/cr200101d.

36. Sánchez-Carnerero, E.M.; Agarrabeitia, A.R.; Moreno, F.; Maroto, B.L.; Muller, G.; Ortiz, M.J.; De La Moya, S. Circularly Polarized Luminescence from Simple Organic Molecules. *Chem. - A Eur. J.* **2015**, *21*, 13488–13500, doi:10.1002/chem.201501178.

37. Deng, Y.; Wang, M.; Zhuang, Y.; Liu, S.; Huang, W.; Zhao, Q. Circularly polarized luminescence from organic micro-/nano-structures. *Light Sci. Appl.* 2021, *10*, 1–18.

38. Gao, Y.; Ren, C.; Lin, X.; He, T. The Progress and Perspective of Organic Molecules With Switchable Circularly Polarized Luminescence. *Front. Chem.* 2020, *8*, 458.

39. Longhi, G.; Castiglioni, E.; Koshoubu, J.; Mazzeo, G.; Abbate, S. Circularly polarized luminescence: A review of experimental and theoretical aspects. *Chirality* **2016**, *28*, 696–707, doi:10.1002/chir.22647.

40. Sang, Y.; Han, J.; Zhao, T.; Duan, P.; Liu, M.; Sang, Y.; Liu, M.; Zhao, T.; Duan, P.; Han, J. Circularly Polarized Luminescence in Nanoassemblies: Generation, Amplification, and Application. *Adv. Mater.* **2020**, *32*, 1900110, doi:10.1002/ADMA.201900110.

41. Singh, R.; Narayanan Unni, K.N.; Solanki, A.; Deepak Improving the contrast ratio of OLED displays: An analysis of various techniques. *Opt. Mater. (Amst).* **2012**, *34*, 716–723, doi:10.1016/j.optmat.2011.10.005.

42. Heffern, M.C.; Matosziuk, L.M.; Meade, T.J. Lanthanide Probes for Bioresponsive Imaging. *Chem. Rev.* **2013**, *114*, 4496–4539, doi:10.1021/CR400477T.

43. Llunell, M.; Casanova, D.; Cirera, J.; Bofill, J. M.; Alemany, P.; Alvarez, S.; Pinsky, M.; Avnir, D. Program for the Stereochemical Analysis of Molecular Fragments by Means of Continuous Shape Measures and Associated Tools. *SHAPE, v1.1b; Barcelona, Spain* **2005**, 1–35.

44. Blatov, V.A.; Shevchenko, A.P.; Proserpio, D.M. Applied topological analysis of crystal structures with the program package topospro. *Cryst. Growth Des.* **2014**, *14*, 3576–3586,

doi:10.1021/cg500498k.

45. Caravan, P.; Farrar, C.T.; Frullano, L.; Uppal, R. Influence of molecular parameters and increasing magnetic field strength on relaxivity of gadolinium- and manganese-based T_1 contrast agents. *Contrast Media Mol. Imaging* **2009**, *4*, 89–100, doi:10.1002/cmmi.267.

46. Regueiro-Figueroa, M.; Rolla, G.A.; Esteban-Gómez, D.; De Blas, A.; Rodríguez-Blas, T.; Botta, M.; Platas-Iglesias, C. High Relaxivity Mn^{2}+-Based MRI Contrast Agents. *Chem. – A Eur. J.* **2014**, *20*, 17300–17305, doi:10.1002/CHEM.201404673.

47. Phukan, B.; Mukherjee, C.; Goswami, U.; Sarmah, A.; Mukherjee, S.; Sahoo, S.K.; Moi, S.C. A New Bis(aquated) High Relaxivity Mn(II) Complex as an Alternative to Gd(III)-Based MRI Contrast Agent. *Inorg. Chem.* **2018**, *57*, 2631–2638, doi:10.1021/ACS.INORGCHEM.7B03039/SUPPL_FILE/IC7B03039_SI_001.PDF.

48. Wiener, E.; Woertler, K.; Weirich, G.; Rummeny, E.J.; Settles, M. Contrast enhanced cartilage imaging: Comparison of ionic and non-ionic contrast agents. *Eur. J. Radiol.* **2007**, *63*, 110–119, doi:10.1016/J.EJRAD.2007.01.019.

49. Boraschi, P.; Donati, F.; Gigoni, R.; Caramella, D.; Boggi, U.; Falaschi, F.; Bartolozzi, C. Mangafodipir trisodium-enhanced MR imaging of pancreatic disease. *Eur. Radiol.* **2006**, *16*, 988–997, doi:10.1007/s00330-005-0099-8.

50. Cepeda, J.; Rodríguez-Diéguez, A. Tuning the luminescence performance of metal–organic frameworks based on d10 metal ions: from an inherent versatile behaviour to their response to external stimuli. *CrystEngComm* **2016**, *18*, 8556–8573, doi:10.1039/C6CE01706A.

51. Andrea Barbieri; Gianluca Accorsi; Nicola Armaroli; Barbieri, A.; Accorsi, G.; Armaroli, N. Luminescent complexes beyond the platinum group: The d^{10} avenue. *Chem. Commun.* **2008**, *0*, 2185–2193, doi:10.1039/b716650h.

52. Li, P.; Zhou, Z.; Zhao, Y.S.; Yan, Y. Recent advances in luminescent metal–organic frameworks and their photonic applications. *Chem. Commun.* **2021**, *57*, 13678–13691, doi:10.1039/D1CC05541K.

53. Leo, P.; Orcajo, G.; García, J.A.; Ortuño, A.M.; Cuerva, J.M.; Briones, D.; Calleja, G.; Rodríguez-Diéguez, A.; Sanz, R.; Cepeda, J.; et al. An enantiomeric pair of alkaline-earth metal based coordination polymers showing room temperature phosphorescence and circularly polarized luminescence. *J. Mater. Chem. C* **2021**, *9*, 5544–5553, doi:10.1039/d1tc00398d.

Chapter 2

Multifunctional metal-organic frameworks based on 3-amino-4-hydroxibenzoic acid ligand

Summary

This chapter summarizes the synthesis and characterization of three-dimensional multifunctional materials based on 3-amino-4-hydroxybenzoate ligand and it is organized in three main bocks: in the first one, 3d metal-based MOFs will be presented; in the subsequent two sections, lanthanide-based materials will be prepared and their applications explored. The principal novelty of this work can be briefly summarized on the following aspects:

- To start with, 3d (Co^{2+} and Zn^{2+}) metal ion based bifunctionality will allow exploring coordination polymers with magnetic and modulated photoluminescent properties.
- Subsequently, a family of isostructural multifunctional Ln-MOFs will be presented display single-molecule magnet behaviour, photoluminescent properties for thermometry application and CO_2 adsorptive capacity. Along with the catalytic performance in efficient solvent-free cyanosilylation reaction of carbonyl compounds with trimethylsilyl cyanide catalysed by yttrium and europium-based counterparts will be studied.
- Finally, easy handling processing-techniques will be evaluated for shaping bulk material into pellets and membranes. This research will be conducted in terbium-based material allowing a comparation between the emissive capacity of the membrane-immobilized material with respect to pristine MOF. Additionally, water adsorption and proton conductivity of the unshaped material will be carried on.

PART 1

2.1 Introduction. 3-amino-4-hydroxybenzoate and 3d metal ion Based Bifunctional Coordination Polymers. Magnetic and Modulated Photoluminescence properties.

Multifunctional molecular materials (MMMs) are compounds in which two or more physical properties coexist, compete or cooperate.[1] Therefore, combinations such as conductive/optical, magnetic/optical or conductive/magnetically are possible to study giving the opportunity of analysing simultaneously the influence of one (or more) physical property present in these materials. Because of the broad spectrum that these materials can cover, several applications can be addressed to MMMs. Gas separation and storage, heterogeneous catalysis, drug delivery, sensor devices and magnetic and photoluminescence are among them.[2,3]

In this line, the exploration of new metal-organic frameworks (MOFs) with improved physico-chemical properties are an ongoing prerequisite and aim. MOFs offer the possibility to rationally design the structure of the material in order to shaping the desired properties for a particular final application. To that end, the type and properties of the metal ions composing the structure are of great importance. Consequently, the incorporation of different metal ions in the same structure by constructing mixed-metal-organic frameworks (M'MOFs) might be advantageous to prompt a specific application into the material.[4,5]

In this work, we have successfully synthesised a novel cobalt-based MOF and implemented this approach to yield several heterometallic Zn^{2+} doped M'MOFs with the aim of systematically studying their magnetic and spectroscopic properties. For this purpose, we took advantage of the isostructurallity shown by our new cobalt coordination compound to the previously reported zinc counterpart,[6] which has proven to be a MOF with extraordinary acid–based resistance and to efficiently separate acetylene from C_2H_2/CO_2 mixtures under ambient conditions showing the highest C_2H_2/CO_2 uptake ratio reported in bibliography for MOFs so far.[7–10]

On another level, the magnetic behaviour of 3d ions enables their application into molecular magnetism, a field of active research which has contributed in the development of high-density data storage and quantum computation.[11] This magnetic behaviour derives from the slow magnetic relaxation of metal ions with appropriate

coordination shell, in this case Co^{2+}. At this point, the structural design is thus crucial so that the coordination of organic ligands not only favour the occurrence of magnetic anisotropy but also isolate the spin carriers by imposing weak or null exchange interactions in the crystal building to avoid long-range magnetic ordering phenomena, such as ferromagnetism, antiferromagnetism, metamagnetism.[2,12] An alternative to avoid those undesired effects is to physically isolate (dilute) the spin carriers into a diamagnetic matrix that preserves isostructural nature, a process called magnetic dilution, in such a way that magnetic exchange interactions would be partially suppressed to give single ion magnetic properties, and hence single-ion magnets (SIMs).[13] These materials are able to keep the magnetic moment after the exposure to a magnetic field and slowly reorient it as a consequence of the existence of an energy barrier below a blocking temperature. The energy barrier (U_{eff}) for the reversal of spin is dependant of the axial zero-field splitting parameter (D) and the total spin of the complex (S).[14] In general, the magnetic behaviour of these 3d ion–based compounds results from the interaction between ligand-field splitting and spin–orbit interaction, both of which can generate large anisotropy (D). In particular, Co^{2+} complexes are good candidates for the construction of SIMs owing to their large magnetic anisotropy, which is directly influenced by the coordination environment of cobalt ions. Trigonal prismatic coordination geometries lead to highly negative values of D; therefore, they are very appropriate for the preparation of SIMs. Tetrahedral Co^{2+} geometries with $s_i = 3/2$ show a larger spin–orbit coupling constant and hence these complexes can display larger D values.[15] In fact, although the highest effective energy barrier exhibited by a Co^{2+} complex has been observed in a tetrahedral compound [U_{eff} = 118 cm^{-1} at zero direct-current (dc) field], trigonal-prismatic Co^{2+} complexes have also shown interesting SMM properties.[16] However, for 3d ion-based SIMs, the SMM behaviour is usually only visible under a small applied external field that suppresses the fast magnetic tunnelling, making that not much mononuclear complexes based on 3d ions show slow relaxation of the magnetization.[17]

In our attempt to synthesise a multifunctional Mixed Metal-organic framework, zinc incorporation into the network not only play an important role in inducing magnetic dilution but also gives the possibility to study photoluminescent properties. Group12 metals are well known by their lack of luminescence quenching since they afford no d-d transition and exhibit flexible coordination environments associated with closed-shell configuration allowing them to be adapted to a wide range of geometries.[18,19] In this sense, ligand centred (LC) and ligand-to-metal charge transfers (LMCT) may improve

their performance in solid samples.[20,21] Solid-state light emitting MOFs are receiving large attention since they can be used as ideal platforms to boost development of improved devices for applications in light-emitting diodes and optical sensors, among others.

Bearing these ideas in mind, briefly, we have synthesised and characterised a new Co-MOF and studied adsorption capacity and magnetic properties. We performed magnetic dilution of the MOF and studied homometallic Zn and Zn-Co heterometallic photoluminescent properties.

2.2 Materials and methods

All chemicals were of reagent grade and used as commercially obtained.

2.2.1 Compound synthesis

General procedure for the synthesis of single crystal of $\{[CoL]\cdot 0.5DMF\cdot H_2O\}_n$

In a 6 mL screw-capped vial, 0.010 g (0.0625 mmol) of 3-amino-4-hydroxybenzoic acid organic linker and an equivalent of $Co(NO_3)_2\cdot 6H_2O$, 0.018 g (0.0625 mmol), were weighted. Then, 4 mL DMF/ 0.3 mL EtOH/ 0.3 mL MeCN/ 0.1 mL H_2O solvent-mixture was added to the vial, which was sealed and introduced to the oven at 140 °C for 2 hours to give rise rod-shaped single crystals.

General procedure for the scaled-up synthesis: 3-amino-4-hydroxybenzoic acid ligand (0.20 g, 1.2 mmol) was dissolved in 2 mL of DMF/ 2 mL of H_2O solvent mixture. $Co(NO_3)_2\cdot 6H_2O$ (0.35 g, 1.2 mmol) was dissolved in 1 mL of DMF/ 1 mL of H_2O solvent mixture. The metal solution was added dropwise into the ligand solution under magnetic stirring until a purple precipitate was formed. The product was collected by filtration and washed with DMF and H_2O. 0.112 g (yield 44 %). Sample purity was checked by powder X-ray diffraction (Figure A2.2).

General procedure for the synthesis of $[Co_xZn_{1-x}L]_n$ heterometallic materials:

For the synthesis of mixed-metal counterparts an appropriate molar amount of $Co(NO_3)_2\cdot 6H_2O$ and $Zn(NO_3)_2\cdot 6H_2O$ have been employed according to how it is tabulated in Table 2.1 (always accounting a total molar amount of 1.2 mmol). The resulting purple polycrystalline samples (with variable colour intensity dependant of cobalt doping proportion) was filtered off and washed several times with water and dimethylformamide. The purity of heterobimetallic sample was checked by PXRD (for more details check Appendix 2. Figure A2.3).

Table 2.1. Doping percentage, mmols and corresponding weight used in the synthesis of $[Co_xZn_{1-x}L]_n$ heterometallic samples.

% Co	mmol (g)	%Zn	mmol (g)
0	-	**100**	1.20 (0.400)
5	0.06 (0.018)	**95**	1.14 (0.390)
10	0.12 (0.035)	**90**	1.08 (0.320)
30	0.36 (0.105)	**70**	0.84 (0.25)
50	0.60 (0.175)	**50**	0.60 (0.178)
70	0.84 (0.244)	**30**	0.36 (0.107)
90	1.08 (0.314)	**10**	0.12 (0.0357)
100	1.20 (0.350)	**0**	-

2.3 Results and discussion

The solvothermal reaction of the 3-amino-4-hydroxybenzoic acid ligand H_2L with $Co(NO_3)_2 \cdot 6H_2O$ salt in N,N'-dimethylformamide/water (DMF/H_2O) mixture yields a three dimensional MOF of general formulae $\{[CoL] \cdot 0.5DMF \cdot H_2O\}_n$, namely **2.1** or Co_MOF.

2.3.1 Structural characterization

Single-crystal X-ray diffraction analysis reveals that Co_MOF (**2.1**) crystallizes in the tetragonal $P4_2$ space group as a racemic twin probably derived from the lower symmetry present in the crystal structure, a fact that generates a systematic disorder in the framework. Therefore, though the high overall symmetry present in the crystal imposes an asymmetric unit with a unique cobalt ion and a deprotonated ligand, there are indeed two non-equivalent disordered cobalt atoms with distinct coordination environments (Figure 2.1). One is trigonal prism SBU, in which Co^{2+} has 6-connected nodes $–CoN_2O_4$ coordination environment– where the metallic centre is linked by two oxygen atoms from different carboxylate groups, two oxygen atoms from different hydroxyl groups, and two nitrogen atoms from two different amino groups. The other coordination environment corresponds to a tetrahedron SBU, in which Co^{2+} displays 4-connected nodes $–CoO_4$ coordination environment– where two oxygen atoms from different carboxylate groups and two oxygen atoms from different hydroxyl groups complete the coordination sphere. Continuous SHAPE measurements (CShMs)[22] revealed Co based polyhedra resemble a trigonal prism (TPR-6) and a tetrahedron (T-4), respectively (see Tables A2.7 and A2.8). On its part, the organic ligand, 3-amino-4-hydroxy benzoato, is also disordered into two equivalent dispositions and shows a tetradentate μ_4-κO:κO':κO'',N:κO''' coordination mode by using the carboxylate, hydroxyl and amino groups to link to both metal centres. The linkage of both SBUs by means of the ligands generates a dimeric core that is further extended in the three directions to give rise to a ***pts*** topological network with the $(4^2 \cdot 8^4)$ point symbol according to the topological analysis performed with TOPOS software.[23]

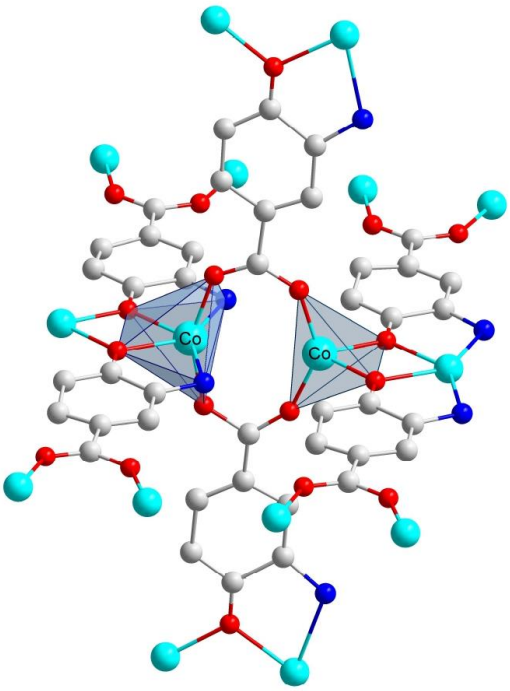

Figure 2.1. Excerpt of the crystal structure of compound **2.1** showing the trigonal prismatic and tetrahedral the coordination polyhedra.

The growth of the 3D open framework leaves tubular microchannels of an approximate diameter of 9.1 Å, which are occupied by crystallization DMF and water molecules (Figure 2.2). The void volume corresponds to *ca*. 43 % of the unit cell volume according to the geometrical calculation of the pore volume by PLATON-v1.18 program.

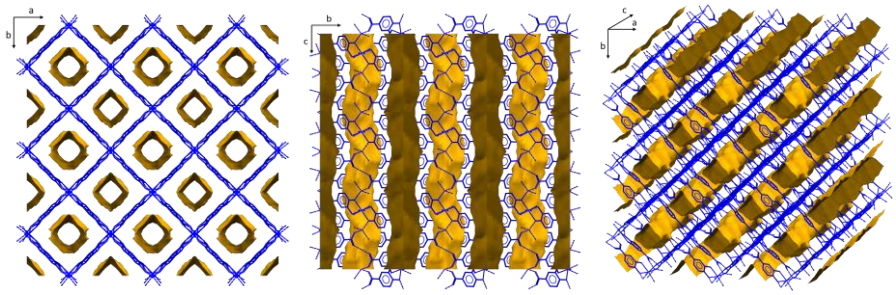

Figure 2.2. View of the packing of **2.1** showing the solvent-accessible voids.

In our attempt to design multifunctional materials, we analysed Co_MOF (**2.1**) magnetic properties.

2.3.2 Magnetic properties

Temperature-dependent magnetic susceptibility was measured on polycrystalline samples of **2.1** in the range of 2–300 K and was given in the Figure 2.3. Upon cooling, the value of $\chi_M T$ gradually decreases from 6.8 $cm^3 \cdot K \cdot mol^{-1}$ at 300 K to 4.7 $cm^3 \cdot K \cdot mol^{-1}$ at 50 K and then drops fast to 0.03 $cm^3 \cdot K \cdot mol^{-1}$at 2 K. Below 8 K, $\chi_M T$ seems to suffer a slope change and thus appears to increase to reach a maximum of at 5.75 K (1.15 $cm^3 \cdot K \cdot mol^{-1}$) to subsequently reach the minimum value at 2 K. This behaviour derives from the occurrence of antiferromagnetic interactions. In addition, at the highest temperature the magnetic value is higher than the expected spin only value (1.875 $cm^3 \cdot K \cdot mol^{-1}$, S = 3/2) indicating a high g value (g > 2.0). The decrease of the $\chi_M T$ at lower temperatures can be attributed combination of two factors: from one side, zero-field splitting of the ground state and from the other, intramolecular interactions.[2,24]

On the other hand, *dc* magnetization measurements were carried out at 2–7 K range showing a gradual increase with the applied external field without reaching a complete saturation of magnetization, this behaviour could be derived by the presence of significant anisotropy in the ground state and/or accessible low-lying excited states that are partially (thermally and field-induced) populated at these temperature range, in other words, probably, the highest available field (7 T) may not be sufficient to fully populate the excited states to reach magnetization saturation for the studied complex.[25,26]

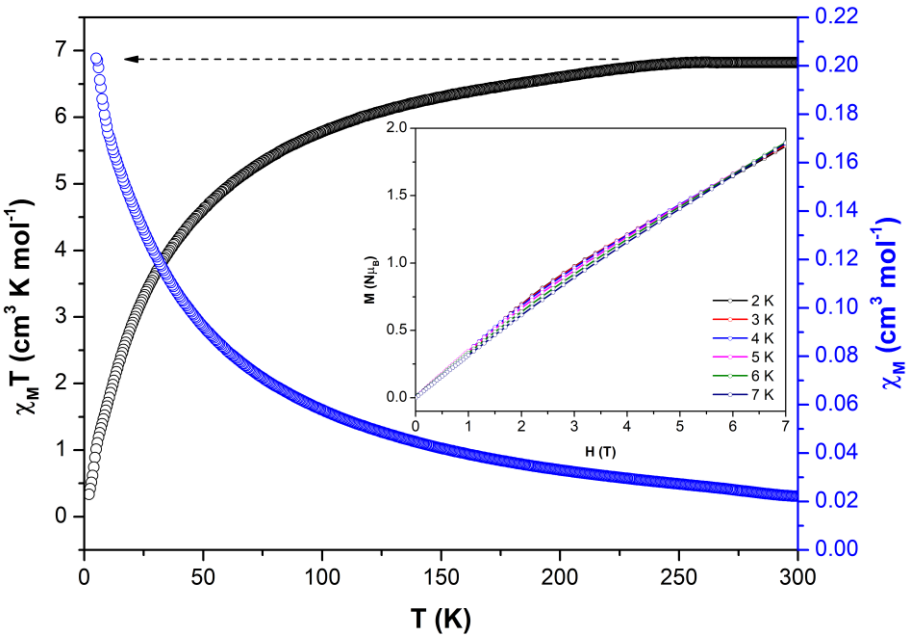

Figure 2.3. Temperature dependence of the $\chi_M T$ product at 1000 Oe for complex **2.1** Inset: M vs H at 2**–**7 K. The lines are a guide to the eye.

Additionally, DFT calculations were conducted over each cobalt environment, distorted trigonal prismatic (TPR) and tetrahedral (Td), in an independent way (Figure 2.4). According to the energetical distribution of the molecular orbitals both trigonal prismatic and tetrahedral environments exhibit very similar energetical distribution but differs from the theoretical distribution which could be derived by the big environmental distortion, particularly in TPR, which is confirmed by SHAPE.

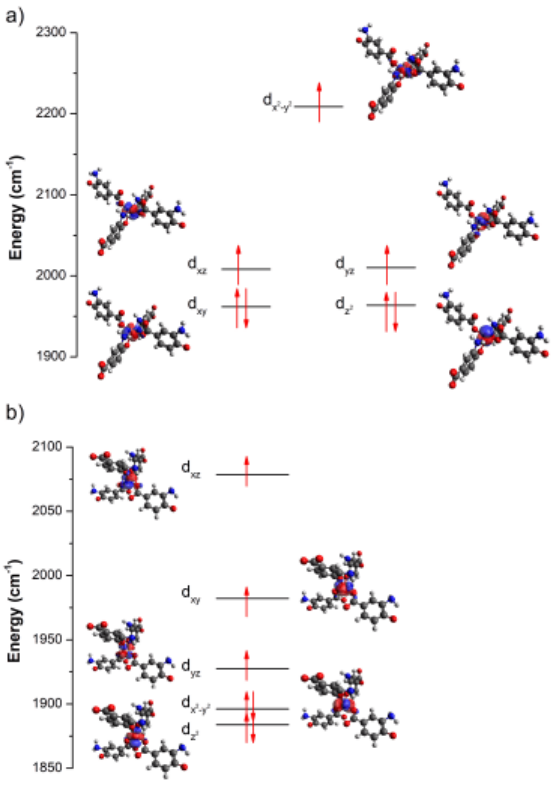

Figure 2.4. Molecular orbital representation of **a)** TPR coordinated and **b)** Td coordinated respectively.

With the aim to find out if compound **2.1** shows slow relaxation of the magnetization or not, dynamic alternating-current (*ac*) magnetic measurements were performed. Despite the expected large anisotropy of the cobalt ions, compound **2.1** did not show any out-of-phase χ_M'' signal under zero external field, which may be due to the fast resonant zero-field quantum tunnelling of the magnetization (QTM) through degenerate energy levels.[16] When the *ac* measurements were performed in the presence of an external *dc* field of 1000 Oe, complexes **2.1** showed weak frequency dependency, but with the maxima of χ_M'' appearing below the instrument detection limit (Figures A2.20). Thus, the energy barrier (U_{eff}) and relaxation time (τ_0) cannot be obtained *via* convectional Arrhenius method. However, if we assume that there is only one relaxation process, the Debye model (Equation 2.1) could provide a rough estimation of U_{eff} and τ_0 values,[27]

$$\ln {\chi_M''}/{\chi_M'} = \ln(2\pi\nu\tau_0) + {E_a}/{k_B T}$$ **Equation 2.1**

yielding U_{eff} value of 8.92 K and relaxation times (τ_0) of $4.25 \cdot 10^{-8}$ s (see Figure A2.21). In this particular case, the contribution and exchange interaction of both tetrahedral and trigonal prismatic Co^{2+} centres are taken into account to estimate the energy barrier of the magnetization reversal.

However, with the aim of isolating magnetic centres, Zn^{2+} based magnetic dilution was carried out. Magnetic dilution involves the doping of Co^{2+} paramagnetic centres into Zn^{2+} diamagnetic matrix yielding heterometallic compounds. This strategy has shown to be an interesting approach to isolate paramagnetic centres since it avoids magnetic exchange interactions, supressing long-range order, so that the material behaves as a single ion magnet (SIM).[28] In particular, analysis of the more diluted compound $[Co_{0.05}Zn_{0.95}L]_n$, (composed of 95 % zinc in the metal stoichiometry) reveals slow magnetic relaxation with $\tau_0 = 2.09\ 10^{-5}$ s and $U_{eff} = 6.31$ K according to the best fitted with Orbach and Raman relaxation processes ($B = 1.23\ s^{-1} \cdot K^{-n}$ and $n = 5.75$).

$$\tau^{-1} = \tau_0^{-1} \exp(-U_{eff}/k_B T) + BT^n$$ **Equation 2.2**

2–6 K range generated Cole–Cole plots display well-defined semicircles that may be fitted with the generalised Debye model,[29] to estimate the nature of the relaxation processes. The obtained α values are within the range of 0.09 (2 K)–0.04 (6 K), suggesting a single mechanism involved in magnetic relaxation. However, when ln(τ) versus 1/T feature is plot Arrhenius plots present a curved shape. Thus, fitting the high-temperature data to Raman process gives $\tau_0 = 8.44\ 10^{-7}$s and $U_{eff} = 18.82$ K. In any case, taking into account the shape of the curve, the relaxation times were fitted to an expression that considered the presence of simultaneous Orbach and Raman relaxation processes. Several examples in bibliography had shown that either tetrahedral[28,30,31] and trigonal prismatic[16,26,32,33] cobalt environments tend to relax by multiple relaxation pathways where the relaxation data should be modelled with accounting for the contributions from direct, QTM, Raman and Orbach relaxation processes. In our case, as cobalt environment are supposed to be ideally isolated wherein the network, the contribution of both relaxation modes corresponding to its centre have been considered for the best fitting.

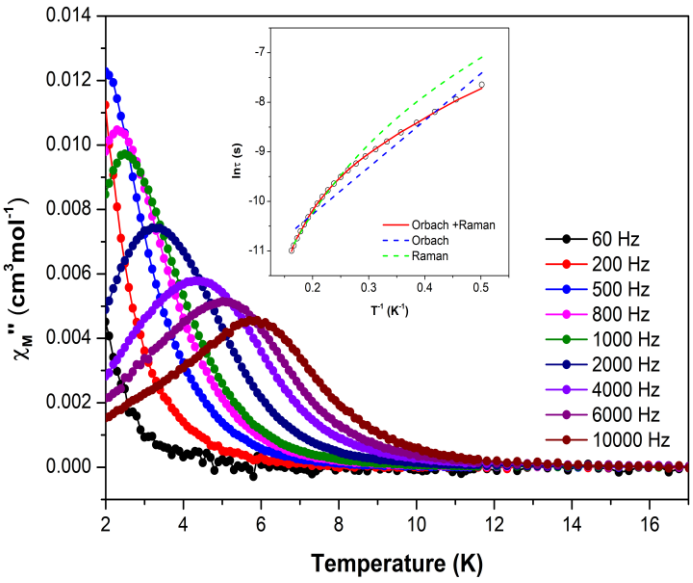

Figure 2.5. Temperature dependence of out-of-phase components of the *ac* susceptibility in a *dc* applied field of 1000 Oe for heterometallic $[Co_{0.05}Zn_{0.95}L]_n$. Inset: Arrhenius plots. The black line accounts for the best fit considering Orbach relaxation, and the red line corresponds to Orbach plus Raman relaxation.

Interestingly, the presence of Zn^{2+} in the heterometallic samples imbues them with photoluminescent properties. Motivated by this, we decided to explore photoluminescent properties of $[Co_xZn_{1-x}L]_n$ heterometallic compounds as well the pure zinc based material. To that end, we took advantage of the fact that these compounds were isostructural to the a zinc-based counterpart previously reported in bibliography.[6] That Zn^{2+} based metal-organic framework described by Zhang *et al.* had proved to have an extraordinary acid–based resistance and was able to efficiently separate acetylene from C_2H_2/CO_2 mixtures under ambient conditions.

For the synthesis of heterometallic compounds several proportions of Zn^{2+} to Co^{2+} combinations were employed. (See Table 2.1 for more details). Chemical and physical characterization as well as PXRD data confirmed the success of partial replacement in the result heterometal counterparts (Figure A2.3). Additionally, we further confirm the presence of both metals by EDX mapping (Figure A2.16).

2.3.3 Photoluminescent properties

The solid-state photoluminescence spectra were recorded at ambient temperature for polycrystalline homometallic (Zn^{2+} and Co^{2+}) and $[Co_xZn_{1-x}L]_n$ heterometallic samples. We first decided to explore homometallic Zn^{2+} emission capacity given that group 12 metals are known to be particularly suitable for their use in photoluminescence, contrarily to what occurs for Co^{2+}.[34] The closed-shell electronic configuration affords no d-d transitions, which could enhance ligand-centred (LC) emission.[35] Furthermore, the presence of these ions may also promote ligand-to-metal charge transfer (LMCT) as metal ions possess empty orbitals that can be populated in the excited state, and therefore the photoluminescence (PL) emission may be modulated with regard to the ligand-centred (LC) emissions.[36] Upon excitation with 330 nm light, the zinc-based compound shows three maxima peaking at 361, 391 and 460 nm, among which the second one dominates the emission spectrum. The excitation spectrum focusing on the main emission line exhibits several absorption bands located in the ultraviolet region with four maxima at around 288, 307, 322 and 332 nm, which resemble the excitation spectra found for the previously reported ligand.[37] Therefore, the observed bands can be attributed to inner π– π* transitions occurring in the aromatic ring of the 3-amino-4-hydroxybenzoic acid ligand. In order to get deeper insight into the emission mechanism, TD-DFT calculations were performed on suitable model of homometallic zinc compound. The calculated spectra reprocess fairly well the experimental one, indicating that the process is conducted by three main transitions between the molecular orbitals depicted in Figure 2.6. Nonetheless a shift of around 50 nm is observable in first two transitions, thus correlating the transition calculated at 308 nm to the experimental 361 nm transition and the calculated 342 nm transition to the 391 nm experimental transition, respectively. The electron density of HOMO orbitals HOMO-5 and HOMO-3 is extended over the aromatic ring what suggest a π orbital, whereas LUMO orbital feature a π* character. Thus, it can be confirmed that the transitions involved in the photoluminescence are mainly of π*←π nature induced by ligand centred emission, as further confirmed by the agreement of experimental data and TD-DFT calculations.

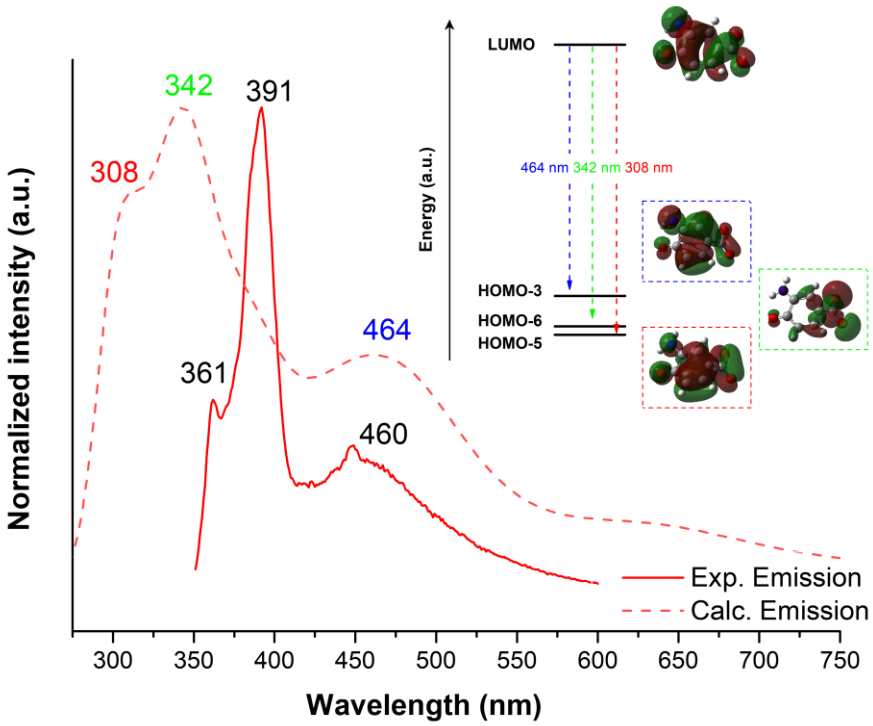

Figure 2.6. Room temperature Time-dependent density-functional theory (TD-DFT) computed (dashed lines) and experimental (solid lines) photoluminescence under λ_{ex} = 330 nm polycrystalline homometallic Zn-MOF. The insets show the most representative molecular orbitals involved in the electronic transitions**.**

The emission and excitation spectra of compound **2.1** (based on the cobalt counterpart) show similar patterns (for more detailed information check Appendix 2. Figure A2.38) with much less emission intensity due to the quenching exerted by this ion.

With the aim of integrating the photoluminescence properties into the magnetic compound **2.1**, the heterometallic mixtures were further studied. The main emission bands of $[Co_xZn_{1-x}L]_n$ materials keep the same shape but are somewhat structured compared to homometallic compounds. Additionally, the minor shoulder peaking at λ_{em} = 448 nm presents relatively lower intensity for the heterometallic materials than for the zinc analogue. No remarkable shift of the main bands is observed between homo- and heterometallic compounds. In fact, the inset in Figure 2.7 reveals that there is a linear relationship between the intensity of the main signal (peaking at 392 nm) and the Co^{2+} proportion, since it acts as a luminescent quencher. Thus, the quenching efficiency

was estimated applying the Stern-Volmer equation which correlates the quencher concentration with the fluorescence decrease by a quencher constant.

$$I/I_0 = 1 + k_{sv}Q \qquad \textbf{Equation 2.3}$$

being I the fluorescence intensity of heterometallic compound, I_0 the reference fluorescence intensity of the Zn counterpart and Q the quencher (Co^{2+}) concentration.

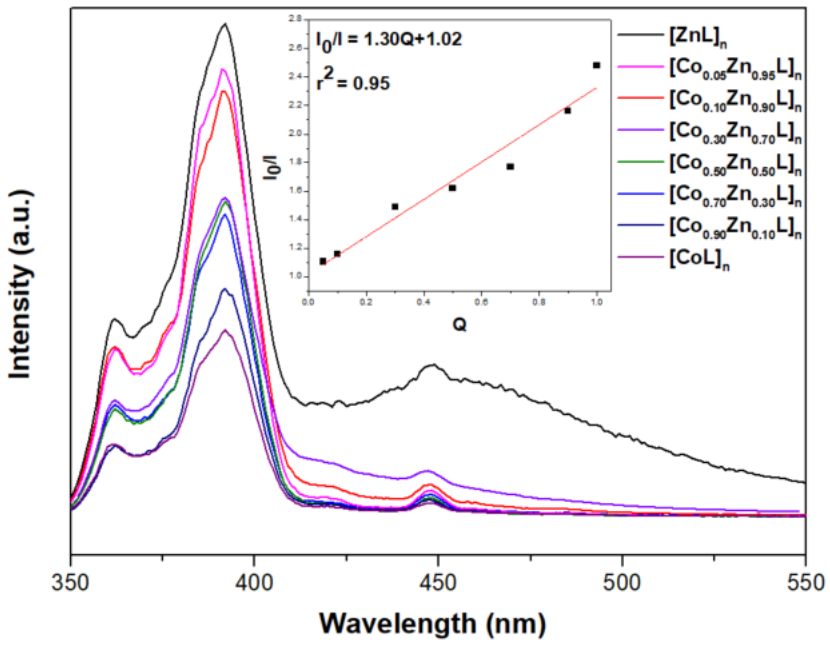

Figure 2.7. Fluorescence spectra of homometallic zinc and cobalt compounds and $[Co_xZn_{1-x}L]_n$ (where x= 0.9-0.1 stands for the proportion of Zn in the formula) at RT (λ_{ex} = 330 nm). Inset graph: Stern-Volmer plot with regard to the relative intensity of the main emission band.

The linear fitting of Equation 2.3 gives a value of k_{sv} value of 1.30(0.1), meaning that the quenching capacity of cobalt(II) ions is relatively low and that the resulting materials may be considered to be bifunctional. Among all the studied samples, that containing the lowest proportion of Co(II), namely $[Co_{0.05}Zn_{0.95}L]_n$, is probably the most interesting one, since it presents both single-ion magnet and photoluminescence properties.

2.4 Conclusions

In conclusion, we have successfully synthesised a novel Co_MOF (**2.1**) by solvothermal reaction. $[CoL]_n$ possess a 3D porous network connected ***tps*** topology structure which is constructed by the connection of $Co(NO_3)_2 \cdot 6H_2O$ and 3-amino-4-hydroxybenzoic acid ligand. In the attempt to add multifunctionality to Co_MOF (**2.1**), diamagnetic-matrix based dilution allowed to obtain a material with single ion magnet behaviour showing a magnetic barrier for the reversal of magnetization of U_{eff} = 6.31 K. Additionally, the photoluminescent studies of heterometallic Zn-Co and homometallic isostructural zinc materials showed linear response in the fluorescent intensity decrease with respect to Co^{2+} quencher incorporation in the structure. Overall, this work will prompt further design of multifunctional porous cobalt-based MOF that is able to show single ion magnet behaviour in a diluted matrix as well as emissive properties.

PART 2

2.5 Introduction. Multifunctional Lanthanide-based Metal-organic Frameworks derived from 3-amino-4-hydroxybenzoate: Single-molecule magnet behaviour, luminescent properties for thermometry, CO_2 adsorptive capacity and catalysts for efficient solvent-free cyanosilylation reaction

Metal-organic frameworks (MOFs) are organic–inorganic hybrid materials self-assembled by metal ions/clusters with organic linkers through metal–organic linker coordination bonds. As metal ions/clusters generally display certain preferred coordination geometries, self- assembly of these moieties (known as nodes) with organic ligands (linkers) of predetermined shapes and predictable coordination patterns can give rise to rationally designed MOFs with anticipated structures.[38] These materials are also well-known by their permanent porosity with significantly high surface area which make them very promising for applications related to gas capture.[39] In this regard, pore surface's tunability by pre- or post-synthetic modifications permit convenient optimization and maximization of the pore size and shape to fully exploit pore space for selective adsorption and storage. Moreover, the crystallinity of these materials allows the precise analysis of adsorption sites, which helps to understand the magnitude of adsorbate-adsorbent interactions is within the pores.[40] In particular, lanthanide-based MOFs (Ln-MOFs) are a class of crystalline materials that have attracted great attention during the last decades due to their intrinsic advantages such as coordination versatility and broad application-spectrum owing to their unique properties based on f-electrons.[41] In fact, lanthanide ions offer the possibility to incorporate both luminescent-centres and magnetic properties in a single material, enabling combinations that are ideally shaped for a particular application while the material is imbued with multifunctional character.[42,43]

Lanthanide's electrons are located in 4f orbitals which are shielded by occupied $5s^2$ and $5p^6$ orbitals from ligand field. Because of this fact, the coordination environment around the 4f ion keeps almost undisturbed giving rise to high spin-orbit coupling interactions. Therefore, when describing magnetic properties of lanthanide ions, it is necessary to consider a spin-orbit coupling term which is described by M_J quantum number. Overall, the rational design of materials with single-molecule magnet (SMMs)

behaviour require, in addition to a well-defined ground state with the highest M_J value, sizeable energy separation with the excited $M_{J\pm1}$ sublevels in order to get high energy barriers (U_{eff}) for the reversal of magnetization and thus, high performance SMMs. This energy barrier is dependant of a parameter called the anisotropy, which is an intrinsic characteristic of lanthanide ions and their coordination sphere. The electronic cloud of each lanthanide ion disposes a particular shape in each M_J level, although, when stabilizing the ground state M_J sublevel, two main shapes are distinguished: oblate and prolate.[44] In order to enhance magnetic anisotropy in the ground state M_J sublevel, it is important to suitably select the coordination environment of the metal, i.e. the ligand distribution around the metal centre (in other words ligand field), in order to favour anisotropic electron density of the lanthanide ion, and thus, rationally design materials with greater energy barriers. In this regard, according to the lanthanide ions' anisotropic electron density–leaving apart Gd^{3+} which is isotropic–, oblate ions (e.g. Dy^{3+} and Tb^{3+} ions) should possess ligand donor atoms with the greatest electron density coordinated at the axial positions, whereas prolate ions (e.g. Er^{3+} and Yb^{3+}) acknowledge the coordination of ligand donor atoms with greatest electron density coordinated at the equatorial positions in order to maximize the anisotropy of the metal centre.[44]

Apart from exploiting magnetic properties, lanthanide ions offer interesting photoluminescence properties characterized by emissions that cover a vast range of the electromagnetic spectrum. Even if they show small absorptive coefficients, each lanthanide ion shows characteristic hypersensitive and narrow emissive lines converting these metals particularly suitable for the elaboration of light-emitting devices.[45] In the particular case of lanthanide-based MOFs, the photoluminescence properties arise from both the metal centre and the organic ligand, which makes the afore mentioned structural design of high importance in order to modulate the emission to a specific application such as sensing, diodes, display technology, etc.[20,46] Notably, among aforementioned applications, in recent years, much effort has been devoted to the development of Ln^{3+} ratiometric thermometers.[47] Comparing to conventional contact thermometry, luminescent thermometry exhibits a non-invasive and robust technique with faster response, higher accuracy and spatial resolution where generally conventional thermometry lacks of effectiveness.[48] In general, absolute temperature in lanthanide-based luminescent thermometers is optically determined, preferably, via intensity-ratio of two Ln^{3+} emitting centres. Often, Eu–Tb-mixed MOF are presented as good candidates where the intensity-ratio of the $^5D_4 \rightarrow {}^7F_5$ and of the $^5D_0 \rightarrow {}^7F_2$ transitions of Tb^{3+} and Eu^{3+} respectively are compared.[48] It must be noted that since 2012, when the

first example of ratiometric Eu-Tb mixed MOF luminescent thermometer was described,[49] the number of these materials has potentially increased. So far, the reported luminescent thermometers display greater thermal sensitivity for a specific temperature-range and they are, hence, classified among the temperature region in which they can perform. In this way, thermometers performing in the cryogenic region- (<100 K), in medium (100–300 K), in biological (298–323 K), and in high-temperature domains (>400 K) may be distinguished. In particular, thermometers performing at cryogenic region are in great demand since they can find application in fields of superconducting magnets, aerospace, and nuclear fusion power.[50–52] However, at present, the number of lanthanide based MOFs thermometers covering the cryogenic range is still very limited.[53–55]

As previously stated, MOF's porosity and high surface areas enable their application in gas adsorption/separation processes. Among other gases, the current rise of atmospheric CO_2 concentration levels, resulting from combustion of fossil fuels, is nowadays a worldwide environmental concern. Up to now great efforts are being done to develop new methodologies and technologies to effectively capture this gas in order to mitigate its emission into the atmosphere.[56,57] While still at it infancy, a significant progress has been made in the development of MOFs for CO_2 capture in recent years. Nonetheless, the implementation of MOFs as CO_2 adsorbents is still a challenging matter.[40] Four main mechanisms rule the selective adsorption of CO_2 using MOFs as adsorbents: 1) the size and shape exclusion, only molecules with a specific shape and below certain size could only break through the pore, this effect is called the molecular sieving effect, 2) the interaction between the pore surface and the adsorbate, 3) the control over the pore size of the adsorbent and the kinetic diameter of two molecules required to be separated and 4) the diffusion speed of guest molecules and compatibility of the pore diameter will determine selective-adsorption process.[43,58] Additionally, it must be noted that for MOFs being used as CO_2 adsorbents before the adsorption process, an activation may be required via applying vacuum and/or high temperatures with the goal of removing coordinated and crystallization solvents molecules to give rise to open metal sites or coordinatively unsaturated sites (*cus*) with which guest-molecule will interact. The strength of this interaction is defied by the heat of enthalpy or isosteric heat (Q_{st}) and describes the affinity of the MOF to adsorb CO_2.[40] Generally, material activation promotes an uptake of guest molecules, CO_2 in this case, improving by far the adsorption capacity of the MOFs.

Additionally, another heightening field in which metal–organic frameworks (MOFs) have garnered significant attention by the scientific community as potential functional materials of use in heterogeneous catalysis.[59,60] The high degree of synthetic tunability in coordination modes and number, allowed to the synthesis of materials with different properties such as surface area, porosity, pore size and shape, density and stability.[61] MOFs main advantage lie in (1) their high internal surface area, which provides space for reactions; (2) catalytic activity toward organic reactions stemming from both metal and organic active functionalities; (3) selectivity originating from the well-defined pore environment; and (4) architectural and chemical stability endowed by the robust linkages made up of organic units and metal-based clusters, which enables recycling them as catalysts.[62] One subset of MOFs that are of interest from a synthetic and application points of view are those assembled using rare-earth metal nodes, where yttrium and scandium are included together with the series of fifteen lanthanides.[63] Contrary to *d*-block metals, the coordination chemistry of rare-earth metals is very diverse, with only small energetic differences between different coordination numbers and geometries, and where geometry is dictated primarily by ligand steric effects.[64]

In recent years, various studies have been conducted towards the use of rare-earth MOFs as heterogeneous catalysts for organic reactions, being one of these benchmark transformations the cyanosilylation of carbonylic compounds.[63] This reaction is a powerful synthetic tool for the C−C bond formation in organic chemistry and provides access to versatile cyanohydrins that can be easily transformed to plenty of useful compounds in the chemical industry.[65]

As already mentioned, cyanohydrins are versatile building blocks for the synthesis of a great variety of fine chemicals (organic compounds such as α-hydroxy acids, α-hydroxy aldehydes and β-amino alcohols)[37,65] agrochemicals and pharmaceuticals.[66] For the synthesis of this type of compounds, trimethylsilyl cyanide (TMSCN) is presented as the best cyanation agent; indeed, the hydrolysis of TMSCN results in the in situ generation of HCN. Most interestingly, the direct use of TMSCN leads to the formation of more stable O-silyl protected cyanohydrin, which can be handled more safely and employed for further transformations.[67,68] More importantly, due to its higher atom economy without formation of side products leaving apart the use of more toxic reagent (such as NaCN, KCN or HCN). Moreover, it is environmentally friendly, cost-efficient and selective towards extremely versatile organic molecules, which is in total agreement with some of the twelve principles of green chemistry.[69,70]

From the viewpoint of green chemistry, modern chemical research must make progress on the basis of sustainable and environmentally benign practices.[71] Anastas and Warner[69] introduced the concept of "Green Chemistry" with the aim of overcoming environmental and health problems generated by chemical industry by designing innovative eco-friendly reactions that would lead to cleaner processes. Basically, this concept emphasizes efficient use of the starting materials (preferably recycled) and minimization of waste generation in addition to the use of toxic or hazardous reagents in the manufacture and application of chemicals. In this context, a chemical process can be evaluated by green chemistry metrics.[72] Atomic economy (AE), mass intensity (MI), reaction mass efficiency (RME) and carbon efficiency (CE) parameters have been proposed as a measure of environmental sustainability in terms of minimizing the theoretical amount of waste. The green metrics are calculated by Constable eta al.[72] equation and ideally for AE, RME, and CE should be 100 % and for MI close to 1.

In the following lines, green metrics will be defined. AE is a theoretical measure of the chemical and environmental efficiency of a reaction taking into account reaction stoichiometry; solvents, possible excess of reagents, formation of unwanted products, etc. are not taken into account.[73] MI considers the yield, stoichiometry and also the solvent and the reagent employed in the reaction. RME allows for the effect of yield and the excess or catalytic amount of reactants used without considering the solvent. CE is the percentage of carbon in the reactants that remains in the final product and principally reflects the yield of reactions.

$$MI = \frac{Total\ mass\ used\ in\ a\ process/\ process\ step\ (g)}{Mass\ of\ product\ (g)} \qquad \textbf{Equation 2.4}$$

$$RME\ \% = \frac{\Sigma\ mass\ of\ products}{\Sigma\ mass\ of\ reactants} x100 \qquad \textbf{Equation 2.5}$$

$$CE\ \% = \frac{mol\ of\ product\ x\ N^{o}\ of\ carbons\ in\ the\ product}{\Sigma\ (mol\ of\ reactant\ x\ N^{o}\ of\ carbons\ in\ the\ reactant\ )} x100 \qquad \textbf{Equation 2.6}$$

Regarding to the catalytic cycle followed in the TMSCN assisted cyanosilylation reaction two possibilities are usually proposed (Scheme 2.1).[37] In both of them, the

coordination of the carbonylic substrate to the unsaturated metallic centre is presented as the first step of the reaction; this coordination leads on partially positively charged carbonyl carbon atom (carbon activation) favouring the subsequent nucleophilic attack of the TMSCN. The molecular rearrangement results in the formation of the main product; the catalytic cycles reported differ in the order of the mentioned rearrangement. The products were replaced by aldehydes or ketones, and the catalysts were continued to activate further carbonylic substrates in subsequent catalytic cycles, as so far has been described previously for similar compounds in bibliography.[74–76]

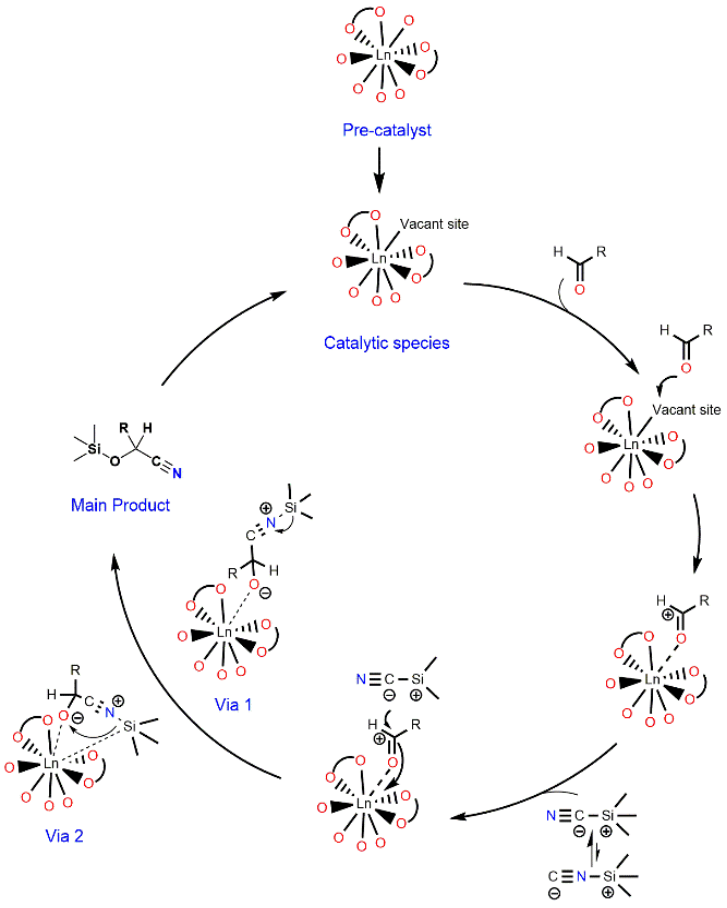

Scheme 2.1. A plausible mechanism for the cyanosilylation reaction catalysed by Y- and Eu-MOFs.[63,76,77]

In the vast majority of the examples reported cyanosilylation reaction is performed by homogeneous catalyst, where the catalyst is responsible for the activation of the carbonyl substrate. Lewis acids,[78,79] Lewis bases,[80,81] organic-inorganic salts,[82,83] or nucleophilic catalysts[84] among others[70] are some of those catalyst

that have been extensively investigated exhibiting relatively high efficiency. Nonetheless, separation difficulties and recyclability hinder the process. Although recently a catalyst-free protocol for cyanosilylation of aldehydes[85] has been proposed, it required a high temperature and showed no activity when less-reactive ketones were employed.[86] Therefore, catalytic methods are more commonly applied as they provide better results with mild experimental conditions.

Form the sustainability point of view, easily separable solid catalysts are the preferable choice since they present good recyclability, easy processability and economic viability derived from its low cost and lack of catalyst contamination within the final product. Regarding the classification of heterogeneous catalyst developed for cyanosilylation reaction three major categories are differentiated: (i) polyoxometalates, which in most cases act as Lewis bases; (ii) organocatalyits and (iii) metal-organic frameworks, which act as Lewis's acids. When comparing organocatalysts to metal-based counterparts, the former are exempt from possible metal leaching and thus product contamination; however, they are generally less reactive and need stronger reaction conditions.[86]

Cyanosillation reaction was firstly reported in 1994 by Fujita and co-workers using a Cd based coordination polymer being used as catalyst,[87] and here after, a plethora of diverse works have been applied to this specific reaction using metal-MOF such as based on *d*-block metals.[88–94]

A bit later, concretely in 2004 Schlichte et al reported Cu-HKUST-1 being able to catalyse cyanosilylation reaction of aldehydes in reasonable yield (70 %) after 48 h reaction time and 5 mol% catalyst loading.[95,96] More recently, various known MOFs such as Cr-MIL-101, Zr-UiO-66 and bisphenol-based has exhibited remarkably accelerated cyanosilylation of various carbonylic substrates in excellent yield (98 %), albeit the rate depended on the type of organic solvent.[90,91] 3d metal based systems among which manganese[92] and cobalt [93,94] MOFs have also been investigated for carbon–carbon forming cyanosilylation reaction being the former used a catalyst loading as high as 11 mol%, whereas the latter used a significantly reduced amount of 2 mol%.

However, if attention is focused on lanthanide-based MOFs able to catalyse cyanosilylation reaction, no more than 15 examples have been reported so far, where the catalytic activity of the material is demonstrated by using catalyst loadings in the

range of 1 to 10 mol%, and using in all of them reactive aldehydes as electrophiles.[74,76,105–108,97–104]

In fact, there are only three examples where the use of less reactive ketones were investigated with these rare-earth metal-MOFs giving rise to the formation of highly interesting quaternary centres. The first one, was reported by Gustafsson et al. in 2010.[109] In that work, Nd(btc)·H_2O (btc = 1,3,5-benzenetricarboxylate) was used as catalyst in a 4.5 mol% loading at room temperature and dichloromethane (DCM) as solvent, reaching 91 % of conversion after 18 h. To the best of our knowledge, this is the highest conversion reached so far when using ketones as electrophiles. Later on, Ce-MOF (3 mol%)[110] and Tm-BDC (BDC = 1,4-benzenedicarboxylate) (2 mol%)[111] catalysts where tested under solvent-free conditions being not able to overpass previous results yielding only an 8 or 31 % of conversion, respectively.

Having all this in mind, our research group has paid attention to the preparation of Ln-MOFs for adsorption processes and focused on designing novel multifunctional metal-organic frameworks exhibiting magnetic, photoluminescent, adsorptive, and catalytic properties. In this work, we report on a novel family of isostructural porous compounds formulated as $\{[Ln_5L_6(OH)_3(DMF)_3]\cdot 5H_2O\}_n$ based on 3-amino-4-hydroxybenzoic acid ligand (H_2L).[37] In addition to the synthesis and physico-chemical characterization, magnetic properties have been accomplished based on samples containing oblate and prolate lanthanide(III) ions as well as on magnetically diluted materials. Moreover, photoluminescence properties of ligand and Tb^{3+} and Eu^{3+} samples have been studied and the performance as ratiometric thermometers in heterometallic materials. Furthermore, adsorptive capacity of dysprosium counterpart to adsorb CO_2 has been also analysed both at ambient pressure and at high pressure conditions. To conclude, we report yttrium- and europium-based MOFs for solvent-free catalytic cyanosilylation reaction of a bunch of carbonylic substrates. The study of the catalytic performance has enabled comparing their ability towards different aldehydic and ketonic substrates.

2.6 Materials and methods

All chemicals were reagent grade and were used as commercially obtained without any further purification.

2.6.1 Compound synthesis

General procedure for the synthesis of single crystal of $\{[Ln_5L_6(OH)_3(DMF)_3]\cdot 5H_2O\}_n$ where Ln = Nd (**2.2**), Sm (**2.3**), Eu (**2.4**), Gd (**2.5**), Tb (**2.6**), Dy (**2.7**), Ho (**2.8**), Er (**2.9**), Tm (**2.10**), Yb (**2.11**), Y (**2.12**). 0.010 g (0.0625 mmol) of 3-amino-4-hydroxybenzoic acid organic linker was dissolved in 0.5 mL of DMF containing 10 µL of Et_3N (0.072 mmol). 0.0434 mmol of the corresponding lanthanide nitrate salt, was dissolved into a 0.5 mL of distilled water in a separate vial. Once dissolved, 0.5 mL of H_2O was added to the ligand solution and 0.5 mL of DMF to the metal solution. The metal solution was added dropwise to the ligand solution under magnetic stirring. The resulting brownish-yellow solution was poured into a screw-capped vial (6 mL) and introduced to the oven at 100 °C for 2 hours to give rise hexagonal shaped single crystals. Single-crystal X-ray structure determination, elemental analysis (EA) and TGA confirm the general formula $\{[Ln_5L_6(OH)_3(DMF)_3]\cdot 5H_2O\}_n$.

General procedure for the scaled-up synthesis: 0.2 g (1.2 mmol) of 3-amino-4-hydroxybenzoic acid ligand was weighted and dissolved in 3 mL/2mL DMF/H_2O solvent mixture containing 200 µL of Et_3N (1.44 mmol). To this solution, a solution containing 0.868 mmol of $Ln(NO_3)_3\cdot nH_2O$, dissolved in 1 mL water, was added dropwise. A precipitate seems to be formed in the beginning though it is eventually redissolved to give rise to a brownish-yellow solution. This solution was placed in a microwave and heated at 100 °C for two hours to get around 60-85 mg of Ln-MOF (yielding ~18-26 %). The purity of the product was confirmed by PXRD.

General procedure for the synthesis of heterometallic materials:

Synthesis of heterometallic materials for magnetic dilution: 0.100 g (0.625 mmol) of 3-amino-4-hydroxybenzoic acid organic linker was dissolved in 3 mL/2mL DMF/H_2O solvent mixture containing 100 µL of Et_3N (0.720 mmol). To this solution, a solution containing 0.434 mmol of the corresponding salt mixture was dissolved in 1 mL water, was added dropwise. For the synthesis of magnetically diluted samples, yttrium was employed as diamagnetic metallic-centre. Three heterometallic Y^{3+}–Ln^{3+} compounds were prepared where Ln^{3+} = Dy^{3+} (**2.13**), Er^{3+} (**2.14**) or Yb^{3+} (**2.15**) with 30:1 %

Y^{3+}:Ln^{3+}doping proportion. The metal mixture solution was added dropwise to the ligand solution under magnetic stirring. The resulting brownish-yellow solution was placed in a microwave and heated at 100 °C for two hours. The purity of the product was confirmed by PXRD.

Heterometallic materials tested in ratiometric thermometry: 0.100 g (0.625 mmol) of 3-amino-4-hydroxybenzoic acid organic linker was dissolved in 3 mL/ 2mL DMF/H_2O solvent mixture containing 100 µL of Et_3N (0.720 mmol). To this solution, a solution containing 0.434 mmol of the corresponding lanthanide salt mixture was dissolved in 1 mL water, was added dropwise. Accordingly, three additional heterometallic compounds with Y^{3+} or Gd^{3+} and Tb^{3+}/Eu^{3+} mixed lanthanide ions were prepared with the following doping proportions Y^{3+}:Tb^{3+}:Eu^{3+} 50:45:5 % and 50:40:10 %, and Gd^{3+}:Tb^{3+}:Eu^{3+} 50:40:10 %, compounds **2.16**, **2.17** and **2.18**, respectively. The heterometal solution was added dropwise to the ligand solution under magnetic stirring. The resulting brownish-yellow solution was placed in a microwave and heated at 100 °C for two hours. The purity of the product was confirmed by PXRD.

General procedure for the synthesis $\{[Eu_5L_6(OH)_3(H_2O)_3]\cdot 5DMF\}_n$, Eu-MOF or (**2.19**). 0.010 g (0.0625 mmol) of 3-amino-4-hydroxybenzoic acid organic linker was dissolved in 0.2 mL of DMF containing 10 µL of Et_3N (0.072 mmol). 0.019 g (0.0434 mmol) of $Eu(NO_3)_3\cdot 5H_2O$, was dissolved into a 0.8 mL of distilled water in a separate vial. Once dissolved, 0.8 mL of H_2O was added to the ligand solution and 0.2 mL of DMF to the metal solution. Metal solution was added dropwise to the ligand solution keeping magnetic stirring. The resulting brownish-yellow solution was poured into a screw-capped vial (6 mL) and introduced to the oven at 100 °C for 2 hours to give rise hexagonal shaped single crystals.

General procedure for the scale-up synthesis of Eu MOF (2.19): 0.2 g (1.2 mmol) of 3-amino-4-hydroxybenzoic acid ligand was weighted and dissolved in 1.2 mL/ 3 mL DMF/H_2O solvent mixture containing 200 µL of Et_3N (1.44 mmol). To this solution, a solution containing 0.38 g (0.868 mmol) $Eu(NO_3)_3\cdot 5H_2O$ dissolved in 1.8 mL water, was added dropwise. A precipitate seems to form but ends up redissolving to give rise to a brownish-yellow solution. This solution was placed in an oven and heated at 100 ºC for two hours to get 80 mg of Eu-MOF. The purity of the product was confirmed by PXRD.

2.6.2 Catalysis

General procedure for the cyanosilylation reaction: In a 1 ml vial with a septum screw capped equipped with a stirring bar, 0.5 mol% catalyst (2.3 mg for Y-MOF (**2.12**) and 2.5 mg for Eu-MOF (**2.19**), respectively) was weighed. Subsequently, the corresponding amount of carbonylic compound **2** (0.25 mmol) was added followed by trimethylsilyl cyanide (TMSCN) (34 µL, 0.275 mmol, 1.1 equiv.) and the reaction was stirred under inert N_2 atmosphere at room temperature during the corresponding time. Once the reaction was finished the catalyst was removed by centrifugation (8000 rpm, 3 min) and washed with DCM (2 x 0.5 mL) obtaining the corresponding pure product **3** or **4** after removal of the solvent with rotary evaporator. When not fully conversion was reached, the product was purified by column chromatography using hexane as eluent.

2.7 Results and discussion

2.7.1 Structural characterization

Single-crystal X-ray crystallographic studies on $\{[Ln_5L_6(OH)_3(DMF)_3]\cdot 5H_2O\}_n$ (where Ln = Nd (**2.2**), Sm (**2.3**), Eu (**2.4**), Gd (**2.5**), Tb (**2.6**), Dy (**2.7**), Ho (**2.8**), Er (**2.9**), Tm (**2.10**), Yb (**2.11**), Y (**2.12**)) reveal three dimensional (3D) lanthanide MOFs **2.2**-**2.12** crystallize in the hexagonal *P6₃/m* space group (for details, see Table A2.3). Furthermore, X-ray crystallographic analysis suggested that **2.2**-**2.11** are isostructural compounds. So, in the following section we will only discuss the structure of $\mathbf{2.7_{Dy}}$ in detail as a representative example of the family. The asymmetric unit of $\mathbf{2.7_{Dy}}$ is comprised of two crystallographically independent Dy^{3+} ions and a deprotonated ligand, as well as a coordinated DMF solvent-molecule. The organic linker, 3-amino-4-hydroxybenzoic acid, coordinates to the lanthanide ion by the carboxylate moiety in a bidentate way, along with the hydroxyl and amino groups in a monodentate way.

Dy1/ Dy2 atoms present nine-coordinated and eight-coordinated environments, respectively. Dy1 exhibits $[DyN_3O_6]$ environment composed by the coordination of three nitrogen atoms and three oxygen atoms belonging to amino and hydroxy groups of the organic ligand, whereas the remaining three oxygen atoms pertain to hydroxyl anions. Instead, Dy2 completes the coordination shell by six donor atoms belonging to the carboxylate moiety of the ligand in addition to the hydroxyl anion and a DMF solvent molecule. Continuous shape measurements (CShMs)[22] reveal that Dy1 and Dy2 atoms build different polyhedra, with that of Dy1 resembling a spherical tricapped trigonal prism (TCTPR-9) and that of Dy2 a triangular dodecahedron (TDD-8), see (Tables A2.8 and A2.9 for more detailed information).

Growing the asymmetric unit, it can be seen that both coordination environments are interconnected by hydroxyl anions, which act as μ_3-O to give rise to $Ln_5(OH)_3$ clusters (Figure 2.8), which can be considered the secondary building unit (SBUs) of the structure. Each of these clusters is joined to six neighbouring SBUs in such a way that it may be referred to as a six-connected node. The analysis of the topology by means of TOPOS Pro software[23] reveals that $\mathbf{2.7_{Dy}}$ presents a 6- connected uninodal net with the $(4^9\cdot 6^6)$ point symbol and **acs** topology. The growth of the structure along *c* axis leaves narrow microchannels that correspond to the 19.3 % of the unit cell volume according to the geometrical calculations performed with PLATON-v1.18 program.[112] Additionally,

the porous nature of this MOF forces it to crystallize with several solvent molecules within the pores, which account for five crystallization water molecules according to the thermogravimetric analysis.

a) **b)**

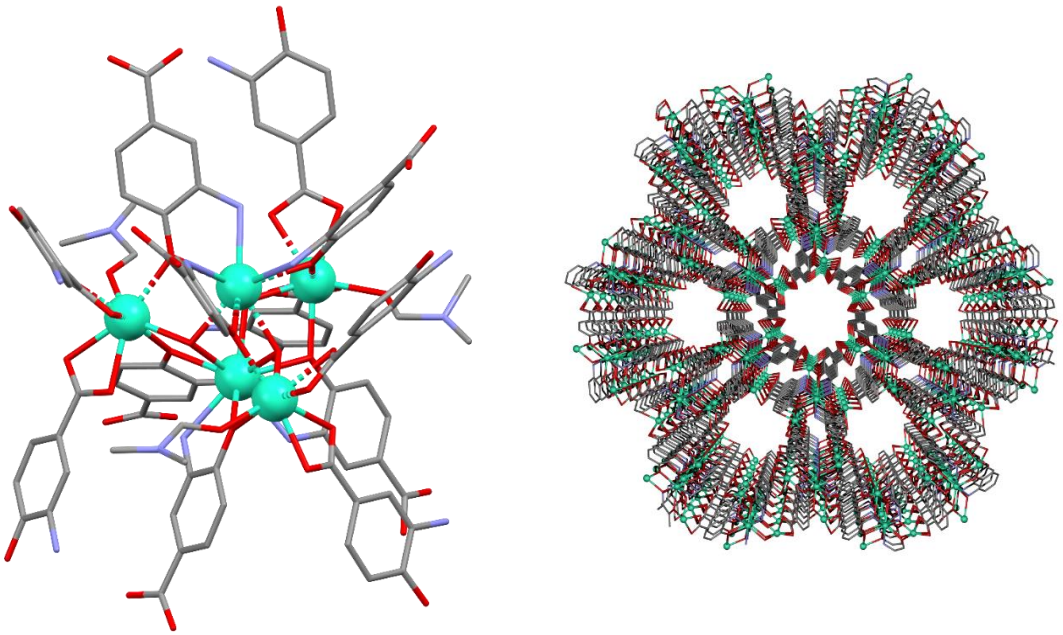

Figure 2.8. a) Excerpt of the coordination mode of the 3-amino-4-hydroxybenzoic acid ligand among the pentanuclear node, hydrogen atoms have been omitted for the sake of clarity and **b)** perspective view along the crystallographic c axis showing the microchannels.

Compounds **2.2**-**2.11** are also isotypic to an yttrium based MOF previously reported by our group.[37] Even though, Ln1 and Ln2 coordination environment in compounds **2.2**-**2.11** is exactly the same as in yttrium-based MOF, in advance compound **2.12**, single-crystal parameters of the latter diamagnetic counterpart differ slightly, a reason why powder X ray diffraction pattern shows slightly shifted diffraction maxima that is probably caused by the smaller size of yttrium(III) ion compared to lanthanide(III) ions (see Figure A2.5). At this point, it is worth highlighting that depending on the Y^{3+} to Ln^{3+} doping proportion, PXRD patterns present diffraction maxima corresponding to both pure compounds **2.12** and **2.2**-**2.11** (see Figure A2.7). Nevertheless, the occurrence of a phase segregation has been discarded by SEM mapping experiments, which clearly confirm random distribution of the three elements along a single crystal (for more details see Figure A2.17-19).

In this work, the yttrium-based material gives us the opportunity to get a deeper insight into both magnetic and luminescence properties of the Ln-MOF family. On the one hand, its diamagnetic nature allows to magnetically dilute paramagnetic centres to further examine the slow relaxation processes of single ions. On the other hand, Y-based compound can be used as a matrix to be doped with Eu^{3+} and Tb^{3+} ions to modulate the emission signal and evaluate their possible application in ratiometric thermometers. Finally, this structure has allowed us carrying on catalytic studies, concretely in cyanosilylation reaction of carbonyl substrates in presence of TMSCN.

Also, considering that our isostructural MOFs exhibit large channels in which coordinated DMF molecules are pointing put pore, we thought about the possibility of these coordinated solvent molecules being removable and creating vacant coordination sites that could serve as Lewis acid catalytic sites. In this context, we carried out cyanosilylation reaction of a bunch of aliphatic and aromatic carbonyl compounds under solvent-free media with yttrium analogous (**2.12$_Y$**) and with the aim of easing solvent discoordination, we tried to synthesise an analogous structure modifying synthetic procedure and increasing water to DMF ratio.

In such conditions, we obtained single-crystal of Eu-MOF (**2.19$_{Eu}$**) $\{[Eu_5L_6(OH)_3(H_2O)_3]\cdot 5DMF\}_n$ which exhibits exactly the same coordination mode as the previously discussed structures with the difference of having a water coordinated molecules instead of DMF in the asymmetric unit. In this latter case, again, large channels along *c* crystallographic axis corresponding to ca. 19 % of the unit cell have shown to host crystallization DMF molecules, which according to TG calculations come in accordance with five DMF molecules.

Growing the structure along *c* axis we realized that as for the analogous counterparts coordinated water molecules to Eu2 site was pointing out the pore which made us think about the possibility of being more easily displaced a coordinated water molecule than a DMF molecule and that the process of removing the coordinated solvent molecule to create vacant coordination sites that could serve as active Lewis acid catalytic sites would be favorized in this latter case. Because of that, compound **2.19$_{Eu}$** has been tested for the cyanosilylation reaction of carbonyl compounds, especially for the less reactive ketones.

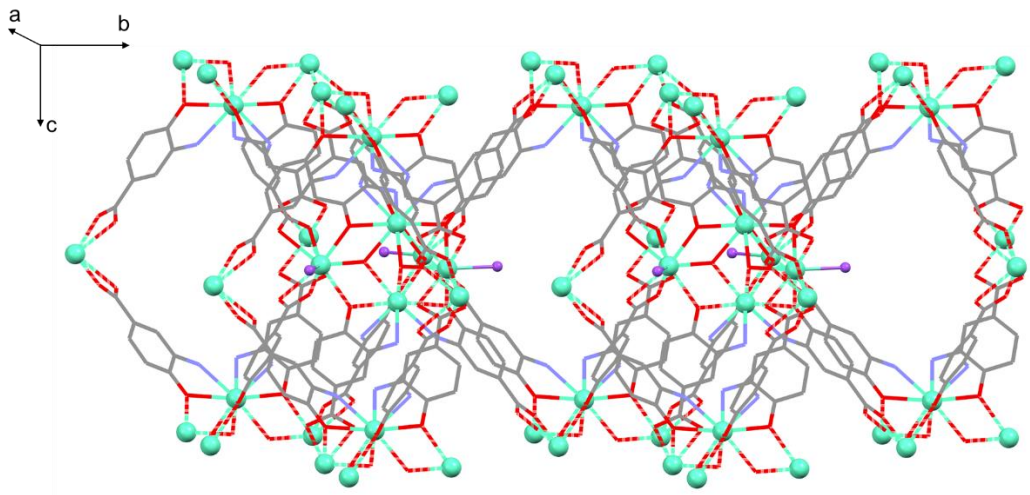

Figure 2.9. Pentametallic nodous showing the two different Eu(III) coordination environments (up) and perspective view of the packing of **2.19** where coordinated water molecules (coloured in purple) are displayed pointing out the pore **2.19$_{Eu}$**.

2.7.2 Magnetic properties

2.7.2.1 *DC* Magnetic Properties

Magnetic molar susceptibility (χ_M) measurements were acquired on polycrystalline samples in compounds **2.5-2.7, 2.10** and **2.11** in the temperature range of 2–300 K. Obtained room temperature $\chi_M T$ values are very close to the theoretical expected for five free non-interacting ions considering a regular population of the Stark sublevels in their ground states ($\chi T_{free\ ion}$ 40, 60, 71, 58 and 13 $cm^3\ K\ mol^{-1}$ for Gd^{3+}(**2.5**), Tb^{3+}(**2.6**), Dy^{3+}(**2.7**), Er^{3+}(**2.10**) and Yb^{3+} (**2.11**), respectively,

Figure **2.10**. Cooling down the samples, $\chi_M T$ product shows a progressive drop up to 50 K and a sharp drop at low temperature in compounds $\mathbf{2.5_{Gd}}$, $\mathbf{2.6_{Tb}}$, $\mathbf{2.7_{Dy}}$, and $\mathbf{2.10_{Er}}$. On its part, compound $\mathbf{2.11_{Yb}}$ experiments a much slower decay of to reach a value of 4.20 $cm^3\ K\ mol^{-1}$ at 2.0 K. Although the general trend of the $\chi_M T$ product may be associated to the thermal depopulation for the excited M_J sublevels derived from the crystal-field splitting of the corresponding ground term of the Ln^{3+} ions ($^8S_0$, $^7F_6$, $^6H_{15/2}$, $^5I_8$ and $^2F_{7/2}$ respectively for $\mathbf{2.5_{Gd}}$, $\mathbf{2.6_{Tb}}$, $\mathbf{2.7_{Dy}}$, $\mathbf{2.10_{Er}}$ and $\mathbf{2.11_{Yb}}$), the decrease of $\chi_M T$ product in compound $\mathbf{2.5_{Gd}}$ indicates that the occurrence of antiferromagnetic interactions must not be discarded. The field dependence of the magnetization was investigated in the range of 0–7 T at 2–7 K temperature range. Isothermal reduced magnetization curves (insets) display saturation for compound $\mathbf{2.5_{Gd}}$ reaching a maximum of 35 NμB, which comes in line with the value expected for the pentanuclear node. The saturation in reduced magnetization curves and the superimposition in M vs H/T plots is an expected feature due to the isotropic nature of Gd^{3+} ion. Instead, these curves (insets) lack of saturation (far for the expected saturation values of 9, 10, 9 and 4 NμB expected for one Tb^{3+}, Dy^{3+} Er^{3+} and Yb^{3+} ion, respectively) for the rest of compounds, which in addition to the non-superimposition of the M vs H/T plots corroborates the presence of magnetic anisotropy in compounds $\mathbf{2.6_{Tb}}$, $\mathbf{2.7_{Dy}}$, $\mathbf{2.10_{Er}}$ and $\mathbf{2.11_{Yb}}$.

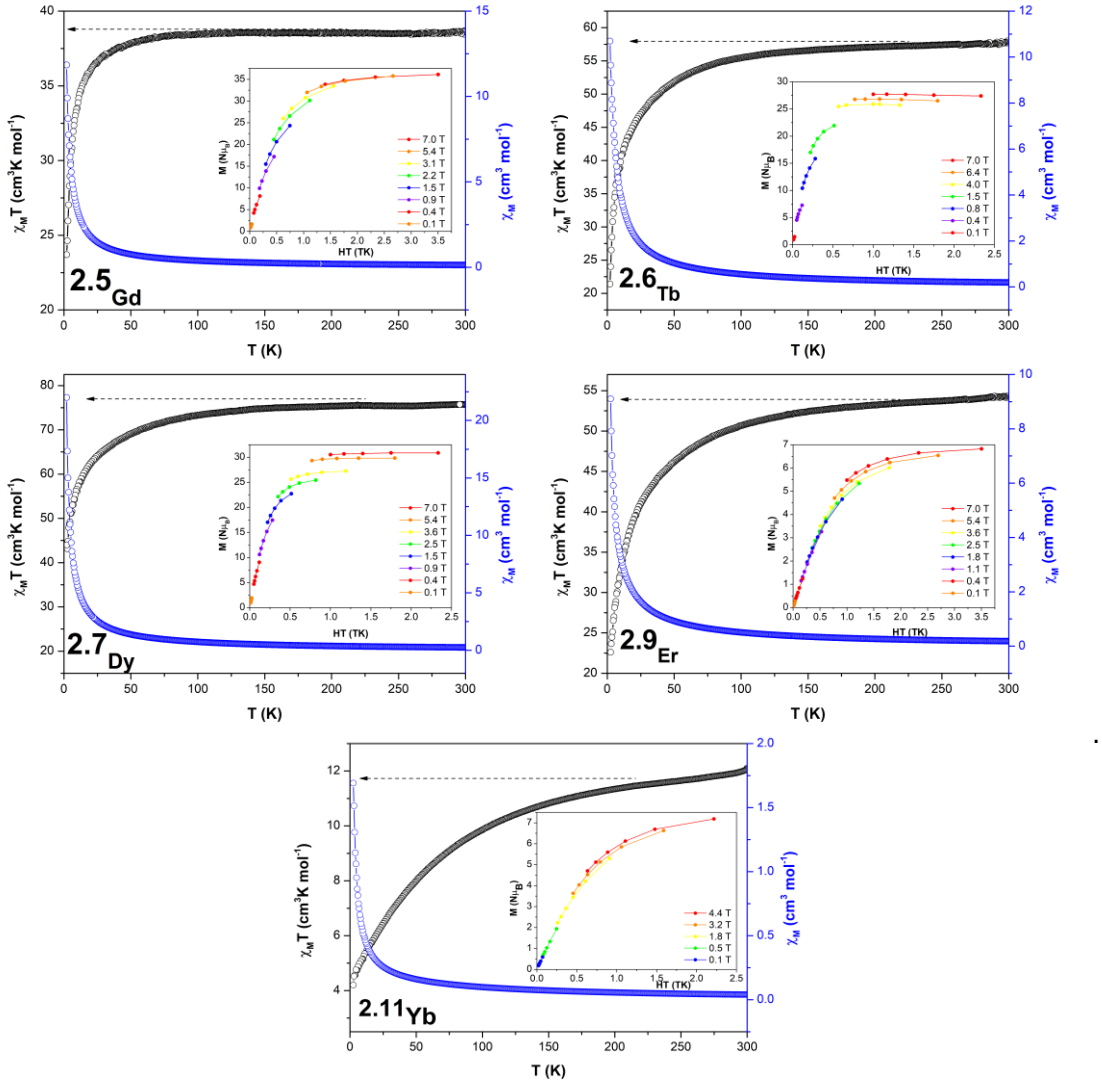

Figure 2.10. Temperature dependence of the $\chi_M T$ product at 1000 Oe for complexes **2.5$_{Gd}$-2.7$_{Dy}$, 2.9$_{Er}$** and **2.11$_{Yb}$**. Inset: isothermal reduced magnetization curves in the 2-7 K temperature range. Solid lines are a guide to the eye.

2.7.2.2 *Ac* Magnetic Properties

Dynamic ac magnetic susceptibility measurements were performed in compounds **2.7$_{Dy}$**, **2.9$_{Er}$** and **2.11$_{Yb}$**. We carefully selected those materials as they show different shape of free-ion electron density. Ln^{3+} ions with anisotropic electronic density are classified into two groups: oblate and prolate. Dy^{3+} is an oblate-type ion so, in order to enhance its anisotropy, the ligand donor atoms with greatest electron density should coordinate at axial positions, whereas Er^{3+} and Yb^{3+} ions are prolate, meaning that the

largest axial anisotropy is obtained by equatorial ligand coordination. In an attempt to understand which type of ion would better suit to present SMM behaviour in this particular system consisting of pentanuclear clusters, both type of ions have been studied. Dy^{3+} based SMMs are among the most prolific examples among lanthanide clusters with interesting single-molecule magnet property, in contrast to Yb^{3+} analogues, which are very scarce.[113,114] One of the main reasons is the shape of free-ion electron density. Moreover, the ligand field seems to cause a deeper effect in breaking the degeneration of M_J sublevels for Dy^{3+} ion than for Er^{3+} and Yb^{3+} ions, in such a way that the former often presents greater magnetic anisotropy.[115]

Ac measurements under an alternating field of 3.5 Oe reveal that none of the compounds exhibit frequency dependent signals above 2 K under a zero applied dc field. This effect can be connected to the relaxation of the magnetization via quantum tunnelling (QTM),[116] (in other words, bypassing between degenerated energy levels not needing to overcome the thermal energy barrier) and to the relatively weak coupling interactions among 4f ions which lead to weak interactions that could facilitate the fast relaxation of the magnetization hiding the SMM behaviour. A strategy to overcome this problem is known to be the application of an external magnetic field that would break degeneracy among M_J energetic levels and provoke tunnelling conditions to be lost, or at least partly. Therefore, a static field of 1000 Oe was applied to try to suppress QTM relaxation process. Only compound **2.11$_{Yb}$** showed signal dependency among frequency. This was an expected feature, since results obtained from Magellan software[117] demonstrated that anisotropic axis in pentanuclear node in compound **2.7$_{Dy}$** lies perpendicular. Dy1 anisotropic axis cross perpendicularly to Dy2 ion anisotropy axis, an undesired effect since it could counteract the anisotropy effect of the ion. Taking into account that the oblate ion anisotropy axes lie perpendicular towards the ion electronic cloud distribution, we believe that in this particular system prolate type ions (such as Er^{3+} and Yb^{3+}) are more suitable in order to design materials showing SMM behaviour. This is the case of compounds with prolate type ions with well-defined axiality, in which the electron distribution is parallel to the anisotropy axis. In the present case, the highest negative net charge among ligand donor atoms comes from the phenoxo bridge giving rise to the shortest bond distances. These bonds are parallelly lined up to the anisotropy axis of prolate ions enhancing ion anisotropy and contributing to a possible SMM behaviour (Supporting Figure A2.23).

Many examples of Yb^{3+} SMMs are reported in the literature composed by discrete molecules,[118–123] nonetheless, as far as we know, very few examples of polynuclear Yb^{3+} compounds can be found in the literature, and in most cases slow relaxation of magnetization is only visible under an applied constant field.[118,124] In those reported examples, Yb^{3+} relaxation process occurs preferably by, Raman, direct and quantum tunnelling rather than most usual Orbach processes. Even more surprising, there are no high nuclearity complexes involving Yb^{3+} ions with single-molecule magnet (SMM) behaviour that have been covered to date, since only discrete molecules or mono-dimensional coordination polymers have been reported so far.[125,126] In this sense compound **10_{Yb}** is the first porous three dimensional metal-organic framework exhibiting SMMs behaviour in the presence of an external magnetic field.

Relaxation of the magnetization can occur through diverse mechanisms. Purely Orbach type, which follows Arrhenius law and gives a value of the effective energy barrier directly, although it scarcely happens alone. In most common cases, relaxation of the magnetization takes place through the combination of several paths which can be summarized by fitting parameters referred in Equation 2.7.

$$\tau^{-1} = \tau_0^{-1}\exp(-U_{eff}/k_B T) + AT + BT^n + \tau_{QTM}^{-1} \qquad \textbf{Equation 2.7}$$

The first parameter stands for the Orbach relaxation process, the second parameter (AT) to the direct relaxation path, the third (BT^n) to the Raman relaxation and τ_{QTM}^{-1} makes reference to the quantum tunnelling of magnetization relaxation pathway.

Under an external field of 1000 Oe, compound **2.11_{Yb}** reveals slow magnetic relaxation according to the best fitted obtained taking into consideration Raman and QTM relaxation processes (Equation 2.8). These results come in line with the semi-circular nature of the Cole-Cole plots and α values (0.28–0.23) and different temperature which wards off from 0 values, suggesting a combination multiple relaxation processes is taking place. The fitting data were in agreement with the experimental data, as depicted in Figure 2.11 (inset), affording $\tau_{QTM} = 6.75 \cdot 10^{-5}$ s, $B = 10.56\ s^{-1} \cdot K^{-n}$ and $n = 6.802$ (Figure **2.11**).

$$\tau^{-1} = \tau_{QTM}^{-1} + BT^n \qquad \textbf{Equation 2.8}$$

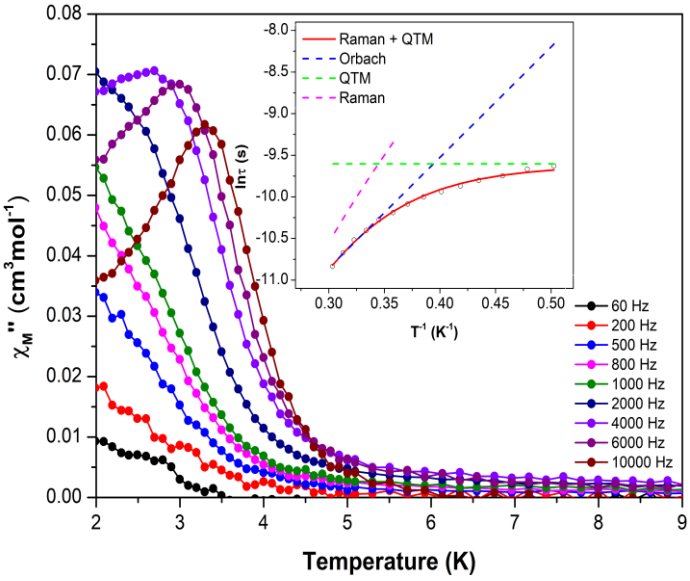

Figure 2.11. Temperature dependence of out-of-phase components of the ac susceptibility in a dc applied field of 1000 Oe for **2.11**$_{Yb}$. Insets: Arrhenius plots. The black line accounts for the best fit considering Orbach relaxation, and the red line corresponds to Raman plus QTM relaxation.

However, in view of the residual unquenched QTM occurring in pure samples, we also explored the magnetic dilution strategy with Y^{3+}. We tried to isolate paramagnetic centres in a diamagnetic matrix in order to avoid weak exchange interactions among lanthanide atoms which could negatively contribute and favour the single-ion effect. To perform magnetic dilution, we selected 30:1 Y^{3+} to Ln^{3+} dilution ratio with the aim of isolating a paramagnetic centre in each pentanuclear node. The diluted samples were prepared by co-crystallization of the diamagnetic counterpart along with the paramagnetic ion (see Figure A2.6 for more details in characterization of doped samples). Following the aforementioned procedure compounds **2.13**$_{Y\text{-}Dy}$, **2.14**$_{Y\text{-}Er}$ and **2.15**$_{Y\text{-}Yb}$ have been prepared. To explore the slow magnetic relaxation in the diluted samples, magnetic ac susceptibilities were measured in the 60–10000 Hz frequency range. As for pure counterparts, none of diluted compounds **2.13**–**2.15** show frequency dependent signals without the presence of an external magnetic field (Figure A2.26, Figure 2.11 and Figure 2.12), so the measurements were repeated applying a magnetic field of 1000 Oe. In case of compound **2.13**$_{Y\text{-}Dy}$, no maxima can be found in out of phase molar magnetic susceptibility and the frequency dependent χ_M'' peaks seem to appear below 2 K, out from the detection limit of the equipment. Fortunately, a pair of maxima and a nice set of maxima in χ_M'' curves are present for compounds **2.14**$_{Y\text{-}Er}$ and **2.15**$_{Y\text{-}Yb}$,

respectively. These results reinforce our first hypothesis being prolate-type ions more suitable to show single molecule behaviour in this particular system.

Despite the fact that compound **2.13$_{Y\text{-}Dy}$** did not show a maximum, the energy barrier (U_{eff}) and relaxation time (τ_0) can be estimated if we assume that a single relaxation process is contributing in the ion relaxation. According to Debye mode applying Equation 2.9 a rough estimation of U_{eff} and τ_0 values can be obtained, yielding U_{eff} values of 17.43 K and relaxation time (τ_0) of $3.34 \cdot 10^{-8}$ s^{-1} (Figure A2.30).

$$ln\frac{\chi_M''}{\chi_M'} = \ln(2\pi\nu\tau_0) + \frac{E_a}{k_B T}$$ **Equation 2.9**

In compounds **2.14$_{Y\text{-}Er}$** and **2.15$_{Y\text{-}Yb}$**, even after magnetic dilution, a remaining non-negligible fast tunnelling relaxation is still observed (Figure 2.11 and Figure 2.12). However, it seems that is mostly suppressed since better-defined maxima and shifted to higher temperature are obtained. We must notice that the magnetic dilution performed for Er^{3+} in compound **2.14$_{Y\text{-}Er}$** allowed showing SMM behaviour. In this compound, the maximum was only clearly visible at 6000 and 10000 Hz frequencies. The best fitting of the data was achieved with Equation 2.10 which accounts for Orbach relaxation process yielding U_{eff} values of 13.09 K and relaxation time (τ_0) of $6.46 \cdot 10^{-8}$ s^{-1}.

$$\tau^{-1} = \tau_0^{-1}\exp(-U_{eff}/k_B T)$$ **Equation 2.10**

In case of compound **2.15$_{Y\text{-}Yb}$**, the relaxation times present a curvature pathway and as for compound **2.11$_{Yb}$** the best fitting has been obtained taking into consideration simultaneously Raman and QTM relaxation processes (Equation 2.8), which gives rise to the following parameters: $\tau_{QTM} = 2.15 \cdot 10^{-2}$ s, $B = 7.2$ $s^{-1} \cdot K^{-n}$ and $n = 5.87$.

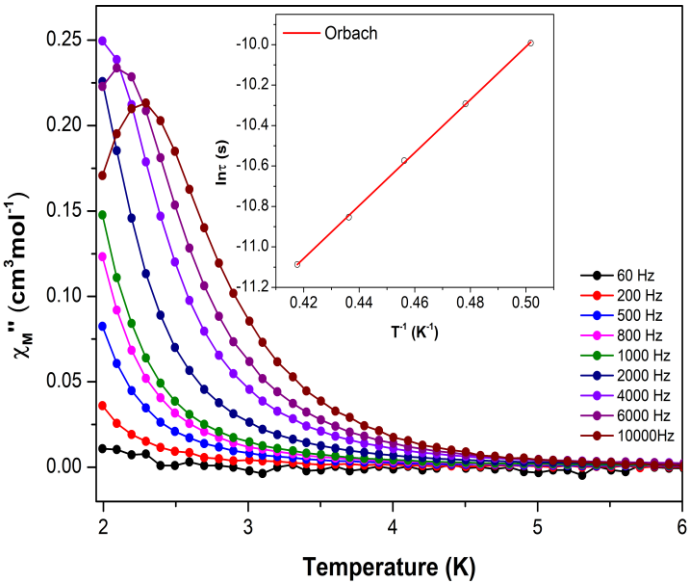

Figure 2.12. Temperature dependence of out-of-phase components of the ac susceptibility in a dc applied field of 1000 Oe for compound **2.14**$_{\text{Y-Er}}$**.** Insets: Arrhenius plots. The black line accounts for the best fit considering Orbach relaxation.

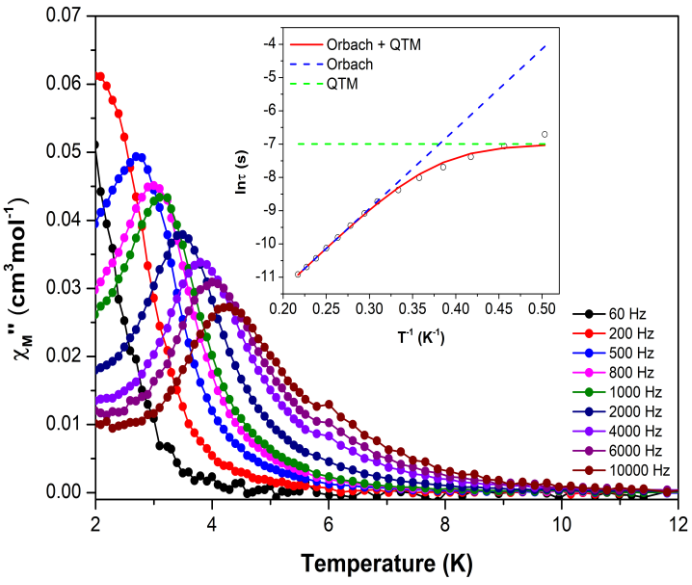

Figure 2.13. Temperature dependence of out-of-phase components of the ac susceptibility in a dc applied field of 1000 Oe for compound **2.15**$_{\text{Y-Yb}}$**.** Insets: Arrhenius plots. The black line accounts for Orbach fitting, and the red line corresponds to the best fitting obtained combining Raman plus QTM relaxation processes.

2.7.3 Photoluminescence properties

Lanthanide centred emission, characterised by narrow signals in the UV-visible and near-infrared regions, is of great interest given its large applicability in many different areas moving from bioimaging to photovoltaics.[127] Motivated by these possible applications, in this work, photoluminescence properties have been studied for pure Eu^{3+} (**2.4$_{Eu}$**) and Tb^{3+} (**2.6$_{Tb}$**) compounds as well as for mixtures of lanthanide elements in the Y^{3+} based matrix, using polycrystalline samples in all cases. In particular, our interest was focused on networks bearing Y^{3+} or Gd^{3+}, Tb^{3+} and Eu^{3+} in view of their potential application in optical thermometry. Accordingly, three additional heterometallic compounds with Y^{3+} or Gd^{3+} and Tb^{3+}/Eu^{3+} mixed lanthanide ions were prepared with the following doping proportions Y^{3+}:Tb^{3+}:Eu^{3+} 50:45:5 % and 50:40:10 %, rendering compounds **2.16$_{Y\text{-}Tb\text{-}Eu5\%}$** and **2.17$_{Y\text{-}Tb\text{-}Eu10\%}$** respectively, and Gd^{3+}:Tb^{3+}:Eu^{3+} 50:40:10 %, compound **2.18$_{Gd\text{-}Tb\text{-}Eu10\%}$**. With the last two samples thermometry studies were carried out.

The excitation spectra of compounds **2.12$_{Y}$**, **2.6$_{Tb}$**, **2.4$_{Eu}$** and **2.16$_{Y\text{-}Tb\text{-}Eu5\%}$** recorded at 12 K are presented in Figure 2.14. The excitation spectrum of **2.12$_{Y}$**, monitoring the ligand emission at 410 nm, consist of main broad UV bands, ranging from 230 to *ca.* 380 nm and peaking at 255 and 312 nm, attributed to the transitions from the ground to the low-lying excited states ($S_0 \rightarrow S_{2,1}$) of the organic ligand.

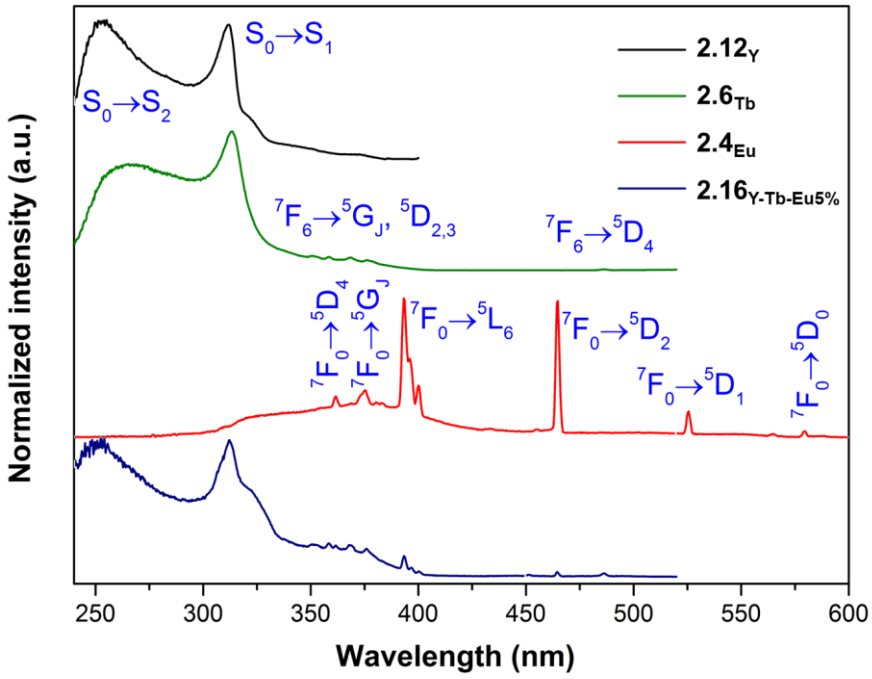

Figure 2.14. 12 K excitation spectra of **2.12$_{Y}$** (black; $\lambda_{Em.}$ = 410 nm), **2.6$_{Tb}$** (green; $\lambda_{Em.}$ = 544 nm), **2.4$_{Eu}$** (red; $\lambda_{Em.}$ = 620 nm) and **2.16$_{Y\text{-}Tb\text{-}Eu5\%}$** (blue; $\lambda_{Em.}$ = 614 nm).

On its part, the excitation spectrum recorded for compound **2.4$_{Eu}$** at 12 K detecting the strongest Eu^{3+} emission at 620 nm is dominated by a set of sharp spectral lines ascribed to the Eu^{3+} intra-4f transitions, from the fundamental $^7F_0$ level to the $^5D_{0\text{-}4}$, $^5L_6$ and ^5G_J excited levels. The ligand excitation bands are almost absent in this spectrum, some residual ligand signal is still noticeable at wavelengths above 300 nm. Contrary to that, the 12 K excitation spectrum of compound **2.6$_{Tb}$** is completely dominated by the ligand excitation bands, which are similar to the ones observed for compound **2.12$_{Y}$**. This demonstrates an effective energy transfer from the ligand to the Tb^{3+}. The typical Tb^{3+} intra-4f transitions, from the fundamental $^7F_6$ level to the $^5D_{4\text{-}2}$ and ^5G_J excited levels appears with residual intensities. The excitation spectrum of compound **2.16$_{Y\text{-}Tb\text{-}Eu5\%}$**, monitoring the Eu^{3+} emission at 614 nm, is also dominated by the ligand excitation broad bands with a profile resembling the one of compound **2.12$_{Y}$**, with the maxima peaks slightly shifted to 250 nm and 325 nm, respectively. The most intense Eu^{3+} excitation lines are also present in this spectrum, even if with relative low intensities. In addition, it is also identifiable the first excitation transition of Tb^{3+}, $^7F_6 \rightarrow {}^5D_4$ at 485 nm, resulting from the Tb^{3+}-to-Eu^{3+} energy transfer process.

To get deeper insights into the distinct photoluminescence performance of the Tb^{3+} and Eu^{3+} compounds we have determined the triplet zero phonon energy of the ligand. For that, stationary-state and time-resolved emission spectra of **2.12**$_Y$ have been recorded at 12 K under 310 nm excitation light (Figure 2.15). As observed, the stationary state emission spectrum displays two broad bands, from 315 to ca. 550 nm, attributed to the $S_1 \rightarrow S_0$ ligand fluorescence (peaking at 340 nm) and $T_1 \rightarrow S_0$ ligand phosphorescence (peaking at 450 nm). This assignment is supported by the time-resolved emission spectra, which allowed isolating the fluorescence and phosphorescence emissions by using faster and slower detection conditions, respectively. The zero-phonon energy level of the ligand phosphorescence, related to the energy of the emitting triplet states, is estimated at 410 nm (24390 cm^{-1}). This level is relatively close to Tb^{3+} first excited state ($^5D_4$, 585 nm / 20619 cm^{-1}) and far from the energy of the lowest-lying excited level of Eu^{3+} ($^5D_0$, 580 nm / 17241 cm^{-1}), explaining why the energy transfer is more efficient to the former lanthanide ion according to Latva's law.[128]

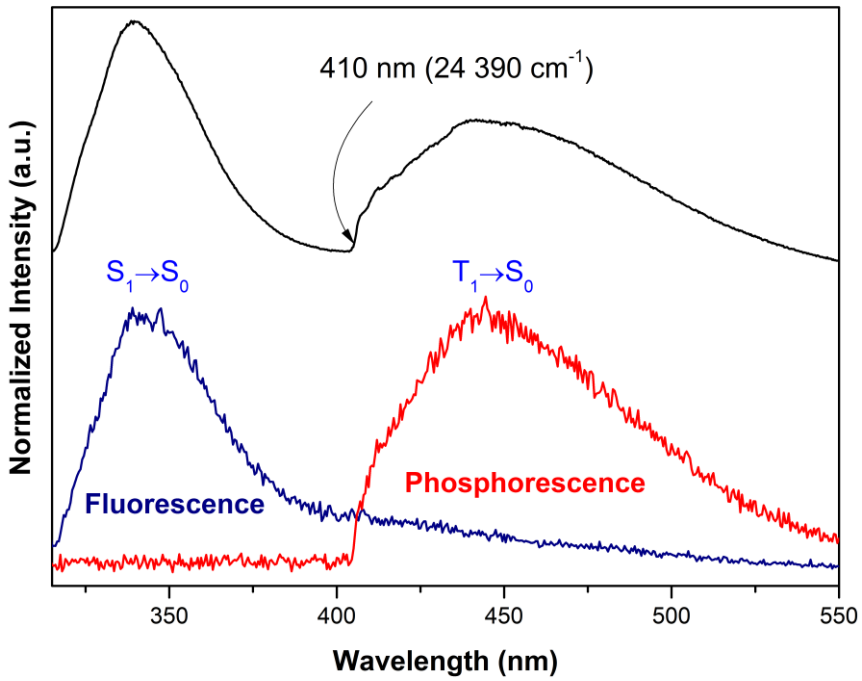

Figure 2.15. Stationary emission spectra of **2.12**$_Y$ (black line) and corresponding time-resolved emission spectra showing the separation of the fluorescence (blue line; initial delay of 0.01 ms and integration time of 0.1 ms) and the phosphorescence (red line; initial delay of 0.1 ms and integration time of 10 ms) recorded at 12 K under 310 nm excitation. The time-resolved spectra were not corrected for the detection and optical spectral response of the spectrofluorometer.

The emission spectrum of **2.6$_{Tb}$** recorded at 12 K and excited at 315 nm (Figure 2.16a) presents the typical narrow lines attributed to the Tb^{3+} $^5D_4 \rightarrow {}^7F_{6-0}$. The emission spectra of **2.4$_{Eu}$** recorded at 12 K with the excitation selected at 393.5 nm ($^5L_6$ excited level) and at 335 nm (ligand band) are shown in Figure 2.16. The spectra exhibit the characteristic sharp intra-4f emission lines of Eu^{3+} attributed to the $^5D_0 \rightarrow {}^7F_{0-4}$ transitions. In particular, in the $^5D_0 \rightarrow {}^7F_2$ transition region at least six Stark components can be observed, 4 main lines and two smaller lines in the low energy part. The intensity of the two low energy Stark components clearly increases with the 335 nm excitation. This unequivocally proves the presence of the two independent Eu^{3+} sites as described in the structural section. The dominance of the $^5D_0 \rightarrow {}^7F_2$ transitions over the $^5D_0 \rightarrow {}^7F_1$ transition is typical of Eu^{3+} environments without inversion centres, in line with that previously described in the structural section. In addition, the $^5D_0$ Eu^{3+} decay curve, recorded at 12 K while monitoring the strongest emission at 616 nm under direct excitation at 393.5 nm (insert of Figure 2.16b), is only properly fitted by a second order exponential function yielding two lifetimes of 0.08 ± 0.01 and 0.27 ± 0.01 ms, and with an averaged lifetime of 0.25 ms. This is again in accordance with the presence of two Eu^{3+} sites in the **2.4$_{Eu}$** structure. Identical conclusion is obtained for **2.6$_{Tb}$**, for which the corresponding $^5D_4$ Tb^{3+} decay curve recorded at 12 K also yields two lifetimes of 0.08 ± 0.01 and 0.36 ± 0.01 ms, resulting in an averaged lifetime of 0.29 ms.

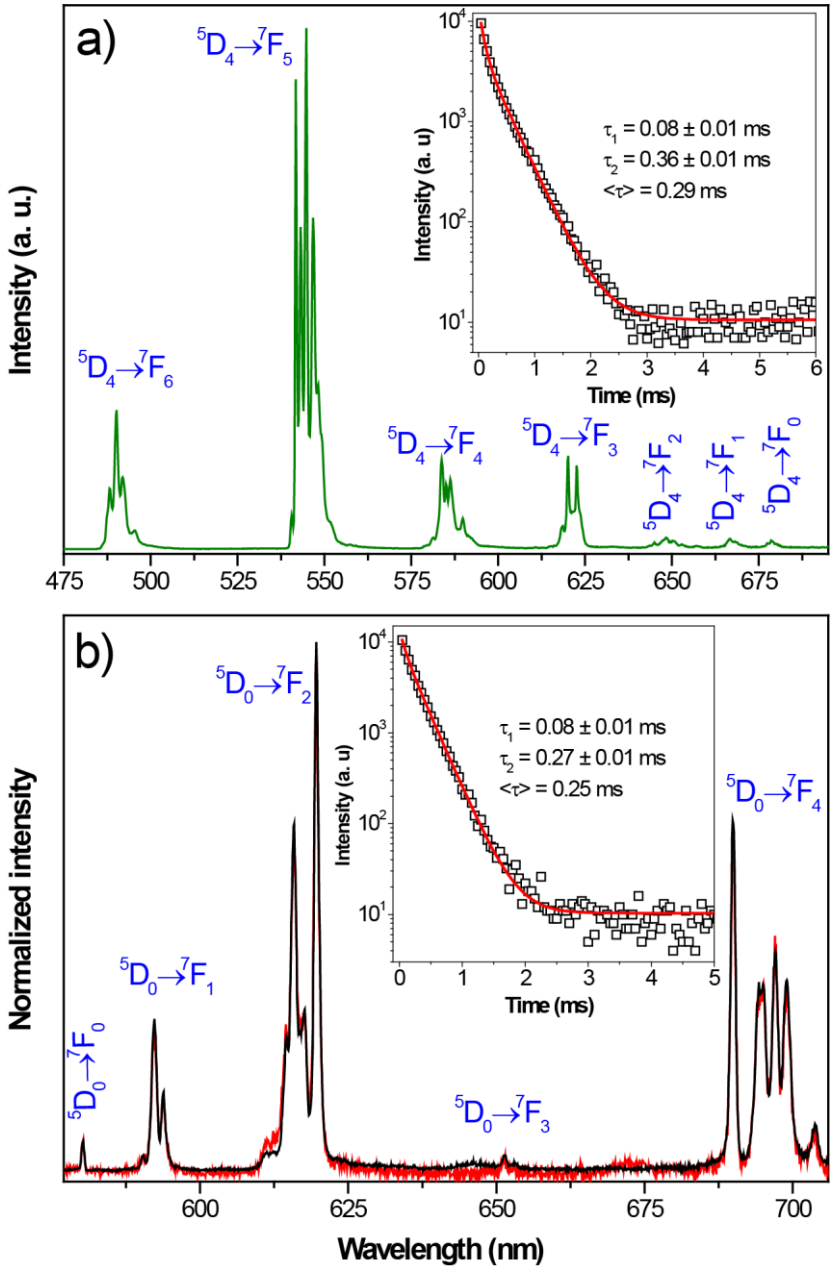

Figure 2.16. 12 K emission spectra of (a) **2.6$_{Tb}$** (green line) excited at 315 nm, and of (b) **2.4$_{Eu}$** with the excitation fixed at 335 nm (red line) and 393.5 nm (black line). The inserts show the corresponding (a) $^5D_4$ and (b) $^5D_0$ decay curves monitoring the emissions at 544.5 and 616 nm with the excitations selected at 377 nm and 393.5 nm, respectively for **2.6$_{Tb}$** and **2.4$_{Eu}$;** the solid red lines are the best fits using second-order decay functions, y = y0 + $A_1 \cdot \exp(-x/\tau_1)$ + $A_2 \cdot \exp(-x/\tau_2)$ ($r^2 > 0.999$). The average lifetimes were calculated according to the formula $<\tau> = (A_1\tau_1^2 + A_2\tau_2^2)/(A_1\tau_1 + A_2\tau_2)$.

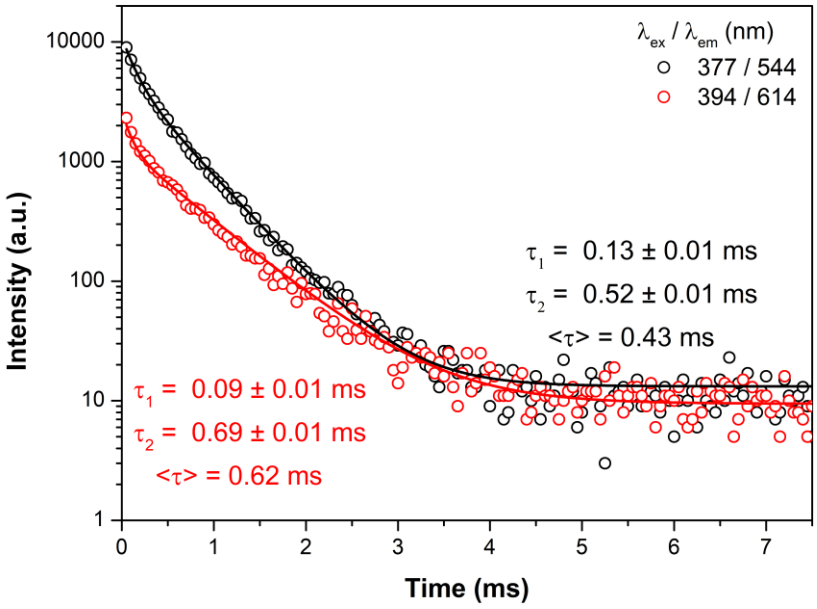

Figure 2.17. 2.16$_{Y\text{-}Tb\text{-}Eu5\%}$12 K Decay curves monitoring the emission at 544 nm and 614 nm with the excitation selected at 377 nm (black), and 394 nm (red); the solid lines are the best fits using second-order decay functions, $y = y_0 + A_1 \cdot \exp(-x/\tau_1) + A_2 \cdot \exp(-x/\tau_2)$ ($r^2 > 0.999$). The average lifetime was defined as $< \tau >= (A_1\tau_1^2 + A_2\tau_2^2)/(A_1\tau_1 + A_2\tau_2)$.

Heterometallic compound **2.16$_{Y\text{-}Tb\text{-}Eu5\%}$** decay curves collected at 12 K have been acquired by monitoring the strongest emission lines for both Tb^{3+} ($^5D_4 \rightarrow {}^7F_5$ transition, 544 nm) and Eu^{3+} ($^5D_0 \rightarrow {}^7F_2$ transition, 614 nm), using the excitations at 377 nm and 394 nm, respectively (Figure 2.17). All curves are well fitted by a second order exponential decay functions yielding average lifetimes: of 0.43 ms and 0.62 ms, respectively for Tb^{3+} and Eu^{3+}, in one hand, both lifetimes are larger than the ones obtained for the pure Tb^{3+} (**2.6$_{Tb}$**) and Eu^{3+} (**2.4$_{Eu}$**) samples, resulting from the suppression of the self-quenching due to the dilution of the optically active elements. On the other hand, contrary to the pure Tb^{3+} and Eu^{3+} samples, the Eu^{3+} lifetimes are larger than the ones of Tb^{3+}, due to the aforementioned Tb^{3+}-to-Eu^{3+} energy transfer process.

Temperature induced changes on the emission spectrum motivated us to studying the capacity of the mixed compounds for luminescent thermometry. For that purpose, we carefully selected compounds **2.17$_{Y\text{-}Tb\text{-}Eu10\%}$** and **2.18$_{Gd\text{-}Tb\text{-}Eu10\%}$** because the metals mixing proportion are equal among them. Y^{3+} and Gd^{3+} complexes were selected since former allows Ln-MOFs doping withing an optically inert Ln matrix and the latter, displays high-energy of the first excited state which prevents from participation in the studied electron transfer mechanism.[129,130] Following this strategy, in compounds

2.17$_{\text{Y-Tb-Eu10\%}}$ and **2.18**$_{\text{Gd-Tb-Eu10\%}}$, Ln centres are prompted to be adequately distributed withing the net avoiding non-radiative energy transfer mechanisms derived by intermetallic energy transfer processes which could overall reduce luminescence efficiency.[131]

I_{Tb} and I_{Eu} were determined by integrating the emission spectra in the ranges of 538–552 nm and 609–619 nm for **2.17**$_{\text{Y-Tb-Eu10\%}}$ and in the range of 536–556 nm and 610–618 nm for **2.18**$_{\text{Gd-Tb-Eu10\%}}$. Figure 2.18 presents the temperature-dependent emission spectra of the compounds **2.17**$_{\text{Y-Tb-Eu10\%}}$ and **2.18**$_{\text{Gd-Tb-Eu10\%}}$ in the 12−320 K range. As expected, the emission spectra highly resemble to what was obtained for analogous compound **2.16**$_{\text{Y-Tb-Eu5\%}}$.

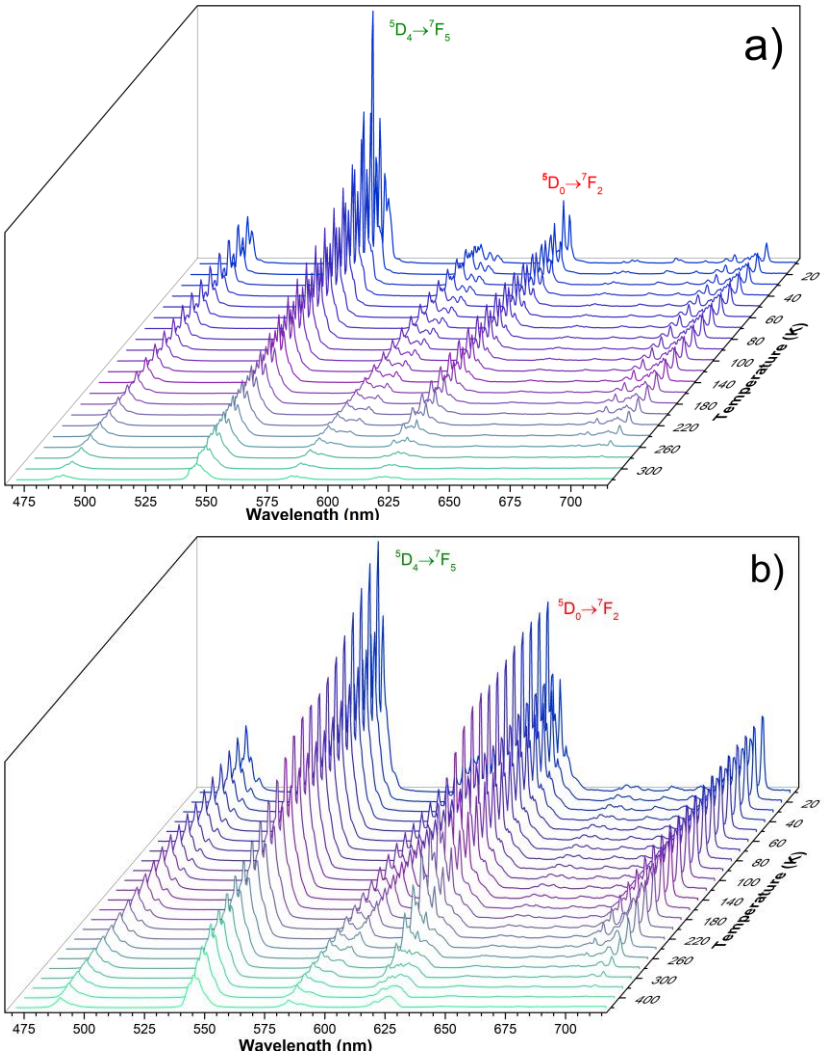

Figure 2.18. a) Emission spectra of **2.17**$_{\text{Y-Tb-Eu10\%}}$ in the 12–320 K range with the excitation selected at 312 nm and **b)** emission spectra of **2.18**$_{\text{Gd-Tb-Eu10\%}}$ in the same range and fixing the excitation at the same wavelength.

Afterwards, temperature dependence of the integrated intensity of the emissions was calculated and are depicted in Figure 2.19. Based on the integrated areas of Tb^{3+} $^5D_4 \rightarrow {}^7F_5$ (I_{Tb}) and Eu^{3+} $^5D_0 \rightarrow {}^7F_2$ (I_{Eu}) emissions, a thermometric parameter may be defined, $\Delta = I_{Tb}/I_{Eu}$, allowing to convert emission intensities into absolute temperature values.[54] It was estimated an instrumental error of 0.1 % to estimate the standard deviation of each experimental data.[132] The emission of Tb^{3+} decreases by 93 % and 94 % from 12 to 340 K, and the Eu^{3+} emissions decrease by 65 % and 77 % for **2.17**$_{\text{Y-Tb-Eu10\%}}$ and **2.18**$_{\text{Gd-Tb-Eu10\%}}$ compounds, respectively.

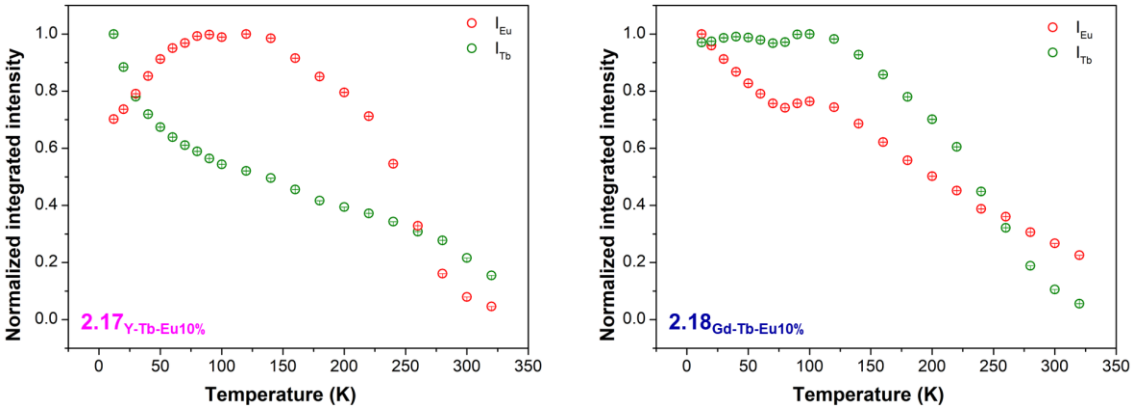

Figure 2.19. Temperature dependence of I_{Tb} (green) and I_{Eu} (red) in the 12–320 K range of **2.17**$_{\text{Y-Tb-Eu10\%}}$ left and of **2.18**$_{\text{Gd-Tb-Eu10\%}}$ (right).

The temperature dependence of the thermometric parameter Δ in the range of 12–320 K and the corresponding relative sensitivities, defined as $S_r = |\partial\Delta|/\partial T$ in the same temperature range for compounds **2.17**$_{\text{Y-Tb-Eu10\%}}$ and **2.18**$_{\text{Gd-Tb-Eu10\%}}$ are shown in Figure 2.20 and Figure 2.21, respectively.

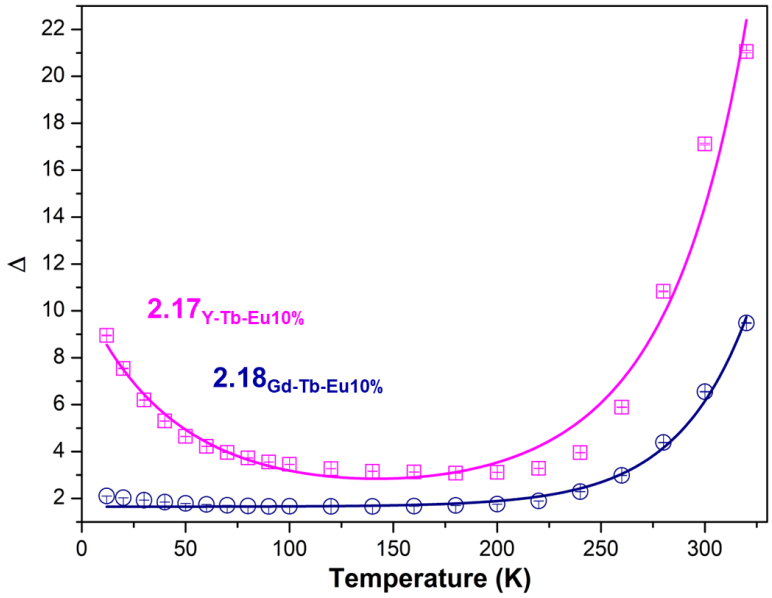

Figure 2.20. Variation of the ratiometric intensity parameter Δ as a function of temperature in the 12–320 K range, for **2.17**$_{\text{Y-Tb-Eu10\%}}$ and for **2.18**$_{\text{Gd-Tb-Eu10\%}}$. The solid lines result from the fits considering the following empirical exponential functions: $\Delta(T) = \exp(a+bT+cT^2)$ ($r^2 = 0.96$) and $\Delta(T) = \Delta_0 + A\text{^}(R_0T)$ ($r^2 = 0.99$) for **2.17**$_{\text{Y-Tb-Eu10\%}}$ and **2.18**$_{\text{Gd-Tb-Eu10\%}}$, respectively. The bars depict the errors in the thermometric parameter resulting from the propagation of the 0.1 % errors determined for I_{Tb} and I_{Eu}.[132]

Compound **2.17** display two distinct regimens in the sensitivity, whereas for compound **2.18** a single temperature-sensing regime can be observed. For **2.17**$_{\text{Y-Tb-Eu10\%}}$ the maximal relative sensitivity is obtained at T_m 12 K with S_m 1.202 % K^{-1}; above mentioned temperature a tendency of decreasing relative sensitivity is observed. This behaviour is followed until 150 K, afterwards relative sensitivity increases up to 320 K. In case of compound **2.18**$_{\text{Gd-Tb-Eu10\%}}$, the maximum relative sensitivity is obtained at T_m 320 K yielding S_m 2.43 % K^{-1}. These values come in line with the compounds that have been reported so far in bibliography.[132]

The temperature uncertainty, the minimum temperature change that can be ascertained in a given measurement, is defined as, $\delta T = 1/S_r\,(\delta\Delta/\Delta)$, where $\delta\Delta/\Delta$ is the relative error in the determination of the thermometric parameter.[132] The minimum temperature uncertainties of both compounds (see Figure 2.21) follows exactly the corresponding maximum sensitivities, 0.08 K at 320 K for **2.18**$_{\text{Gd-Tb-Eu10\%}}$ and 0.16 K at 12 K for **2.17**$_{\text{Y-Tb-Eu10\%}}$.

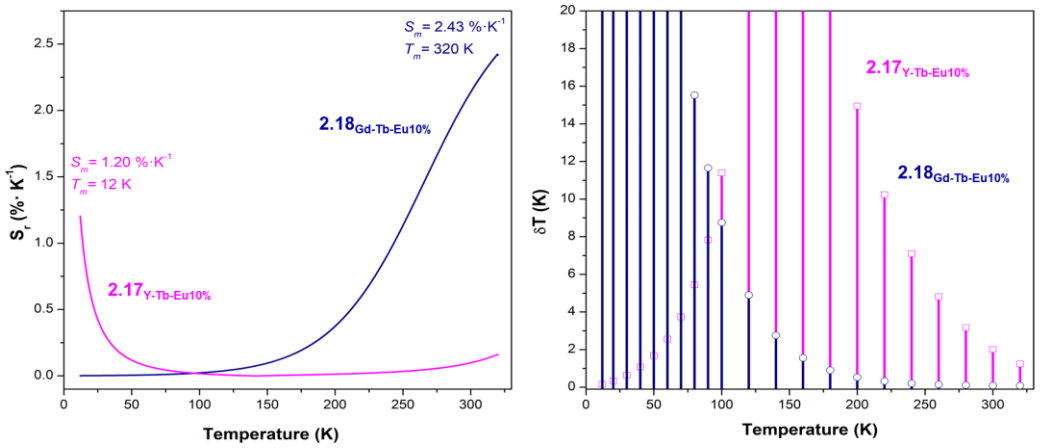

Figure 2.21. Temperature sensitivity (S_r) in the 12–320 K range for **2.17$_{Y\text{-}Tb\text{-}Eu10\%}$** and for **2.18$_{Gd\text{-}Tb\text{-}Eu10\%}$** left**,** and corresponding temperature uncertainty (δT) (right). For clarity only uncertainty values below 20 K are shown.

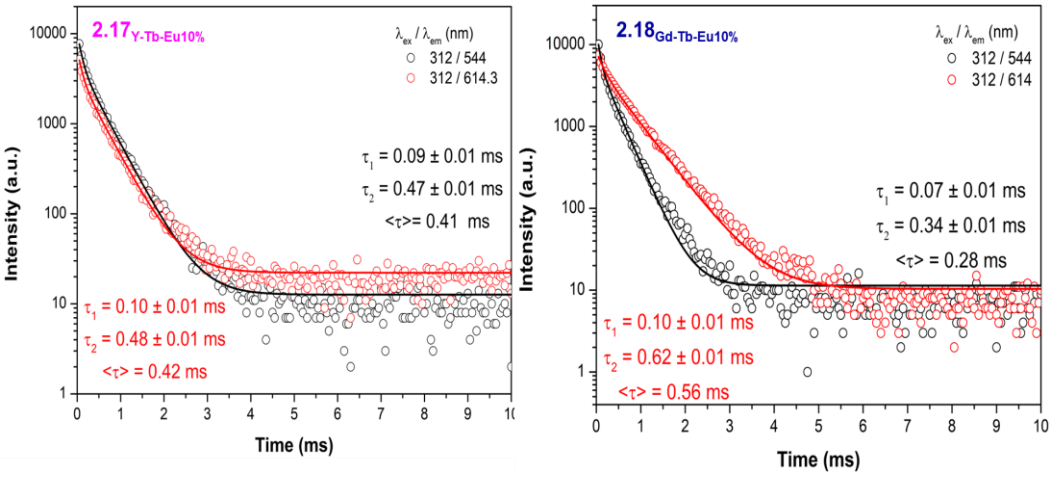

Figure 2.22. Decay curves of **2.17$_{Y\text{-}Tb\text{-}Eu10\%}$** (left) and **2.18$_{Gd\text{-}Tb\text{-}Eu10\%}$** (right) acquired at 12 K monitoring the Tb^{3+}emission at 544 nm (black) and the Eu^{3+}emission at 614 nm (red) with the excitation fixed at 312 nm. The solid lines are the best fits using second order exponential decay function $y = y_0 + A_1 \cdot \exp(-x/\tau_1) + A_2 \cdot \exp(-x/\tau_2)$ ($r^2 > 0.999$). Average lifetime was calculated according to the formula $< \tau >= (A_1\tau_1^2 + A_2\tau_2^2)/(A_1\tau_1 + A_2\tau_2)$.

Finally, $^5D_4$ Tb^{3+} and $^5D_0$ Eu^{3+} decay curves, monitoring the emissions at 544 and 614 nm, respectively, were collected for compounds **2.17$_{Y\text{-}Tb\text{-}Eu10\%}$** and **2.18$_{Gd\text{-}Tb\text{-}Eu10\%}$** at 12 K with the excitation fixed at 312 nm (Figure 2.22). The average lifetimes shows that compound **2.17$_{Y\text{-}Tb\text{-}Eu10\%}$** ($< \tau_{544} >= 0.41\ \text{ms}$, $< \tau_{614} >= 0.42\ \text{ms}$) presents the larger Tb^{3+} lifetimes and the shorter Eu^{3+} lifetimes relatively to compound **2.18$_{Gd\text{-}Tb\text{-}Eu10\%}$**

($< \tau_{544} > = 0.28$ ms, $< \tau_{614} > = 0.56$ ms). In both cases, lifetimes increase relatively to the values obtained at 12 K for the pure **2.4$_{Eu}$** ($< \tau > = 0.27$ ms) and **2.6$_{Tb}$** ($< \tau > = 0.29$ ms) compounds. This results from the Tb^{3+}-to-Eu^{3+} energy transfer, that shortens the Tb^{3+} lifetimes and increases the Eu^{3+} lifetimes, and from the dilution of the optically active ions, that eliminates the self-quenching effect.

2.7.4 Adsorption capacity

With the aim of getting preliminary data on the porosity of the material, the pore size distribution, accessible surface area and pore volume of **2.7$_{Dy}$**, was computed by a Monte Carlo code developed by Herdes and Sarkisov.[133,134] In the light of the results, the calculations (Figure A2.44) show that coordinated DMF molecules are exposed to voids and their removal generates more accessible pores displaying 3D pores in the range of 4.89-6.35 Å diameter and exhibiting a surface area 713.2 m^2/g and pore volume of 0.319 cm^3/g and porosity of 50.9 %.

The porous structure of **2.7$_{Dy}$** led us to assess its experimental gas adsorption behaviour. The accessibility of gaseous probe molecules into the porous framework of **2.7$_{Dy}$** was first evaluated by recording adsorption isotherms of N_2 at 77 K. Regretfully, probably due to the narrow pore size of the compound, the study of porosity by means of this gas at 77 K revealed no adsorption capacity. Even though, CO_2 molecules could diffuse through the porous, as the latter molecule has a smaller kinetic radius compared to the former and comparatively, CO_2 establishes stronger interactions with the amino group of the ligand. In general, it is known that MOFs with polar (–OH, –N=N–, $–NH_2$ and –N=C(R)–) pores show a higher CO_2 adsorption than non-polar MOFs.[135] Therefore, CO_2 adsorption isotherms were recorded at 273 K and 298 K in compound **2.7$_{Dy}$**.

Regarding CO_2 adsorption capacity reached at 1 bar (Figure 2.23), compound **2.7$_{Dy}$** loads 2.1 mmol/g at 273 K and 1.6 mmol/g at 298 K. These obtained values can be considered as moderate values when compared with those achieved by referential MOFs.[136] Particularly, obtained adsorption both at 273 K and 298 K comes very good in line with those observed in TMOF-1 which exhibited a CO_2 uptake 2.2 mmol/ g (273 K) and 2.2 mmol/g (298 K).[137] Contrarily the isosteric heats of CO_2 adsorption of **2.7$_{Dy}$** (Figure 2.24) can be considered as relatively high (see below). In this sense, despite low uptake capacity of **2.7$_{Dy}$** rules out its application in CO_2 storage, its high adsorption heats makes this material more suitable for separation and purification technologies of this greenhouse gas.[138–141]

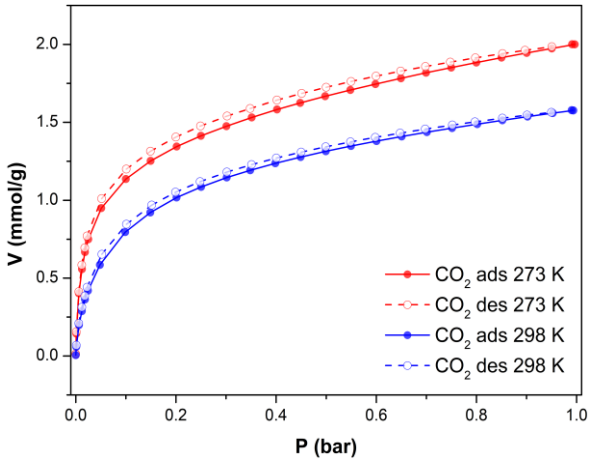

Figure 2.23. CO_2 adsorption isotherms at 273 K (red) and 298 K (blue) for **2.7$_{Dy}$.**

The isosteric heat of adsorption (Q_{st}) was calculated from the adsorption isotherms at 273 and 298 K to evaluate the strength of the interaction between the adsorbent and adsorbate according to Clausius-Clapeyron equation, Equation 2.11.[142]

$$Q_{st} = -R\,[\Delta(lnP)/\Delta(T^{-1})]_N \qquad \textbf{Equation 2.11}$$

where Q_{st}, *R*, *P*, *T* and *N* correspond to isosteric heat of adsorption, constant for ideal gases, pressure, temperature and the amount of adsorbed CO_2, respectively. Enthalpy of adsorption (Q_{st}) value demonstrates the strength of the interaction between the host and guest molecules. Indeed, the magnitude of the Q_{st} is a function of the binding strength indicating the amount of the required energy for the regeneration process. The higher Q_{st} of adsorption, the higher will be the affinity that the adsorbent has to adsorb a gas, CO_2 in this case. Nevertheless, its regeneration process would require high energy to regenerate the adsorbent. Thus, an equilibrium or balance is needed between the affinity that MOFs has to uptake a gas a specific gas, the enthalpy of adsorption, and the energy required to regenerate the material.[135]

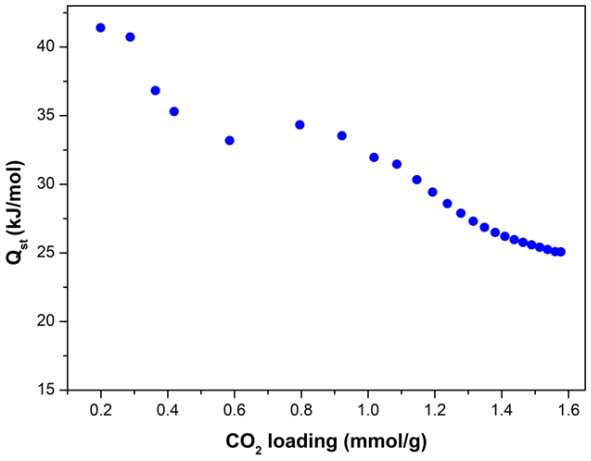

Figure 2.24. Isosteric heats of adsorption (Q_{st}) of CO_2 for compound **2.7$_{Dy}$**.

At near zero-coverage, the Q_{st} of CO_2 in compound **2.7$_{Dy}$** is 41.4 kJ/mol. This value for CO_2 is comparable to other previous works,[57] as well as for some reputed MOFs such as Ni-MOF-74 (42 kJ/mol),[143] $Zn_2(ox)(atz)_2$ (41 kJ/mol),[144] and Pd(μ-F-pymo-N^1,N^3)$_2$ (40 kJ/mol).[145] Meanwhile, the Q_{st} values show a staggered decrease with the increasing loading of adsorbate molecules in the MOF, which is related with gradual decrease in the availability of the best performing adsorption sites. Precisely, the isosteric heat of adsorption profile shows three main steps and when considering Q_{st} vs CO_2 loading per cluster (Figure A2.41, left) it could be ascribed to the successive occupation of the three coordinatively unsaturated sites (*cus*) available after the removal of the coordinating solvent molecules during the activation of the MOF (Figure A2.41, right).

In comparison to other MOFs containing open-metal sites (in which values around 30-60 kJ/mol are obtained),[142] **2.7$_{Dy}$** exhibits relatively high isosteric heat (41.4 kJ/mol), which also suggests a direct interaction between CO_2 and *cus*. These coordinatively unsaturated metal sites are available for adsorbate interaction only after carrying solvent-exchange procedure. As described in the supplementary information, solvent-exchange procedure with MeOH allowed partly/fully replaced coordinated DMF molecules, which by sample activation were removed allowing the structure to contain three *cus* per formula. Generally, as-synthesized MOFs are prone to contain fully coordinated metal ions/ clusters with fully completed coordination spheres by bonds formed with solvents and organic ligands. Provided that those bonds can be removed, materials activation can provide accessible *cus*, which act as Lewis acid sites on the

surface specifically interacting with gas host-molecules. *Cus* are usually the first loading sites as they may serve as charge-dense binding-sites that strongly interact with gas molecules. Therefore, it is possible that, after a removal of solvent and subsequent activation of the material, to transform these sites into *cus* that increase adsorbate/surface interactions during the adsorption process as it happens in our particular case.[146]

We subsequently performed high pressure adsorption isotherms of N_2 and CO_2. As it is depicted in Figure 2.25, even at the highest pressure, at 8 bar, compound **2.7$_{Dy}$** shows relatively low affinity towards N_2 and exhibits an adsorption uptake of 1.10 mmol/ g, much lower than for CO_2, which are of 4.59 mmol/g and 3.84 mmol/g for 273 K and 298 K, respectively. Interestingly the adsorption occurs in two well-distinguishable steps that occurs at almost the same loading regardless the adsorption temperature. Such behaviour could be ascribed to a reorganization of the CO_2 at a critical loading in order to render more room for next incoming adsorbate molecules.

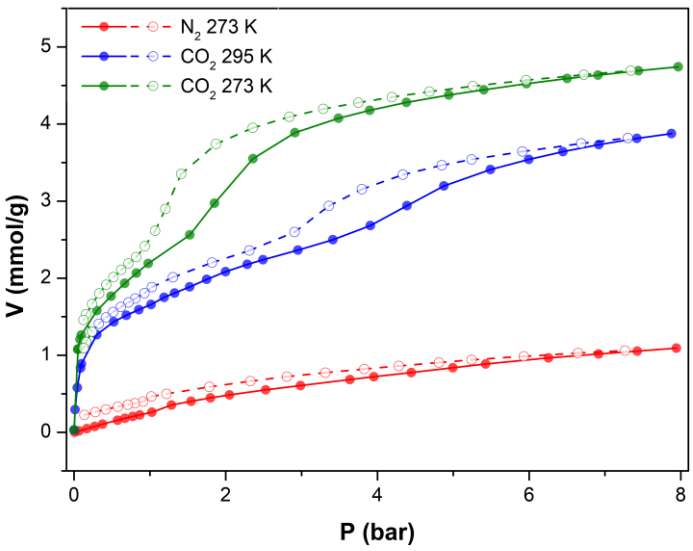

Figure 2.25. High pressure adsorption isotherms of N_2 at 273 K (red) and CO_2 at 273 K (green) and 298 K (blue), respectively.

2.7.5 Catalytic activity

Porous nature of the structure displaying cavities asses accessibility of external molecules to interact with metallic centres. In this scenario, and having in mind that coordinated solvent molecules disposition (pointing out the pore) favour structure desolvatation and aforementioned interaction, cyanosilylation catalytic reaction was performed in a bunch of carbonylic substrates in presence of trimethylsilyl cyanide (TMSCN) and solvent-free media. For that study to be performed, Y^{3+} and Eu^{3+} counterparts, compounds **2.12**$_Y$ and **2.19**$_{Eu}$, respectively have been selected as catalyst.

2.7.5.1 Establishing optimal reaction conditions

To begin with, catalysis conditions were established. For that purpose, benzaldehyde (**2**) and trimethylsilyl cyanide (TMSCN) were chosen as starting reagents and the reaction was carried out at room temperature and no solvent (Scheme 2.2). The criteria followed for this reaction being chosen was that this benchmark-reaction is taken as reference in many examples of the bibliography.[105,147–150] To begin with, the role of the catalyst was tested; for that purpose, the reaction was carried in catalyst absence under 1:2 benzaldehyde to TMSCN ratio.

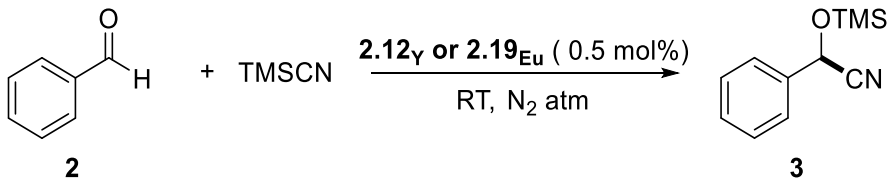

Scheme 2.2. Optimization of the reaction conditions.

The blank reaction exhibited the formation of product **3** after 14 h of reaction with only 8 % of conversion corroborating that cyanosilylation reaction do not go ahead in catalyst absence.

After several experiments, the optimized catalytic protocol was fixed decreasing the amount of TMSCN down to 1.1 equiv and using a catalyst loading of 0.5 mol%. Monitoring of the reaction by ^{1}H NMR, allowed us studying the time required to obtain full conversion as well as analysing the influence in catalyst-loading reduction over the time required to reaction completion.

When comparing both MOFs behaviour, the time required to reach full conversion varies significantly from Y to Eu-MOF. Under the same catalytic loading (0.5 mol%) **2.19$_{Eu}$** reaches full conversion at 5 min reaction time whereas **2.12$_{Y}$** needs 5 hours.

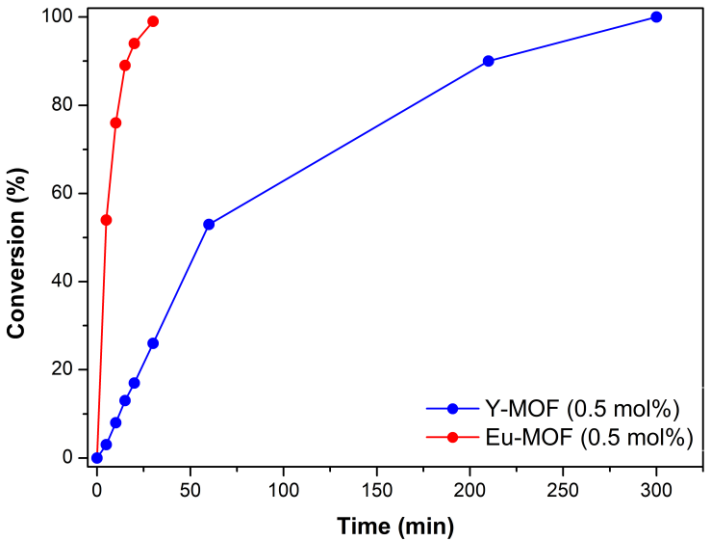

Figure 2.26. Kinetic profile of the reaction using 0.5 mol% of **2.12$_{Y}$** catalyst (red data) and **2.19$_{Eu}$** (black data) in a 1:1.1 ratio benzaldehyde to TMSCN under nitrogen atmosphere at room temperature.

The turnover frequency (TOF) of catalyst was calculated as a function of conversion stabilising the relationship between mmol product per mmol catalyst per unit time obtaining a maximum of 106 h^{-1} at 1 hour reaction time (53 % of conversion) for Y-MOF and 1301 h^{-1} at 5 min reaction time (54 % of conversion). These results remarkably overpass those found with Y-based MOF catalysts but also those reported with any MOF based on lanthanides (Table 2.2). Remarkably, Eu-MOF catalysts at 0.5 mol% uses 2.5 mol% of Europium metal, which is one of the most reduced catalyst loading among the rest of described MOF catalysts based on Europium, which are usually in the range of 5 to 20 mol%. When the loading is reduced down to 0.1 mol% the achieved TOF after the same 5 min of reaction (13 % of conversion) was as high as 783 h^{-1} (Figure 2.27).

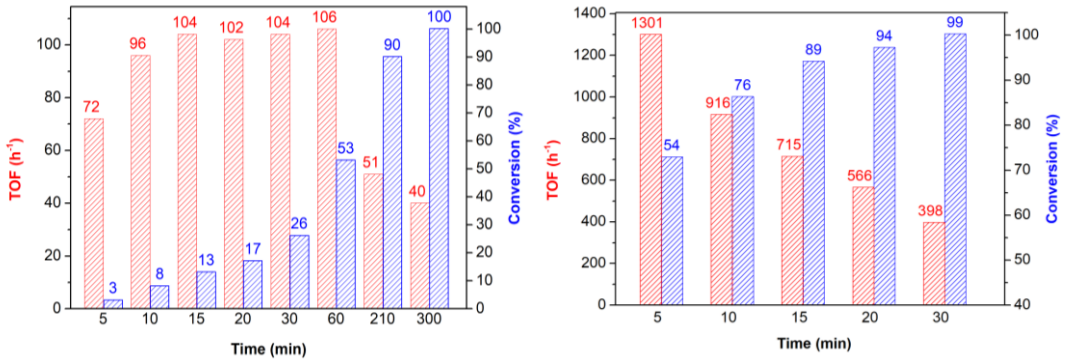

Figure 2.27. Analysis of the TOF (h^{-1}) and reaction conversions obtained with Y-MOF (left) and Eu-MOF (right) in optimized reaction conditions at different reactions times.

Table 2.2 exhibits performances of benzaldehyde cyanosilylation reaction being catalysed by lanthanide-based metal-organic frameworks reported in bibliography. When comparing our MOFs performances, we can highlight that both Y- and Eu-MOFs reach the highest TOF values at the lowest catalytic loading of 0.5 mol% catalytic loading.

Table 2.2. Catalytic cyanosilylation of benzaldehyde performances of Ln-MOFs reported in the literature.

MOF	mol% MOF	Recyclability Nº of cycles	Conversion	Conditions	Ratio[a]	TOF h^{-1}
$Eu_2(MELL)(H_2O)_6$[b] [106]	10	5	>99 % 3h	RT, MeCN	1:2	3.2 h^{-1}
[Sm/Dy/Yb(3,5-DSB)(Phen)(H_2O)]·H_2O[c] [74–76]	2	4	>99 % 3 h (Sm) 70 %, 3 h (Dy) 50 %, 3 h (Yb)	40 ºC,	1:1.5	6-79 h^{-1}
Sm/Eu/Gd/Tb/Eu-Gd/Eu-Tb-psa[d] [104]	5	3	70 %, <2 h (Eu) 80 %, <2 h (Sm) 87 %, <2 h (Eu-Gd) 74 %, <2 h (Tb) 94 %, <2 h (Eu-Tb)	RT, DCM	1:1.5	84-112 h^{-1}
Nd/Eu/Sm/Ho/Yb/Er-dms[e] [151]	5	3	85 %, < 1h (Nd) 96 %, < 1h (Eu) 92 %, <2 h (Sm) 79 %, <2 h (Ho) 98 %, <2 h (Yb) 93 %, <2 h (Er)	RT, DCM	1:1.5	159-234 h^{-1}
Nd, Ho, Er, Yb-btc[f] [109]	4.5	5	>99 %, 2 h	RT, DCM	1:2	1-11 h^{-1}
$Tm(BDC)_{1.5}$(DMF)-(H_2O)[g] [111]	2	[h]	57 %, 5 h	RT	1:1	[h]

La/Ce/Nd/Sm/Dy(L)(NO_3)$(DMF)_2]_n$·n(DMF)[i] [110]	3	5	93 %, 2 h (La) 94 %, 2 h (Ce) 91 %, 2 h (Nd) 89 %, 2 h (Sm) 90 %, 2 h (Dy)	RT	1:4	2-16 h^{-1}
Tb-TCA[j] [98]	2	[h]	78 %, 4 h	RT, DCM[k]	1:2.4	9.8 h^{-1}
[Sm(L-H_2)(R-L-H_3)$(H_2O)_4$]·nH_2O[l] [102]	10	[h]	69 %, 16 h	RT, DCM	1:2	0.4 h^{-1}
[$Yb_2(L)_2(H_2O)_3$]·2H_2O[m] [101]	1.4	5	>99 %, 24 h	RT	1:2	5 h^{-1}
[Pr(L^{OMe})$(H_2O)_4$]·2.5DMA·3H_2O[n] [152]	1.9	2	99 %, 14 h	RT	1:2	3.8 h^{-1}
[Sm$(H_2O)_5$][Sm$(H_2O)_7$][$Co_2Mo_{10}H_4O_{38}$]·6H_2O [99]	2	3	98 %, 5 h	RT	1:3	9.8 h^{-1}
[La/Ce/Nd$(H_2O)_5]_2Mo_6V_2O_{26}$·8H_2O [100]	1	3	94 %, 5 h (La) 90 %, 5 h (Ce) 96 %, 5 h (Nd)	RT	1:3	10.4 h^{-1} 10.0 h^{-1} 13.7 h^{-1}
Our Y-MOF catalyst [37]	0.5	7	>99 %, 5 h	RT	1:1	106 h^{-1}
Our Eu-MOF	0.5	7	>99 %, 30 min	RT	1:1	1301 h^{-1}

[a] Ratio between benzaldehyde **1a** and TMSCN; [b] MELL = mellitic acid; [c] 3,5-DSB = 3,5-disulfobenzoate, Phen = 1,10-phenanthroline; [d] psa = 2-phenylsuccinate; [e] dms = 2,3-dimethylsuccinate; [f] btc = 1,3,5-benzenetricarboxylate; [g] BDC = 1,4-benzenedicarboxylate; [h] Not given; [i] L = 5-[2-{2,4,6-trioxotetrahydropyrimidin-5(2*H*)-ylidene}hydrazinyl]isophthalate; [j] TCA = tricarboxytriphenylamine; [k] The aldehyde employed is 2-nitrobenzaldehyde. [l] L-H_4 = 2,2'-diethoxy-1,1'-binaphthalene-6,6'-bisphosphonic acid. [m] L = 4,4′,4″-((2,4,6-trimethylbenzene-1,3,5-triyl)tris(methylene))tribenzoate; [n] L^{OMe} = 3,3′-((2,3,6,7-tetramethoxyanthracene-9,10-diyl)bis(4,1-phenylene))diacrylate.

2.7.5.2 Y-MOF and Eu-MOF catalysed cyanosilylation reaction of carbonyl compounds

Once having optimized reaction conditions (1.1 equiv. TMSCN, 0.5 mol% catalyst, room temperature), a bunch of aldehydic and ketonic substrates, including aromatic, heteroaromatic and aliphatic were subjected to cyanosilylation reaction in presence of Y-MOF or Eu-MOF. We choose Y-MOF for aldehydic substrates and Eu-MOF for less reactive ketones in view of results obtained with benzaldehyde cyanosilylation.

The scope of cyanosilylation reaction of aldehydes catalysed by Y-MOF is summarized in Scheme 2.3. Reaction was carried out using the corresponding aldehydic substrate **2** (25 µL, 0.25 mmol, 1 equiv.) and TMSCN (34 µL, 0.275 mmol, 1.1 equiv.) with 0.5 mol% (2.3 mg) Y-MOF catalyst loading under inert N_2 atmosphere at room temperature. After 5 h reaction time desired cyanohydrin product **3** was obtained at over 99 % conversion.

The results showed that the reaction has broad tolerance for a wide variety of substrates. Under standard conditions, the corresponding products were obtained in quantitative conversions after 5 hours whether using aldehydes with electron-donating groups (**2b**-**d**), with electron-withdrawing groups (**2e**), with different position of the substituents or using heteroaromatic systems (**2f**-**i**). It should be noticed that in the case of **2c** the reaction needed 48 h to reach full conversion. This slowdown behaviour in aldehydes bearing electron-donating groups has been previously described for lanthanide MOFs.[110] The examples of aliphatic aldehydes **3j**-**k** are remarkably significant since usually aliphatic aldehydes typically give lower catalytic efficiency that aromatic ones due to their innate reduced reactivity. In our hands, our Y-MOF catalyst performed both reactions in a quantitative manner within 5 hours.

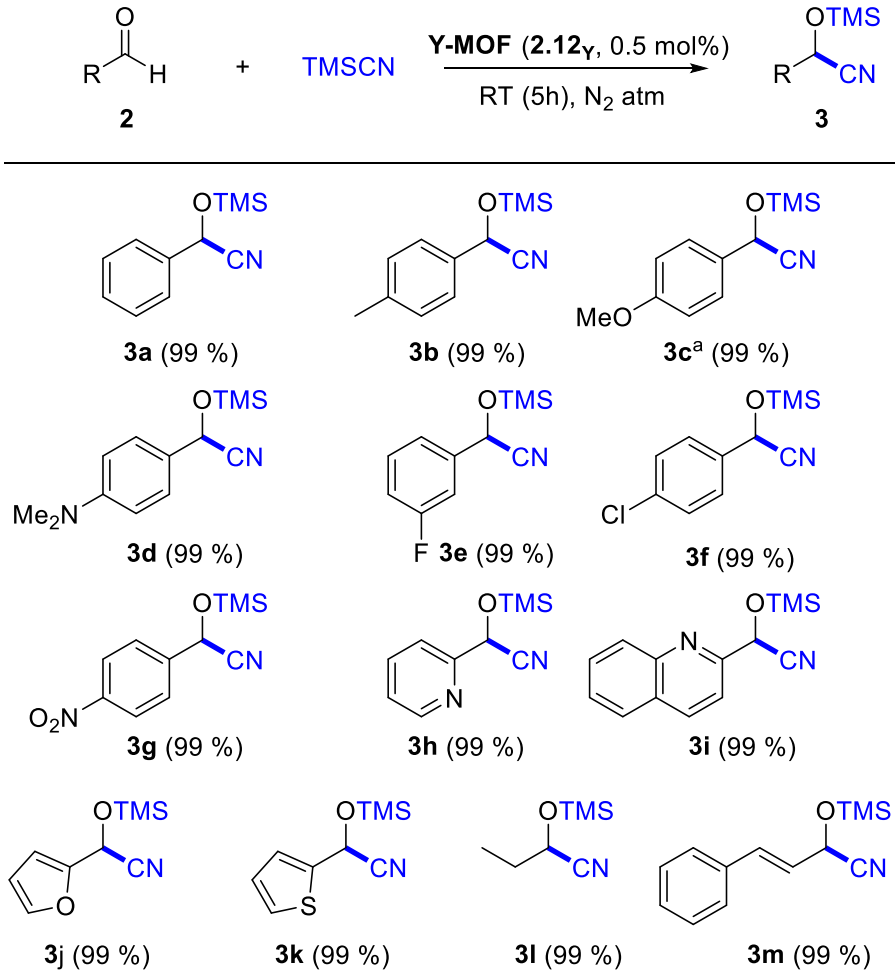

Scheme 2.3. Scope of the cyanosilylation reaction of aldehydes. Conversion is given in brackets and in bold is represented the new carbon-carbon bond. [a] Reaction time of 48 h.

We also wanted to test whether Y-MOF was able to perform cyanosilylation reaction of ketones. Therefore, we subsequently explored the use of less reactive ketones giving rise to the generation of quaternary stereocentres (Scheme 2.4) in 8 different substrates **2l**-**s**. We found quantitative conversions after 24 or 48 h of reaction time featuring aryl-alkyl (**3l, 3m**), aryl-aryl (**3n**) as well as alkyl-alkyl (**3o-3s**) cyanohydrin silyl ethers (Scheme 2.4). Even cyclic ketones such as **2p**-**r** were converted into their corresponding cyanohydrins, although in the case of the sterically demanding **2r** the conversion was of 63 % after 48 h of reaction.

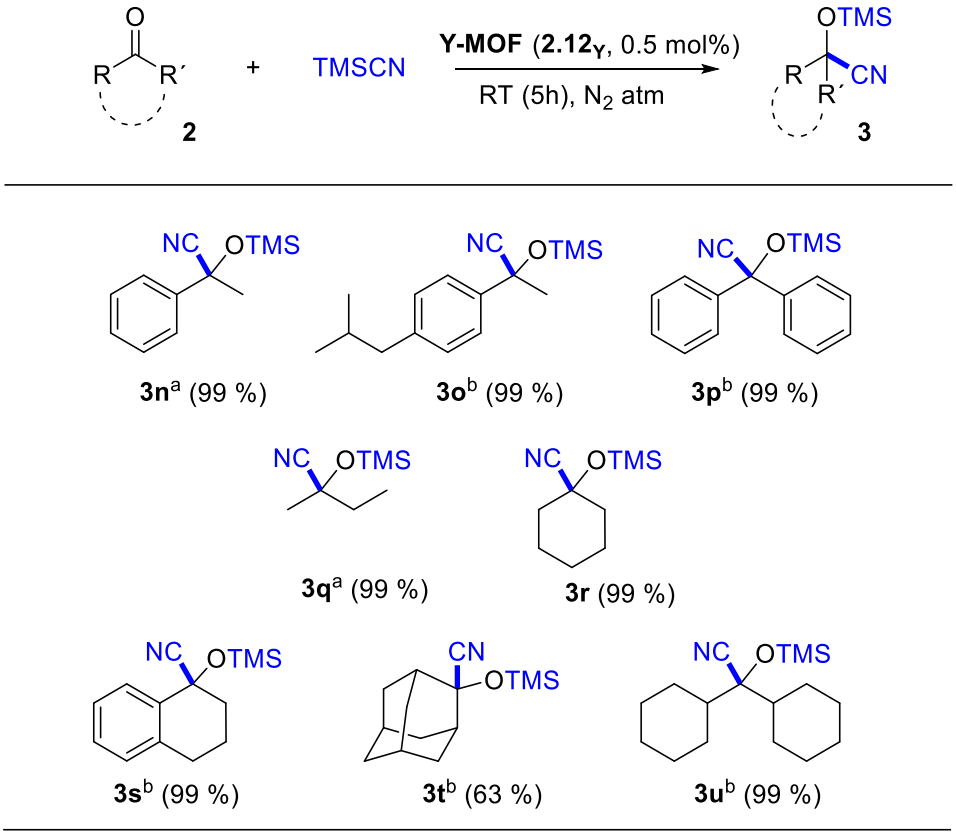

Scheme 2.4. Scope of the cyanosilylation reaction of ketones. Conversions are given in brackets in bold is represented the new carbon-carbon bond.[a] Reaction time of 24 h.[b] Reaction time of 48 h.

Afterwards, we explored isostructural Eu-MOF for the scope of the reaction using overall of 17 types of ketones. Great variety of aryl alkyl ketones were tested. As a prove of concept, we also assayed three different aldehydes just to check Eu-MOF ability to carry on cyanosilylation reaction.

Reaction was carried out using the corresponding ketonic substrate **2** (0.25 mmol) and TMSCN (34 µL, 0.275 mmol, 1.1 equiv.) with 0.5 mol% (2.5 mg) Eu-MOF catalyst loading under inert N_2 atmosphere and at room temperature. After 24 h reaction time, desired cyanohydrin product **4** was obtained. In all cases, conversion of the reaction was calculated relative to compound **2** and was determined by ^{1}H NMR of the reaction crude.

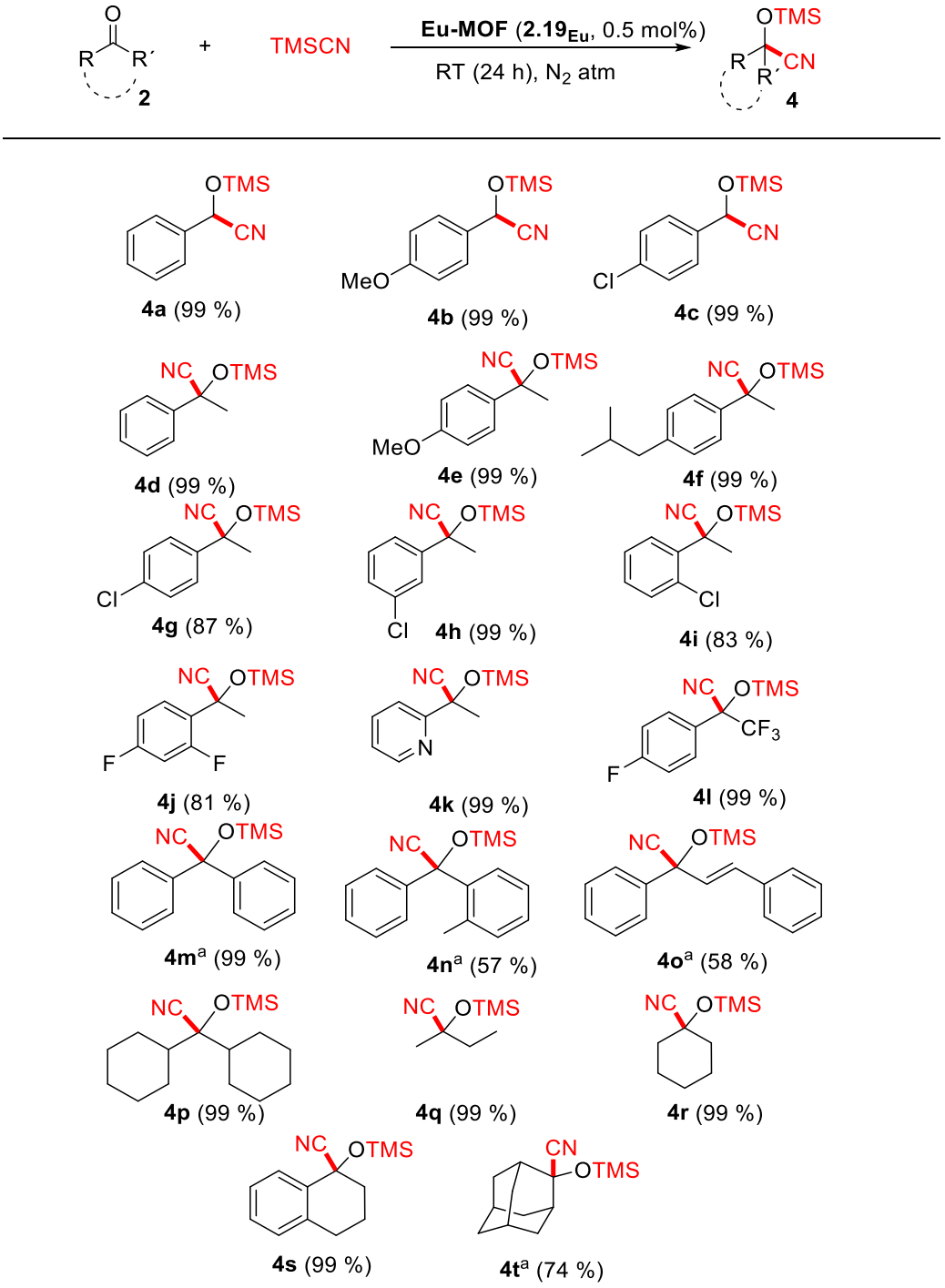

Scheme 2.5. Scope of cyanosilylation reaction of ketones. Conversion is given in brackets and in bold is represented the new carbon-carbon bond.[a] Reaction time of 48 h.

In view of results, it can be highlighted that within 24 h reaction high conversions were obtained both for aldehydic and ketonic substrates, only with a slight reduction

when the aromatic ring contained electron-withdrawing groups whether at the *para*- or at the *ortho*-positions (**4g** and **4i**-**4j**). The evaluation of diaryl ketones (**4m**- **4n**) required 48 h to achieve moderate to good results, probably due to the steric hindrance of the substrates. The use of α,β-unsaturated ketones (**4o**) was also assayed but unfortunately only a conversion of 58 % was obtained. The use of aliphatic ketones (**4p**- **4q**) provided full conversions after 24 h of reaction.

Finally, we decided to test cyclic ketones which are usually less employed. In our hands, full conversion of **4r-4s** was obtained after 24 h, although an extra 24 hours were needed in order to fully convert the most sterically demanding 2-adamantanone **4t**.

The possibility of scaling-up the process was also pursued by performing the reaction with aldehyde **2j**, giving rise to the formation of almost a gram of product **4j** and an isolated yield of 98 %. This cyanohydrin silyl ether is of great interest in the agri-food sector since it has been described as a very useful precursor of 5-(2,4-difluorophenyl)-4-imino-5-methyl-3-(phenylamino)oxazolidin-2-one, a potent fungicide (Scheme **2.6**).[153]

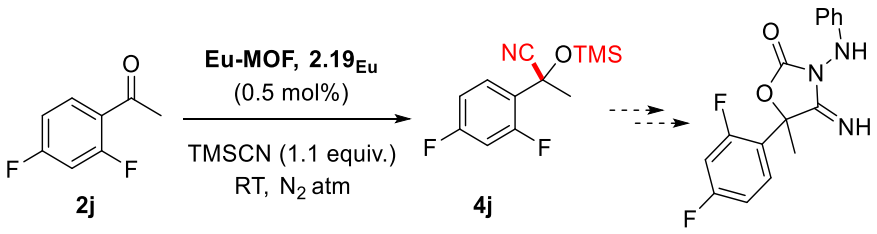

Scheme 2.6. Application of the cyanohydrin product **4j** towards the synthesis of a fungicidal active compound.

2.7.5.3 Catalyst recyclability

Reusability of the heterogeneous catalyst is of remarkable importance from a green chemistry point of view. For this reason, recyclability tests were conducted with benzaldehyde (**2**) and TMSCN as the model reaction under standard optimized reaction conditions (Scheme 2.7).

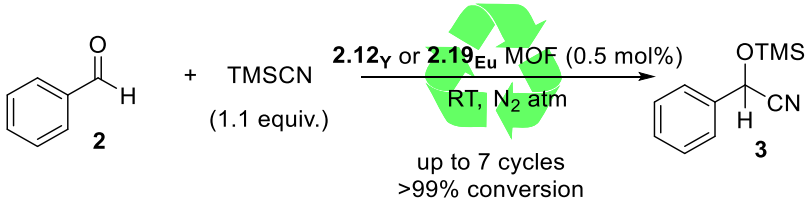

Scheme 2.7. Y-MOF and Eu-MOF catalyst recyclability test.

Concretely, in a 1 mL vial with a septum screw capped equipped with a stirring bar, the catalyst Y or Eu-MOF (0.5 mol%, 2.3 mg and 2.5 mg, respectively) was weighed. Then, the corresponding amount of carbonylic compound **2** (25 µL, 0.25 mmol) followed by TMSCN (34 µL, 0.275 mmol, 1.1 equiv.) were added and the reaction was stirred under inert N_2 atmosphere at room temperature during 0.5 h. After reaction was complete, the catalyst was easily separated from the reaction solution by centrifugation (3 min at 8000 rpm), washed with dichloromethane (2 x 1.5 mL) and dried before being reused under the same reaction conditions. As shown in Figure 2.28, both Y-MOF and Eu-MOF remain intact and maintain the active during 7 consecutive cycles without any erosion of the catalytic activity.

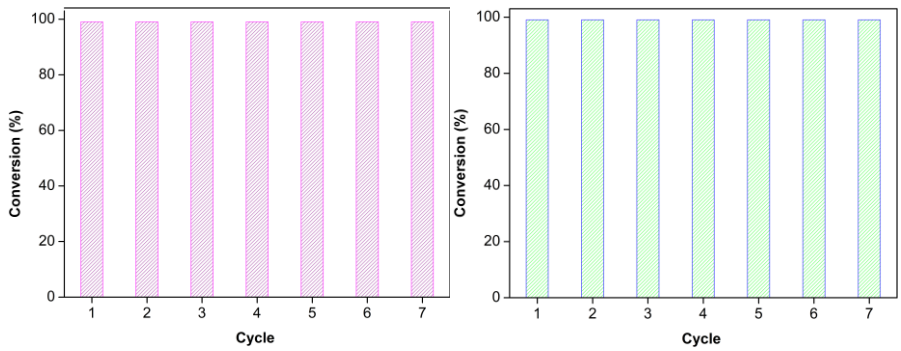

Figure 2.28. Recyclability of Y-MOF (left) and Eu-MOF (right) catalysts during 7 consecutive cycles.

Catalyst was characterised after each cycle by powder X-ray diffraction revealing no appreciable structural changes with respect to the pattern recorded before catalytic cycles confirming that the crystallinity of the structures was unaltered after the reaction demonstrating their heterogeneous nature.

2.7.5.4 Catalyst leaching

Further studies were carried out in order to evaluate catalyst leaking. To that end, after the second and seventh cycle, reaction crude was centrifuged to recover the catalyst and the supernatant filtered off thorough a plug of celite and washed with dichloromethane (2 x 0.5 mL) and dried under vacuum. Subsequently, compound **2h** for Y-MOF reaction supernatant and compound **2d** were added to Eu-MOF reaction supernatant and was added and the reaction was stirred under N_2 atmosphere at room temperature. Analysing an aliquot by ^1H NMR after 5 h revealed only 6 % of product **3h** and no product (**4d**) was observed after 24 h corroborating that almost no leaching of Y^{3+} neither Eu^{3+} take place.

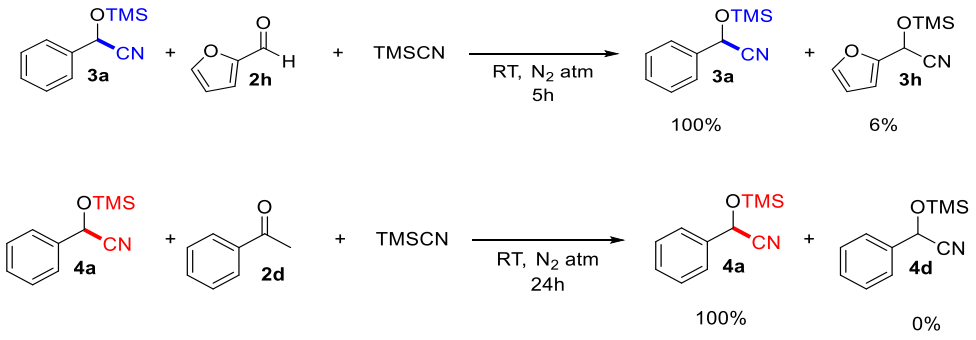

Scheme 2.8. Catalyst leaching test performed for Y-MOF (top) and Eu-MOF (down) catalysed cyanosilylation reaction.

Finally, we evaluated overall transformation according to green-chemistry metrics in the optimized catalytic conditions in the cyanosilylation of benzaldehyde with TMSCN in presence of Y-MOF or Eu-MOF catalyst. Calculated values are summarized in Table 2.3 and it can be stated that overall transformation is eco-friendly and overcome health and environmental problems derived from the chemical industry. Also, it must be noticed that obtained values are comparable to those reported previously for related lanthanide-based MOFs.[104,105]

Table 2.3. Green metrics values (AE, MI, RME and CE) obtained with Y-MOF and Eu-MOF catalysed reaction in the cyanosilylation of benzaldehyde with TMSCN.

Green Chemistry Metrics	Y-MOF catalysed	Eu-MOF catalysed
Atomic economy (AE)	99.8 %	99.8 %
Mass Intensity (MI)	1.10	1.05
Reaction mass efficiency (RME)	91.4 %	95.7 %
Carbon Efficiency (CE)	96.0 %	96.8 %

2.8 Conclusions

All in all, we report a family of novel three-dimensional metal-organic frameworks based on 3-amino-4-hydroxybenzoate and Ln^{3+} ions. These coordination networks are isostructural among them and crystalise in hexagonal $P6_3/m$ space group showing $\{[Ln_5L_6(OH)_3(DMF)_3]\cdot 5H_2O\}_n$ formula. With the aim of exploiting potential multifunctional character of these Ln-MOFs, their single molecule magnet behaviour, photoluminescent properties and adsorption capacity have been studied. Starting by magnetic properties, none of these compounds (**2.7$_{Dy}$**, **2.9$_{Er}$** and **2.11$_{Yb}$**) exhibit frequency-dependence without an external magnetic field due to the effect of quantum tunnelling of magnetization. When 1000 Oe static field of was applied to suppress QTM relaxation process, only compound **2.11$_{Yb}$** showed signal dependency among frequency, which, as far as we are aware, constitutes the first porous three-dimensional Yb-based MOF exhibiting field-induced SMM behaviour. In view of residual unquenched QTM occurring in pure samples, magnetic dilution strategy was performed (in this case with Y^{3+}) yielding compounds **2.13$_{Y\text{-}Dy}$**, **2.14$_{Y\text{-}Er}$** and **2.15$_{Y\text{-}Yb}$**. The procedure of isolating paramagnetic centres in a diamagnetic matrix was successful in the latter two compounds since the position of the maxima in χ_M'' was shifted towards higher temperatures. Compounds **2.14$_{Y\text{-}Er}$** and **2.15$_{Y\text{-}Yb}$** present Orbach- (with U_{eff} = 13.09 K and $\tau_0 = 6.46\cdot10^{-8}$ s^{-1}) and QTM plus Raman- ($\tau_{QTM} = 2.15\cdot10^{-2}$ s, $B = 7.2$ $s^{-1}\cdot K^{-n}$ and $n = 5.87$) mediated relaxation mechanisms, whereas compound **2.13$_{Y\text{-}Dy}$** shows no maxima in out of phase molar magnetic susceptibility. These results may be explained according to the electron density shape of the lanthanide(III) ion, since the system benefits prolate-type ions (Er^{3+} and Yb^{3+}) rather than oblate ions (Dy^{3+}).

On another level, compounds **2.4$_{Eu}$** and **2.6$_{Tb}$** present characteristic emissions of the ions, among which Tb^{3+} ion shows more brilliant and long-lived emission than Eu^{3+} because the ligand-to-lanthanide energy transfer is more efficient for the former owing to the low energy gap between their excited states. Three additional Y^{3+}-or Gd^{3+}-and Tb^{3+}/Eu^{3+}-mixed lanthanide networks were prepared with the following Y^{3+}:Tb^{3+}:Eu^{3+} doping proportions of 50:45:5 % (**2.16**) and 50:40:10 % (**2.17**), and Gd^{3+}:Tb^{3+}:Eu^{3+} of 50:40:10 % for compound **2.18**, and exploited for potential application in thermometry. Interestingly, compounds **2.17** and **2.18** perform as luminescent thermometers showing a maximal relative sensitivity of S_m 1.202 % K^{-1} obtained at T_m 12 K and S_m 2.43 % K^{-1} at T_m 320 K, respectively.

This family of compounds possess porous structures characterized by narrow microchannels along *c* axis which additionally allowed us exploring adsorption capacity of the synthesised materials at low pressure and high-pressure conditions. Although, compound **2.7$_{Dy}$** adsorption isotherms of N_2 revealed no adsorption capacity, CO_2 molecules could diffuse through the pore exhibiting 44.6 cm^3/g (2.1 mmol/g) uptake of CO_2 physiosorbed at 273 K (at STP conditions), and a volume of 35.1 cm^3/g (1.6 mmol/g) at 298 K. In comparison to other MOFs containing open-metal sites, **2.7$_{Dy}$** exhibits relatively high isosteric heat (41.4 kJ/mol) that supports the strong interaction between CO_2 and the first of the three *cus* centres present in the network. Upon loading the framework with the gas, the interaction progressively decreases showing two more steps in the profile that perfectly matches with the coordination of CO_2 with the remaining two *cus* pertaining to the pentanuclear cluster.

Finally, motivated by the porous nature and accessibility of external molecules to MOFs metallic clusters two analogous yttrium- (**2.12$_{Y}$**) and europium (**2.19$_{Eu}$**)-based metal–organic supramolecular porous systems have been tested in the catalytic cyanosilylation reaction of aldehydic and ketonic substrates, of different nature, avoiding the use of volatile organic compound (VOC), favouring the transformation to the final cyanohydrin product under green conditions (solvent free and at ambient temperature).

Importantly, preliminary studies conducted in **2.12$_{Y}$** demonstrated working as heterogeneous catalyst, working as Lewis acid after solvent decordination, in the cyanosylylation reaction of several aldehydes. Therefore, we designed a strategy modifying synthetic procedure to obtain this family of compounds and decided to increment water ratio in the initial solvent mixture; having in mind that, at higher water proportion, coordination of the less volatile solvent would be favourised and therefore, the desolvatation would be eased yielding more easily a vacant position in metal centre and acting as Lewis acid catalyst. In such conditions, we obtained Eu-MOF, compound **2.19$_{Eu}$** which contains water molecule instead of DMF, as compound **2.12$_{Y}$** did. We subsequently, tested it in the cyanosilylation reaction of aldehydes and ketones exhibiting great ability heterogeneously catalysing cyanosilylation reaction of the less reactive ketones demonstrating the effectiveness of our approach.

More concretely, Eu-MOF displayed activity as heterogeneous catalyst in cyanosilylation with TMSCN of various ketones at solvent-free and ambient temperature conditions. Among lanthanide-based catalyst reported so far, **2.19$_{Eu}$** displayed the one

of the highest activities with a TOF value of 1301 h^{-1}, and with the impressive possibility of recyclability for at least seven cycles without any change on structure and with no leak during them.

In this context, motivated by obtained the proved capability of **2.12$_{Y}$** and **2.19$_{Eu}$** MOFs working as heterogeneous catalyst in the cyanosilylation reaction of carbonylic substrates in environmentally friendly conditions, we thought about the possibility of synthesising a heterobimetallic Y-Eu MOF **2.19$_{Eu}$** material with enhanced catalytic activity derived by the synergy of both materials properties as future work.

PART 3

2.9 Introduction. Easy handling and cost-efficient processing-techniques of a three-dimensional Tb^{3+}-MOF. Emission capacity of the membrane-immobilized material and water adsorption and proton conductivity of the pristine MOF.

Metal-organic frameworks are relatively new materials that nowadays are reaching the market. Since the first porous three-dimensional example, MOF-5, reported by Yaghi's group in the nineties,[154] an immense number of MOFs have been described in the last years finding application in multiple fields.[98,155–158] However, for these materials being implemented in industry several technical barriers have to be overcame so far.[159] Among others can be mentioned: the availability at large-scale which not only depends on reactants but also in whole process production-costs, MOF's physical properties maintenance when manufacturing at high scale, the importance of formulation for finetuning of MOFs' physical properties when shaping for a particular application, in addition to the performance of final material under realistic operating industrial conditions such as moisture, pressure or temperature.[160]

In fact, MOF's synthetic-procedures yield as final product very insoluble and low-density loose powders that often are difficult to handle and can be problematic to incorporate into devices in industry, since they can easily blow off and contaminate pipes.[161] Therefore, shaping of MOF is mandatory for using them in real industrial applications. Generally, the selection of processing or shaping technique depends on the synthetic-procedure and textural properties of the MOF material.[161,162]

Essentially, as advantage, after carrying out MOF's processing, mechanical strength and resistance enhancement is expected in the final product with respect to bulk non-processed material. Additionally, the shaping must be cost effective.[162] Even if shaping of MOFs for specific applications is still in its infancy great efforts have still to be dedicated to the rational study of this process so as to access to the real commercial application.[161]

Monoliths, beads and pellets, are conferred as suitable processed-materials with maximised bulk density and minimized wasted space.[162] Among the recent mentioned transformed materials, pelletization technique is presented as the most common method

for densifying MOF's by applying pressure. However, this process encounters several disadvantages such as, that excessive pressure can crush MOF's structure and reduce mechanical stability, as well as the use of binders (which are generally added to improve cohesion) can dilute porous powder and cause pore blockage.[161]

Another interesting approach for transforming materials without the need of external pressure, can be to assemble MOFS into polymeric membranes to give rise to mixed-matrix membranes (MMMs).[163] This strategy results appealing from the industrial point of view since membranes have low productions cost and exhibit relatively high mechanical properties such as, flexibility, softness, and thermal and chemical stability, among others.[163–165]

From a practical point of view, once processing, shaped materials are required to apart from keeping structural robustness, be stable under humidity, temperature or pressure operating conditions.[162] Thus, testing shaped materials towards these variables becomes of great importance towards optimal performance in industrial implementation.

Also, in recent years, MOFs investigation for being used in the proton conduction field is gaining importance and is presented advantageous field for MOF application since they can possibly be implemented in solid-state electrolytes.[166] The interest towards MOF's particularly relies on their intrinsic large surface area, long-range ordered and porous cavities where proton-carries can be incorporated as guest molecules enabling control over conductivity at the molecular level.[166]

Proton conduction in a MOF can be originated by two types of pathways. In the called, "vehicle mechanism" proton-diffusion occurs enabled by water molecules which act as vehicles, and in the "grotthus mechanism" conduction do not necessarily depend on water transport but proton-motion occurs through hydrogen bonds established among neighbouring water molecules. In this latter case, a minimum relative humidity is required in order to water molecules creating a hydrogen-bond pathways from which protons would be conducted. A part form conducting mechanism, the character of the MOF is of great importance and plays key role. So as, hydrophilic MOFs display strong water affinity and are able to absorb large water uptake at even under low humidity conditions.[167] Additionally, the presence of acidic protons or metal-coordinated water molecules facilitates hydrogen bond formation path inside the pore promoting proton-conduction.[168]

As already stated, proton-conduction process is directly correlated to water-adsorption capacity of the MOF. Among water-adsorption mechanisms, three types are described: vapour adsorption on the metallic cluster (chemisorption), layer adsorption (this process is reversible and is correlated to physisorption) and capillary condensation (this process is reversible).[168] Since the first copper based two dimensional coordination polymer able to conduct protons reported by Kanda et al. in 1979,[169] several examples have been published, nonetheless the challenge in this line relies on designing MOFs able to reversibly uptake large water uptakes within a narrow relative humidity range.[166]

Having all this in mind, in this work, we propose easy handling techniques for shaping compound **2.6$_{Tb}$**, which exhibits {[$Tb_5L_6(OH)_3(DMF)_3$]·$5H_2O$}$_n$ formula, in pellets and membranes and study shaped material's performance against temperature and moisture conditions in order to simulate possible industrial operating conditions. Additionally, as a proof of principle, we embed luminescent compound **2.6$_{Tb}$** into PMMA membrane to explore photoluminescent properties of mixed- matrix membrane, more or less in the line with the work performed by Dechnik eta al. who described the first luminescent MOF mixed-matrix.[170] Also, motivated by, compound **2.6$_{Tb}$** relatively high vapour-adsorption capacity and structure stability, proton conductivity of **2.6$_{Tb}$** was studied.

2.10 Materials and methods

2.10.1 Compound synthesis

Single crystal synthetic procedure of $\{[Tb_5L_6(OH)_3(DMF)_3]\cdot 5H_2O\}_n$, $\mathbf{2.6_{Tb}}$

The synthetic procedure to obtain single crystal and scale up procedures have been already described above in 2.6.1 synthesis.

2.10.2 MOF processing techniques

2.10.2.1 Membrane's preparation and Characterization

For $\mathbf{2.6_{Tb}}$ being integrated into membranes, two polymeric-matrixes have been selected: Polysulphone (PSF) and polymethylmethacrylate (PMMA).

In both matrixes, membranes preparations conditions were optimized by testing different polymer-to-MOF ratios in order to achieve a material with balanced mechanical stability and membrane coverage homogeneity; since, excessive MOF proportions with respect to polymer diminish mechanical stability and makes membranes more breakable; and, also, low ratios lead on pockets in the material, (areas not covered with the MOF); therefore, an equilibrium is of great importance in order to obtain a material with the best properties.

For these reasons, after several test, the optimal membrane conditions were stablished to be 75 mg MOF in 400 mg polymer. In this way, processed material's mechanical stability and homogeneity could be compared as the same synthetic ratio has been used in both polymeric matrixes. The membrane synthesis was performed according to the following procedure:

400 mg of PSF were weighted and dissolved in 5 mL of CH_2Cl_2 to this dense solution, 75 mg of compound $\mathbf{2.6_{Tb}}$ were added and left stirring for 30 min. The remaining viscous solution was then cast in a glass petri dish and left unstirred at ambient conditions until complete evaporation of the solvents. In case of PMMA, the same solvent volume was measured and to this, first, 400 mg of polymethylmethacrylate were added and, once dissolved, 75 mg of compound $\mathbf{2.6_{Tb}}$ were added and left suspension stirring

for 30 min. The succeeding steps were followed as previously described of PSF based membranes.

MOF incorporation into polymeric membrane was accessed by powder X-ray diffraction and SEM/EDS analysis. Additionally, incorporation is immediately visible to the naked eye as pure PMMA and PSF are transparent while MOF containing membranes had brown dark colour (See Figure A2.46). Also, SEM/EDS mapping of the surface and cross section analysis allowed confirming that **2.6$_{Tb}$** was uniformly distributed throughout the polymeric membrane (Figure A2.20).

2.10.2.2 Pellets preparation and Characterization

A home-made extrusion apparatus (composed by a syringe) allowed pellets to be compressed for which as binding agent, water was used. For pellets preparation, 100 mg of compound **2.6$_{Tb}$** were weighted and 100 µL was added to form a malleable paste. Subsequently, the paste was transferred into a syringe and compressed. With the aid of an external heating source, biding agent elimination allowed obtaining final pelletized material. With the aim of enhancing resistance, some of pellets were coated with polymer, in this case, polysulphone was used for that purpose. For polymer coating, pellet was submerged during 2 s in an already prepared polymer solution of CH_2Cl_2 containing 300 mg of polysulphone. Once dichloromethane being evaporated the coating dried and pellet got its final resistance.

2.11 Results and discussion

2.11.1 Structural characterization

Single-crystal structure discussion has been performed based on the isostructural Dy^{3+} analogue in the 2.7.1 structural characterization section.

2.11.2 Processing into pellets and membranes

In order to incorporate MOFs into devices, bulk material shaping is primordial,[162] in this line, with the aim of exploring processing techniques compound **2.6$_{Tb}$** has been transformed into pellets and membranes.[171]

Once, compound **2.6$_{Tb}$** being transformed into pellets and membranes, the stability of these final processed materials was tested against moisture and temperature cycles. For that purpose, materials were placed for 72 h in a desiccator containing K_2SO_4 saturated solution which simulated 98 % relative humidity (RH) ambient.[172] Afterwards, materials were characterised by PXRD.

2.11.2.1 Moisture stability

PXRD results (Figure A2.47) exhibit that compound **2.6$_{Tb}$** is stable and keeps its structure after being transformed into pellets or membranes and being exposed for 72 h at 98 % RH. Contrary to what happens when material is directly put in contact with water, that evolves into another crystalline phase, long exposure to humidity do not provoke material transformation and remains stable. Due to the amorphous nature of the polymer, only the main intense peaks of compound **2.6$_{Tb}$** stands over the amorphous background in polysulphone (PSF) based membrane's PXRD.

2.11.2.2 Temperature stability

Once carrying out humidity tests, pellets were afterwards treated to temperature cycles. For that aim, four heating and cooling down cycles were performed and materials were characterised by PXRD analysis. Thus, uncoated pellets and polysulphone with coated were first tested against 98 % relative humidity (RH) for 72 h and later tested their thermal stability. For this purpose, temperature cycles of heating to 125 ˚C and cooling down to room temperature were carried out. After each cycle, a photograph of both

pellets (coated and uncoated) was taken in order to check their integrity. Subsequently, PXRD analysis was performed after the second and forth cycle in coated and uncoated pellets. Overall, the compound **2.6$_{Tb}$** coated and uncoated pellets resist perfectly to humidity and subsequent temperature cycles not only keeping their integrity but also their structure according to results obtained by PXRD (Figure A2.48). However, it must be noticed that coated pellets keep better their integrity because of the resistance apported by the polymer.

2.11.3 Water adsorption studies

The gravimetric water vapor sorption kinetic measurements of compound **2.6$_{Tb}$** and composite membranes (Figure 2.29) were performed using a Dynamic Vapor Sorption (DVS) system at 25 °C over a wide range of relative humidity (0% to 95% RH). The isotherm of **2.6$_{Tb}$** display a IUAPC's Type I shape typical of microporous materials such as MOFs, although the slight increase of water mass above 80% RH (seen as a hint of a Type II isotherm) can be seen as an indication of a minor contribution of multilayer adsorption on the external surface of the particles. The overall increase in mass of compound **2.6$_{Tb}$** is quite substantial reaching *ca*. 18 *wt*.% at P/P_0 = 95%. There is also a slight but obvious hysteresis between the adsorption and desorption, which extends to the low-pressure range, indicating the retention of water molecules within the MOF framework. This apparently irreversible water uptake may be related to the swelling of the MOF structure or a chemical interaction with the water molecules.

The isotherm of the **2.6$_{Tb}$@PSF** membrane displays a similar shape to that of **2.6$_{Tb}$**, in turn very different from the Type III observed for pure PSF,[173] and thus suggesting that the overall mass change is essentially determined by the fraction of **2.6$_{Tb}$** in the membrane. As expected, **2.6$_{Tb}$@PSF** adsorbs much less water than **2.6$_{Tb}$**, reaching a maximum 2.86 *wt*.% at P/P_0 = 95%. Assuming that pure PSF adorbs *ca*. 0.8 *wt*.% of water also at P/P_0 = 95%,[173] one can crudely estimate the weight fraction of **2.6$_{Tb}$** in PSF to be 12%, which his is in reasonable agreement with the nominal composition.

2.6$_{Tb}$@PMMA absorbs nearly the same amount of water near saturation (2.70 *wt*.% at P/P_0 = 95%) than **2.6$_{Tb}$@PSF**, but the shape of the isotherm for low RH indicates a much smaller fraction of the micropores accessible for adsorption. The poor affinity of PMMA for water (adsorbs *ca*. 0.06 *wt.%* at P/P_0 = 95% [174]) could explain this behavior.

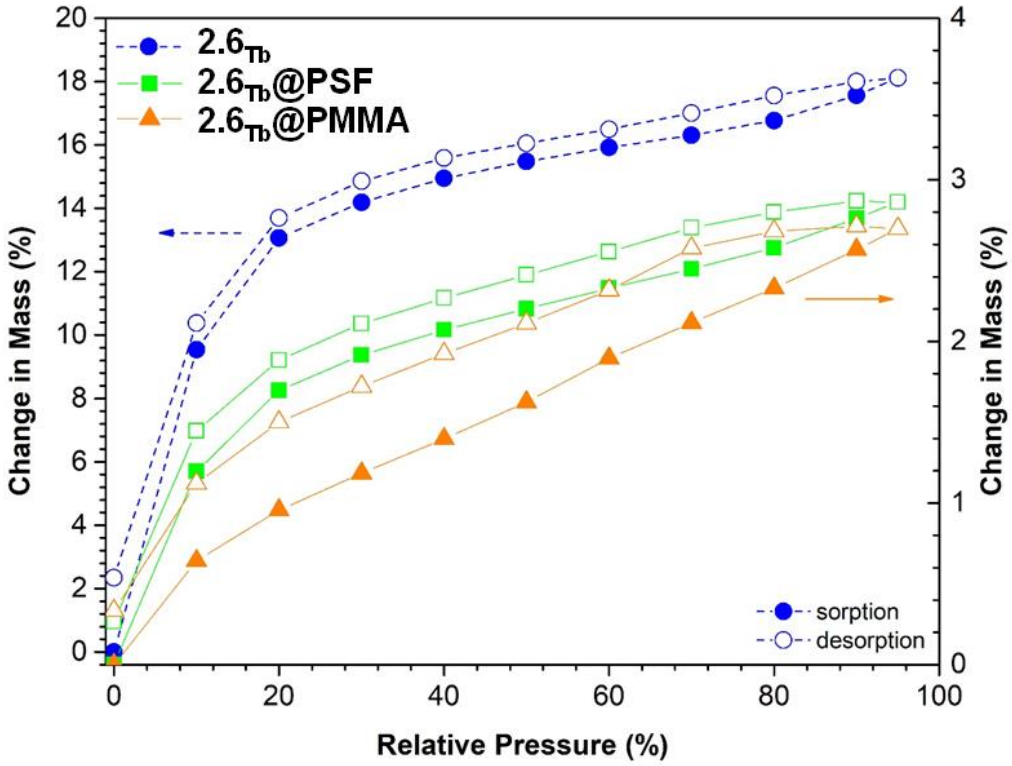

Figure 2.29 Water vapour adsorption (solid symbols) and desorption (open symbols) isotherm curves for compound **2.6$_{Tb}$**, and the **2.6$_{Tb}$@PSF** and **2.6$_{Tb}$@PMMA** membranes**.**

2.11.4 Ionic Conductivity

Motivated by the relatively high-water vapour uptake, we decided to test compound **2.6$_{Tb}$** for proton conductivity. Conductivity measurements carried out in pelletized sample of compound **2.6$_{Tb}$** with increasing temperature at each RH (1st cycle) and cooling down (2nd cycle). As expected for water-mediated proton conducting MOFs proton conductivity increases with the augmentation of humidity.

The Arrhenius plots of the ionic conductivity of compound **2.6$_{Tb}$** and **2.6$_{Tb}$@PSF** membrane measured under the variable temperature (40-94 °C) and relative humidity (20-95 %), RH, are presented in Figure 2.30. The ionic conductivity results of the **2.6$_{Tb}$@PMMA** membrane are not represented in Figure 2.30, since the electrical resistance of these samples was higher than 10 MΩ, and thus impossible to determine due to limitations of the LCR meter. According to the data depicted in Figure 2.30, the ionic conductivity of the materials increases with the temperature and RH. In the case of compound **2.6$_{Tb}$**, at temperatures higher than 60 °C and RH ≥ 40 % the conductivity started to decrease. The maximum ionic conductivity observed for compound **2.6$_{Tb}$** was 3.2×10^{-8} Scm^{-1} at 60 °C and 95% RH. From DVS data one would expect higher conductivity values, which may be explained by i) some degradation of the MOF bulk framework during ionic conductivity measurements, ii) the pelletization of the MOF which decreases the available surface area. The addition of compound **2.6$_{Tb}$** to the PSF membrane leads to a decrease of the conductivity when compared with pristine PSF membrane (2.50×10^{-4} Scm^{-1}, at room temperature and equilibrated with deionized water for 24 h),[175] but on the other side PSF seems to increase the stability of the MOF since the decrease of the conductivity with temperature was no longer observed.

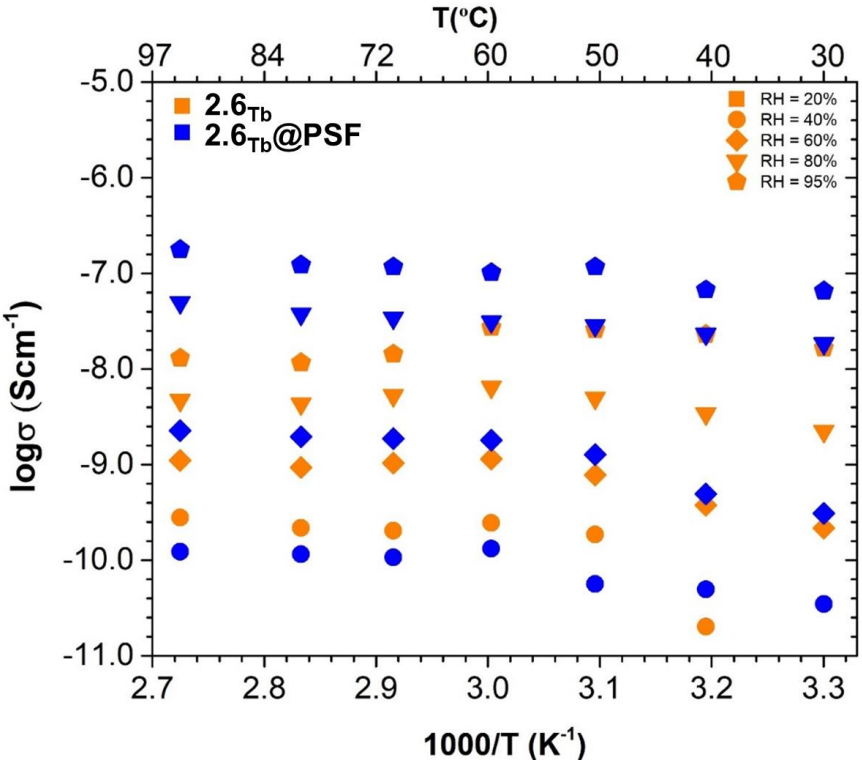

Figure 2.30. Arrhenius plots for the ionic conductivity of compound **2.6$_{Tb}$** and **2.6$_{Tb}$@PSF** membrane measured under variable RH and temperature.

2.11.5 Photoluminescent properties

In view of the promising applications that lanthanide centred MOFs can have derived by their characteristic narrow signals ranging from UV to near IR, we decided to study photoluminescent properties Tb^{3+} in PMMA supported MOF to compare with pristine MOF emission, recently reported in our group[176] as well as working in the approach to implement luminescent materials into devices. For this purpose, we carefully selected PMMA as polymeric membrane with the aim of avoiding any possible interreference between Tb-MOF and polymeric matrix intrinsic emission.

The excitation spectra of compound **2.6$_{Tb}$@PMMA** was recorded at 12 K features two broad UV bands maxima, ranging from 240 to *ca.* 310 nm and peaking at 254 and 288 nm. The pattern of this spectrum presents high resemblance with isostructural Y^{3+} and Tb^{3+} pristine MOF excitation spectra reported lately.[176] In all cases, ligand excitation lines rule excitation demonstrating an efficient energy transfer from ligand to Tb^{3+}.

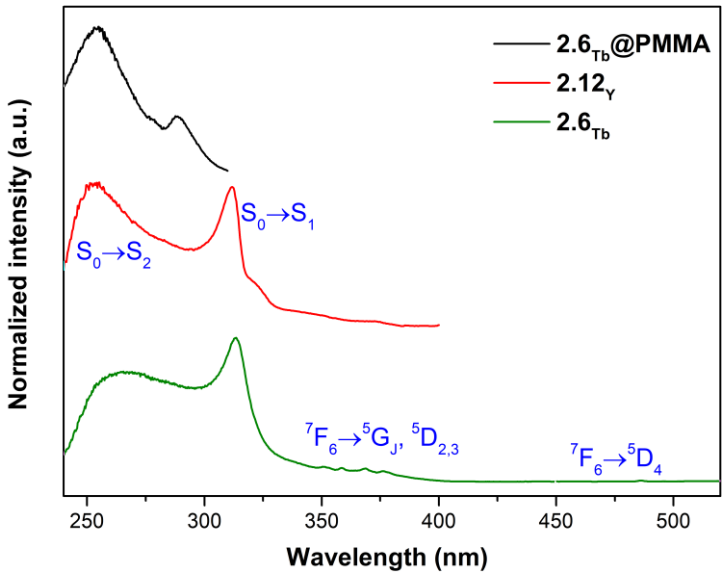

Figure 2.31. 12 K excitation spectra of **2.6$_{Tb}$@PMMA** (black; $\lambda_{Exc.}$ = 320 nm), isoestructural **2.12$_{Y}$** (red; $\lambda_{Exc.}$ = 410 nm)**, 2.6$_{Tb}$** pristine Tb^{3+} MOF (green; $\lambda_{Exc.}$ = 544 nm).

On its part, upon excitation at 315 nm emission spectrum of MOF loaded polymeric membrane display characteristic emission bands corresponding to Tb^{3+}. More concretely, the emission spectra of Tb^{3+} excited in the ligand recorded at ambient temperature (at 294 K) and at 12 K exhibited Tb^{3+} $^5D_4 \rightarrow {}^7F_{0\text{-}6}$ transition characteristic

sharp lines what comes in line with an efficient antenna effect where ligand is able to transfer energy from the ligand excited triplet state to the Tb^{3+} excited levels. As expected, decreasing temperature non-radiative relaxation pathways dimmish and increment emission intensity.

$^5D_4$ decay curves fixing the excitation at 315 nm and monitoring at 543.4 nm (Figure 2.32, inset) has been recorded at room temperature (294 K) and 12 K, in both cases, the spectrum is only properly fitted by a second order exponential function yielding two lifetimes with an averaged lifetime of $\tau_{294\,K} >= 0.350$ ms and $< \tau_{12\,K} >= 0.326$ ms. This evidence is in accordance with the presence of two Tb^{3+} distinct sites in the structure.

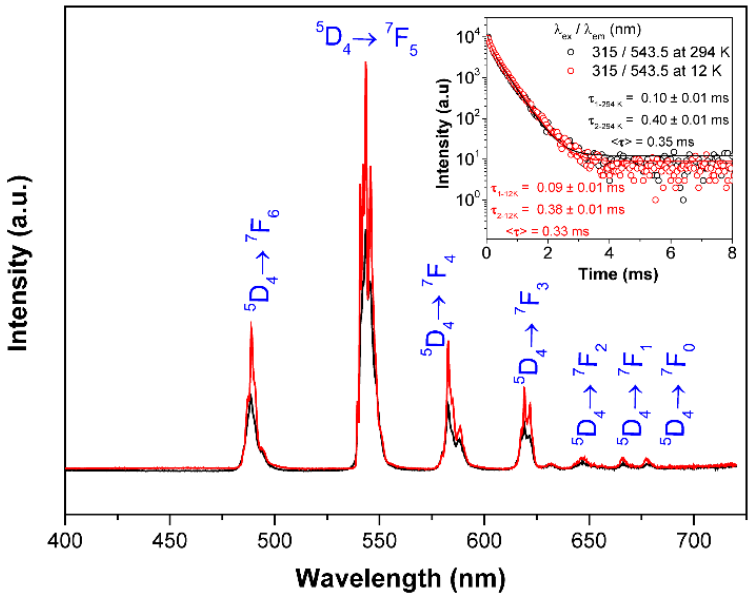

Figure 2.32. Emission spectra of Tb recorded at 294 K (black) and 12 K (red) monitoring the emission at 315 nm. Inset: $^5D_4$ decay curves of Tb acquired at 294 K (black) and 12 K (red) monitoring the Tb^{3+} emission at 544 nm. The excitation was fixed at 315 nm all measurements. The solid lines are the best fits using second order exponential decay function $y = -y_0 + A_1 \cdot \exp(-x/\tau_1) + A_2 \cdot \exp(-x/\tau_2)$ ($r^2 > 0.999$).

The time-resolved emission spectra recorded at 12 K excited at 290 nm allows to compare and differentiate ligand fluorescence ($S_1 \rightarrow S_0$ transition) from the phosphorescence ($T_1 \rightarrow S_0$). The broad band has a much faster time dependence of the $S_1 \rightarrow S_0$ transition compared to the transition $T_1 \rightarrow S_0$ since the former band is completely suppressed by a time delay of only 0.05 ms. The total suppression of the low- energy

$T_1 \rightarrow S_0$ ligand emission denotes a complete energy transfer from the triplet excited state to the Tb^{3+} excited levels. The zero-phonon energy level of the ligand phosphorescence emitting triplet states, is estimated at 390 nm (25641 cm^{-1}), is relatively close to Tb^{3+} first excited stated ($^5D_4$, 585 nm / 20619 cm^{-1}). These results confirm what was mentioned above, ligand triplet state is near Tb^{3+} first exited state (located at 485 nm corresponding to $^5D_4$) is energetically close to ligand triplet state and thus energy transfer occur from ligand triplet state to Tb^{3+} first excited estate and posteriorly from Tb^{3+} first excited state.

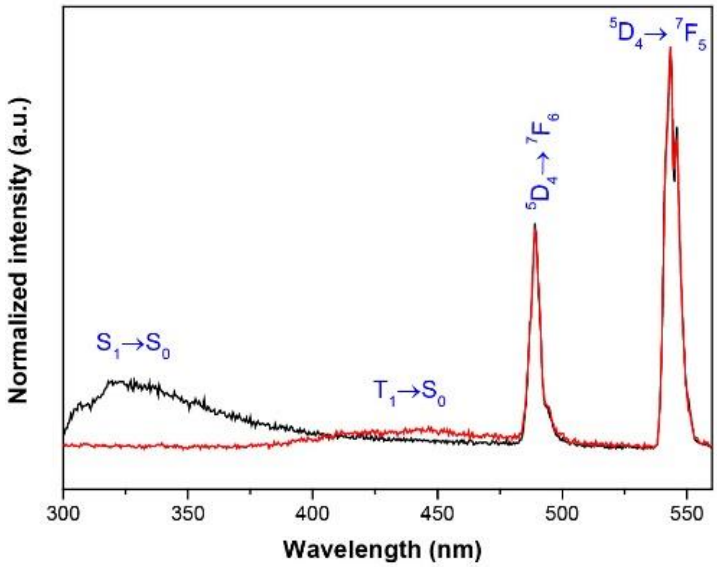

Figure 2.33. Time-resolved emission spectra showing the selected region of **2.6$_{Tb}$@PMMA** membrane recorded at measured with 290 nm excitation. Black line: initial delay of 0.01 ms and integration time of 0.1 ms; red line: initial delay of 0.05 ms and integration time of 5 ms. Time-resolved emission spectra were not corrected for detection and optical spectral response of the spectrofluorometer. The average lifetime was calculated according to the formula $< \tau >= (A_1\tau_1^2 + A_2\tau_2^2)/(A_1\tau_1 + A_2\tau_2)$.

2.12 Conclusions

Herein, we presented a non-complicated easy handling and cost-efficient method for the processing MOFs into pellets and membranes, exhibiting in both cases adequate resistance and mechanical stability in the final shaped material towards high humidity and temperature cycling conditions.

Membrane supported **2.6$_{Tb}$** material photoluminescent properties have been investigated proving that terbium based-MOF is able to keep its emissive properties subsequent processing into membranes; thus, this alternative is presented as an effective approach towards implementation into devices of luminescent Ln-MOFs. Additionally, as a prove of concept, processed materials (pellets and membranes) have been tested against high humidity and temperature conditions exhibiting relatively good resistance and performance under industrial operating conditions. Finally, motivated by the stability and resistance towards RH shaped materials had shown, water adsorption isotherms have been collected showing 18 % increment in mass at higher measured relative pressure, which corresponds to 95 %.

In this line, as a possible application, proton-conduction has been tested. As expected for water-mediated proton conducting MOFs proton conductivity increases with the augmentation of humidity obtaining maximum ionic conductivity value of 2.7×10^{-8} Scm^{-1} at 60 °C for **2.6$_{Tb}$**: Comparing with the results in bibliography which exhibit conductivity values close to 1.1×10^{-4} Scm^{-1} for purely 3D carboxylate-based MOFs[177] **2.6$_{Tb}$** exhibit relatively modest conductivity. From water adsorption (DSV) data, it would be expected higher conductivity values nonetheless, obtained results could be explained by MOF degradation in addition to diminishing available surface area by material processing.

2.13 References

1. Ouahab, L. *Multifunctional Molecular Materials*; Stanford P.; New York, 2012;

2. Pajuelo-Corral, O.; Zabala-Lekuona, A.; San Sebastian, E.; Rodríguez-Diéguez, A.; García, J.A.; Lezama, L.; Colacio, E.; Seco, J.M.; Cepeda, J. Modulating Magnetic and Photoluminescence Properties in 2-Aminonicotinate-Based Bifunctional Coordination Polymers by Merging 3d Metal Ions. *Chem. - A Eur. J.* **2020**, *26*, 13484–13498, doi:10.1002/chem.202002755.

3. Warrier, M.; Bhardwaj, U.; Bukkuru, S. Multifunctional Materials Related content Rays, Waves and Photons: Mirrors-through one darkly-Multi-scale Modeling of Radiation Damage: Large Scale Data Analysis. **2018**, doi:10.1088/2399-7532/aada7b.

4. Li, Y.-W.; Liu, S.-J.; Hu, T.-L.; Bu, X.-H. Doping cobalt into a [Zn_7] cluster-based MOF to tune magnetic behaviour and induce fluorescence signal mutation. *Dalton Trans.* **2014**, *43*, 11470–11473, doi:10.1039/C4DT00894D.

5. Caskey, S.R.; Matzger, A.J. Selective Metal Substitution for the Preparation of Heterobimetallic Microporous Coordination Polymers. *Inorg. Chem.* **2008**, *47*, 7942–7944, doi:10.1021/IC8007427.

6. Zhang, L.; Jiang, K.; Li, L.; Xia, Y.P.; Hu, T.L.; Yang, Y.; Cui, Y.; Li, B.; Chen, B.; Qian, G. Efficient separation of C_2H_2 from C_2H_2/CO_2 mixtures in an acid-base resistant metal-organic framework. *Chem. Commun.* **2018**, *54*, 4846–4849, doi:10.1039/c8cc02235f.

7. Fischer, M.; Hoffmann, F.; Fröba, M. New Microporous Materials for Acetylene Storage and C_2H_2/CO_2 Separation: Insights from Molecular Simulations. *ChemPhysChem* **2010**, *11*, 2220–2229, doi:10.1002/CPHC.201000126.

8. Li, P.; He, Y.; Zhao, Y.; Weng, L.; Wang, H.; Krishna, R.; Wu, H.; Zhou, W.; O'Keeffe, M.; Han, Y.; et al. A Rod-Packing Microporous Hydrogen-Bonded Organic Framework for Highly Selective Separation of C_2H_2/CO_2 at Room Temperature. *Angew. Chemie* **2015**, *127*, 584–587, doi:10.1002/ANGE.201410077.

9. Cui, X.; Chen, K.; Xing, H.; Yang, Q.; Krishna, R.; Bao, Z.; Wu, H.; Zhou, W.; Dong, X.; Han, Y.; et al. Pore chemistry and size control in hybrid porous materials for acetylene capture from ethylene. *Science (80-.).* **2016**, *353*, 141–144, doi:10.1126/SCIENCE.AAF2458.

10. Luo, F.; Yan, C.; Dang, L.; Krishna, R.; Zhou, W.; Wu, H.; Dong, X.; Han, Y.; Hu, T.-L.; O'Keeffe, M.; et al. UTSA-74: A MOF-74 Isomer with Two Accessible Binding Sites per Metal Center for Highly Selective Gas Separation. *J. Am. Chem. Soc.* **2016**, *138*, 5678–5684, doi:10.1021/JACS.6B02030.

11. Sessoli, R.; Gatteschi, D.; Caneschi, A.; Novak, M.A. Magnetic bistability in a metal-ion cluster. *Nat. 1993 3656442* **1993**, *365*, 141–143, doi:10.1038/365141a0.

12. Mínguez Espallargas, G.; Coronado, E. Magnetic functionalities in MOFs: from the framework to the pore. *Chem. Soc. Rev.* **2018**, *47*, 533–557, doi:10.1039/C7CS00653E.

13. Craig, G.A.; Murrie, M. 3d single-ion magnets. *Chem. Soc. Rev.* 2015, *44*, 2135–2147.

14. Bar, A.K.; Pichon, C.; Sutter, J.P. Magnetic anisotropy in two- to eight-coordinated transition–metal complexes: Recent developments in molecular magnetism. *Coord. Chem. Rev.* **2016**, *308*, 346–380, doi:10.1016/J.CCR.2015.06.013.

15. Murrie, M. Cobalt(II) single-molecule magnets. *Chem. Soc. Rev.* **2010**, *39*, 1986–1995, doi:10.1039/B913279C.

16. Villa-Pérez, C.; Oyarzabal, I.; Echeverría, G.A.; Valencia-Uribe, G.C.; Seco, J.M.; Soria, D.B. Single-Ion Magnets Based on Mononuclear Cobalt(II) Complexes with Sulfadiazine. *Eur. J. Inorg. Chem.* **2016**, *2016*, 4835–4841, doi:10.1002/EJIC.201600777.

17. Peng, Y.; Bodenstein, T.; Fink, K.; Mereacre, V.; Anson, C.E.; Powell, A.K. Magnetic anisotropy of a Co^{II} single ion magnet with distorted trigonal prismatic coordination: theory and experiment. *Phys. Chem. Chem. Phys* **2016**, *18*, 30135, doi:10.1039/c6cp03157a.

18. Pamei, M.; Puzari, A. Luminescent transition metal–organic frameworks: An emerging sensor for detecting biologically essential metal ions. *Nano-Structures and Nano-Objects* **2019**, *19*, 100364, doi:10.1016/j.nanoso.2019.100364.

19. Majee, P.; Singha, D.K.; Mondal, S.K.; Mahata, P. Effect of charge transfer and structural rigidity on divergent luminescence response of a metal organic framework towards different metal ions: luminescence lifetime decay experiments and DFT calculations. *Photochem. Photobiol. Sci.* **2019**, *18*, 1110–1121, doi:10.1039/C9PP00024K.

20. Cui, Y.; Yue, Y.; Qian, G.; Chen, B. Luminescent functional metal-organic frameworks. *Chem. Rev.* **2012**, *112*, 1126–1162, doi:10.1021/cr200101d.

21. García-Valdivia, A.A.; Pérez-Yáñez, S.; García, J.A.; Fernández, B.; Cepeda, J.; Rodríguez-Diéguez, A. Magnetic and Photoluminescent Sensors Based on Metal-Organic Frameworks Built up from 2-aminoisonicotinate. *Sci. Reports 2020 101* **2020**, *10*, 1–17, doi:10.1038/s41598-020-65687-6.

22. Llunell, M.; Casanova, D.; Cirera, J.; Bofill, J. M.; Alemany, P.; Alvarez, S.; Pinsky, M.; Avnir, D. Program for the Stereochemical Analysis of Molecular Fragments by Means of Continuous Shape Measures and Associated Tools. *SHAPE, v1.1b; Barcelona, Spain* **2005**, 1–35.

23. Blatov, V.A.; Shevchenko, A.P.; Proserpio, D.M. Applied topological analysis of crystal structures with the program package topospro. *Cryst. Growth Des.* **2014**, *14*, 3576–3586, doi:10.1021/cg500498k.

24. Singh Pannu, A.P.; Kapoor, P.; Hundal, G.; Kapoor, R.; Corbella, M.; Aliaga-Alcalde, N.; Singh Hundal, M. Magneto-structural studies of two new cobalt(II)-N, N-diisobutylisonicotinamide compounds: $[ColCl_2]_n$ and $[Co(L)_2(H_2O)_4][CoLBr_3]_2 \cdot 2H_2O$. *J. Chem. Soc. Dalt. Trans.* **2011**, *40*, 12560–12569, doi:10.1039/c1dt10991j.

25. Oyarzabal, I.; Ruiz, J.; Mota, A.J.; Rodríguez-Diéguez, A.; Seco, J.M.; Colacio, E. An experimental and theoretical magneto-structural study of polynuclear Ni^{II} complexes assembled from a versatile bis(salicylaldehyde)diamine polytopic ligand. *Dalton Trans.* **2015**, *44*, 6825–6838, doi:10.1039/C5DT00356C.

26. Peng, Y.; Bodenstein, T.; Fink, K.; Mereacre, V.; Anson, C.E.; Powell, A.K. Magnetic anisotropy of a Co^{II} single ion magnet with distorted trigonal prismatic coordination: theory and experiment. *Phys. Chem. Chem. Phys.* **2016**, *18*, 30135–30143, doi:10.1039/C6CP03157A.

27. Zhao, X.Q.; Wang, J.; Bao, D.X.; Xiang, S.; Liu, Y.J.; Li, Y.C. The ferromagnetic $[Ln_2Co_6]$ heterometallic complexes. *Dalton Trans.* **2017**, *46*, 2196–2203, doi:10.1039/c6dt04375e.

28. Zadrozny, J.M.; Telser, J.; Long, J.R. Slow magnetic relaxation in the tetrahedral cobalt(II) complexes $[Co(EPh)_4]^{2-}$ (Edouble bondO, S, Se). *Polyhedron* **2013**, *64*, 209–217,

doi:10.1016/J.POLY.2013.04.008.

29. Cole, K.S.; Cole, R.H. Dispersion and Absorption in Dielectrics I. Alternating Current Characteristics. *J. Chem. Phys.* **2004**, *9*, 341, doi:10.1063/1.1750906.

30. Zadrozny, J.M.; Long, J.R. Slow Magnetic Relaxation at Zero Field in the Tetrahedral Complex $[Co(SPh)_4]^{2-}$. *J. Am. Chem. Soc.* **2011**, *133*, 20732–20734, doi:10.1021/JA2100142.

31. Rechkemmer, Y.; Breitgoff, F.D.; van der Meer, M.; Atanasov, M.; Hakl, M.; Orlita, M.; Neugebauer, P.; Neese, F.; Sarkar, B.; van Slageren, J. A four-coordinate cobalt(II) single-ion magnet with coercivity and a very high energy barrier. *Nat. Commun. 2016 71* **2016**, *7*, 1–8, doi:10.1038/ncomms10467.

32. Novikov, V. V.; Pavlov, A.A.; Nelyubina, Y. V.; Boulon, M.-E.; Varzatskii, O.A.; Voloshin, Y.Z.; Winpenny, R.E.P. A Trigonal Prismatic Mononuclear Cobalt(II) Complex Showing Single-Molecule Magnet Behavior. *J. Am. Chem. Soc.* **2015**, *137*, 9792–9795, doi:10.1021/JACS.5B05739.

33. Yao, B.; Deng, Y.-F.; Li, T.; Xiong, J.; Wang, B.-W.; Zheng, Z.; Zhang, Y.-Z. Construction and Magnetic Study of a Trigonal-Prismatic Cobalt(II) Single-Ion Magnet. *Inorg. Chem.* **2018**, *57*, 14047–14051, doi:10.1021/acs.inorgchem.8b02692.

34. García-Valdivia, A.A.; Echenique-Errandonea, E.; Ramírez-Rodríguez, G.B.; Delgado-López, J.M.; Fernández, B.; Rojas, S.; Cepeda, J.; Rodríguez-Diéguez, A. Photoluminescent Coordination Polymers Based on Group 12 Metals and 1H-Indazole-6-Carboxylic Acid. **2021**, doi:10.3390/inorganics9030020.

35. Cepeda, J.; Rodríguez-Diéguez, A. Tuning the luminescence performance of metal-organic frameworks based on d^{10}metal ions: From an inherent versatile behaviour to their response to external stimuli. *CrystEngComm* **2016**, *18*, 8556–8573, doi:10.1039/c6ce01706a.

36. Barbieri, A.; Accorsi, G.; Armaroli, N. Luminescent complexes beyond the platinum group: The d^{10} avenue. *Chem. Commun.* **2008**, 2185–2193, doi:10.1039/b716650h.

37. Echenique-Errandonea, E.; Pérez, J.M.; Rojas, S.; Cepeda, J.; Seco, J.M.; Fernández, I.; Rodríguez-Diéguez, A. A novel yttrium-based metal-organic framework for the efficient solvent-free catalytic synthesis of cyanohydrin silyl ethers. *Dalton Trans.* **2021**, *50*, 11720–11724, doi:10.1039/d1dt01953h.

38. O'Keeffe, M.; Yaghi, O.M. Deconstructing the Crystal Structures of Metal–Organic Frameworks and Related Materials into Their Underlying Nets. *Chem. Rev.* **2011**, *112*, 675–702, doi:10.1021/CR200205J.

39. Aniruddha, R.; Sreedhar, I.; Reddy, B.M. MOFs in carbon capture-past, present and future. *J. CO_2 Util.* 2020, *42*, 101297.

40. Zhang, Z.; Yao, Z.Z.; Xiang, S.; Chen, B. Perspective of microporous metal-organic frameworks for CO_2 capture and separation. *Energy Environ. Sci.* **2014**, *7*, 2868–2899, doi:10.1039/c4ee00143e.

41. Roy, S.; Chakraborty, A.; Maji, T.K. Lanthanide-organic frameworks for gas storage and as magneto-luminescent materials. *Coord. Chem. Rev.* **2014**, *273–274*, 139–164, doi:10.1016/j.ccr.2014.03.035.

42. Black, C.A.; Costa, J.S.; Fu, W.T.; Massera, C.; Roubeau, O.; Teat, S.J.; Aromí, G.;

Gamez, P.; Reedijk, J. 3-D Lanthanide Metal-Organic Frameworks: Structure, Photoluminescence, and Magnetism. *Inorg. Chem.* **2009**, *48*, 1062–1068, doi:10.1021/IC8017826.

43. Li, B.; Dong, J.-P.; Zhou, Z.; Wang, R.; Wang, L.-Y.; Zang, S.-Q. Robust lanthanide metal–organic frameworks with “all-in-one” multifunction: efficient gas adsorption and separation, tunable light emission and luminescence sensing. *J. Mater. Chem. C* **2021**, *9*, 3429–3439, doi:10.1039/D0TC05707J.

44. Rinehart, J.D.; Long, J.R. Exploiting single-ion anisotropy in the design of f-element single-molecule magnets. *Chem. Sci.* **2011**, *2*, 2078–2085, doi:10.1039/c1sc00513h.

45. Bünzli, J.C.G.; Eliseeva, S. V. Intriguing aspects of lanthanide luminescence. *Chem. Sci.* **2013**, *4*, 1939–1949, doi:10.1039/c3sc22126a.

46. Haldar, R.; Bhattacharyya, S.; Maji, T.K. Luminescent metal–organic frameworks and their potential applications. *J. Chem. Sci.* **2020**, *132*, 1–25, doi:10.1007/s12039-020-01797-y.

47. Ananias, D.; Almeida Paz, F.A.; Carlos, L.D.; Rocha, J. Near-Infrared Ratiometric Luminescent Thermometer Based on a New Lanthanide Silicate. *Chem. - A Eur. J.* **2018**, *24*, 11926–11935, doi:10.1002/chem.201802219.

48. Trannoy, V.; Carneiro Neto, A.N.; Brites, C.D.S.; Carlos, L.D.; Serier-Brault, H. Engineering of Mixed Eu^{3+}/Tb^{3+} Metal-Organic Frameworks Luminescent Thermometers with Tunable Sensitivity. *Adv. Opt. Mater.* **2021**, *9*, doi:10.1002/ADOM.202001938.

49. Cui, Y.; Xu, H.; Yue, Y.; Guo, Z.; Yu, J.; Chen, Z.; Gao, J.; Yang, Y.; Qian, G.; Chen, B. A luminescent mixed-lanthanide metal-organic framework thermometer. *J. Am. Chem. Soc.* **2012**, *134*, 3979–3982, doi:10.1021/ja2108036.

50. Liu, X.; Akerboom, S.; Jong, M. de; Mutikainen, I.; Tanase, S.; Meijerink, A.; Bouwman, E. Mixed-Lanthanoid Metal–Organic Framework for Ratiometric Cryogenic Temperature Sensing. *Inorg. Chem.* **2015**, *54*, 11323–11329, doi:10.1021/ACS.INORGCHEM.5B01924.

51. Wang, Z.; Ananias, D.; Carné-Sánchez, A.; Brites, C.D.S.; Imaz, I.; Maspoch, D.; Rocha, J.; Carlos, L.D. Lanthanide-organic framework nanothermometers prepared by spray-drying. *Adv. Funct. Mater.* **2015**, *25*, 2824–2830, doi:10.1002/adfm.201500518.

52. Ren, M.; Brites, C.D.S.; Bao, S.-S.; Ferreira, R.A.S.; Zheng, L.-M.; Carlos, L.D. A cryogenic luminescent ratiometric thermometer based on a lanthanide phosphonate dimer. *J. Mater. Chem. C* **2015**, *3*, 8480–8484, doi:10.1039/C5TC01468A.

53. N’Dala-Louika, I.; Ananias, D.; Latouche, C.; Dessapt, R.; Carlos, L.D.; Serier-Brault, H. Ratiometric mixed Eu-Tb metal-organic framework as a new cryogenic luminescent thermometer. *J. Mater. Chem. C* **2017**, *5*, 10933–10937, doi:10.1039/c7tc03223d.

54. Brites, C.D.S.; Lima, P.P.; Silva, N.J.O.; Millán, A.; Amaral, V.S.; Palacio, F.; Carlos, L.D. Thermometry at the nanoscale. *Nanoscale* 2012, *4*, 4799–4829.

55. Kaczmarek, A.M.; Liu, J.; Laforce, B.; Vincze, L.; Hecke, K. Van; Deun, R. Van Cryogenic luminescent thermometers based on multinuclear Eu^{3+}/Tb^{3+} mixed lanthanide polyoxometalates. *Dalton Trans.* **2017**, *46*, 5781–5785, doi:10.1039/C7DT01058C.

56. Chen, C.; Lee, Y.R.; Ahn, W.S. CO_2 adsorption over metal-organic frameworks: A mini review. *J. Nanosci. Nanotechnol.* **2016**, *16*, 4291–4301, doi:10.1166/jnn.2016.10971.

57. Saha, S.; Chandra, S.; Garai, B.; Banerjee, R. Carbon dioxide capture by metal organic frameworks. *Indian J. Chem. - Sect. A Inorganic, Phys. Theor. Anal. Chem.* **2012**, *51*, 1223–1230.

58. Li, J.-R.; Kuppler, R.J.; Zhou, H.-C. Selective gas adsorption and separation in metal–organic frameworks. *Chem. Soc. Rev.* **2009**, *38*, 1477–1504, doi:10.1039/B802426J.

59. Yadav, A.; Kanoo, P. Metal-Organic Frameworks as Platform for Lewis-Acid-Catalyzed Organic Transformations. *Chem. - An Asian J.* **2019**, *14*, 3531–3551, doi:10.1002/asia.201900876.

60. Lee, J.; Farha, O.K.; Roberts, J.; Scheidt, K.A.; Nguyen, S.T.; Hupp, J.T. Metal-organic framework materials as catalysts. *Chem. Soc. Rev.* **2009**, *38*, 1450–1459, doi:10.1039/b807080f.

61. Bavykina, A.; Kolobov, N.; Khan, I.S.; Bau, J.A.; Ramirez, A.; Gascon, J. Metal–Organic Frameworks in Heterogeneous Catalysis: Recent Progress, New Trends, and Future Perspectives. *Chem. Rev.* **2020**, *120*, 8468–8535, doi:10.1021/ACS.CHEMREV.9B00685.

62. Alzamly, A.; Bakiro, M.; Hussein Ahmed, S.; Alnaqbi, M.A.; Nguyen, H.L. Rare-earth metal–organic frameworks as advanced catalytic platforms for organic synthesis. *Coord. Chem. Rev.* **2020**, *425*, 213543, doi:10.1016/j.ccr.2020.213543.

63. Saraci, F.; Quezada-Novoa, V.; Donnarumma, P.R.; Howarth, A.J. Rare-earth metal-organic frameworks: From structure to applications. *Chem. Soc. Rev.* 2020, *49*, 7949–7977.

64. Seitz, M.; Oliver, A.G.; Raymond, K.N. The lanthanide contraction revisited. *J. Am. Chem. Soc.* **2007**, *129*, 11153–11160, doi:10.1021/ja072750f.

65. Kikukawa, Y.; Suzuki, K.; Sugawa, M.; Hirano, T.; Kamata, K.; Yamaguchi, K.; Mizuno, N. Cyanosilylation of carbonyl compounds with trimethylsilyl cyanide catalyzed by an yttrium-pillared silicotungstate dimer. *Angew. Chemie - Int. Ed.* **2012**, *51*, 3686–3690, doi:10.1002/anie.201200486.

66. Gregory, R.J.H. Cyanohydrins in Nature and the Laboratory: Biology, Preparations, and Synthetic Applications. *Chem. Rev.* **1999**, *99*, 3649–3682, doi:10.1021/cr9902906.

67. Gawronski, J.; Wascinska, N.; Gajewy, J. Recent Progress in Lewis Base Activation and Control of Stereoselectivity in the Additions of Trimethylsilyl Nucleophiles. *Chem. Rev.* **2008**, *108*, 5227–5252, doi:10.1021/CR800421C.

68. Evans, D.A.; Carroll, G.L.; Truesdale, L.K. Synthetic Applications of Trimethylsilyl Cyanide. An Efficient Synthesis of β-Aminomethyl Alcohols. *J. Org. Chem.* **1974**, *39*, 914–917, doi:10.1021/jo00921a012.

69. Anastas, P. T.; Warner, J.C. *Green Chemistry: Theory and Practice*; Oxford University Press: New York, 1998;

70. Tiago, G.A.O.; Mahmudov, K.T.; F, M.; Guedes, C.; Ribeiro, A.P.C.; Branco, C.; Zubkov, F.I.; Pombeiro, A.J.L. in Conventional and in Ionic Liquid Media. *Catalysts* **2019**, *9*, 284–300, doi:10.3390/catal9030284.

71. Sarkar, A.; Santra, S.; Kundu, S.K.; Hajra, A.; Zyryanov, G. V.; Chupakhin, O.N.; Charushin, V.N.; Majee, A. A decade update on solvent and catalyst-free neat organic reactions: A step forward towards sustainability. *Green Chem.* **2016**, *18*, 4475–4525,

doi:10.1039/c6gc01279e.

72. Constable, D.J.C.; Curzons, D.; Cunningham, V.L. Metrics to ‘ green ’ chemistry — which are the best ? Green Context. **2002**, 521–527, doi:10.1039/b206169b.

73. M., T.B. The Atom Economy - A search for synthetic efficiency. *Science (80-.).* **1991**, *254*, 1471–1477.

74. Dvries, R.F.; De La Peña-Oshea, V.A.; Snejko, N.; Iglesias, M.; Gutiérrez-Puebla, E.; Monge, M.Á. Insight into the correlation between net topology and ligand coordination mode in new lanthanide MOFs heterogeneous catalysts: A theoretical and experimental approach. *Cryst. Growth Des.* **2012**, *12*, 5535–5545, doi:10.1021/cg301096d.

75. Dvries, R.F.; Iglesias, M.; Snejko, N.; Gutiérrez-Puebla, E.; Monge, M.A. Lanthanide metal-organic frameworks: Searching for efficient solvent-free catalysts. *Inorg. Chem.* **2012**, *51*, 11349–11355, doi:10.1021/ic300816r.

76. Dvries, R.F.; Snejko, N.; Iglesias, M.; Gutiérrez-Puebla, E.; Monge, M.A. Ln-MOF pseudo-merohedral twinned crystalline family as solvent-free heterogeneous catalysts. *Cryst. Growth Des.* **2014**, *14*, 2516–2521, doi:10.1021/cg5002336.

77. Zhang, Z.; Chen, J.; Bao, Z.; Chang, G.; Xing, H.; Ren, Q. Insight into the catalytic properties and applications of metal-organic frameworks in the cyanosilylation of aldehydes. *RSC Adv.* **2015**, *5*, 79355–79360, doi:10.1039/c5ra13102b.

78. Saravanan, P.; Vijaya Ananad, R.; Singh, V.K. HR • H. *Tetrahedron Lett.* **1998**, *39*, 3823–3824.

79. De, S.K.; Gibbs, R.A. Vanadyl triflate as an efficient and recyclable catalyst for trimethylsilyl cyanide addition to carbonyl compounds. *J. Mol. Catal. A Chem.* **2005**, *232*, 123–125, doi:10.1016/j.molcata.2005.01.034.

80. Tian, S.K.; Deng, L. A highly enantioselective chiral Lewis base-catalyzed asymmetric cyanation of ketones [2]. *J. Am. Chem. Soc.* **2001**, *123*, 6195–6196, doi:10.1021/ja010690m.

81. Denmark, S.E.; Chung, W. Lewis Base Catalyzed Addition of Trimethylsilyl Cyanide to Aldehydes Table of Contents. *J. Org. Chem.* **2006**, *61801*, 4002–4005.

82. Wang, X.; Tian, S.K. Catalytic cyanosilylation of ketones with simple phosphonium salt. *Tetrahedron Lett.* **2007**, *48*, 6010–6013, doi:10.1016/j.tetlet.2007.06.132.

83. Kurono, N.; Yamaguchi, M.; Suzuki, K.; Ohkuma, T. Lithium chloride: An active and simple catalyst for cyanosilylation of aldehydes and ketones. *J. Org. Chem.* **2005**, *70*, 6530–6532, doi:10.1021/jo050791t.

84. Suzuki, Y.; Bakar, M.D., A.; Muramatsu, K.; Sato, M. Cyanosilylation of aldehydes catalyzed by N-heterocyclic carbenes. *Tetrahedron* **2006**, *62*, 4227–4231, doi:10.1016/j.tet.2006.01.101.

85. Wang, W.; Luo, M.; Yao, W.; Ma, M.; Pullarkat, S.A.; Xu, L.; Leung, P.H. Catalyst-free and Solvent-free Cyanosilylation and Knoevenagel Condensation of Aldehydes. *ACS Sustain. Chem. Eng.* **2019**, *7*, 1718–1722, doi:10.1021/acssuschemeng.8b05486.

86. Ferlin, F.; Valentini, F.; Brufani, G.; Lanari, D.; Vaccaro, L. Waste-Minimized Cyanosilylation of Carbonyls Using Fluoride on Polymeric Ionic Tags in Batch and under Continuous Flow Conditions. *ACS Sustain. Chem. Eng.* **2021**, *9*, 5740–5749,

doi:10.1021/ACSSUSCHEMENG.1C01138/SUPPL_FILE/SC1C01138_SI_001.PDF.

87. Fujita, M.; Washizu, S.; Ogura, K.; Kwon, Y.J. Preparation, Clathration Ability, and Catalysis of a Two-Dimensional Square Network Material Composed of Cadmium(II) and 4, 4'-Bipyridine. *J. Am. Chem. Soc.* **1994**, *116*, 1151–1152.

88. Hu, Z.; Zhao, D. Metal–organic frameworks with Lewis acidity: synthesis, characterization, and catalytic applications. *CrystEngComm* **2017**, *19*, 4066–4081, doi:10.1039/C6CE02660E.

89. Ohmori, O.; Fujita, M. Heterogeneous catalysis of a coordination network: cyanosilylation of imines catalyzed by a Cd(II)-(4,4′-bipyridine) square grid complex. *Chem. Commun.* **2004**, *4*, 1586–1587, doi:10.1039/B406114B.

90. Henschel, A.; Gedrich, K.; Kraehnert, R.; Kaskel, S. Catalytic properties of MIL-101. *Chem. Commun.* **2008**, 4192–4194, doi:10.1039/b718371b.

91. Iwanami, K.; Choi, J.C.; Lu, B.; Sakakura, T.; Yasuda, H. Remarkable acceleration of cyanosilylation by the mesoporous Al-MCM-41 catalyst. *Chem. Commun.* **2008**, *0*, 1002–1004, doi:10.1039/b718462j.

92. S, H.; M, D.; K, T.; JR, L. Size-selective Lewis acid catalysis in a microporous metal-organic framework with exposed Mn^{2+} coordination sites. *J. Am. Chem. Soc.* **2008**, *130*, 5854–5855, doi:10.1021/JA800669J.

93. Dai, X.-P.P.; Hou, Y.-Z.Z.; Guan, J.; Liu, L.-B. Bin; Wang, H.; Zhou, L.-B.B. A Highly Porous Co-MOF for Cyanosilylation Reaction and Inhibition on P. gingivalis Growth and rgp and kgp Expression for Periodontal Treatment. *J. Clust. Sci. 31*, 1077–1085.

94. Zhang, F.; Zhang, J.; Zhang, B.; Zheng, L.; Cheng, X.; Wan, Q.; Han, B.; Zhang, J. Improved catalytic performance of Co-MOF-74 by nanostructure construction. *Green Chem.* **2020**, *22*, 5995–6000, doi:10.1039/D0GC02048F.

95. Schlichte, K.; Kratzke, T.; Kaskel, S. Improved synthesis, thermal stability and catalytic properties of the metal-organic framework compound $Cu_3(BTC)_2$. *Microporous Mesoporous Mater.* **2004**, *73*, 81–88, doi:10.1016/j.micromeso.2003.12.027.

96. Zhu, H.L.; Zhang, J.; Yao, F.-Y.Y.; Zheng, Y.Q.-Q. Copper(II), zinc(II), and cadmium(II) coordination polymers with 2-methylglutarato and 4,4′-dipyridyldisulfide. *Russ. J. Coord. Chem.* **2014**, *40*, 54–62, doi:10.1134/S1070328414010114.

97. Pagis, C.; Ferbinteanu, M.; Rothenberg, G.; Tanase, S. Lanthanide-Based Metal Organic Frameworks: Synthetic Strategies and Catalytic Applications. *ACS Catal.* **2016**, *6*, 6063–6072, doi:10.1021/acscatal.6b01935.

98. Wu, P.; Wang, J.; Li, Y.; He, C.; Xie, Z.; Duan, C. Luminescent Sensing and Catalytic Performances of a Multifunctional Lanthanide-Organic Framework Comprising a Triphenylamine Moiety. *Adv. Funct. Mater.* **2011**, *21*, 2788–2794, doi:10.1002/adfm.201100115.

99. An, H.; Wang, L.; Hu, Y.; Fei, F. Temperature-induced racemic compounds and chiral conglomerates based on polyoxometalates and lanthanides: Syntheses, structures and catalytic properties. *CrystEngComm* **2015**, *17*, 1531–1540, doi:10.1039/c4ce01802h.

100. Fei, F.; An, H.; Meng, C.; Wang, L.; Wang, H. Lanthanide-supported molybdenum-vanadium oxide clusters: syntheses, structures and catalytic properties. **2015**, 18796–18805, doi:10.1039/c4ra16237d.

101. Wang, X.; Zhang, L.; Yang, J.; Liu, F.; Dai, F.; Wang, R.; Sun, D. Lanthanide metal-organic frameworks containing a novel flexible ligand for luminescence sensing of small organic molecules and selective adsorption. *J. Mater. Chem. A* **2015**, *3*, 12777–12785, doi:10.1039/c5ta00061k.

102. Evans, O.R.; Ngo, H.L.; Lin, W. Chiral porous solids based on lamellar lanthanide phosphonates. *J. Am. Chem. Soc.* **2001**, *123*, 10395–10396, doi:10.1021/ja0163772.

103. Zhu, C.; Xia, Q.; Chen, X.; Liu, Y.; Du, X.; Cui, Y. Chiral metal−Organic framework as a platform for cooperative catalysis in asymmetric cyanosilylation of aldehydes. *ACS Catal.* **2016**, *6*, 7590–7596, doi:10.1021/acscatal.6b02359.

104. Gomez, G.E.; Kaczmarek, A.M.; Van Deun, R.; Brusau, E. V.; Narda, G.E.; Vega, D.; Iglesias, M.; Gutierrez-Puebla, E.; Monge, M.Á. Photoluminescence, Unconventional-Range Temperature Sensing, and Efficient Catalytic Activities of Lanthanide Metal-Organic Frameworks. *Eur. J. Inorg. Chem.* **2016**, *2016*, 1577–1588, doi:10.1002/ejic.201501402.

105. Gomez, G.E.; Brusau, E. V.; Sacanell, J.; Soler Illia, G.J.A.A.; Narda, G.E. Insight into the Metal Content–Structure–Property Relationship in Lanthanide Metal–Organic Frameworks: Optical Studies, Magnetism, and Catalytic Performance. *Eur. J. Inorg. Chem.* **2018**, *2018*, 2452–2460, doi:10.1002/ejic.201701474.

106. Batista, P.K.; Alves, D.J.M.; Rodrigues, M.O.; De Sá, G.F.; Junior, S.A.; Vale, J.A. Tuning the catalytic activity of lanthanide-organic framework for the cyanosilylation of aldehydes. *J. Mol. Catal. A Chem.* **2013**, *379*, 68–71, doi:10.1016/j.molcata.2013.07.016.

107. Wu, X.; Lin, Z.; He, C.; Duan, C. Catalytic performance of lanthanide molecular solids containing well-modified metal-organic octahedra. *New J. Chem.* **2012**, *36*, 161–167, doi:10.1039/c1nj20736a.

108. Vries, R.F.D.; Iglesias, M.; Snejko, N.; Gutie, E.; Monge, M.A. Lanthanide Metal − Organic Frameworks: Searching for Efficient Solvent-Free Catalysts. *Inorg Chem* **2012**, *51*, 11349–11355.

109. Gustafsson, M.; Bartoszewicz, A.; Martiín-Matute, B.; Sun, J.; Grins, J.; Zhao, T.; Li, Z.; Zhu, G.; Zou, X. A family of highly stable lanthanide metal-organic frameworks: Structural evolution and catalytic activity. *Chem. Mater.* **2010**, *22*, 3316–3322, doi:10.1021/cm100503q.

110. Karmakar, A.; Rúbio, G.M.D.M.; Paul, A.; Guedes da Silva, M.F.C.; Mahmudov, K.T.; Guseinov, F.I.; Carabineiro, S.A.C.; Pombeiro, A.J.L. Lanthanide metal organic frameworks based on dicarboxyl-functionalized arylhydrazone of barbituric acid: Syntheses, structures, luminescence and catalytic cyanosilylation of aldehydes. *Dalton Trans.* **2017**, *46*, 8649–8657, doi:10.1039/c7dt01056g.

111. He, H.; Ma, H.; Sun, D.; Zhang, L.; Wang, R.; Sun, D. Porous lanthanide-organic frameworks: Control over interpenetration, gas adsorption, and catalyst properties. *Cryst. Growth Des.* **2013**, *13*, 3154–3161, doi:10.1021/cg400531j.

112. Spek, A.L. Structure validation in chemical crystallography. *Acta Crystallogr. Sect. D Biol. Crystallogr.* **2009**, *65*, 148–155, doi:10.1107/S090744490804362X.

113. Lin, P.-H.; Sun, W.-B.; Tian, Y.-M.; Yan, P.-F.; Ungur, L.; Chibotaru, L.F.; Murugesu, M. Ytterbium can relax slowly too: a field-induced Yb2 single-molecule magnet. *Dalton Trans.* **2012**, *41*, 12349–12352, doi:10.1039/C2DT31677C.

114. Liu, T.-Q.; Yan, P.-F.; Luan, F.; Li, Y.-X.; Sun, J.-W.; Chen, C.; Yang, F.; Chen, H.; Zou, X.-Y.; Li, G.-M. Near-IR Luminescence and Field-Induced Single Molecule Magnet of Four Salen-type Ytterbium Complexes. *Inorg. Chem* **2015**, *54*, 221–228, doi:10.1021/ic502194d.

115. Li, X.L.; Li, F.C.; Zhang, X.L.; Liu, Y.F.; Wang, A.L.; Tian, J.F.; Xiao, H.P. Synthesis, crystal structures and magnetic properties of two tetranuclear lanthanide-hydroxo cubane clusters. *Synth. Met.* **2015**, *209*, 220–224, doi:10.1016/J.SYNTHMET.2015.07.035.

116. Langley, S.K.; Wielechowski, D.P.; Vieru, V.; Chilton, N.F.; Moubaraki, B.; Chibotaru, L.F.; Murray, K.S. Modulation of slow magnetic relaxation by tuning magnetic exchange in {Cr2Dy2} single molecule magnets. *Chem. Sci.* **2014**, *5*, 3246–3256, doi:10.1039/c4sc01239a.

117. Chilton, N.F.; Collison, D.; McInnes, E.J.L.; Winpenny, R.E.P.; Soncini, A. An electrostatic model for the determination of magnetic anisotropy in dysprosium complexes. *Nat. Commun. 2013 41* **2013**, *4*, 1–7, doi:10.1038/ncomms3551.

118. Pointillart, F.; Cador, O.; Le Guennic, B.; Ouahab, L. Uncommon lanthanide ions in purely 4f Single Molecule Magnets. *Coord. Chem. Rev.* **2017**, *346*, 150–175, doi:10.1016/J.CCR.2016.12.017.

119. Wang, J.; Zakrzewski, J.J.; Heczko, M.; Zychowicz, M.; Nakagawa, K.; Nakabayashi, K.; Sieklucka, B.; Chorazy, S.; Ohkoshi, S.I. Proton Conductive Luminescent Thermometer Based on Near-Infrared Emissive {YbCo2} Molecular Nanomagnets. *J. Am. Chem. Soc.* **2020**, *142*, 3970–3979, doi:10.1021/JACS.9B13147/SUPPL_FILE/JA9B13147_SI_003.CIF.

120. Gavrikov, A. V.; Efimov, N.N.; Ilyukhin, A.B.; Dobrokhotova, Z. V.; Novotortsev, V.M. Yb^{3+} can be much better than Dy^{3+}: SMM properties and controllable self-assembly of novel lanthanide 3,5-dinitrobenzoate-acetylacetonate complexes. *Dalton Trans.* **2018**, *47*, 6199–6209, doi:10.1039/c8dt00624e.

121. Guégan, F.; Jung, J.; Le Guennic, B.; Riobé, F.; Maury, O.; Gillon, B.; Jacquot, J.F.; Guyot, Y.; Morell, C.; Luneau, D. Evidencing under-barrier phenomena in a Yb(III) SMM: A joint luminescence/neutron diffraction/SQUID study. *Inorg. Chem. Front.* **2019**, *6*, 3152–3157, doi:10.1039/c9qi00726a.

122. Fondo, M.; Corredoira-Vázquez, J.; García-Deibe, A.M.; Sanmartín-Matalobos, J.; Amoza, M.; Botas, A.M.P.; Ferreira, R.A.S.; Carlos, L.D.; Colacio, E. Field-induced slow magnetic relaxation and luminescence thermometry in a mononuclear ytterbium complex. *Inorg. Chem. Front.* **2020**, *7*, 3019–3029, doi:10.1039/D0QI00637H.

123. Gendron, F.; Pietro, S. Di; Galan, L.A.; Riobé, F.; Placide, V.; Guy, L.; Zinna, F.; Di Bari, L.; Bensalah-Ledoux, A.; Guyot, Y.; et al. Luminescence, Chiroptical, Magnetic and Ab-initio Crystal-Field Characterizations of an Enantiopure Helicoidal Yb(III) Complex: The van Vleck Rennaissance. *ChemRxiv* **2020**, 1–19.

124. Gonzalez, J.F.; Douib, H.; Guennic, B. Le; Pointillart, F.; Cador, O. Ytterbium-Centered Isotopic Enrichment Leading to a Zero-Field Single-Molecule Magnet. *Inorg. Chem.* **2021**, *60*, 540–544, doi:10.1021/ACS.INORGCHEM.0C02652.

125. Wang, M.M.; Wei, X.Q.; Zhu, J.L.; Wang, J.; Wang, M.; Liu, L.Z.; Sun, T.M.; Tang, Y.F. An infrequent luminescent Yb(III)−based single−molecule magnet. *J. Solid State Chem.* **2020**, *283*, 121172, doi:10.1016/J.JSSC.2020.121172.

126. Calahorro, A.J.; Oyarzabal, I.; Fernández, B.; Seco, J.M.; Tian, T.; Fairen-Jimenez, D.;

Colacio, E.; Rodríguez-Diéguez, A. Rare earth anthracenedicarboxylate metal–organic frameworks: slow relaxation of magnetization of Nd3+, Gd3+, Dy3+, Er3+ and Yb3+ based materials. *Dalton Trans.* **2015**, *45*, 591–598, doi:10.1039/C5DT03946K.

127. Su, Q.; Sun, L.; Hemmer, E.; Jang, H.S. *Editorial: Women in Lanthanide-Based Luminescence Research: From Basic Research to Applications*; 2021; Vol. 9; ISBN 9782889667727.

128. Latva, M.; Takalob, H.; Mukkala, V.M.; Matachescu, C.; Rodríguez-Ubis, J.C.; Kankare, J. Correlation between the lowest triplet state energy level of the ligand and lanthanide(III) luminescence quantum yield. *J. Lumin.* **1997**, *75*, 149–169, doi:10.1016/S0022-2313(97)00113-0.

129. Marin, R.; Millan, N.C.; Kelly, L.; Liu, N.; Rodrigues, E.M.; Murugesu, M.; Hemmer, E. Luminescence thermometry using sprayed films of metal complexes. *J. Mater. Chem. C* **2022**, *10*, 1767–1775, doi:10.1039/D1TC05484H.

130. Chamberlain, T.W.; Perrella, R. V.; Oliveira, T.M.; Filho, P.C. de S.; Walton, R.I. A Highly Stable Yttrium Organic Framework as a Host for Optical Thermometry and D_2O Detection. *Chem. – A Eur. J.* **2022**, *28*, e202200410, doi:10.1002/CHEM.202200410.

131. Einkauf, J.D.; Rue, K.L.; Ten Hoeve, H.A.; de Lill, D.T. Enhancing luminescence in lanthanide coordination polymers through dilution of emissive centers. *J. Lumin.* **2018**, *197*, 412–417, doi:10.1016/J.JLUMIN.2018.01.045.

132. Brites, C.D.S.; Millán, A.; Carlos, L.D. Lanthanides in Luminescent Thermometry. *Handb. Phys. Chem. Rare Earths* **2016**, *49*, 339–427, doi:10.1016/bs.hpcre.2016.03.005.

133. Sarkisov, L.; Harrison, A. Computational structure characterisation tools in application to ordered and disordered porous materials. *Mol. Simul.* **2011**, *37*, 1248–1257, doi:10.1080/08927022.2011.592832.

134. Herdes, C.; Sarkisov, L. Computer Simulation of Volatile Organic Compound Adsorption in Atomistic Models of Molecularly Imprinted Polymers. *Langmuir* **2009**, *25*, 5352–5359, doi:10.1021/LA804168B.

135. Ghanbari, T.; Abnisa, F.; Wan Daud, W.M.A. A review on production of metal organic frameworks (MOF) for CO_2 adsorption. *Sci. Total Environ.* **2020**, *707*, 135090, doi:10.1016/J.SCITOTENV.2019.135090.

136. Ding, M.; Flaig, R.W.; Jiang, H.L.; Yaghi, O.M. Carbon capture and conversion using metal–organic frameworks and MOF-based materials. *Chem. Soc. Rev.* **2019**, *48*, 2783–2828, doi:10.1039/C8CS00829A.

137. Zhang, G.; Wei, G.; Liu, Z.; Oliver, S.R.J.; Fei, H. A Robust Sulfonate-Based Metal-Organic Framework with Permanent Porosity for Efficient CO_2 Capture and Conversion. *Chem. Mater.* **2016**, *28*, 6276–6281, doi:10.1021/ACS.CHEMMATER.6B02511/SUPPL_FILE/CM6B02511_SI_002.CIF.

138. Bae, Y.-S.; Snurr, R.Q. Carbon Dioxide Capture Development and Evaluation of Porous Materials for Carbon Dioxide Separation and Capture., doi:10.1002/anie.201101891.

139. Chowdhury, P.; Bikkina, C.; Gumma, S. Gas adsorption properties of the chromium-based metal organic framework MIL-101. *J. Phys. Chem. C* **2009**, *113*, 6616–6621, doi:10.1021/jp811418r.

140. Manna, K.; Zhang, T.; Lin, W. Postsynthetic metalation of bipyridyl-containing metal-

organic frameworks for highly efficient catalytic organic transformations. *J. Am. Chem. Soc.* **2014**, *136*, 6566–6569, doi:10.1021/ja5018267.

141. Elhenawy, S.E.M.; Khraisheh, M.; Almomani, F.; Walker, G. Metal-organic frameworks as a platform for CO_2 capture and chemical processes: Adsorption, membrane separation, catalytic-conversion, and electrochemical reduction of CO_2. *Catalysts* **2020**, *10*, 1–33, doi:10.3390/catal10111293.

142. Kökçam-Demir, Ü.; Goldman, A.; Esrafili, L.; Gharib, M.; Morsali, A.; Weingart, O.; Janiak, C. Coordinatively unsaturated metal sites (open metal sites) in metal-organic frameworks: Design and applications. *Chem. Soc. Rev.* **2020**, *49*, 2751–2798, doi:10.1039/c9cs00609e.

143. Chavan, S.; Vitillo, J.G.; Groppo, E.; Bonino, F.; Lamberti, C.; Dietzel, P.D.C.; Bordiga, S. CO Adsorption on CPO-27-Ni Coordination Polymer: Spectroscopic Features and Interaction Energy. *J. Phys. Chem. C* **2009**, *113*, 3292–3299, doi:10.1021/JP809872W.

144. Navarro, J.A.R.; Barea, E.; Salas, J.M.; Masciocchi, N.; Galli, S.; Sironi, A.; Ania, C.O.; Parra, J.B. Borderline microporous-ultramicroporous palladium(II) coordination polymer networks. Effect of pore functionalisation on gas adsorption properties. *J. Mater. Chem.* **2007**, *17*, 1939–1946, doi:10.1039/b617698d.

145. Vaidhyanathan, R.; Liang, J.; Iremonger, S.S.; Shimizu, G.K.H. A route to functionalised pores in coordination polymers via mixed phosphonate and amino-triazole linkers. *Supramol. Chem.* **2011**, *23*, 278–282, doi:10.1080/10610278.2010.523119.

146. Yang, Y.; Shukla, P.; Wang, S.; Rudolph, V.; Chen, X.M.; Zhu, Z. Significant improvement of surface area and CO_2 adsorption of Cu-BTC via solvent exchange activation. *RSC Adv.* **2013**, *3*, 17065–17072, doi:10.1039/c3ra42519c.

147. Yang, Z.; Yi, Y.; Zhong, M.; De, S.; Mondal, T.; Koley, D.; Ma, X.; Zhang, D.; Roesky, H.W. Addition Reactions of Me_3SiCN with Aldehydes Catalyzed by Aluminum Complexes Containing in their Coordination Sphere O, S, and N Ligands. *Chem. - A Eur. J.* **2016**, *22*, 6932–6938, doi:10.1002/chem.201505162.

148. Ding, C.; Zhang, W.; Xu, Z.; Zhang, H.; Zheng, J. A new heterometallic MOF with 1D nano-sized channels for cyanosilylation reaction and prevention effect against arrhythmia by reducing the sympathetic excitability. *J. Exp. Nanosci.* **2020**, *15*, 87–96, doi:10.1080/17458080.2020.1729356.

149. Pérez, J.M.; Rojas, S.; García-García, A.; Montes-Andrés, H.; Martínez, C.R.; Romero-Cano, M.S.; Choquesillo-Lazarte, D.; Abdelkader-Fernández, V.K.; Pérez-Mendoza, M.; Cepeda, J.; et al. Catalytic Performance and Electrophoretic Behavior of an Yttrium–Organic Framework Based on a Tricarboxylic Asymmetric Alkyne. *Inorg. Chem.* **2022**, acs.inorgchem.1c02864, doi:10.1021/ACS.INORGCHEM.1C02864.

150. Cui, X.; Xu, M.C.; Zhang, L.J.; Yao, R.X.; Zhang, X.M. Solvent-free heterogeneous catalysis for cyanosilylation in a dynamic cobalt-MOF. *Dalton Trans.* **2015**, *44*, 12711–12716.

151. Gomez, G.E.; Brusau, E. V.; Sacanell, J.; Soler Illia, G.J.A.A.; Narda, G.E. Insight into the Metal Content-Structure-Property Relationship in Lanthanide Metal-Organic Frameworks: Optical Studies, Magnetism, and Catalytic Performance. *Eur. J. Inorg. Chem.* **2018**, *2018*, 2452–2460, doi:10.1002/ejic.201701474.

152. Liu, X.; Lin, H.; Xiao, Z.; Fan, W.; Huang, A.; Wang, R.; Zhang, L.; Sun, D. Multifunctional lanthanide–organic frameworks for fluorescent sensing, gas separation and catalysis.

2016, *45*, 3743–3749, doi:10.1039/c5dt04339e.

153. Sternberg, Jeffrey Arthur; Adams, J.B. EP0503798A1_Original_document_20210421152633.pdf 1992, 120.

154. 0. M. Yaghi, G.L.& H.L. Selective binding and removal of guests in a microporous metal-organic framework. *Lett. to Nat.* **1995**, *378*, 703–706.

155. Silva, P.; Vilela, S.M.F.; Tomé, J.P.C.; Almeida Paz, F.A. Multifunctional metal-organic frameworks: From academia to industrial applications. *Chem. Soc. Rev.* **2015**, *44*, 6774–6803, doi:10.1039/c5cs00307e.

156. Cui, Y.; Yue, Y.; Qian, G.; Chen, B. Luminescent Functional Metal–Organic Frameworks. *Chem. Rev.* **2011**, *112*, 1126–1162, doi:10.1021/CR200101D.

157. Kirchon, A.; Feng, L.; Drake, H.F.; Joseph, E.A.; Zhou, H.-C. From fundamentals to applications: a toolbox for robust and multifunctional MOF materials. *Chem. Soc. Rev.* **2018**, *47*, 8611–8638, doi:10.1039/C8CS00688A.

158. García, H.; Navalon, S. *Metal-Organic Frameworks : Applications in Separations and Catalysis*; ISBN 978-3-527-80910-3.

159. Chen, Z.; Wasson, M.C.; Drout, R.J.; Robison, L.; Idrees, K.B.; Knapp, J.G.; Son, F.A.; Zhang, X.; Hierse, W.; Kühn, C.; et al. The state of the field: From inception to commercialization of metal-organic frameworks. *Faraday Discuss.* **2021**, *225*, 9–69, doi:10.1039/d0fd00103a.

160. Casaban, J.; Zhang, Y.; Pacheco, R.; Coney, C.; Holmes, C.; Sutherland, E.; Hamill, C.; Breen, J.; James, S.L.; Tufano, D.; et al. Towards MOFs' mass market adoption: MOF Technologies' efficient and versatile one-step extrusion of shaped MOFs directly from raw materials. *Faraday Discuss.* **2021**, *231*, 312–325, doi:10.1039/d1fd00025j.

161. Rubio-Martinez, M.; Avci-Camur, C.; Thornton, A.W.; Imaz, I.; Maspoch, D.; Hill, M.R. New synthetic routes towards MOF production at scale. *Chem. Soc. Rev.* **2017**, *46*, 3453–3480, doi:10.1039/c7cs00109f.

162. Ren, J.; Langmi, H.W.; North, B.C.; Mathe, M. Review on processing of metal-organic framework (MOF) materials towards system integration for hydrogen storage. *Int. J. Energy Res.* **2015**, *39*, 607–620, doi:10.1002/er.3255.

163. Dechnik, J.; Gascon, J.; Doonan, C.J.; Janiak, C.; Sumby, C.J. Mixed-Matrix Membranes. *Angew. Chemie - Int. Ed.* **2017**, *56*, 9292–9310, doi:10.1002/anie.201701109.

164. Qiu, S.; Xue, M.; Zhu, G. Metal-organic framework membranes: From synthesis to separation application. *Chem. Soc. Rev.* **2014**, *43*, 6116–6140, doi:10.1039/c4cs00159a.

165. Feng, T.; Ye, Y.; Liu, X.; Cui, H.; Li, Z.; Zhang, Y.; Liang, B.; Li, H.; Chen, B. A Robust Mixed-Lanthanide PolyMOF Membrane for Ratiometric Temperature Sensing. *Angew. Chemie - Int. Ed.* **2020**, *59*, 21752–21757, doi:10.1002/anie.202009765.

166. Lim, D.W.; Kitagawa, H. Rational strategies for proton-conductive metal-organic frameworks. *Chem. Soc. Rev.* **2021**, *50*, 6349–6368, doi:10.1039/d1cs00004g.

167. Kwei, T.K.; Kunins, C.A. Polymer–filler interaction: Vapor sorption studies. *J. Appl. Polym. Sci.* **1964**, *8*, 1483–1490, doi:10.1002/APP.1964.070080337.

168. Canivet, J.; Fateeva, A.; Guo, Y.; Coasne, B.; Farrusseng, D. Water adsorption in MOFs:

Fundamentals and applications. *Chem. Soc. Rev.* 2014, *43*, 5594–5617.

169. Kanda Seiichi, Yamashita Kenichi, O.K. A Proton Conductive Coordination Polymer. I. [N,N′-Bis(2-hydroxyethyl)dithiooxamido]copper(II). *Bull. Chem. Soc. Jpn.* **1979**, *52*, 3296–3301, doi:10.1246/bcsj.52.3296.

170. Dechnik, J.; Mühlbach, F.; Dietrich, D.; Wehner, T.; Gutmann, M.; Lühmann, T.; Meinel, L.; Janiak, C.; Müller-Buschbaum, K. Luminescent Metal–Organic Framework Mixed-Matrix Membranes from Lanthanide Metal–Organic Frameworks in Polysulfone and Matrimid. *Eur. J. Inorg. Chem.* **2016**, *2016*, 4408–4415, doi:10.1002/ejic.201600235.

171. Figueira, F.; Mendes, R.F.; Domingues, E.M.; Barbosa, P.; Figueiredo, F.; Paz, F.A.A.; Rocha, J. Easy processing of metal-organic frameworks into pellets and membranes. *Appl. Sci.* **2020**, *10*, doi:10.3390/app10030798.

172. F E M O'Brien The Control of Humidity by Saturated Salt Solutions. *J. Sci. Instrum.* **1948**, *25*, 73–76.

173. Schult, K.A.; Paul', D.R. Water Sorption and Transport in a Series of Polysulfones., doi:10.1002/(SICI)1099-0488(19961130)34:16.

174. Thijs, H.M.L.; Becer, C.R.; Guerrero-Sanchez, C.; Fournier, D.; Hoogenboom, R.; Schubert, U.S. Water uptake of hydrophilic polymers determined by a thermal gravimetric analyzer with a controlled humidity chamber. *J. Mater. Chem.* **2007**, *17*, 4864–4871, doi:10.1039/B711990A.

175. Mangukiya, S.; Prajapati, S.; Kumar, S.; Aswal, V.K.; Murthy, C.N. Polysulfone-based composite membranes with functionalized carbon nanotubes show controlled porosity and enhanced electrical conductivity. *J. Appl. Polym. Sci.* **2016**, *133*, 43778, doi:10.1002/APP.43778.

176. Echenique-Errandonea, E.; Mendes, R.F.; Figueira, F.; Choquesillo-Lazarte, D.; Beobide, G.; Cepeda, J.; Ananias, D.; Rodríguez-Diéguez, A.; Almeida Paz, F.A.; Seco, J.M. Multifunctional Lanthanide-based Metal-organic Frameworks derived from 3-amino-4-hydroxybenzoate: Single-molecule magnet behaviour, luminescent properties for thermometry and CO_2 adsorptive capacity. *Inorg. Chem.* **2022**, In revision.

177. Vilela, S.M.F.; Devic, T.; Várez, A.; Salles, F.; Horcajada, P. A new proton-conducting Bi-carboxylate framework. *Dalton Trans.* **2019**, *48*, 11181–11185, doi:10.1039/c9dt02009h.

Chapter 3

Antibacterial activity and adsorptive capacity of a copper and 3,4-dihydroxybenzoate based MOF

Summary

This chapter encompasses the synthesis and characterization of a novel copper-based metal-organic framework based on 3,4-dihydroxybenzoic acid ligand. The novelty of this work can be briefly summarized on the following aspects:

- To begin with, a novel copper based three-dimensional structure has been synthesised and thoroughly characterized exhibiting the formula $\{[Cu_3L_2(DMF)_2]\cdot 3H_2O\}_n$.
- Subsequently, in view of the microporosity of the structure, adsorptive capacity has been assessed.
- Additionally, material shaping-techniques have allowed processing the new Cu-MOF into pellets and membranes.
- Finally, 3,4-dihydroxybenzoic acid ligand presents well-known antibacterial activity; therefore, we performed preliminary evaluation and comparison of our copper-based materials' antibacterial properties with respect its precursors by disk diffusion method.

3.1 Introduction

Infections caused by pathogenic bacteria have been considered as one of the most concerning menaces of global consideration that affect public healthcare. To tackle this problem, over years, antibiotics have been administrated to treat bacterial infection. However, due to the growing resistance of pathogens to convectional antibiotics, often, treatment has become less effective or even ineffective. Consequently, the need to develop new effective solutions to broad antibacterial agents and combat infections more effectively has set of great importance.[1,2]

In this context, metal-organic frameworks are presented as promising materials. Bacterial activity in MOFs can be conducted by two different mechanisms.[2] The most probable mechanism involves that MOFs can act as reservoirs of metal ions that can provide gradual release resulting of sustained antibacterial effect with high durability. In this case, the gradual release of the metal ions, either in the form of cations or small parts of the MOF, that compose the MOF by biodegradation of the framework is the reason for biotoxicity. The other mechanism supports that antibacterial activity can be due to interactions between bacterial surface and the active site of the MOF surface. In this latter case, active centres present in MOFs are stabilized by strong chemical bonds becoming the material robust enough to keep its structure but at the same time weak enough not to block antibacterial activity.[3]

Herein, we will focus on the antibacterial activity promoted by the former described mechanism. In this case, antibacterial properties steam not only from release of bioactive metal-ions, but also from the organic linkers giving rise to combined synergistic antibacterial effect in the media. Another important factor in promoting antibacterial properties, is the particle size of the MOF.[4] Decreasing particle size to the nanoscale-range results in considerable enhancement of the surface-area allowing greater interaction with the surrounding, even prompting the internalization into the cell. Toxicity is another key factor for MOFs being used as antibacterial agents. It must be taken into consideration that action of MOF associated in the antibacterial process is derived by physical damage to bacterial cells. Consequently, not only toxicity associated with inorganic and organic precursor, but also *in vivo* toxicity data have to be reported; so far available data of the former materials results scarce.[2,5]

Since ancient times, silver (Ag) has been known as antibacterial agent.[6] Copper is presented as an interesting metal ion due to its multifunctional character in interesting

fields such as catalysis or adsorption.[7] It is also very interesting from a biological point of view since it is cheap, abundant and well-known by the capacity of eradicating bacterial infection.[8–10] It has been widely used in clinics; particularly multiple applications of copper-based sterilizing materials have been found.[1,3]

Among copper-based MOFs Cu-BTC, also known as HKUST-1 and MOF-199, has been extensively studied in the field of bactericidal materials due to the simple synthetic route and low toxicity of the ligand.[11] Several approaches to immobilize MOFs into various substrates have been carried out in the last years with the idea of developing new materials with promising properties.[2,12] From textiles that could be used as would-dressing to inhibit bleeding and promote healing to coatings that would prevent bacteria-adhesion to surfaces to avoid biofilm formation, the application spectrum is broad.[12] In this line, Rodríguez et al.[3,13] reported the immobilizing Cu-BTC into cellulose fibres exhibiting good antibacterial activity for E. coli.[13] The immobilization was performed by exposing cellulosic substrates to Cu-BTC MOF precursors to the *in situ* synthesis of the material in a basic media. The antibacterial activity in this case arises from gradual degradation and Cu^{2+} liberation which induces damage to the bacterial envelope.[14]

Another possible shaping and immobilizing procedure can be packing into pellets, monoliths or membranes. As MOFs generally yield insoluble and non-dense products, they tend to display problems when incorporated into devices as they can blow off and contaminate easily pipes in charge/discharge cycles. Thus, bulk-material processing becomes a mandatory procedure for MOFs being implemented in industry as it has been discussed in Chapter 2. The selection of the shaping technique depends on the textural properties of the chosen material and, in general, the shaped material has to at least keep or enhance its mechanical strength and must be simple and cost-effective procedure.[15,16]

Even though, shaping and processing of MOFs for specific application is still in an embryonic stage, efforts are being dedicated to give access to MOFs in the direction of real application.[17] Thus, apart from shaping, it becomes mandatory testing processed materials under humidity, applied-pressure conditions or high operating temperatures that can be encountered in industrial processes. In this line, Figueira et al.[18] reported a work where they presented a simple and inexpensive method for the immobilization of MOFs in the form of pellets and membranes and studied the stability of processed materials in terms of temperature and humidity in order to simulate possible operating

industrial conditions. They performed the studies in Cu-BTC and MOF-74 metal-organic frameworks motivated by the well-known capacity of this material to adsorb harmful gases, such as CO_2, and due to the possible competition of ambient water-molecules with the gases that are supposed to be captured in the porous network.[19]

With all the above, in this work we report a novel three-dimensional copper-based MOF composed by 3,4-dihydroxybenzoate ligand displaying the formula $[Cu_3L_2(DMF)_2]\cdot 3H_2O$, namely **3.1$_{Cu}$** in advance, where L^{3-} corresponds to the deprotonated organic linker. Taking into consideration the antibacterial activity of Cu^{2+} ions, and that the organic linker composing the MOF exhibits well-known performance against pathogenic bacteria,[20] antibacterial activity has been studied in both ligand and compound **3.1$_{Cu}$**. Additionally, following the approach of immobilization of the material reported by Figueira et al.[18] **3.1$_{Cu}$** has been shaped into pellets and membranes and the behaviour under thermal and moisture conditions has been studied in transformed materials. Also, microporous structure of **3.1$_{Cu}$** enabled us testing the material for CO_2 adsorption following the strategy of Yang et al.[19] who studied improvement of surface-area and CO_2 adsorption of Cu-BTC via solvent-exchange procedure.

3.2 Materials and methods

3.2.1 Compound synthesis

General procedure for the synthesis of single crystals of $\{[Cu_3L_2(DMF)_2]\cdot 3H_2O\}_n$: 0.010 g (0.065 mmol) of 3,4-dihydroxybenzoic acid (H_3L) organic linker was dissolved in 0.5 mL of DMF. In a separate vial, 0.010 g (0.0434 mmol) of $Cu(NO_3)_2\cdot 2.5H_2O$ was dissolved into 0.5 mL of distilled water. Once dissolved the ligand and metal, 0.5 mL of H_2O was added to the ligand solution and 0.5 mL of DMF to the metal solution. Metal solution was added dropwise to the ligand solution keeping magnetic stirring. The resulting greenish turquoise solution was poured into a screw-capped vial (6 mL) and introduced to the oven at 95 °C for 6 h giving rise to dark brown ribbon-shaped single crystals. Single-crystal X-ray structure determination, elemental analysis (EA) and TGA confirm the general formula $\{[Cu_3L_2(DMF)_2]\cdot 3H_2O\}_n$.

General procedure for the scale-up synthesis: 0.2 g (1.2 mmol) of 3,4-dihydroxybenzoic acid ligand and 0.2 g (0.868 mmol) of $Cu(NO_3)_2\cdot 2.5H_2O$ were weighted and dissolved in 3 mL DMF/3 mL H_2O solvent mixture. This greenish turquoise solution was placed in a microwave and heated at 95 °C for an hour to get around 85 mg of Cu MOF (yielding ~75 %). The purity of the product was confirmed by PXRD (Figure A3.2).

3.2.2 Antibacterial tests

Inhibitory activity against *Staphylococcus Aureus* (*S. aureus*). The pathogenic strains of *Staphylococcus Aureus* (CECT 976, *S. aureus*) were supplied by the Colección Española de Cultivos Tipo (CECT). The pathogenic strain was grown in tryptic soy broth (TSB No2, Sigma-Aldrich) at 30°C, following the supplier recommendations.

The inhibitory activity of copper(II) nitrate, ligand and compound **3.1_{Cu}** was evaluated by agar diffusion assays against *S. aureus*. This assay was carried out as follows: 0.1 mL of an overnight culture of *S. aureus* was spread on petri dishes containing TSA (containing 3 % v/v of TSB and 1.5 % w/v agar). Then, pellets of each sample were placed on agar plates containing the pathogenic bacteria and incubated at 30 °C, the pathogen optimal temperature. After 24 h of incubation, the inhibition zones were imaged and compared. Pellets of 100 mg were prepared by mixing 75 mg of calcium phosphate and 25 mg of the sample (copper(II) nitrate, ligand or compound **3.1_{Cu}**, respectively) and

then pressed using a compact hydraulic press at 10 tons. A pellet with 100 mg of calcium phosphate was also prepared and analysed as negative control. Inhibition experiments were performed in triplicate. Inhibition area was measured with the ImageJ software.[21] It was obtained by subtracting the area of the pellet to the total area. Data are shown as mean value and the corresponding standard deviation (SD).

3.2.3 MOF processing: Transformation into pellets and membranes

3.2.3.1 Pellets preparation and Characterization

A home-made extrusion system allowed compressing **3.1$_{Cu}$** forming pellets; for the purpose of apporting cohesion to the bulk material water has been employed as binding agent. 100 mg of compound **3.1$_{Cu}$** were weighted and 100 µL of water added to yield a malleable paste. Afterwards, the mentioned paste was transferred into a syringe and compressed applying heat with the aim of eliminating the excess of binding agent. With the objective of increasing pellet endurance and resistance, some of the pellets were covered by a polymeric coating. For this purpose, they were submerged for 2 s in a solution of CH_2Cl_2 containing 300 mg of polysulphone (PSF). Solvent evaporation gives place to a transparent film covered pellet of **3.1$_{Cu}$**.

3.2.3.2 Membrane's preparation and Characterization

Compound **3.1$_{Cu}$** has been also immobilized in a polymeric membrane. Shaping of this material was carried out according the following procedure: 400 mg of polysulphone (PSF) were weighted and dissolved in 5 mL of CH_2Cl_2; to this dense solution, 100 mg of compound **3.1$_{Cu}$** were added and left stirring for 30 min. The remaining viscous solution was then cast in a glass petri dish and left unstirred at ambient conditions until complete evaporation of the solvents yielding **3.1$_{Cu}$@PSF**. Note that, membrane preparation conditions have been optimized through assays containing various MOF to polymer ratios with the objective of getting balanced coverage homogeneity and mechanical stability.

MOF palletisation and incorporation into polymeric membrane was accessed by powder X-ray diffraction (Figure 3.4). Additionally, in case of membranes, MOF incorporation is immediately visible to the naked eye as pure PSF is transparent while MOF containing membranes presents brown dark colour.

3.3 Results and discussion

3.3.1 Structural characterization

Single-crystal X-ray crystallographic studies on $\{[Cu_3L_2(DMF)_2]\cdot 3H_2O\}_n$, where L = 3,4-dihydrxybenzoate, exhibit a three dimensional (3D) metal-organic framework that crystallizes in *C*2/*c* monoclinic space group. Asymmetric unit of **3.1$_{Cu}$** is composed of two crystallographically independent Cu^{2+} ions, a 3,4-dihydroxybenzoate ligand and a DMF solvent molecule.

Cu1 and Cu2 exhibit entire and half of occupation, respectively, which give rise to three positive charges being balanced by the completely deprotonated 3,4-dihydroxibenzoate ligand. The organic linker, 3,4-dihydroxibenzoate shows coordination to the metallic centre both from the carboxylate moiety as well as phenoxide groups. Cu1 atom displays a penta-coordinated environment being linked to three ligands and a solvent molecule. Concretely, $[CuO_5]$ environment is composed by the coordination of two phenoxide moieties of one ligand (one oxygen works as a bridge between two neighbour Cu1 centres and the other between Cu1 and Cu2 centres), an additional phenoxide moiety that corresponds to another linker-molecule (which also connects two Cu1 metals), as well as by the coordination of one donor atom belonging to a carboxylate moiety of another ligand-molecule. The surrounding of Cu1 is completed by the coordination of an additional oxygen atom belonging to a DMF solvent molecule which acts as direct bridge between Cu1 and Cu2 metal centres.

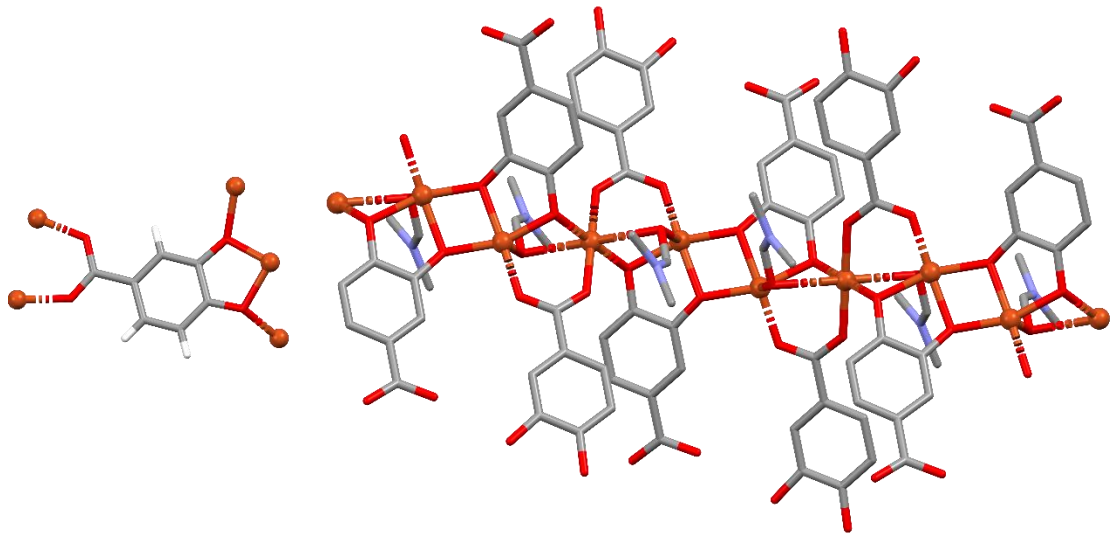

Figure 3.1. Excerpt of the coordination mode of 3,4-dihydroxybenzoic acid ligand in compound **3.1$_{Cu}$,** hydrogen atoms have been omitted for the sake of clarity.

Cu2, instead, presents a hexa-coordinated environment, being linked to four ligands and two solvent molecules. When [CuO_6] surrounding is examined in detail, two oxygen atoms belonging to phenoxide moieties of two distinct linker molecules, which act again as nexus between Cu1 and Cu2 centres, in addition to the coordination of another two oxygen donor atoms belonging to carboxylate moieties corresponding to two distinct linkers and two oxygen atoms coming from two DMF molecules compose the metal surrounding (in this latter case, as for Cu1, the oxygen donor atoms belonging to solvent molecules connect Cu1 and Cu2 metal centres).

Continuous shape measurements (CShMs)[22] revealed that Cu1 and Cu2 atoms build different polyhedra, resembling that Cu1 and Cu2 build square pyramid (SPY-5) and octahedron (OC-6) polyhedra, respectively. See Table A3.4 and Table A3.5 for information that is more detailed. Taking into account the connectivity achieved among secondary building units, SBUs, it may be considered as an ‘‘ABBABBA ’’ model where SBUs arrange along the *b* axis, considering A as Cu2 and B as Cu1 (see Figure A3.8). Cu ions are joined with one another to infinite metal-oxygen SBUs, in such way that these units spread into three dimensions. All in all, considering the connectivity of all metals and ligands, the resulting structure possesses a previously non-described topology that can be simplified by the $(4^2\cdot8^2\cdot10^2)(4^3)_2(4^4\cdot6^3\cdot8^3)_2$ point symbol.[23]

The growth of this structures along *c* axis leaves narrow microchannels that are occupied by disordered water molecules, these coordinated solvent molecules display pointing out disposition through the pore and take advantage of the whole pore cavity. In addition to coordinated DMF solvent molecules TG analysis has confirmed that three crystallization water molecules are present in the lattice within the pore (See Figure A3.4).

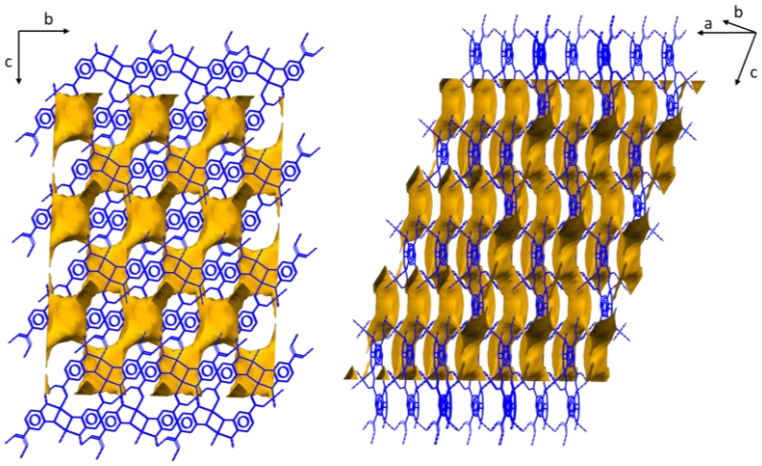

Figure 3.2. View of the packing along the *a* and perspective view showing the solvent accessible voids.

After material characterisation, compound **3.1**$_{Cu}$ processing has been performed in addition to testing shaped materials into moisture and temperature operating conditions. Also, compound **3.1**$_{Cu}$'s adsorptive capacity has been studied, as well as possible competition of water adsorption with the adsorbate gas. For that purpose, solvent exchange procedure has been employed to activate the material at lower temperatures.

Finally, the antibacterial activity of compound **3.1**$_{Cu}$ has been explored by disk-diffusion assays.

3.3.2 Processing into pellets and membranes

Following the approach of Figueira et al.[18] bulk material of **3.1$_{Cu}$** has been transformed into pellets and membranes with the aim of exploring simple and cost effective processing techniques according to the procedure described in 3.2.2 MOF processing section.[18]

After compound **3.1$_{Cu}$** being shaped into pellets and membranes, stability of these processed materials has been examined against possible operating industrial conditions such as moisture and temperature cycles. So, first, pellets and membranes of **3.1$_{Cu}$** have been treated for 72 h in a desiccator containing K_2SO_4 saturated water solution which simulated a 98 % relative humidity (RH) ambient[24] and, subsequently, moisture stability has been checked. Afterwards, pellets have been treated against temperature cycles. In all cases, stability of the processed materials has been determined by PXRD.

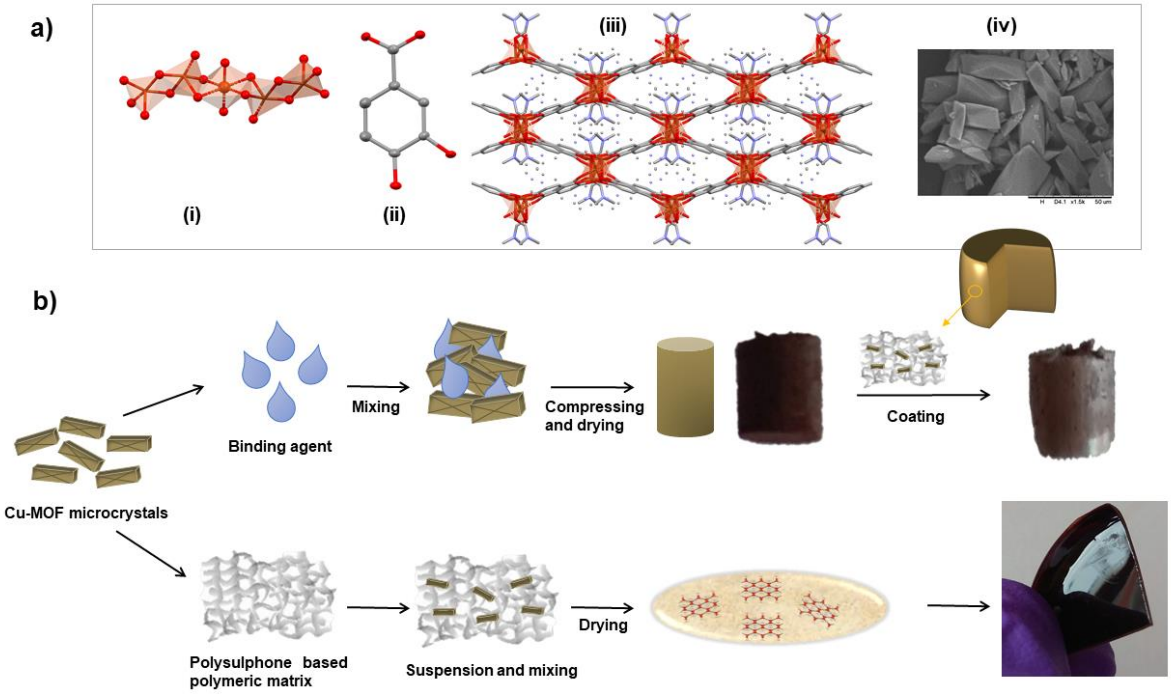

Figure 3.3. a) The crystal structure of **3.1$_{Cu}$** and the corresponding SEM images. **b)** Schematic representation of pellet and membrane preparation.

3.3.2.1 Moisture stability.

Powder X-ray diffraction patterns performed in **3.1$_{Cu}$** demonstrated that pristine MOF as well as shaped materials (pellets and membranes) keep their stability under high relative humidity (98 % RH) conditions for 72 h (Figure 3.4).

In case of membrane immobilized material of **3.1$_{Cu}$** (**3.1$_{Cu}$@PSF**), the amorphous nature of PSF polymeric matrix provokes that only the main intense peaks corresponding to compound **3.1$_{Cu}$** stand over the background as it can be appreciated in Figure 3.4 which summarizes collected PXRD data.

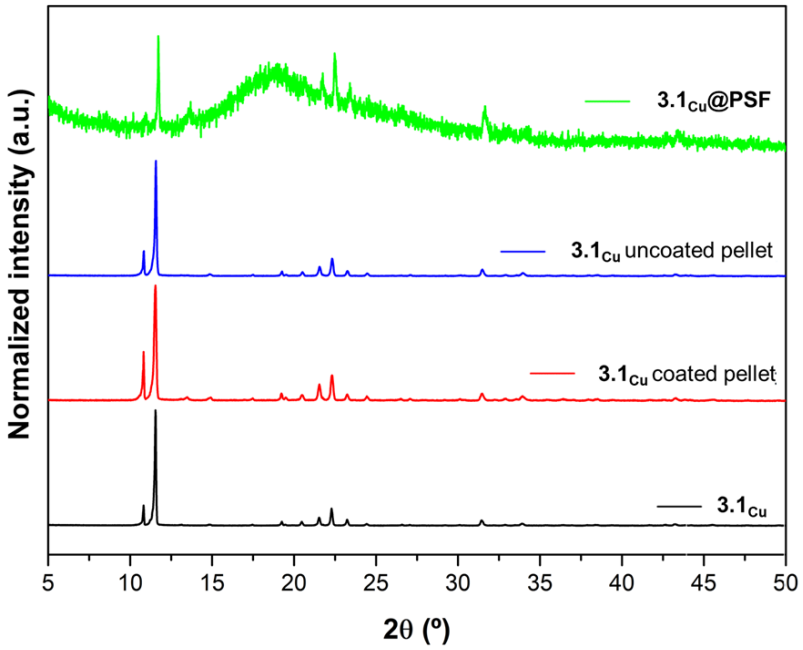

Figure 3.4. Powder X-ray diffractograms of the studied materials, as-synthesized and after processing into pellets and membrane after exposure to humidity.

3.3.2.2 Temperature stability

After performing humidity tests, pellets have been tested against temperature cycles. Four heating and cooling down cycles (from 125 ºC to RT) were conducted on shaped materials and then characterised by PXRD analysis. A photograph taken after each cycle gave an idea of the integrity of the pellet (Figure 3.5, top). Note that, PXRD analysis were conducted after the second and forth cycle in coated and uncoated pellets.

Overall, compound **3.1$_{Cu}$** coated and uncoated pellets exhibit good resistance to humidity and subsequent temperature-cycles keeping pellet integrity and not suffering humidity derived structural transformation. Nonetheless, it must be admitted that coated pellets keep better their integrity because of the resistance apported by the polymer.

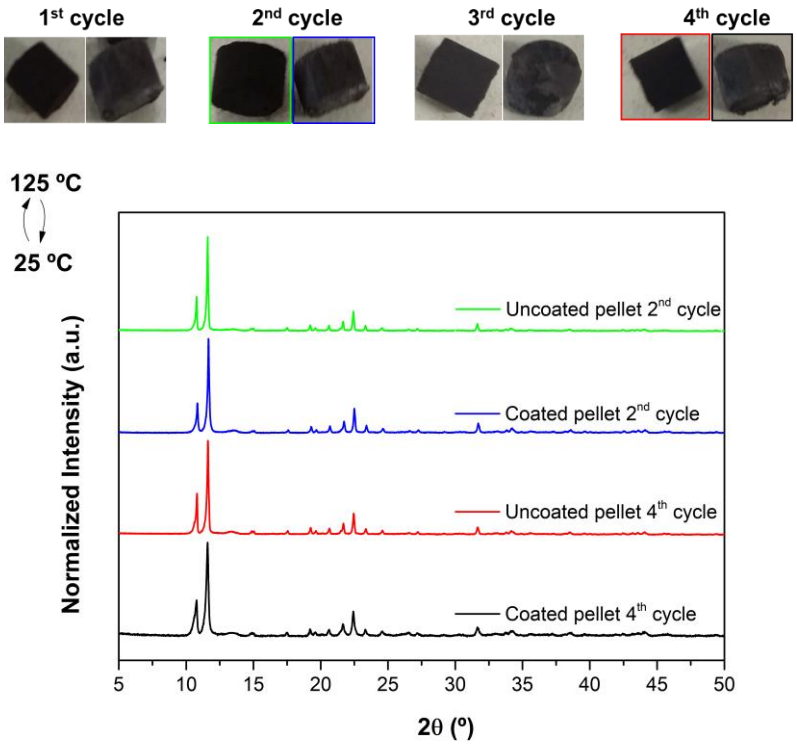

Figure 3.5. Pictures of the prepared pellets (uncoated, left and coated, right) after each temperature cycle and powder X-ray diffractograms of the studied materials after the second and forth cycle.

3.3.3 Adsorption capacity

3.3.3.1 Water adsorption

In view of the good stability of the processed materials under high humidity conditions we decided to experiment whether **3.1$_{Cu}$** was able to adsorb water or not. To that end, water-vapour adsorption isotherms were recorded at 25 ºC in bulk of **3.1$_{Cu}$** in order to ascertain the amount of water adsorbed at different relative humidity (2-98 %). Obtained results are summarized in Figure 3.6.

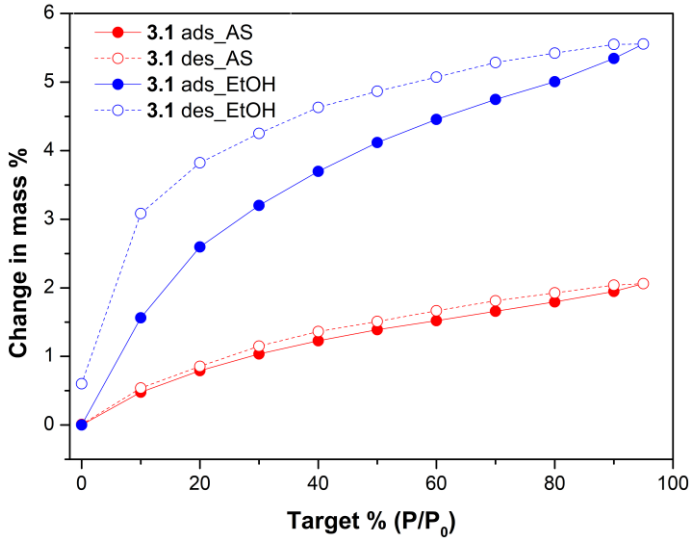

Figure 3.6. Water adsorption isotherms of compound **3.1$_{Cu}$** as synthesised (AS) and after solvent-exchange with EtOH for 16 h.

The results display that as synthesised (AS) compound **3.1$_{Cu}$** presents very low variation in mass change, concretely 1.5 %, which could be indicative of monolayer-type adsorption in the surface of the MOF. We subsequently decided to carry on solvent exchange procedure, in order to substitute coordinated DMF molecules for more volatile solvents which would be more easily displaced creating vacant positions to which water could have accessibility. In addition, we focused on selecting not only more volatile solvents, but also with smaller volume in order to reduce the stearic hindrance and occupation of the pore volume. So, we selected water, methanol and ethanol as possible substitutes. After keeping the materials for 16 h in magnetic agitation we checked whether material stability was kept observing that in the first to solvents there was an evolution towards another crystalline phase (as it ca be appreciated in Figure A3.3). Therefore, we proceed solvent-exchange procedure with ethanol.

Concretely, solvent-exchange procedure was carried out stirring 100 mg of compound **3.1$_{Cu}$** in 4 mL of EtOH during 16 h. According to TG analysis and PXRD (Figure A3.5), it was deduced that the material remains stable and appears that coordinated DMF molecules have been replaced by EtOH molecules, at least partly. In agreement with this, water adsorption isotherms ware repeated exhibiting three times higher change in mass in comparison to the as synthesised compound **3.1$_{Cu}$**, exhibiting an uptake of 6 %. Nonetheless, even if the approach seems to be satisfactory, it must be admitted that compound **3.1$_{Cu}$** exhibits a relatively low uptake, even after solvent-exchange procedure, which could be attributed to the hydrophobic character of the MOF.

N_2 and CO_2 adsorption isotherms

Subsequently, with the aim of assessing data on the porosity of the material we studied Cu-MOF's adsorption capacity towards gases. First, we performed sorption isotherm studies on as synthesised material **3.1$_{Cu}$** towards N_2 and CO_2 adsorbates at 77 K and 273 K, respectively, after an outgassing procedure performed at 170 ºC for 6 h. Regarding N_2 adsorption capacity reached at 1 bar and 0.03 bar (Figure 3.7) Cu-MOF loads 7.5 cm^3/g (0.4 mmol/g) for N_2 and 5 cm^3/g (0.2 mmol/ g) for CO_2 according to Brunauer–Emmett–Teller surface area (SBET) calculations.

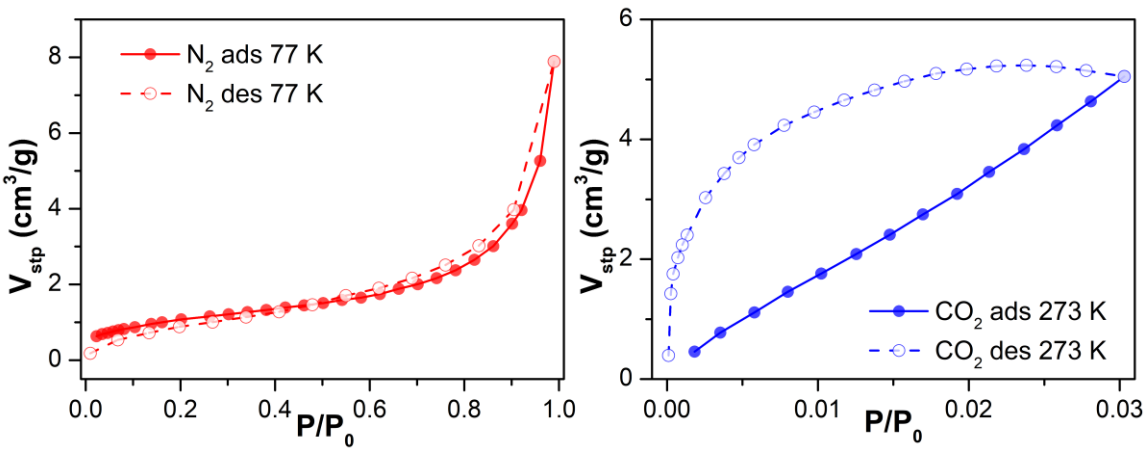

Figure 3.7. N_2 and CO_2 adsorption and desorption isotherms at 77 K and 273 K for **3.1$_{Cu}$**, upon outgassing at 170 ºC for 6 h.

In view of the relatively low uptake both for N_2 and CO_2 we decided to proceed with solvent exchange procedure as for we did for water-adsorption studies. Similarly,

compound **3.1$_{Cu}$** was suspended in ethanol for 16 h and sorption studies have been repeated.

In this latter case, again, the outgassing procedure has been performed as for as synthesised materials, and adsorption capacity reached at 1 bar evaluated for N_2 at 77 K and for CO_2 at 273 K (Figure 3.8) was studied. Under mentioned conditions, **3.1$_{Cu}$** exhibits a similar loading in N_2, indicating that N_2 do not reach to material microporosity although mesoporosity does, exhibiting 20 cm^3/g (0.9 mmol/g) uptake and regarding BET surface it triplicates from 5 cm^2/g to 15 cm^2/g.

Regarding to CO_2 uptake, adsorption in micropores significantly increases (up to 13 cm^3/g corresponding to 0.54 mmol/g) exhibiting according to Dubining equation displaying an increment form 0.15 cm^3/g to 0.5 cm^3/g.

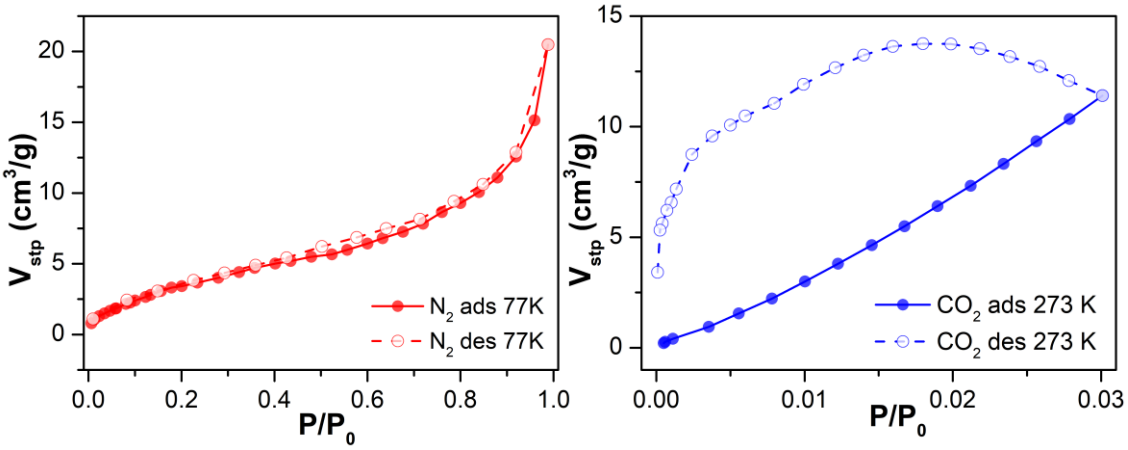

Figure 3.8. N_2 and CO_2 adsorption and desorption isotherms at 77 K and 273 K for **3.1$_{Cu}$**, upon outgassing at 170 ºC for 6 h after solvent exchange with EtOH.

3.3.4 Antibacterial activity

The inhibitory activity of the compound **3.1$_{Cu}$** and its precursors, $Cu(NO_3)_2 \cdot 2.5H_2O$ and 3,4-dihydroxybenzoic acid ligand, was assessed against the pathogenic Gram positive *S. aureus* bacteria; known to cause a wide variety of clinical diseases.[25]

The aforementioned evaluation was performed by disk diffusion method, by comparing the inhibition zone after 24 h of incubation in TSA agar media. Figure 3.9 exhibits the obtained results.

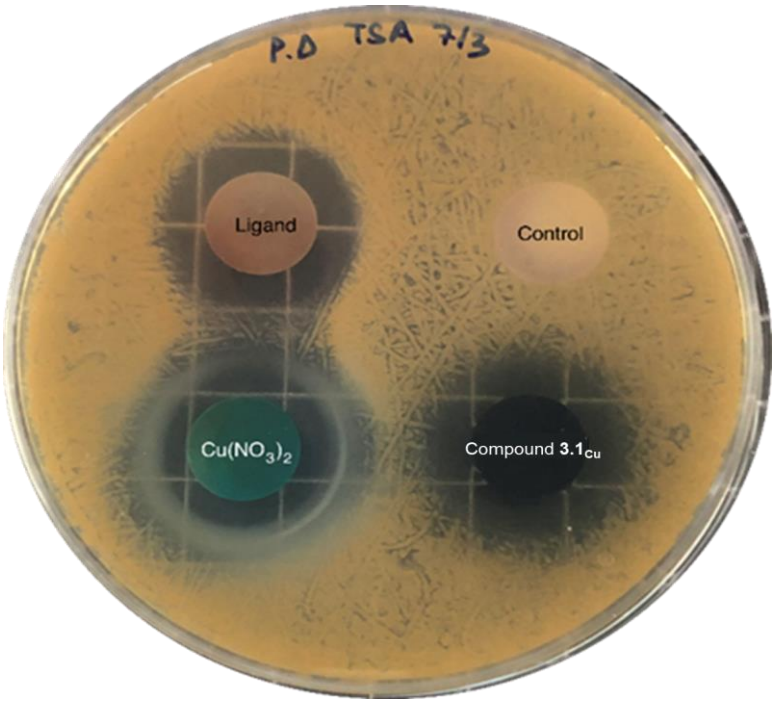

Figure 3.9. Antibacterial disk-diffusion assays showing the inhibitory activity against *S. aureus* of copper nitrate, 3,4-dihydroxybenzoic acid ligand and compound **3.1$_{Cu}$**. The negative control sample, without inhibitory activity, contained calcium phosphate, which was also used as supporting material in the rest of the samples (25 mg of active sample and 75 mg of calcium phosphate).

According to antibacterial disk-diffusion assays, copper(II) nitrate, 3,4-dihydroxybenzoic acid ligand and compound **3.1$_{Cu}$** presented antimicrobial activity against *S. aureus*. As expected, the control sample, which is composed by calcium phosphate, did not inhibit the growth of the pathogenic bacteria. Table 3.1 summarizes the area of inhibition generated around each of the solid sample after 24 h of incubation in the media, which is favourable for the growth of the pathogen.

Table 3.1 Area of inhibition (cm^2) of the tested compounds against *S. aureus* bacteria. Values are shown as mean ± standard deviation (SD, n = 3). The mass of Cu and ligand of each sample is also provided.

Compound	Inhibition area (cm^2)	Mass of Cu (mg)	Mass of ligand (mg)
3,4-dihydroxybenzoic acid ligand	3.6 ± 0.3	-	25
$Cu(NO_3)_2$	4.2 ± 1.7	6.8	-
3.1_{Cu}	4.1 ± 0.8	6.9	10.7

As it can be observed, both samples, copper(II) salt and compound **3.1_{Cu}**, which contained similar mass of Cu^{2+} (Table 3.1), exhibited practically similar area of inhibition. Thus, the pathogenic growth can be likely inhibited upon MOF dissolution and subsequent Cu^{2+} release, which further diffuse through the agar. The ligand release can also partially inhibit the growth. These results confirm that the inhibitory activity of Cu^{2+} and the ligand remain practically unaltered after the formation of the MOF.

At this stage, a comparison among antibacterial activity with MOF degradation would be interesting. For that, it would be required to determine how much ligand and Cu^{2+} is released within 24 h. These results would enable confirming whether the inhibition is derived by Cu^{2+} ions, 3,4-dihydroxybenzoic acid ligand or a combination of both.

3.4 Conclusions

To conclude, we have synthesised a novel copper-based metal-organic framework and shaped it by a simple and non-expensive processing method. Furthermore, we checked shaped material's stability by means of temperature and moisture ambient with the aim of simulating possible industrial operating conditions exhibiting in both scenarios' good mechanical stability and integrity in pelletized materials and membranes. Additionally, microporous structure of the three-dimensional MOF allowed us studying adsorptive capacity of **3.1$_{Cu}$** displaying almost negligible CO_2 uptake in as synthesised material. However, solvent exchange procedure allowed to partly replace coordinated DMF molecules with ethanol keeping structural stability and easing material activation by the replacement of a more volatile solvent. Consequently, sorption isotherms were repeated exhibiting an uptake of 0.54 mmol/g. Finally, motivated by the known antibacterial capacity of Cu^{2+} and 3,4-dihydroxybenzoic acid ligands, we decided to study antibacterial activity of compound **3.1$_{Cu}$** and its precursors by disk-diffusion method towards pathogenic *S. aureus* bacteria exhibiting that the antibacterial activity of both Cu^{2+} and 3,4-dihydroxybenzoic acid ligand remain practically unaltered after the formation of the compound.

Consequently, at this stage, as future work several objectives can be set. From one side, minimum inhibitory concentration (MIC) should be calculated and subsequently, minimum bactericidal concentration (MBC). Additionally, it would be interesting to study the MOFs' degradation process to determine the amount of Cu^{2+} and ligand released within 24 h with the aim of determining whether the inhibition is derived by Cu^{2+} ions, 3,4-dihydroxybenzoic acid ligand or a combination of both. In this regard, it would be interesting to study whether a synergy, indifference or antagonistic effect is derived by ligand and metal combination. Furthermore, the mechanism of action would be interesting to analyse as well as in broaden the studied antibacterial assays to other Gram positive and negative bacterial strains.

3.5 References

1. Zhang, S.; Ye, J.; Liu, Z.; Lu, H.; Shi, S.; Qi, Y.; Ning, G. Superior antibacterial activity of Fe_3O_4@copper(II) metal-organic framework core-shell magnetic microspheres. *Dalton Trans.* **2020**, *49*, 13044–13051, doi:10.1039/d0dt02417a.

2. Wyszogrodzka, G.; Marszałek, B.; Gil, B.; Dorozyński, P. Metal-organic frameworks: mechanisms of antibacterial action and potential applications. *Drug Discov. Today* **2016**, *21*, 1009–1018, doi:10.1016/J.DRUDIS.2016.04.009.

3. Jo, J.H.; Kim, H.-C.; Huh, S.; Kim, Y.; Lee, D.N. Antibacterial activities of Cu-MOFs containing glutarates and bipyridyl ligands. *Dalton Trans.* **2019**, *48*, 8084–8093, doi:10.1039/C9DT00791A.

4. Seil, J.T.; Webster, T.J. Antimicrobial applications of nanotechnology: Methods and literature. *Int. J. Nanomedicine* **2012**, *7*, 2767–2781, doi:10.2147/IJN.S24805.

5. Tamames-Tabar, C.; Cunha, D.; Imbuluzqueta, E.; Ragon, F.; Serre, C.; Blanco-Prieto, M.J.; Horcajada, P. Cytotoxicity of nanoscaled metal–organic frameworks. *J. Mater. Chem. B* **2013**, *2*, 262–271, doi:10.1039/C3TB20832J.

6. Chernousova, S.; Epple, M. Silver as Antibacterial Agent: Ion, Nanoparticle, and Metal. *Angew. Chemie Int. Ed.* **2013**, *52*, 1636–1653, doi:10.1002/ANIE.201205923.

7. Seco, J.M.; Fairen-Jimenez, D.; Calahorro, A.J.; Méndez-Liñán, L.; Pérez-Mendoza, M.; Casati, N.; Colacio, E.; Rodríguez-Diéguez, A. Modular structure of a robust microporous MOF based on Cu_2 paddle-wheels with high CO_2 selectivity. *Chem. Commun.* **2013**, *49*, 11329–11331, doi:10.1039/C3CC44193H.

8. Casey, A.L.; Adams, D.; Karpanen, T.J.; Lambert, P.A.; Cookson, B.D.; Nightingale, P.; Miruszenko, L.; Shillam, R.; Christian, P.; Elliott, T.S.J. Role of copper in reducing hospital environment contamination. *J. Hosp. Infect.* **2010**, *74*, 72–77, doi:10.1016/J.JHIN.2009.08.018.

9. Santo, C.E.; Quaranta, D.; Grass, G. Antimicrobial metallic copper surfaces kill Staphylococcus haemolyticus via membrane damage. *Microbiologyopen* **2012**, *1*, 46–52, doi:10.1002/MBO3.2.

10. Díaz-García, D.; Ardiles, P.R.; Prashar, S.; Rodríguez-Diéguez, A.; Páez, P.L.; Gómez-Ruiz, S. Preparation and Study of the Antibacterial Applications and Oxidative Stress Induction of Copper Maleamate-Functionalized Mesoporous Silica Nanoparticles. *Pharm. 2019, Vol. 11, Page 30* **2019**, *11*, 30, doi:10.3390/PHARMACEUTICS11010030.

11. Chiericatti, C.; Basilico, J.C.; Zapata Basilico, M.L.; Zamaro, J.M. Novel application of HKUST-1 metal–organic framework as antifungal: Biological tests and physicochemical characterizations. *Microporous Mesoporous Mater.* **2012**, *162*, 60–63, doi:10.1016/J.MICROMESO.2012.06.012.

12. Abbasi, A.R.; Akhbari, K.; Morsali, A. Dense coating of surface mounted CuBTC Metal–Organic Framework nanostructures on silk fibers, prepared by layer-by-layer method under ultrasound irradiation with antibacterial activity. *Ultrason. Sonochem.* **2012**, *19*, 846–852, doi:10.1016/J.ULTSONCH.2011.11.016.

13. Rodríguez, H.S.; Hinestroza, J.P.; Ochoa-Puentes, C.; Sierra, C.A.; Soto, C.Y. Antibacterial activity against Escherichia coli of Cu-BTC (MOF-199) metal-organic framework immobilized onto cellulosic fibers. *J. Appl. Polym. Sci.* **2014**, *131*,

doi:10.1002/app.40815.

14. Wang, C.; Qian, X.; An, X. In situ green preparation and antibacterial activity of copper-based metal–organic frameworks/cellulose fibers (HKUST-1/CF) composite. *Cellul. 2015 226* **2015**, *22*, 3789–3797, doi:10.1007/S10570-015-0754-4.

15. Ren, J.; Langmi, H.W.; North, B.C.; Mathe, M. Review on processing of metal-organic framework (MOF) materials towards system integration for hydrogen storage. *Int. J. Energy Res.* 2015, *39*, 607–620.

16. Yuan, J.; Li, J.; Che, S.; Li, G.; Liu, X.; Sun, X.; Zou, L.; Zhang, L.; Liu, Y. Two unique copper cluster-based metal–organic frameworks with high performance for CO_2 adsorption and separation. *Inorg. Chem. Front.* **2019**, *6*, 556–561, doi:10.1039/C8QI01315B.

17. Rubio-Martinez, M.; Avci-Camur, C.; Thornton, A.W.; Imaz, I.; Maspoch, D.; Hill, M.R. New synthetic routes towards MOF production at scale. *Chem. Soc. Rev.* **2017**, *46*, 3453–3480, doi:10.1039/c7cs00109f.

18. Figueira, F.; Mendes, R.F.; Domingues, E.M.; Barbosa, P.; Figueiredo, F.; Paz, F.A.A.; Rocha, J. Easy processing of metal-organic frameworks into pellets and membranes. *Appl. Sci.* **2020**, *10*, doi:10.3390/app10030798.

19. Ghanbari, T.; Abnisa, F.; Wan Daud, W.M.A. A review on production of metal organic frameworks (MOF) for CO_2 adsorption. *Sci. Total Environ.* **2020**, *707*, 135090, doi:10.1016/J.SCITOTENV.2019.135090.

20. Nofrizal; Putra, D.P.; Arbain, D. Antioxidant and antibacterial constituents from two Sumatran ferns, Trichomanes javanicum and Oleandra pistillaris. *Nat. Prod. Commun.* **2017**, *12*, 1263–1264, doi:10.1177/1934578x1701200829.

21. ImageJ Software.

22. Llunell, M.; Casanova, D.; Cirera, J.; Bofill, J. M.; Alemany, P.; Alvarez, S.; Pinsky, M.; Avnir, D. Program for the Stereochemical Analysis of Molecular Fragments by Means of Continuous Shape Measures and Associated Tools. *SHAPE, v1.1b; Barcelona, Spain* **2005**, 1–35.

23. Blatov, V.A.; Shevchenko, A.P.; Proserpio, D.M. Applied topological analysis of crystal structures with the program package topospro. *Cryst. Growth Des.* **2014**, *14*, 3576–3586, doi:10.1021/cg500498k.

24. F E M O'Brien The Control of Humidity by Saturated Salt Solutions. *J. Sci. Instrum.* **1948**, *25*, 73–76.

25. Lowy, F.D. Staphylococcus aureus infections. *N. Engl. J. Med.* **1998**, *339*, 520–532, doi:10.1056/NEJM199808203390806.

Chapter 4

Luminescent Heterobimetallic Ru(II)-Ln(III) MOFs as Catalyst for Diesel Oxidative Desulfurization

Summary

The novelty of this work can be summarized in the following aspects:

- This chapter outlines the synthesis and characterisation of a family of Ln^{3+} based 3D MOFs mediated by metalloligand assisted synthesis. This ruthenium based metalloligand have act as secondary building unit and have been proved to be a good strategy for the synthesis of heterobimetallic complexes exhibiting the formula $\{[(RuL_3)_2Ln_3]ClO_4\}_n$.
- Afterwards, in view of the promising emissive capacity of displayed by lanthanide ions exhibiting narrow emissive lines with pure colours going form the UV-Vis to NIR spectrum, photoluminescent properties have been explored.
- Finally, materials have been tested as heterogeneous catalyst in the oxidative desulfurization reaction.

4.1 Introduction

As previously mentioned in Chapter 2, lanthanide ions offer infinite possibilities in the synthesis of novel MOFs; not only for their multiple and diverse coordination modes giving rise to large coordination spheres but for their exclusive optical properties. This feature becomes them appealing candidates to be implemented in optical devices since their electronic f-f transitions cover from UV-Vis to the near-infrared region of the electromagnetic spectrum. In addition, lanthanides display narrow emissive lines with pure emission colours.[1] Nonetheless, they encounter low adsorption coefficients (ε) and direct excitation results are generally inefficient since 4f-4f transitions are forbidden by Laporte's law.[2] Therefore, lanthanide centred emission should be sensitized by organic conjugated systems generating an energy transition from the ligand moiety to the lanthanide to enhance its emissive intensity. This effect is called antenna and consists of an energy conversion between ligand single-excited state; that may typically convert to triplet state by intersystem crossing, and lanthanide ion triplet excited state that needs to be energetically close to efficiently accept energy from the chromophore to then relax via radiative pathways.[3]

Consequently, the selection of appropriate chromophores displays a key role. In this sense, the attempt to design multifunctional luminescent materials based on metal complex ligands, known as metalloligands, is a promising method since it allows to incorporate photofunctional molecules into the coordination network allowing to develop of responsible materials with high sensitivity.[4,5] By definition, metalloligands are metal-containing complexes that present binding sites from which the coordination to a second metal ion or cluster is allowed. Therefore, they are particularly suitable for the preparation of novel MOFs through stepwise synthesis since enables straightforward immobilization of functional sites, such as catalytically active metal sites, or photoactive metal sites, among others.[6]

An example of a metalloligand mediated synthesis of a novel MOF finding application in catalysis was reported by Han et al.[7] Concretely, they presented a copper and ytterbium based MOF with the formula $\{[Yb_6Cu_{12}(OH)_4(PyC)_{12}(H_2O)_{36}]\cdot(NO_3)_{14}\cdot xS\}_n$ (QUST-81) for efficient removal of heterocyclic organosulfur compounds from fuel. In fact, nowadays, approximately 90 % of the global energy resources are originated from fossil fuels, and their demand is increasing day after day. Nonetheless, fossil fuels generally encounter the problem of impurities, a great concern that needs to be removed

before utilization. Some of the mentionable contaminants that can be found in are sulphur and nitrogen-containing organic molecules. Even if in low concentration, those substances affect the efficacy and promote catalytic deactivation. Therefore, novel cost effective technologies capable to be implemented in industrial processes that would provide low nitrogen and sulphur levels in fuels are in great demand.[8,9]

In this scenario, the investigation of MOFs as heterogeneous catalysts involved in the diesel desulfurization process becomes a spreading field. To date, MOFs have been more regularly applied as scaffolds for active material such as POMs;[9,10] in consequence, relatively scarce examples are found where the MOF itself acts as catalyst.[8] Therefore, in this work a family of novel lanthanide based materials have been synthesised assisted by ruthenium(II)-tris(2,2'-bipyridine-5,5'-dicarboxylic acid) metalloligand to be tested as heterogeneous catalyst in the oxidative desulfurization reaction. Finally, photoluminescence properties of the synthesised materials will be explored.

4.2 Materials and methods

4.2.1 Compound synthesis

For the synthesis of this family of compounds, we started by oxidizing 5,5'-dimehtyl-2,2'-bipyridine to obtain 2,2,'-bipyridine-5,5'-dicarboxylic (L) according to the procedure reported by Constable et al.[11,12] The purity of the final product was confirmed by ^{1}H-RMN (Figures A4.2). Subsequently, we prepared ruthenium metalloligand and make it react with the corresponding lanthanide salt to give rise to the corresponding three-dimensional structure. Suddenly, procedures are reported in detail:

General procedure for Ru-metalloligand synthesis: Two synthetic pathways have been followed for the synthesis of Ru-metalloligand. According to the first procedure, 0.0856 g (0.38 mmol) of $RuCl_3 \cdot nH_2O$ and 0.278 g (1.14 mmol) of 2,2'-bipyridine-5-5'-dicarboxylic acid were mixed and placed in a solvothermal reactor and added 10 mL of water before heating 3 h at 220 ºC. As a result, black single-crystals were obtained with a 50 % yield. The crystals were collected by filtration and cleaned with water confirming the formula $[RuL_3]$ (Table A4.3 and Figure A4.7, up).

In the attempt to scale up reaction a second procedure was employed.[13] In this case, 0.12 g (0.53·mmol) of $RuCl_3 \cdot nH_2O$ and 0.45 g (1.84·mmol) of 2,2'-bipyridine-5-5'-dicarboxylic acid were refluxed in DMF for 24 h. After this reaction-time a brown precipitate appears and it was collected by filtration and cleaned with acetonitrile and dichloromethane (obtained yield 75 %). The purity of the final $[RuL_3]Cl_2$ product was confirmed by ^{1}H-RMN (Figures A4.3).

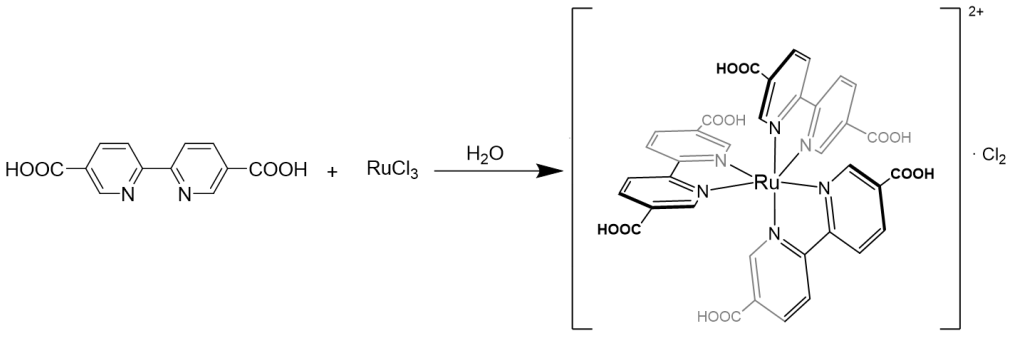

Scheme 4.1. Synthetic procedure to obtain $[RuL_3]Cl_2$.

General procedure for the synthesis of compounds $\{[(RuL_3)_2Ln_3]ClO_4\}_n$ where L = 2,2'-bipyridine-5-5'-dicarboxylic acid Ln = Nd (**4.1**), Sm (**4.2**), Eu (**4.3**), Gd (**4.4**), Tb (**4.5**), Dy (**4.6**), Er (**4.7**), Yb (**4.8**). 0.02 g (0.02 mmol) of ruthenium metalloligand and 0.06 mmol of the corresponding hydrated lanthanide salt (nitrate or chloride) were weighted and dissolved in 3 mL/ 3 mL DMF/H_2O solvent mixture containing 0.8 mL perchloric acid. The remaining intense red solution was placed in an oven and heated at 100 °C for 24 h to get single crystal. Single-crystal X-ray structure determination, elemental analysis (EA) and TGA confirm the general formula $\{[(RuL_3)_2Ln_3]ClO_4\}_n$. The purity of the product was confirmed by PXRD (Figure A4.4).

4.2.2 Extraction and Catalytic Oxidative Desulfurization (ECODS)

General procedure for oxidative desulfurization of model diesel catalysed by $\mathbf{4.3_{Ru\text{-}Eu}}$. Desulfurization experiments were conducted in a closed borosilicate 5 mL reaction vessel under constant magnetic stirring heated in a paraffin bath at 70 ºC. ECODS was performed in a biphasic system composed by an ionic liquid (1-butyl-3-methylimidazolium hexafluorophosphate, $[BMIM]PF_6$, a viscous, colourless, hydrophobic and non-water-soluble ionic liquid) and a model diesel consisting of four refractory aromatic sulphur compounds yielding a total sulphur concentration of 2000 ppm. Concretely, those compounds were 1-benzothiophene (1-BT), dibenzothiophene (DBT), 4-methyldibenzothiophene (4- MDBT), and 4,6-dimehtyldibenzothiophene (4,6-DMDBT) in n-octane.

In a typical experiment, 0.75 mL of extraction solvent, 0.75 mL of model diesel and the corresponding catalytic loading (5 mg, 10 mg or 20 mg) were mixed in the reaction vessel. The extraction-oxidation desulfurization includes two main steps. An initial extraction obtained by stirring both immiscible phases for 10 min at 70 ºC where an equilibrium between the sulphur compounds that are transferred form model diesel to ionic liquid is obtained and a subsequent catalytic step initiated by the addition of H_2O_2 oxidant (75 µL, 0.74 mol).

The catalytic oxidation occurs principally in the extractive phase, $[BMIM]PF_6$, since catalyst is dispersed in this layer in addition to the high solubility of the oxidized products in this media.

The total sulphur content was periodically quantified by gas chromatography using tetradecane as external standard. For this purpose, aliquots were taken at 10 min, 30 min, 1 h, 2 h, 3 h and 4 h reaction times (after the addition of oxidant) with a microsyringe from the model diesel phase.

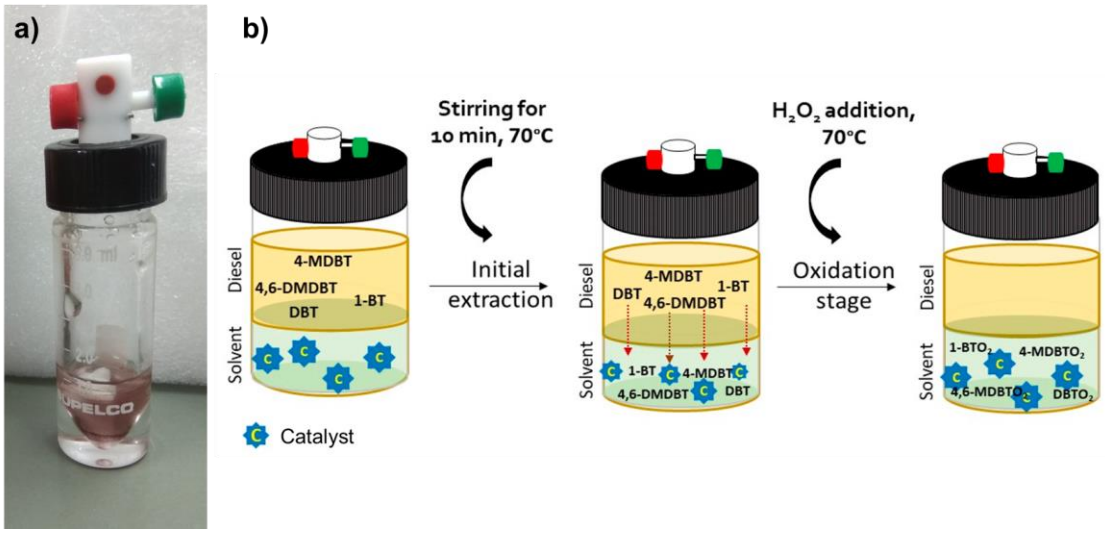

Figure 4.1. a) Picture of the reaction vessel and **b)** Schematic representation of the desulfurization reaction conciliating initial extraction and oxidative catalytic processes.[14]

4.3 Results and discussion

4.3.1 Structural characterization

In the following section, a tentative model of the three-dimensional structure will be described. Because of the poor quality of the obtained single-crystals, X-ray crystallographic studies allowed for proposing an approximated formula. Accordingly, proposed formula, $\{[(RuL_3)_2Ln_3]ClO_4\}_n$, was backed up by the analysis of several single-crystals in addition to other characterisation techniques as elemental analysis (Table A4.1), FT-IR (Figure A4.1), TG (Figure A4.6), ICP-AES (Table A4.2) and SEM-EDX (Figure A4.9). For a detailed explanation please check Appendix 4 supporting information of chapter 4. ICP-AES analysis, conducted in compound **4.6**$_{\mathbf{Ru\text{-}Dy}}$, exhibited a dysprosium content of 1652 mg/L (corresponding to 10.2 mM of Dy^{3+}) and ruthenium content of 686 mg/L (6.8 mM Ru^{2+}). Calculated Dy^{3+} to Ru^{2+} proportion sums 1.5, which is perfectly in line with the proposed formula. Additionally, SEM-EDX mapping performed in one single crystal of the isostructural **4.3**$_{\mathbf{Ru\text{-}Eu}}$ counterpart, confirms that both metals are present in single crystal and exhibits a surficial proportion of 1.43 Eu^{3+} with respect to Ru^{2+} (Figure A4.9).

Therefore, the proposed formula, $\{[(RuL_3)_2Ln_3]ClO_4\}_n$ where L = 2,2'-bipyridine-5,5'-dicarboxylic acid and Ln = Nd (**4.1**), Sm (**4.2**), Eu (**4.3**), Gd (**4.4**), Tb (**4.5**), Dy (**4.6**), Er (**4.7**), Yb (**4.8**) is derived by the combination of single crystal X-ray diffraction, powder X-ray diffraction, SEM–EDX, and ICP-AES, is consistent and summarizes the best approximation for data obtained in the aforementioned techniques.

Single crystal X-ray diffraction studies reveals that compounds **4.1**-**4.7** consists of three dimensional (3D) isostructural cationic lanthanide-MOFs crystallizing in the orthorhombic *Cmca* space group. Because of the isostructural nature of the synthesised materials, **4.6**$_{\mathbf{Ru\text{-}Dy}}$ structure will be described in the following section as a representative material for this family of compounds.

Proposed model formula consists of a cationic coordination compound where ruthenium(II) metalloligand contributes in eight negative charges and three lanthanide atoms in nine positive charges which are balanced by a perchlorate counterion. The asymmetric unit of **4.6**$_{\mathbf{Ru\text{-}Dy}}$ is comprised of two crystallographically independent Dy^{3+}ions and one Ru^{2+} ion (in all cases, the metallic centres show half of occupation), one and a half deprotonated 2,2'-bipyridine-5,5'-dicarboxylic acid ligand as well as half of a

perchlorate anion and a coordinated water molecule. Note that, asymmetric unit do not yield a neutral sum as previously state because of the poor quality of the single crystal.

2,2'-bipyridine-5,5'-dicarboxylic organic linker, displays multiple coordination possibilities. From nitrogen atoms of the bipyridyl group ligand displays coordination to the Ru^{2+} of the asymmetric unit, giving rise to RuL_3 metalloligand. Two of the ligands that composes Ru-metalloligand display the same coordination to Dy^{3+} centres. One of the carboxylate moieties shows coordination in a bidentate way to two neighbouring Dy1 atoms and from the other side, the other moiety shows monodentate coordination to another Dy1 centre. The remaining ligand comprising Ru-metalloligand displays coordination to two Dy2 atoms in a chelate way.

Dy1 atoms present six-coordinated [DyO_6] and environments while Ru1/Dy2 exhibits six-coordinated and penta-coordinated [RuN_6] and [DyO_5] environments, respectively. Dy1 exhibits DyO_6 environment composed by the coordination of four donor oxygen atoms belonging to ligand carboxylate moiety that exhibits chelate among two neighbouring Dy centres and two oxygen atoms belonging to ligand carboxylate moiety exhibiting monodentate coordination. Ru1 instead, shows RuN_6 surrounding comprising the structure of the Ru metalloligand and is completed by the coordination of six nitrogen atoms belonging to three bipyridyl moieties of 2,2'-bipyridine-5,5'-dicarboxylic ligand. Finally, Dy2 display DyO_5 coordination comprised by four donor oxygen atoms belonging to ligand and the coordination environment is completed by the coordination of a water solvent molecule. Continuous shape measurements (CShMs)[15] revealed that Dy1, Ru1 and Dy2 atoms build different polyhedra, resembling that Dy1 build spherical trigonal prism (TPR-6), Ru1 octahedron (OC-6) and Dy2 square pyramid (SPY-5) polyhedra respectively. See Table A4.5 and Table A4.6 for more detailed information.

Growing the asymmetric unit, it can be seen that coordination environments of Dy1 and Dy2 show "ABAB.." connection model where A can be considered as two Dy ions interconnected as it can be for B where two Dy2 metals appear are interconnected. The connection between A and B is done by hydrogen bonding throw the proton of the coordinated water molecule in Dy2 to the non-coordinating oxygen of the carboxylate group of the 2,2'-bipyridine-5,5'-dicarboxylic ligand. Additionally, the highly packed nature of the structure does not display porous available to acquiring solvent lattice molecules. Instead, perchlorate anion occupies this cavity (Figure A4.5).

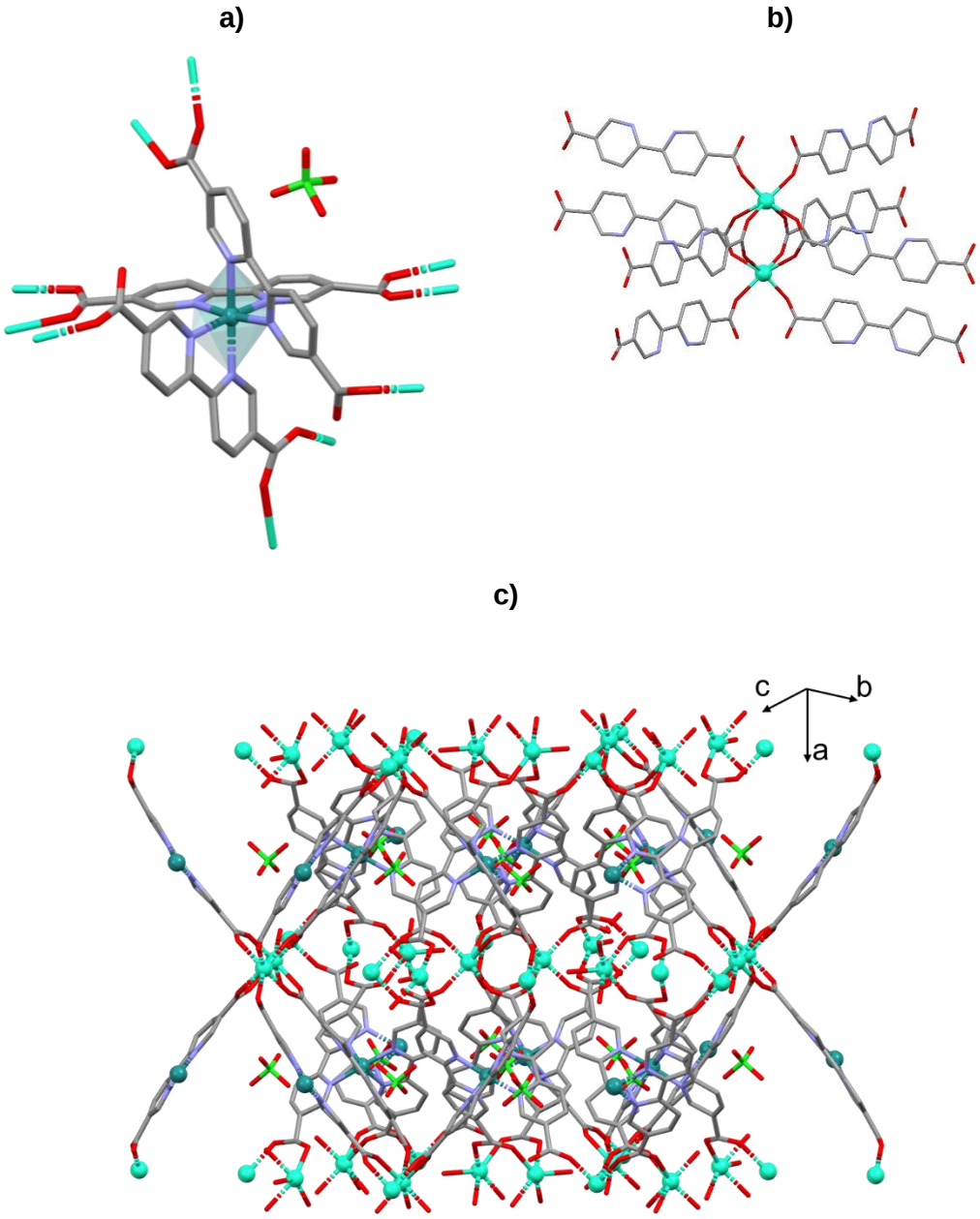

Figure 4.2. a) Excerpt of the coordination mode of ruthenium(II) metalloligand and **b)** Dy1 coordination environment and **c)** perspective view in compound **4.6**$_{\text{Ru-Dy}}$, hydrogen atoms have been omitted for the sake of clarity.

4.3.2 Extraction and Catalytic Oxidative desulfurization (ECODS) performance

Desulfurization studies were performed by increasing heterogeneous **4.3**$_{Ru\text{-}Eu}$ catalyst loading. An initial extraction desulfurization of approximately 49 % was achieved after 10 min at 70 ºC. After the addition of the oxidant, only a slightly increased tendency was appreciated when 10 mg catalytic loading was used, reaching a conversion of 51 %. When smaller or bigger loadings are used (5 mg or 20 mg catalyst, respectively), total conversion was not increased during oxidative desulfurization stage.

Furthermore, at different reaction times a fluctuational tendency is observed indicating that the catalyst is not active using this solvent extraction. This tendency is also found when 10 mg catalytic loading is employed at 2 h reaction time. Nonetheless, in the regime of 10 minutes to 1 h reaction an increasing tendency (from 51 % to 59 % conversion) followed by a stabilization appreciated at 3-5 h reaction time is appreciated overall reaching the 64 % conversion.

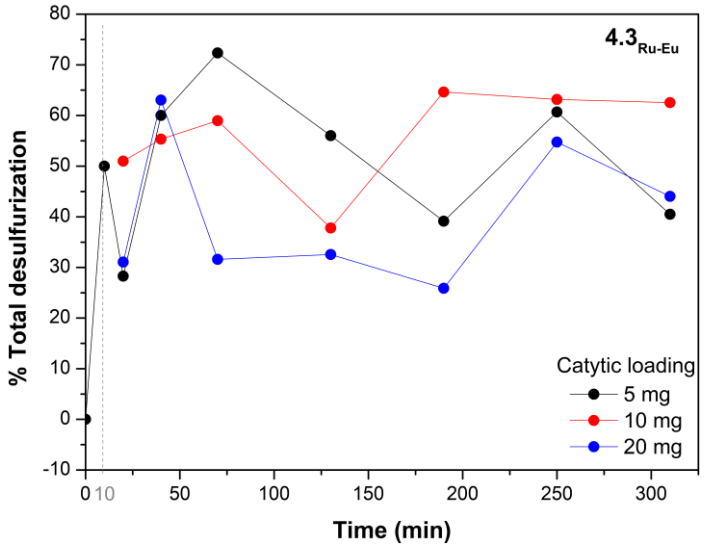

Figure 4.3. Desulfurization of a multicomponent model diesel (2000 ppm S) catalysed by heterogeneous **4.3**$_{Ru\text{-}Eu}$ catalyst at three catalytic loadings using equal volumes of model diesel end extraction solvent and H_2O_2 at 70 ºC. The vertical dashed line indicates the instant that oxidative catalytic reaction was started by the addition of oxidant.

Subsequently, we analysed stability of the catalyst after catalytic reaction by powder X-ray diffraction. As it is depicted in Figure 4.4, **4.3**$_{Ru\text{-}Eu}$ catalyst had suffered a

transformation into another crystalline phase not corresponding to the initial product nor metal oxides.

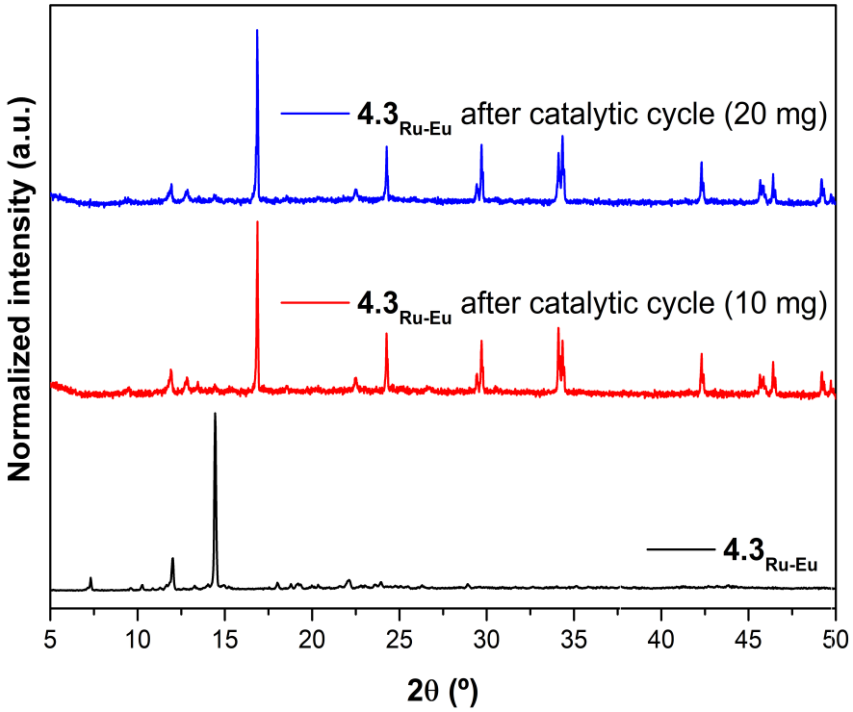

Figure 4.4. Powder X-ray diffraction patterns of **4.3**$_{\text{Ru-Eu}}$ before and after ECODS cycles when 10 mg (red) and 20 mg catalytic loading (blue) was employed.

In view of the obtained results, even if at first stage we could think the catalytic loading may have an important role and that 10 mg catalytic loading could be the most suitable for this system, taking into consideration that only a final conversion enhancement of the 15 % (from initial 50 % to final 65 %) is obtained a poor catalytic performance can be assigned. Additionally, a structural transformation in the catalyst phase at the end of the catalytic activity was observed. In this scenario, even if reported results are a sum of preliminary data and further experimentation may be required to determine at what stage stars catalyst evolution and to what final product evolves, we decided to focus on other potential application of this family of compounds: photoluminescent properties.

4.3.3 Photoluminescence measurements

In the following section, solid state photoluminescent properties of 2,2'-bipyridine-5,5'-dicarboxylic acid ligand (L), Ru(II)metalloligand and compounds **4.1**$_{Ru-Nd}$, **4.3**$_{Ru-Eu}$, **4.4**$_{Ru-Gd}$, **4.5**$_{Ru-Tb}$ and **4.7**$_{Ru-Er}$ will be explored in detail motivated by the diverse applications that lanthanide-based material found in optical devices.[16,17]

Excitation spectra of 2,2'-bipyridine-5,5'-dicarboxylic acid collected at 294 K monitoring the emission at 570 nm consists of a broad UV band (350–450 nm) with a maximum located at 390 nm which can be attributed to organic linker π–π* transitions. This spectrum coincides with solid-state emission spectrum of the organic linker previously reported in bibliography.[18] Ligand emission spectrum acquired at 294 K exhibits a broad band ranging from 400 to *ca.* 700 nm with two maxima peaking at 457 nm and 554 nm, respectively.

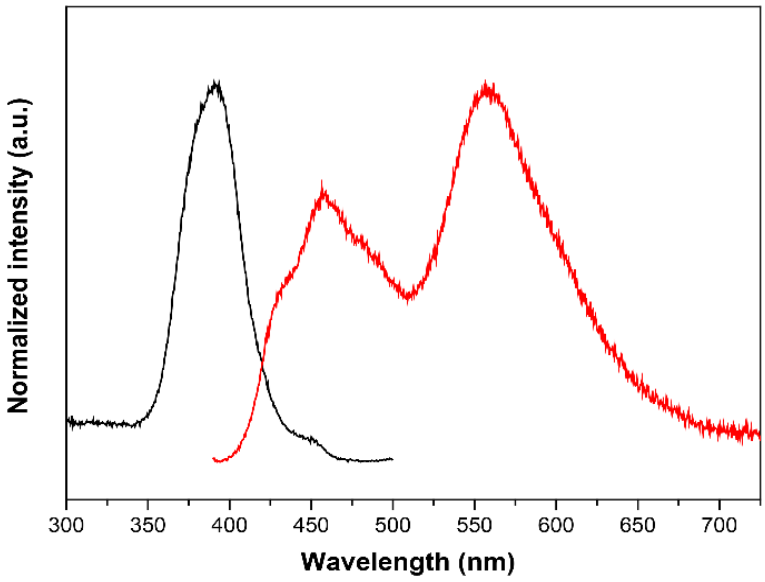

Figure 4.5. Excitation spectra of 2,2'-bipyridine-5,5'-dicarboxylic acid recorded at 294 K monitoring the emission at 570 nm (black) and emission spectra of the ligand at ambient temperature (294 K) with the excitation fixed at 375 nm (red).

Subsequently, excitation spectrum of Ru(II)metalloligand was acquired at ambient temperature (294 K) recording the emission at 730 nm. The spectrum consists of a main broad band ranging from 250 nm to *ca.* 650 nm with three different maxima peaking at 267 nm, 370 nm and 526 nm (Figure 4.6). On its part, 294 K excitation spectra of **4.4**$_{Ru-Gd}$ recorded at 730 nm exhibits similar pattern displaying a broad UV in the

aforementioned region peaking at 271 nm, 366 nm and 560 nm. The excitation spectrum of compound **4.5$_{Ru-Tb}$** recorded at 294 K monitoring emission 730 nm, presents high resemblance to $[RuL_3]Cl_2$ and **4$_{Ru-Gd}$** excitation spectra displaying a broad band 250 nm to *ca.* 650 nm with three different maxima peaking at 258 nm 366 nm 562 nm, respectively. Note that, the spectrum do not show any characteristic sharp lines ascribed to Tb^{3+}in the recorded emission wavelength which demonstrates that compounds **4.4$_{Ru-Gd}$** and **4.5$_{Ru-Tb}$** excitation is clearly dominated by $[RuL_3]Cl_2$ metalloligand.

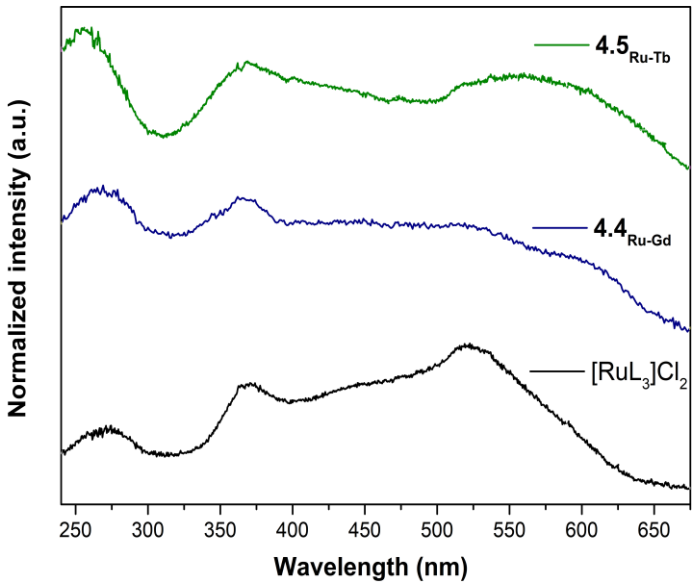

Figure 4.6. Excitation spectra of $[RuL_3]Cl_2$ (black, λ_{Em} = 730 nm), **4.4$_{Ru-Gd}$** (blue, λ_{Em} = 730 nm) and **4.5$_{Ru-Tb}$** (green, λ_{Em} = 730 nm) recorded at 294 K.

The emission spectrum of Ru(II)metalloligand recorded at 294 K excited at 375 nm (Figure 4.7) presents a broad band, from 600 to ca. 850 nm with the maxima located at 700 nm. Similarly, 294 K emission spectra of **4.4$_{Ru-Gd}$** and **4.5$_{Ru-Tb}$** recorded at 375 nm and 377 nm, presents a spectrum dominated by the aforementioned band peaking at 725 nm and 714 nm, respectively.

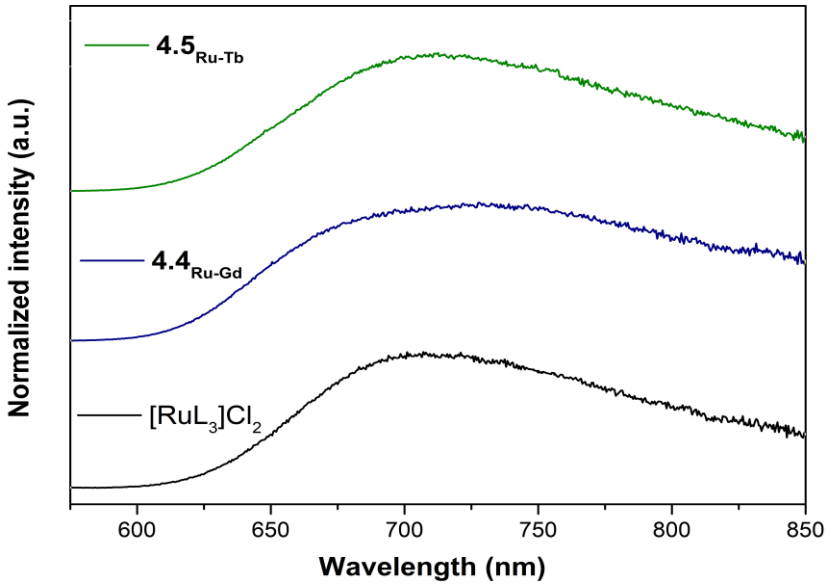

Figure 4.7. Ambient temperature (294 K) emission spectra of $[RuL_3]Cl_2$ (black, λ_{Exc} = 375 nm), **4.4**$_{Ru-Gd}$ (blue, λ_{Exc} = 375 nm) and **4.5**$_{Ru-Tb}$ (green, λ_{Exc} = 377 nm).

Temperature induced changes in the emission spectrum motivated us studying **4.4**$_{Ru-Gd}$ and **4.5**$_{Ru-Tb}$ emission profile at variable temperature.

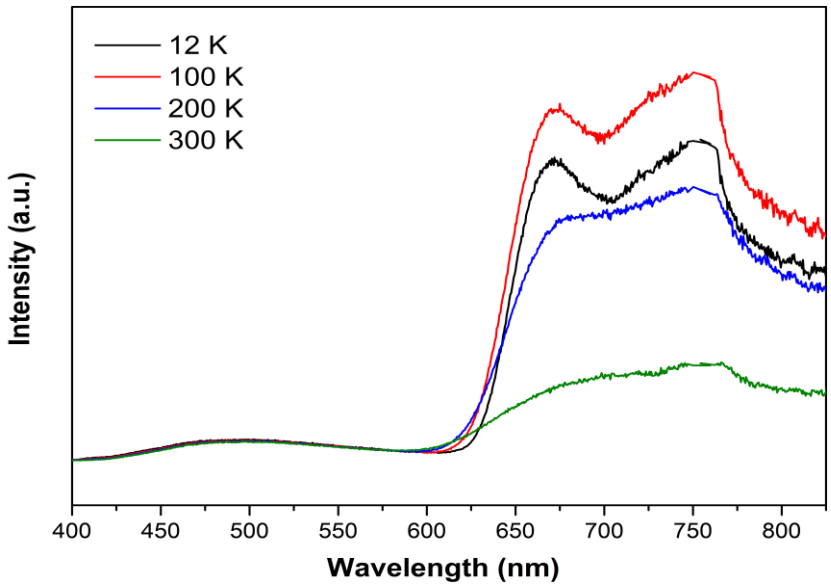

Figure 4.8. Emission spectra of **4.4**$_{Ru-Gd}$ recorded at 12 K, 100 K, 200 K and at 300 K monitoring the excitation at 375 nm.

Temperature increasing emission spectra of **4.4**$_{Ru-Gd}$ recorded at 12 K and incrementing by 100 K step with the excitation fixed at 375 nm is represented in Figure

4.8. As expected, temperature increasement directly repercuss on spectral intensity being the most prominent intensity diminishment in 200 K to 300 K step. The profile shown at low temperature is ascribed to first excited states being overpopulated and promoted a more efficient relaxation via fluorescent radiative pathways. Additionally, structural ordination and rigidity achieved at low temperature may promote enhancement in emissive intensity. Note that, temperature decreasing allows definition of spectra exhibiting at 12 K and 100 K well defined two maxima peaking at 654 nm and 753 nm.

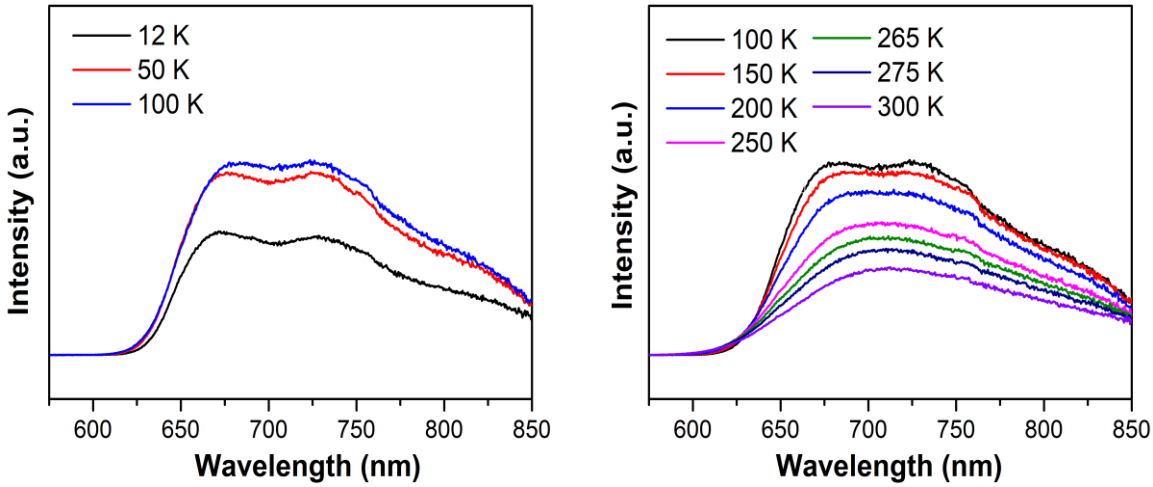

Figure 4.9. Emission spectra of **4.5**$_{\text{Ru-Tb}}$ recorded at 12 K, 50 K, 100 K, 150 K, 200 K, 250 K, 265 K, 275 K and 300 K with the excitation fixed at 377 nm.

On its part, temperature increasing emission spectrum of **4.5**$_{\text{Ru-Tb}}$ recorded at 12 K, 50 K, 100 K, 150 K, 200 K, 250 K, 265 K, 275 K and 300 K monitoring the excitation at 377 nm, $^5D_3$ excitation line, presents high remembrance with **4.4**$_{\text{Ru-Gd}}$ counterpart exhibiting a broad, from 600 nm to ca. 850 nm, with one or two maxima depending on the collecting temperature. In general, low temperature allows better spectral definition exhibiting two well defined maxima peaking at 668 nm and 745 nm. It is important to highlight that, two regimes can be differentiated in temperature increasing emission spectrum: from 12 K to 100 K, two maxima are appreciated and spectral intensity is favoured as temperature increases (Figure 4.13, left). Then, as temperature continues increasing from, 150 K to 300 K, as expected, signal intensity decreases and a single broad band peaking at 725 nm can be appreciated (Figure 4.13, right).

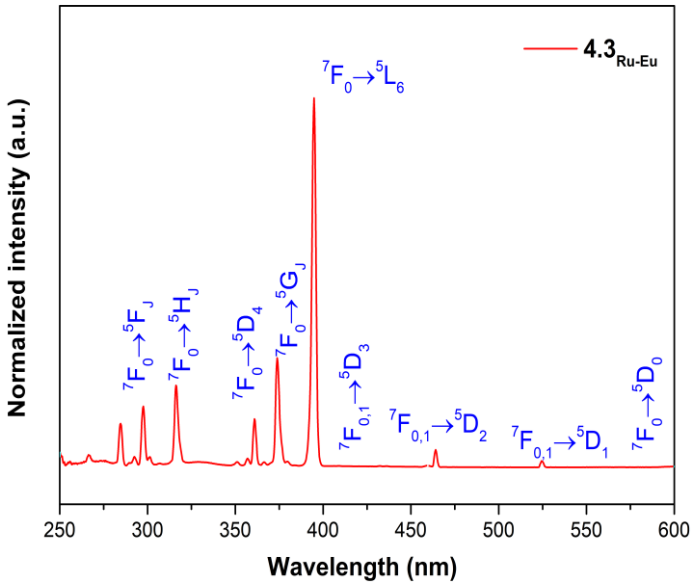

Figure 4.10. Excitation spectra of **4.3$_{Ru-Eu}$** recorded at 12 K and at monitoring the emission at 614.8 nm.

The excitation spectra of **4.3$_{Ru-Eu}$** recorded at 12 K detecting the strongest Eu^{3+} emission at 614.8 nm shows a set of sharp lines ascribed to the Eu^{3+} intra-4f transitions from the fundamental $^7F_0$ level to the $^5D_{0-4}$, $^5L_6$ and ^5G_J excited levels being completely absent Ru(II)metalloligand excitation bands in this spectrum (Figure 4.10).

The emission spectra of **4.3$_{Ru-Eu}$** recorded at 12 K with the excitation selected at 394.7 nm, Eu^{3+} $^5L_6$ level, is shown in Figure 4.11. The spectrum exhibits the characteristic sharp lines of the Eu^{3+} $^5D_0 \rightarrow {}^7F_{0-4}$ transitions. The dominance of the $^5D_0 \rightarrow {}^7F_2$ transitions over the $^5D_0 \rightarrow {}^7F_1$ transition is typical of Eu^{3+} environments without inversion centres, in line with that previously described in the structural section. Furthermore, the $^5D_0$ Eu^{3+} decay curve, recorded at 12 K monitoring the strongest emission at 614.8 nm under direct excitation at 394.7 nm (inset of Figure 4.18), is only properly fitted by a second order exponential function yielding two lifetimes of 0.22 ± 0.02 ms and 1.09 ± 0.01 ms, and with an averaged lifetime of 1.05 ms. This evidence is again in accordance with the presence of two Eu^{3+} sites in the **4.3$_{Ru-Eu}$** structure.

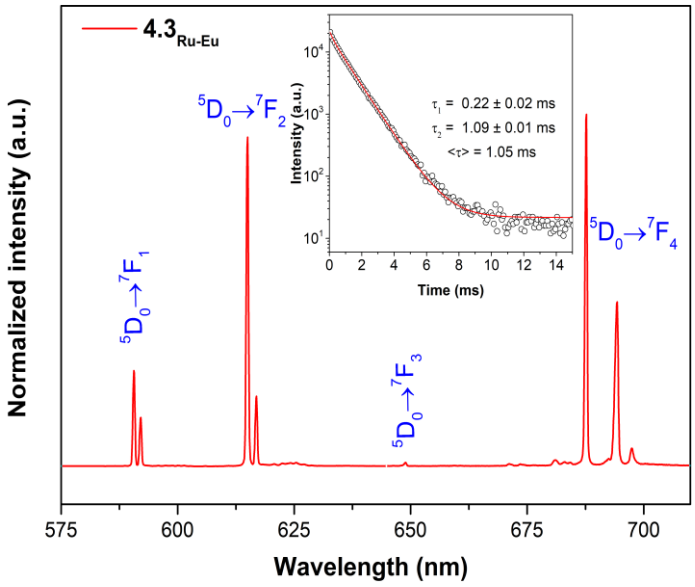

Figure 4.11. 12 K emission spectra of **4.3$_{Ru-Eu}$** fixing the excitation at 394.7nm. Inset: 12 K $^5D_0$ decay curve monitoring at 614.8 nm fixing the excitation at 394.7 nm fitted with a second order exponential decay function, $y = y_0 + A_1 \cdot \exp(-x/\tau_1) + A_2 \cdot \exp(-x/\boldsymbol{\tau_2})$ ($r^2 > 0.999$). the average lifetime was defined as $< \boldsymbol{\tau} >= (\boldsymbol{A_1\tau_1^2} + \boldsymbol{A_2\tau_2^2})/(\boldsymbol{A_1\tau_1} + \boldsymbol{A_2\tau_2})$.

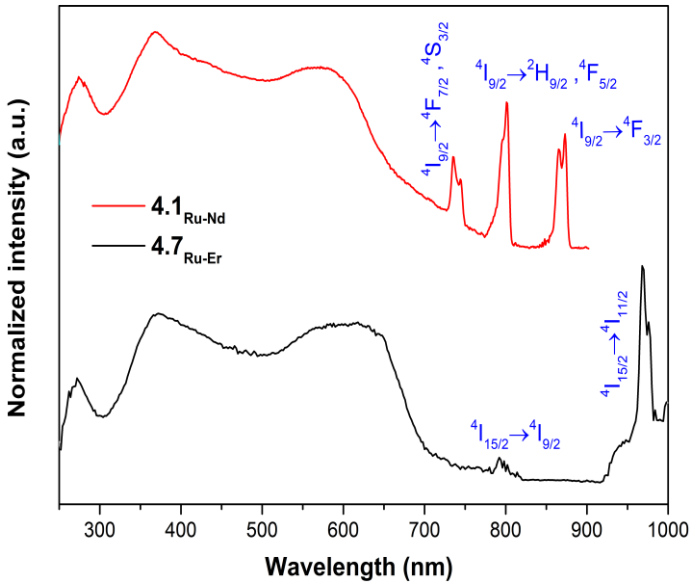

Figure 4.12. 12 K excitation spectra of **4.1$_{Ru-Nd}$** (red) and **4.7$_{Ru-Er}$** (black) monitoring the emission at 1057 nm and 1531 nm, respectively.

Subsequently, our attention was focused on compounds exhibiting emission in the near infrared region. For that purpose, **4.1$_{Ru-Nd}$** and **4.7$_{Ru-Er}$** were explored.

The excitation spectrum of **4.1$_{Ru-Nd}$** recorded at 12 K monitoring the emission at 1057 nm presents a broad band ranging from 250 nm to ca. 700 nm, in addition to a set of typical narrow lines peaking at 274 nm, 369 nm and 583 nm, respectively. Those bands are attributed to Nd^{3+} characteristic sharp emission lines attributed to $^4I_{9/2}\rightarrow{}^4F_{7/2},{}^4S_{3/2}$, $^4I_{9/2}\rightarrow{}^4H_{9/2},{}^4F_{5/2}$ and $^4I_{9/2}\rightarrow{}^4F_{3/2}$ transitions. The excitation spectrum of **4.7$_{Ru-Er}$** recorded at 1531 nm collected the same temperature displays the same broad band, from 250 to ca. 700 nm, in addition to a set of sharp lines located at 271 nm, 363 nm and 604 nm corresponding to Er^{3+} $^4I_{15/2}\rightarrow{}^4I_{9/2}$ and $^4I_{15/2}\rightarrow{}^4I_{11/2}$ transitions.

The emission spectra of **4.1$_{Ru-Nd}$** and **4.7$_{Ru-Er}$** were acquired fixing the excitation at 400 nm at 12 K. Compound **4.1$_{Ru-Nd}$** presents the typical narrow lines attribute to the Nd^{3+} $^4F_{3/2}\rightarrow{}^4I_{11/2}$ and $^4F_{3/2}\rightarrow{}^4I_{13/2}$ transitions. Note that, spectral response of the detector goes from 950-1700 nm, because of this, Nd^{3+} $^4F_{3/2}\rightarrow{}^4I_{9/2}$ emission transition, commonly appearing in the range 850-950 nm, with the maxima located at round 900 nm range is not observed properly in the collected spectra. Compound **4.7$_{Ru-Er}$**, on its part, exhibits characteristic emission lines of Er^{3+}attributed to $^4I_{13/2}\rightarrow{}^4I_{15/2}$ transition.

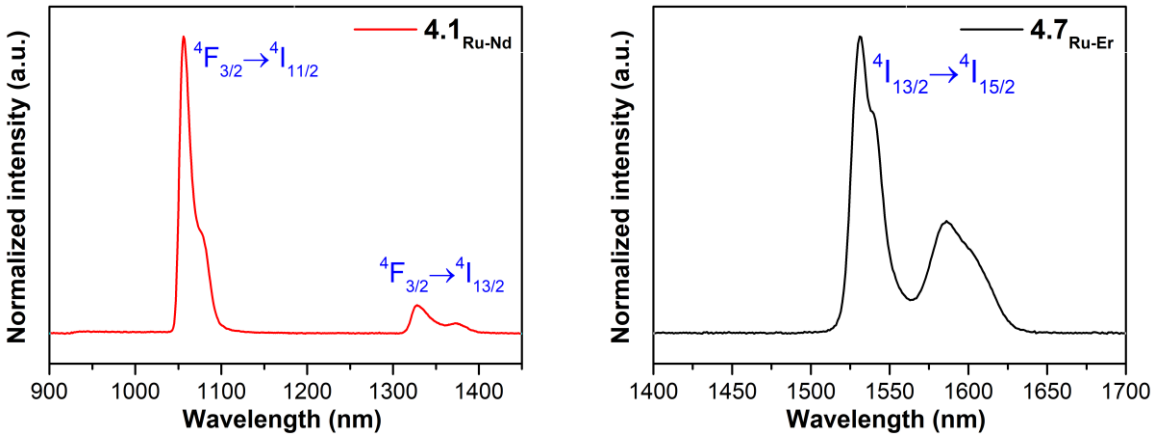

Figure 4.13. 12 K emission spectra of **4.1$_{Ru-Nd}$** (left) and **4.7$_{Ru-Er}$** (right) monitoring the excitation 400 nm.

4.4 Conclusions

To sum up, in this chapter we report the synthesis and characterization of a family of three-dimensional cationic metal-organic framework based on Ru(II)tris(2,2'-bipyridine-5,5'-dicarboxylate) metalloligand and Ln^{3+}. These coordination compounds display an isostructural nature exhibiting the formula $\{[(RuL_3)_2Ln_3]ClO_4\}_n$. In pursue of multifunctional materials, we explore photoluminescent properties and the capacity of being employed as heterogeneous catalyst in oxidative desulfurization.

For the application as heterogenous catalyst, compound **4.3$_{Ru\text{-}Eu}$** has been selected. Three catalytic loadings (5 mg, 10 mg and 20 mg) have been tested and unfortunately none of them shown conversions over 65 %. Additionally, we appreciated that, by the end of the catalytic cycle, catalyst suffers a transformation into another crystalline phase probably originating its deactivation.

On another level, 2,2'-bipyridine-5,5'-dicarboxylic acid ligand (L), ruthenium(II) metalloligand and compounds **4.1$_{Ru\text{-}Nd}$**, **4.3$_{Ru\text{-}Eu}$**, **4.4$_{Ru\text{-}Gd}$**, **4.5$_{Ru\text{-}Tb}$** and **4.7$_{Ru\text{-}Er}$** photoluminescent properties has been explored. Emission spectra of compounds **4.4$_{Ru\text{-}Gd}$** and **4.5$_{Ru\text{-}Tb}$** had demonstrated to be clearly dominated by a broad UV-Vis band similarly found in the emission of Ru(II)metalloligand. In the **4.5$_{Ru\text{-}Tb}$** case, contrary to what happens in compound **4.3$_{Ru\text{-}Eu}$** where characteristic emission of the ion is observed, none of the Tb^{3+} lines are appreciable. In view of the broad emission associated with the ligand, we decided to explore the emission of compounds with emissive properties in the near infrared region. Consequently, first, **4.1$_{Ru\text{-}Nd}$** and **4.7$_{Ru\text{-}Er}$** compounds excitation spectra were collected in the metal centred maximum excitation line, and subsequently, emission spectra centred in ligand associated maximum (at 400 nm) for both compounds. The emission spectra of **4.1$_{Ru\text{-}Nd}$** and **4.7$_{Ru\text{-}Er}$** presented the typical narrow lines ascribed to each metallic centre, concretely, $^4F_{3/2} \rightarrow {}^4I_{11/2}$ and $^4F_{3/2} \rightarrow {}^4I_{13/2}$ transitions for Nd^{3+} and $^4I_{13/2} \rightarrow {}^4I_{15/2}$ transition attributed to Er^{3+}; this evidence suggests the existence of an energy transfer from metalloligand excited tripled state and lanthanide excited state for the subsequent relaxation via radiative pathway.

4.5 References

1. Hasegawa, M.; Ohmagari, H.; Tanaka, H.; Machida, K. Luminescence of lanthanide complexes: From fundamental to prospective approaches related to water- and molecular-stimuli. *J. Photochem. Photobiol. C Photochem. Rev.* **2022**, *50*, 100484, doi:10.1016/J.JPHOTOCHEMREV.2022.100484.

2. Liu, H.; Peng, X.; Zeng, H. Synthesis, structure and luminescence property of Eu(III) metal-organic framework based on 2,2′-bipyridine-5,5′-dicarboxylic acid. *Inorg. Chem. Commun.* **2014**, *46*, 39–42, doi:10.1016/j.inoche.2014.04.037.

3. Congiu, M.; Alamiry, M.; Moudam, O.; Ciorba, S.; Richardson, P.R.; Maron, L.; Jones, A.C.; Richards, B.S.; Robertson, N. Preparation and photophysical studies of [Ln(hfac)$_3$DPEPO], Ln = Eu, Tb, Yb, Nd, Gd; interpretation of total photoluminescence quantum yields. *Dalton Trans.* **2013**, *42*, 13537–13545, doi:10.1039/C3DT51380G.

4. Saitoh, E.; Kobayashi, A.; Yoshida, M.; Kato, M. Reduction in Crystal Size of Flexible Porous Coordination Polymers Built from Luminescent Ru(II)-Metalloligands. *Cryst. Growth Des.* **2016**, *16*, 7051–7057, doi:10.1021/acs.cgd.6b01266.

5. Kobayashi, A.; Ohba, T.; Saitoh, E.; Suzuki, Y.; Noro, S.I.; Chang, H.C.; Kato, M. Flexible coordination polymers composed of luminescent ruthenium(II) metalloligands: Importance of the position of the coordination site in metalloligands. *Inorg. Chem.* **2014**, *53*, 2910–2921, doi:10.1021/ic402683j.

6. Zhang, S.R.; Du, D.Y.; Tan, K.; Qin, J.S.; Dong, H.Q.; Li, S.L.; He, W.W.; Lan, Y.Q.; Shen, P.; Su, Z.M. Self-Assembly versus Stepwise Synthesis: Heterometal–Organic Frameworks Based on Metalloligands with Tunable Luminescence Properties. *Chem. – A Eur. J.* **2013**, *19*, 11279–11286, doi:10.1002/CHEM.201301536.

7. Han, Y.; Sinnwell, M.A.; Teat, S.J.; Sushko, M.L.; Bowden, M.E.; Miller, Q.R.S.; Schaef, H.T.; Liu, L.; Nie, Z.; Liu, J.; et al. Desulfurization Efficiency Preserved in a Heterometallic MOF: Synthesis and Thermodynamically Controlled Phase Transition. *Adv. Sci.* **2019**, *6*, doi:10.1002/ADVS.201802056.

8. Mirante, F.; Mendes, R.F.; Almeida Paz, F.A.; Balula, S.S. High catalytic efficiency of a layered coordination polymer to remove simultaneous sulfur and nitrogen compounds from fuels. *Catalysts* **2020**, *10*, 1–15, doi:10.3390/catal10070731.

9. Gao, Y.; Mirante, F.; Castro, B. de; Zhao, J.; Cunha-Silva, L.; Balula, S.S. An Effective Hybrid Heterogeneous Catalyst to Desulfurize Diesel: Peroxotungstate@Metal–Organic Framework. *Mol. 2020, Vol. 25, Page 5494* **2020**, *25*, 5494, doi:10.3390/MOLECULES25235494.

10. Granadeiro, C.M.; Nogueira, L.S.; Julião, D.; Mirante, F.; Ananias, D.; Balula, S.S.; Cunha-Silva, L. Influence of a porous MOF support on the catalytic performance of Eu-polyoxometalate based materials: Desulfurization of a model diesel. *Catal. Sci. Technol.* **2016**, *6*, 1515–1522, doi:10.1039/c5cy01110h.

11. Øien, S.; Agostini, G.; Svelle, S.; Borfecchia, E.; Lomachenko, K.A.; Mino, L.; Gallo, E.; Bordiga, S.; Olsbye, U.; Lillerud, K.P.; et al. Probing reactive platinum sites in UIO-67 zirconium metal-organic frameworks. *Chem. Mater.* **2015**, *27*, 1042–1056, doi:10.1021/cm504362j.

12. Constable, E.C. Homoleptic Complexes of 2,2′-Bipyridine. *Adv. Inorg. Chem.* **1989**, *34*, 1–63, doi:10.1016/S0898-8838(08)60014-8.

13. Eskelinen, E.; Luukkanen, S.; Haukka, M.; Ahlgrén, M.; Pakkanen, T.A. Redox and photochemical behaviour of ruthenium(II) complexes with H2dcbpy ligand (H2dcbpy = 2,2′-bipyridine-4,4′-dicarboxylic acid). *J. Chem. Soc. Dalt. Trans.* **2000**, 2745–2752, doi:10.1039/b004751l.

14. Diesel, D.; Metal, P. An Effective Hybrid Heterogeneous Catalyst to Desulfurize Diesel: Peroxotungstate@Metal– Organic Framework. **2020**, 1–13.

15. Llunell, M.; Casanova, D.; Cirera, J.; Bofill, J. M.; Alemany, P.; Alvarez, S.; Pinsky, M.; Avnir, D. Program for the Stereochemical Analysis of Molecular Fragments by Means of Continuous Shape Measures and Associated Tools. *SHAPE, v1.1b; Barcelona, Spain* **2005**, 1–35.

16. Brites, C.D.S.; Millán, A.; Carlos, L.D. Lanthanides in Luminescent Thermometry. *Handb. Phys. Chem. Rare Earths* **2016**, *49*, 339–427, doi:10.1016/bs.hpcre.2016.03.005.

17. Haldar, R.; Bhattacharyya, S.; Maji, T.K. Luminescent metal–organic frameworks and their potential applications. *J. Chem. Sci.* **2020**, *132*, 1–25, doi:10.1007/s12039-020-01797-y.

18. Li, L.; Tang, S.; Lv, X.; Cai, J.; Wang, C.; Zhao, X. A series of exceptionally robust luminescent coordination polymers based on a bipyridyldicarboxylate ligand and rare-earth-metal ions. *Eur. J. Inorg. Chem.* **2013**, 6111–6118, doi:10.1002/ejic.201301010.

Chapter 5

A family of Ln^{3+} complexes based on diclofenac

El capítulo 5 está sujeto a confidencialidad por la autora

Chapter 6

Annexes

Summary

This last chapter summarizes three experimental projects conducted in parallel to the work presented in previous chapters. Briefly, the novelty of the work can be outlined as:

- I) Based on the 3-amino-4-hydroxybenzoic acid ligand (already discussed in Chapter 2), a novel mixed heterobimetallic Y/Eu-MOF was synthesised looking for synergy and enhancement in properties exhibit in cyanosilylation reaction concerning Y- or Eu-MOFs counterparts. Furthermore, this heterobimetallic MOF has allowed hydroboration of carbonyls to be studied. We decided not to be discussed it in Chapter 2 and to dedicate an independent section for this last reason. This work has already been published.
- II) The combination between 4,4'-azopyridine and dicarboxylic acids (aliphatic or aromatic) presents infinite combinations in the synthesis of porous MOF. With this aim, in this second annexe, we will develop the synthesis and characterization of nine novel structures based on Zn^{2+} and Cd^{2+} and their photoluminescent properties will be explored.
- III) Finally in the third annexe, a novel Zn^{2+} and tetrazole based three-dimensional MOF is presented with promising photoluminescent and adsorption properties.

ANNEXE 1

6.1 Introduction. A Mixed Heterobimetallic Y/Eu-MOF for the Cyanosilylation and Hydroboration of Carbonyls

Metal-organic frameworks are multifunctional inorganic-organic systems composed of organic ligands and metallic nodes and since the 90s have emerged as promising materials for infinite applications, among them heterogeneous catalysis.[1,2]

Their intrinsic porosity along with easy tunability and functionalization are some of their appealing characteristics to be employed in heterogeneous catalysis.[3] The structural porosity provides a confined space to which substrates have access and catalysis can take place. Furthermore, MOFs robustness provides stable skeletons where unsaturated metallic centres can act as Lewis acid catalyst, subsequent displacement of coordinated solvent molecules could occur, and the further activation of the substrates already accessed through the channels might help the catalysis evolve.[4]

In this context, cyanosilylation and hydroboration reactions catalysed by heterogeneous catalysts, such as MOFs, are presented as interesting approaches to the formation of cyanohydrins and alcohols.[5,6] Cyanosilylation reaction is an important synthetic tool for C–C bond formation in organic systems since it gives access to key intermediates of great interest in the field of pesticides and medical applications among which as α-hydroxy acids, α-hydroxy ketones, α-amino acids, and β-amino alcohols can be mentioned.[7,8]

Nonetheless, within this frame of reference, the number of reported Ln-MOF acting as heterogeneous catalyst in cyanosilylation reaction results is relatively scarce (Table 2.2) summarizes the reported examples exhibiting activity, so far).[5,9,18–24,10–17] Moreover, to the best of our knowledge, lanthanide-based heterobimetallic MOFs have never been applied. In the field of hydroboration, the context is even more unexplored. The synthesis of alcohols through this route has been explored through MOF systems based on Ti, Fe, Co and Mg [25–30] but there are no examples with these supramolecular entities built on lanthanides precursors. Therefore, in this work, the first example of yttrium and europium-based mixed-MOF with the formula $\{[Y_{3.5}Eu_{1.5}L_6(OH)_3(H_2O)_3]\cdot 12DMF\}_n$ is presented taking the strong background of our group in the examination of these supramolecular systems in catalysis.[23,24,31]

The heterobimetallic Y/Eu-MOF presented herein was designed looking for synergy and enhanced catalytic activity concerning the isostructural pristine counterparts which were able to exhibit activity for seven cycles (with very low catalytic loading of 0.5 mol%), no catalyst leaking, TOF values of 106 h^{-1} and 1031 h^{-1} and preferred suitability towards aldehydic and ketonic substrates for Y-MOF[23] and Eu-MOF[31], respectively.

Taking all into consideration, our interest lies in exploring the catalytic activity of this novel heterobimetallic MOF based on the 3-amino-4-hydroxybenzoic acid polytopic ligand in the cyanosilylation and hydroboration reactions of aldehydes and ketones of diverse nature under solvent-free and environmentally friendly conditions to eventually conclude whether catalytic activity enhance on concerning to initial counterparts.

6.2 Materials and methods

6.2.1 Compound synthesis

Synthesis of $\{[Y_{3.5}Eu_{1.5}L_6(OH)_3(H_2O)_3]\cdot 12DMF\}_n$, namely $\mathbf{6.1_{Y\text{-}Eu}}$: 3-amino-4-hydroxybenzoic acid (0.010 g, 0.0625 mmol) was dissolved in 0.2 mL of DMF containing 10 µL of Et_3N (0.072 mmol). In a separated vial $Eu(NO_3)_3\cdot 5H_2O$ (0.006 g, 0.0145 mmol) and $Y(NO_3)_3\cdot 6H_2O$ (0.011 g, 0.0289 mmol) salts were dissolved into a 0.8 mL of distilled water. After dissolution, 0.2 mL of DMF and 0.8 mL of H_2O were added to metal and ligand solutions, respectively. Finally, the metal solution was added dropwise and under continuous agitation to the ligand solution. The obtained brown solution was introduced to the oven at 100°C for 2 h in a screw-capped vial (6 mL) to yield hexagonal single crystals.

6.2.2 Catalysis

General procedure for the cyanosilylation reaction: In a 1 mL vial with a septum screw capped equipped with a stirring bar, Y/Eu-MOF catalyst (0.5 mol%) was weighted. Subsequently, the corresponding amount of carbonylic compound $\mathbf{6.1_{Y\text{-}Eu}}$ (0.25 mmol) was added followed by trimethylsilyl cyanide (TMSCN) (34 µL, 0.275 mmol, 1.1 equiv.) and the reaction was stirred under inert N_2 atmosphere at room temperature during 24 h. Once the reaction was finished, the catalyst was removed by centrifugation (1230 rpm, 5 min) and washed with DCM (2 x 0.5 mL) obtaining the corresponding pure products **2** and **3** after removal of the solvent with a rotary evaporator. When not fully conversion was reached the product was purified by column chromatography using hexane as eluent.

General procedure for the hydroboration reaction: In a 1 mL vial with a septum screw capped equipped with a stirring bar, Y/Eu-MOF catalyst (0.5 mol%) was weighted. Subsequently, the corresponding amount of carbonylic compound $\mathbf{6.1_{Y\text{-}Eu}}$ (0.25 mmol) was added followed by pinacolborane (HBPin) (40 µL, 0.275 mmol, 1.1 equiv.) and the reaction was stirred under inert N_2 atmosphere at room temperature during the corresponding time indicated on the table. After that time, the hydrolysis of the final product was carried out by adding NaOH (0.1 M, 0.5 mL) and Et_2O (0.5 mL) and the mixture was stirred overnight. Once the reaction was finished, the catalyst was removed by centrifugation (12300 rpm, 5 min) and washed with DCM (2 x 0.5 mL) obtaining the corresponding product **4** after removal of the solvent wia the rotary evaporator.

6.3 Results and discussion

6.3.1 Structural characterization

The solvothermal reaction between 3-amino-4-hydroxybenzoic acid (H_2L) ligand and Y-Eu metal mixture in a basic media yields a three-dimensional porous metal-organic framework that crystallizes in a hexagonal *P*63/*m* space group. The asymmetric unit of this supramolecular entity is composed of a deprotonated ligand molecule, two metal atoms with special positions in addition to a coordinated water molecule and a hydroxyl bridge which acts as a connector among neighbouring metallic centres. Note that, taking into consideration that metals are randomly distributed within the crystal structure, a tentative formula is presented which is corroborated by the bulk properties of the material (see ICP-MS results in Table A6.2 or SEM-EDX results in Figure A6.3).

Therefore, regarding the metal environment, two surroundings are described: nine coordinated [MN_3O_6] and eight coordinated [MO_8] environments, which according to continuous shape measurements confirm that spherical capped square antiprism (TCTPR-9) and triangular dodecahedron (TDD-8) polyhedra, respectively (Table A6.5 and Table A6.6). The former coordination environment is composed of three hydroxyl oxygens and amino atoms from L in addition to three additional oxygen atoms belonging to a ligand hydroxyl group. The latter metallic nucleus is composed of the coordination of a water solvent molecule oxygen belonging to a hydroxyl bridge along with six oxygen atoms corresponding to two ligand hydroxyl and two carboxylate moieties.

As aforementioned, hydroxyl bridges μ_3-OH^- join metallic centres constructing $M_5(OH)_3$ secondary building units in the structure, being ligand connectors among different sbu. Regarding the connectivity of the supramolecular entity from the topological point of view six-connected nodes are described, which according to TOPOS software [32] examination the framework dispose of ***acs*** network with ($4^9 \cdot 6^6$) point symbol. Intrinsic porosity of **6.1$_{Y\text{-}Eu}$** (according to PLATON-v1.18[33] cavities corresponds with 19 % volume of the structure) enables solvent crystallization molecules to be trapped whiting the pores; concretely, DMF molecules have been demonstrated to be located in the microchannels.

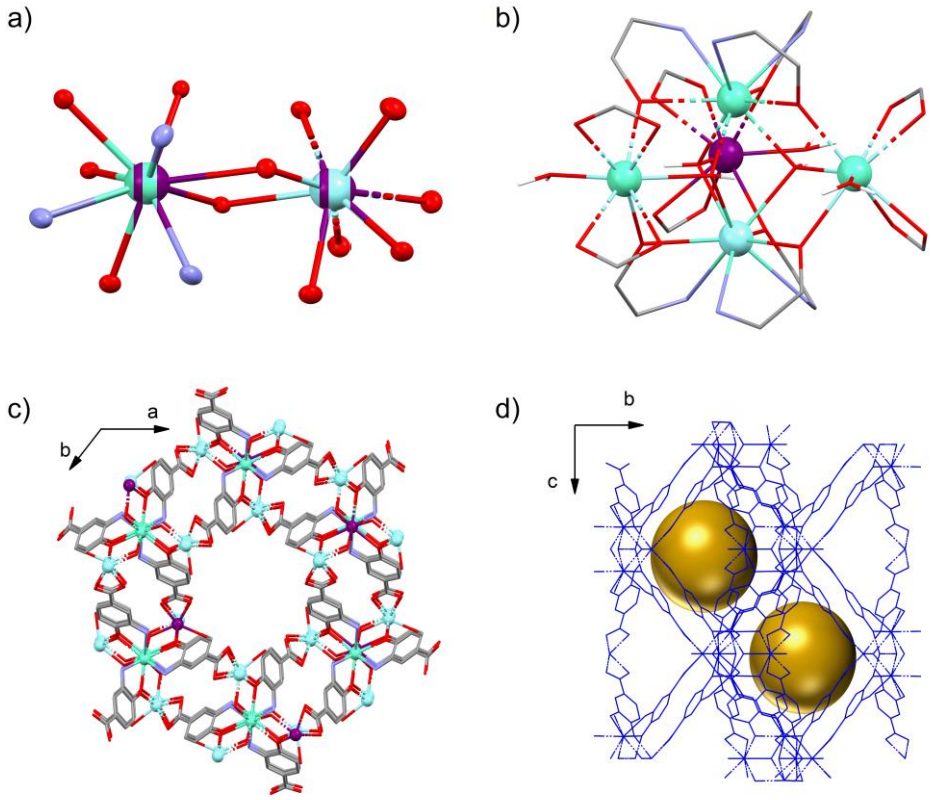

Figure 6.1. Perspective view of the **a)** metal coordination environments found in heterobimetallic compound **6.1$_{Y\text{-}Eu}$. b)** view of the pentametallic nodous where $M_5(OH)_3$ *sbu* are appreciable. **c)** View for the formation of the 1 D channels; **d)** The cavities present in the structure along *a* axis. Color code: Y (green), Eu (purple), C (grey), O (red), N (blue) and H (white). Note that due to the altering and randomly oriented disposition metals an approximated representation has been performed taking into consideration the proposed formula of $\{[Y_{3.5}Eu_{1.5}L_6(OH)_3(H_2O)_3]\cdot 12DMF\}_n$.

Single-crystal X-ray diffraction allowed proposing an approximated formula of the heterobimetallic catalyst which was further confirmed by FT-IR, ICP-AES, PXRD and SEM-EDX. For a detailed explanation of FT-IR and PXRD please check supporting information in Figure A6.1 and Figure A6.2, respectively.

ICP-AES analysis conducted in heterobimetallic compound **6.1$_{Y\text{-}Eu}$** exhibited an yttrium content of 1672 mg /L (corresponding to 18.8 mM of Y^{3+}) and a europium content of 1268 mg /L (8.34 mM Eu^{3+}). The calculated Y to Eu relationship gives 2.25 which is very much in line with the proposed formula where a proportion of 2.33 is expected. Additionally, SEM-EDX mapping confirms that both metals are present in a single crystal. However, the mapping spectrum performed in one single crystal showed a relatively higher Y^{3+} to Eu^{3+} proportion; for the crystal in which the spectrum was collected a relationship of 3.25 regarding Y^{3+} to Eu^{3+} was calculated. This is due to the uneven

distribution of metals through catalyst structure. Nonetheless, the proposed formula which is derived by single crystal X ray diffraction, powder X-ray diffraction, SEM-EDX and ICP-AES is consistent and summarizes the best approximation for data obtained in the aforementioned techniques.

6.3.2 Catalytic activity

6.3.2.1 Establishing optimal reaction conditions

The catalytic activity of Y/Eu-MOF, in advance **6.1**$_{\mathbf{Y\text{-}Eu}}$ (0.5 mol%) was initially evaluated in the cyanosilylation reaction of carbonyl compounds (**1**) using TMSCN as a nucleophile, solvent free reaction conditions, room temperature and N_2 atmosphere. We started by employing the same conditions used in Y and Eu counterparts.[23,31], Initially, we test the reaction blank, in the absence of catalyst only 8 % conversion after 14 h.

Subsequently, we performed optimization of the reaction of hydroboration rection according to how is summarized in (Table A6.7). First of all, the reaction was tested with solvents of different nature as well as without solvent (entries 1-5), obtaining the best result in the absence of solvent (entry 1, Table A6.7). Finally, the amount of catalyst was also tested (entries 6-8) observing that with a slight increase from 0.35 to 0.5 mol% the reaction took place with full conversion (entry 6).

6.3.2.2 Y/Eu-MOF catalysed cyanosilylation and hydroboration reaction of carbonyl compounds

Under optimized reaction conditions (1.1 equiv. TMSCN, 0.5 mol% catalyst, room temperature) the scope of the cyanosilylation reaction was evaluated with 5 highly reactive aldehydes of different natures such as aromatic, heteroaromatics and aliphatic, demonstrating that independently of the nature of the substituent, the reaction takes place with very good to excellent conversions (89-99 %) after only 24 h (Scheme 6.1). Later on, less reactive and sterically demanding ketones were tested observing a significant decrease in conversion (74-77 %) when electron-donating or electron-withdrawing substituents were located at *para*-position, whereas again excellent conversion was achieved with aromatic, heteroaromatics and aliphatic substrates (91-99 %) (Scheme 6.1). These results overpass the ones published until the moment in

bibliography[14–16] and have similar catalytic behaviour with our pristine Eu-MOF examined in detail in Chapter 2.

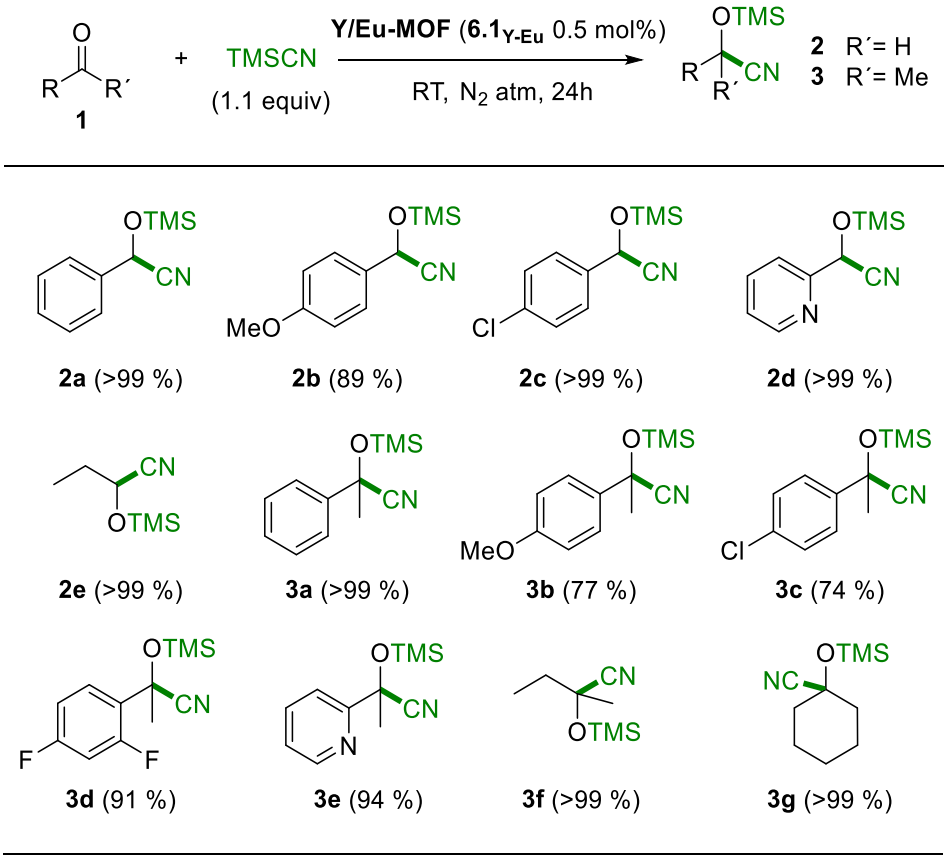

Scheme 6.1. Scope of the cyanosilylation reaction using aldehydes and ketones.

Afterwards, having hydroboration optimal conditions fixed, the scope of the hydroboration reaction was evaluated again using a broad range of different ketones (Scheme 6.2). The use of electron-donating groups in the *para*-position of the aromatic ring negatively influenced the catalytic reaction, causing the reaction time to increase from 24 h to 48 h or even 120 h to obtain moderate conversions (45-67 %). This influence on the increase in reaction time did not take place when electron-withdrawing substituents were used, observing that regardless of the position of the aromatic ring in which the substituents were found, yields were good (71-90 %). Furthermore, heteroaromatics ketones reached good results in only 24 h of reaction (88 %). The steric hindrance of diaryl ketone, as well as α,β-unsaturated ketones, increases the reaction time to 48 h to achieve full conversion. Aliphatic ketones of different nature were tested

providing good results (95-99 %). Finally, we decided to test cyclic ketones, which are usually less employed obtaining moderate results (61-63 %).

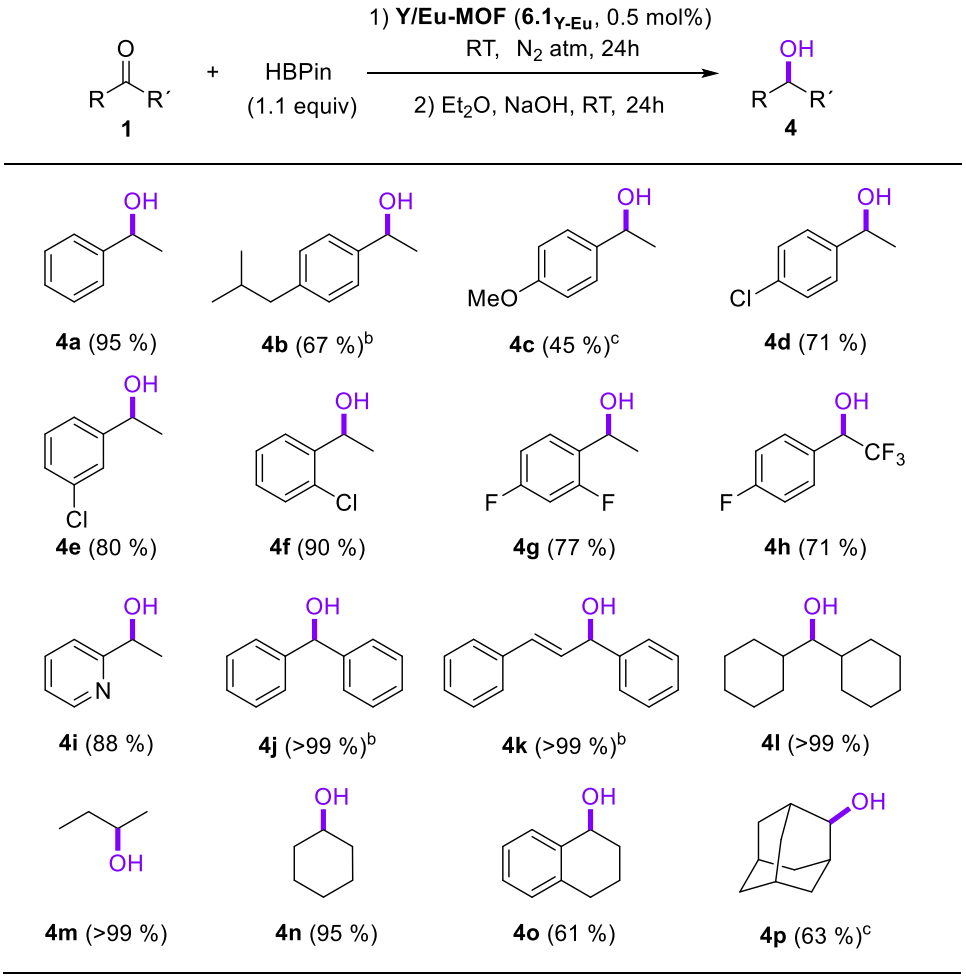

Scheme 6.2. Scope of the hydroboration reaction of ketones. a) Reaction carried out during 24 h. b) Reaction carried out during 48 h. c) Reaction carried out during 120 h.

6.3.2.3 Catalyst recyclability

Recyclability tests were also investigated to study the heterogeneous nature of the catalyst. For a detailed procedure consult Appendix 6.9. The catalyst was dried under vacuum and then charged with a new set of reagents to evaluate its re-cyclability. The corresponding products were obtained in 28 % and 61 % for cyanosilylation and hydroboration, respectively, and in another consecutive cycle, 0 % and 15 % of conversion, respectively, were achieved (Figure 6.2).

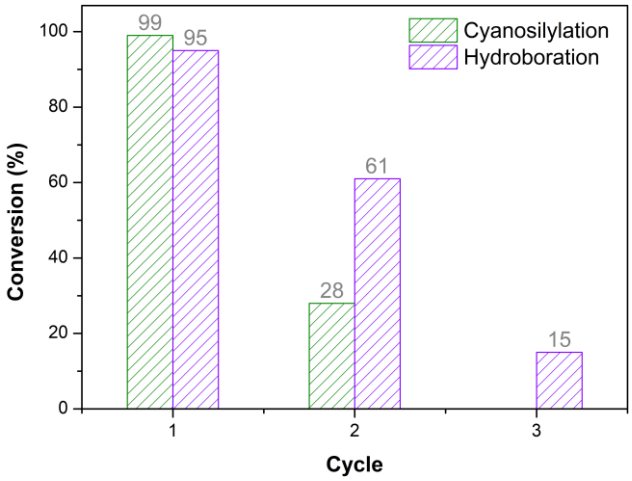

Figure 6.2. Study of the recyclability of Y/Eu-MOF (0.5 mol%) catalyst on the cyanosilylation and hydroboration reaction of acetophenone as carbonyl substrate.

6.3.2.4 Catalyst leaching

A leaching test was also carried out in the case of the hydroboration reaction (Scheme A6.3). For that, after the first and second reaction of the recyclability test, the catalyst was removed by centrifugation and the supernatant was filtered through a plug of celite and dried under vacuum. Then, 1-(pyridin-2-yl)ethan-1-one (1i) and HBPin were added to the crude of the corresponding reaction cycle and the reaction was stirred under an inert N_2 atmosphere at room temperature for 24 h. After that time, an aliquot was analysed by 1H NMR obtaining in the first cycle a 38 % of conversion, and in the second cycle a 13 % of product, corroborating the leaching of Y or Eu.

To conclude, green chemistry metrics such as the atomic economy (AE), mass intensity (MI), reaction mass efficiency (RME), and carbon efficiency (CE) were calculated for both reactions studied (Table 2.3) to evaluate if the reactions are eco-friendly.

Overall transformation according to green-chemistry metrics in the optimized catalytic conditions in the cyanosilylation of benzaldehyde with TMSCN in presence of **6.1**$_{Y\text{-}Eu}$ catalyst was evaluated and calculated values are summarized in Table 2.3. Note that, obtained values are comparable to those reported previously for related lanthanide-based MOFs [12,34] and suggests that overall transformation is eco-friendly and overcome health and environmental problems derived from the chemical industry.

Table 6.1. Green metrics values (AE, MI, RME and CE) were calculated for the Y/Eu-MOF catalyst in the cyanosilylation and hydroboration reaction.

	Y/Eu-MOF catalysed	
Green Chemistry Metrics	**Cyanosilylation**	**Hydroboration**
Atomic economy (AE)	100 %	49.1 %
Mass Intensity (MI)	1.13	2.41
Reaction mass efficiency (RME)	95.7 %	46.8 %
Carbon Efficiency (CE)	96.8 %	52.1 %

6.4 Conclusions

Herein, we report the synthesis and characterisation of, to the best of our knowledge, the first heterobimetallic Y/Eu-MOF based on 3-amino-4-hydroxybenzoic acid ligand. This novel material was synthesised looking for synergy and enhancement in properties exhibit in cyanosilylation reaction concerning Y- or Eu-MOFs counterparts and has been thoroughly characterized by means of X-ray crystallography, FTIR, ICP-MS, and PXRD.

Concretely, Y/Eu-MOF has demonstrated impressive catalytic efficiency in the cyanosilylation and hydroboration reaction of carbonyl compounds with a reduced recyclability compared to related MOFs. Comparing to Y- or Eu-MOFs counterparts, which exhibited no erosion of the catalytic activity in 7 consecutive cycles, the recyclability of the heterobimetallic material is decreased in a 71 % from the first to the second catalytic cycle. Nonetheless, evaluated overall transformation according to green-chemistry metrics in the optimized catalytic conditions for cyanosilylation reaction demonstrates that overall transformation is eco-friendly and overcome health and environmental problems derived from the chemical industry. Also, it must be noticed that obtained values are comparable to those reported previously for related lanthanide-based MOFs and very similar to Y- or Eu-MOFs counterparts.[12,34]

ANNEXE 2

6.5 Introduction. Synergetic combination of 4,4'-azopyridine and diacids for the synthesis of photoluminescent coordination polymers based on d^{10} metals

In the attempt to synthesise novel MOFs, the combination of two or more ligands of diverse nature, presenting different sizes, shapes and coordination features can be a convenient synthetic route. Given that the combination can provide synergetic coordination of such ligands to a metal centre it is possible to produce multifunctional MOFs with tuneable and tailorable functionalities within a single material.[35,36]

In this sense, for this second annexe, we wanted to try this synthetic approach and selected 4,4'-azopyridine and a family of substituted and non-substituted aliphatic diacids for the preparation of novel MOFs based on group 12 metals, concretely, Zn^{2+} and Cd^{2+} for the subsequent analysis of photoluminescent properties. Having in mid that, group 12 metals do not afford d-d transitions due to closed-shell configuration, and consequently, lacking of luminescence quenching.

In general, group 12 based CPs and MOFs afford a wide range of coordination environments[18,19] with improved photoluminescent properties with respect to pristine ligand derived by the robustness and enhanced rigidity to the system by restricting molecular motions/vibrations to minimize the non-radiative loss.

Therefore, herein we will describe the rational synthesis and characterization of a family of compounds based on Zn^{2+} or Cd^{2+}, 4,4'-azopyridine and a dicarboxylic acid (glutaric acid, 3-methylglutaric acid, succinic acid, 2-methylsulccinic acid, L- or D-malic acid and L- or D- tartaric acid) for the study of the photoluminescent properties.

6.6 Materials and methods

6.6.1 Compound synthesis

General procedure for the synthesis of 6.2–6.10: 0.0184 g (0.1 mmol) of 4,4'-azopyridine and 0.1 mmol of the corresponding diacid were dissolved in 1 mL equal DMF/H_2O solvent-mixture. To this solution, 0.1 mmol of the appropriate metal solution dissolved in the same solvent mixture was added dropwise. Table 6.2 summarizes the synthetic combinations employed. The resulting orange solution was placed in a screw-capped vial (6 mL) at 95 ºC overnight to yield an orange single crystal.

Table 6.2. Selected diacid and metals for the synthesis of compounds **6.2**–**6.10**.

Compound	Diacid	Metal
6.2$_{\text{Cd-glu}}$	Glutaric acid	Cd
6.3$_{\text{Cd-3Mglu}}$	3-methyl glutaric acid	Cd
6.4$_{\text{Cd-suc}}$	Succinic acid	Cd
6.5$_{\text{Zn-suc}}$	Succinic acid	Zn
6.6$_{\text{Zn-2Msuc}}$	2-methyl succinic acid	Zn
6.7$_{\text{Cd-Lmal}}$ and **6.8**$_{\text{Cd-Dmal}}$	L-/D- malic acid	Cd
6.9$_{\text{Cd-Ltar}}$ and **6.10**$_{\text{Cd-Dtar}}$	L-/D- tartaric acid	Cd

6.6.2 Chiroptical properties

General procedure for circular dichroism experiments

Samples for CD measurements were prepared as follows: a precision weighted amount of material (2 mg) was suspended in mili-Q H_2O (4 mL) and sonicated over 30 min.

6.7 Results and discussion

6.7.1 Structural characterization

Solvothermal reaction between 4,4'-azopyridine, the corresponding diacid and Cd^{2+} or Zn^{2+} metal solution yields a family of structure with diverse dimensionality. Table 6.3 contains a summary of the obtained type of structure. Single crystals with measurable quality have been acquired for compounds **6.2**, **6.3**, **6.4**, **6.5**, **6.6**, and **6.10**. Nonetheless, PXRD data and CD studies have demonstrated that compound **6.9**$_{\text{Cd-Ltar}}$ and **6.10**$_{\text{Cd-Dtar}}$ are isostructural and enantiomers among them. Additionally, because of the structural similarity between malic acid and tartaric acid and coordination mode displayed by compound that **6.10**$_{\text{Cd-Dtar}}$ we thought about the possibility of being **6.7**-**6.10** isostructural. Therefore, we performed PXRD analysis and confirm the isostructural nature (Figure 6.4).

Table 6.3. Dimensionality of the obtained structures

Compound	Type of structure
6.2$_{\text{Cd-glu}}$	Interpenetrated 3D
6.3$_{\text{Cd-3Mglu}}$	Interpenetrated 3D
6.4$_{\text{Cd-suc}}$	2D
6.5$_{\text{Zn-suc}}$	3D
6.6$_{\text{Zn-2Msuc}}$	2D
6.7$_{\text{Cd-Lmal}}$ and **6.8**$_{\text{Cd-Dmal}}$	2D
6.9$_{\text{Cd-Ltar}}$ and **6.10**$_{\text{Cd-Dtar}}$	2D

In essence, in all cases 4,4'-azopyridine coordinates to metal centre by the nitrogen of the pyridyl group and there are the carboxylate groups of the diacids which rule not only the coordination mode but also the dimensionality of the final structure. Briefly, Figure 6.3 contains a packed structure and an excerpt of the where the coordination mode adopted by each diacid is depicted.

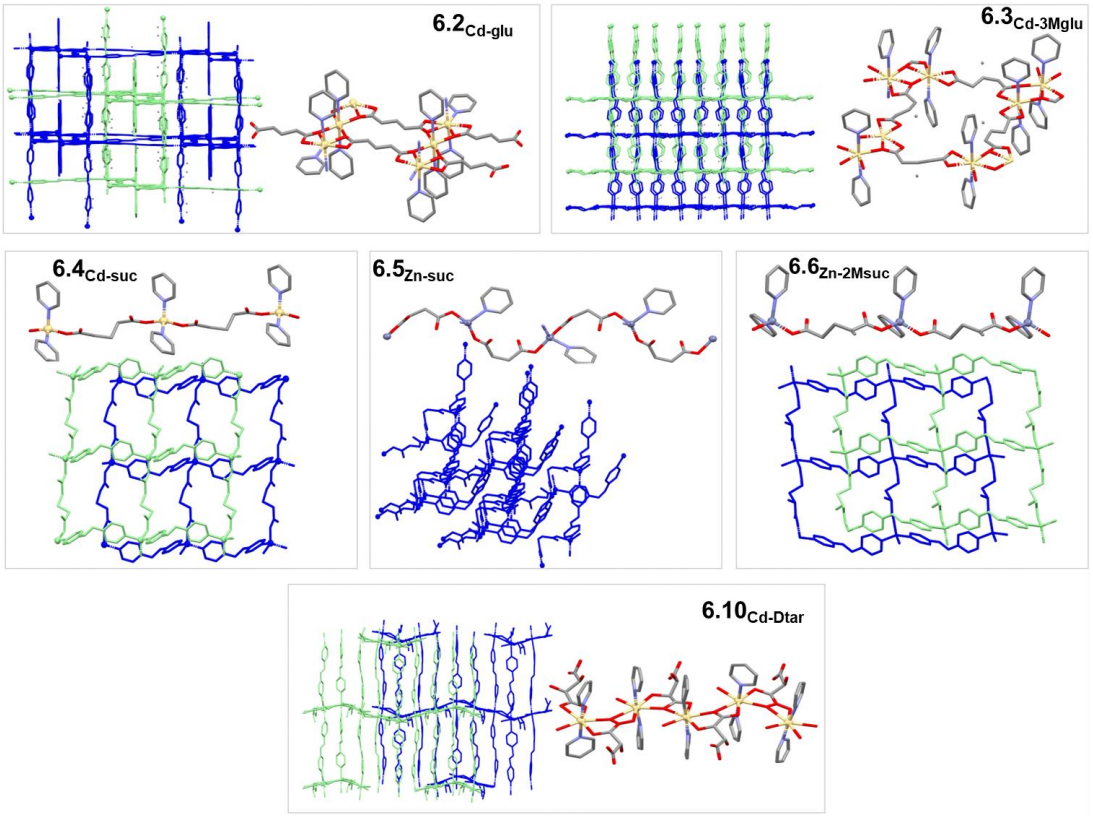

Figure 6.3. Perspective view of the packed structure and view of the diacid coordination mode for compounds **6.2**-**6.10**. In all cases, hydrogens have been omitted and 4,4'-azopyridine ligand coordination been simplified to a pyridine ring for the sake of clarity.

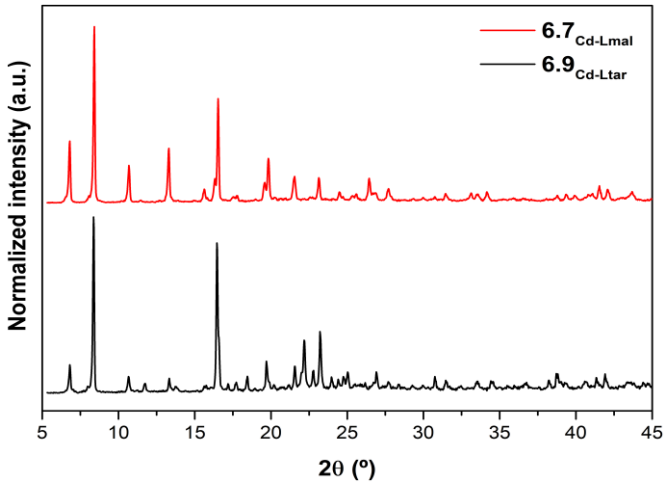

Figure 6.4. Figure of the PXRD patter of compound **6.7**$_{\text{Cd-Lmal}}$ and **6.9**$_{\text{Cd-Ltar}}$.

6.7.2 Photoluminescence measurements

In the following section, solid state photoluminescent properties of the aromatic 4,4'-azopyridine ligand and compounds **6.2**$_{\text{Cd-glu}}$, **6.3**$_{\text{Cd-3Mglu}}$, **6.4**$_{\text{Cd-suc}}$, **6.7**$_{\text{Cd-Lmal}}$ and **6.9**$_{\text{Cd-Ltar}}$ will be explored in detail.

The excitation spectrum of 4,4'-azopyridine collected at 294 K monitoring the emission at 394 nm consists of a broad UV band (300–350 nm) with three maxima located at 306, 320 and 334 nm which can be attributed to organic linker π–π* transitions. Ligand emission spectrum acquired at 294 K fixing the excitation at 325 nm, exhibits a broad band ranging from 350 to *ca.* 400 nm with two maxima peaking at 359 nm and 394 nm.

Given the high resemblance that compound **6.2**-**6.9** excitation and emission spectra present, compound **6.2** will be studied as representative material. The excitation spectrum of **6.2**$_{\text{Cd-glu}}$ collected at ambient temperature (294 K) and monitoring the emission at 394 nm, presents a similar UV-Vis broad band ranging from 300 to *ca.* 350 nm to the presented by 4,4'-azopyridine ligand. Emission spectra recorded at the same temperature (294 K) and fixing the excitation at 325 nm exhibits a broad band (360–410 nm) with a maximum peaking at 394 nm. Consequently, it can be stated that compounds **6.2**-**6.9** photoluminescent properties are driven by π–π* transitions of the aromatic 4,4'-azopyridine ligand. These spectra come very will line with the solid-state photoluminescence spectra reported by Zhu et al. who studied the photoluminescent properties of an analogous Zn^{2+} and 4,4'-azopyridine based coordination compound.[37]

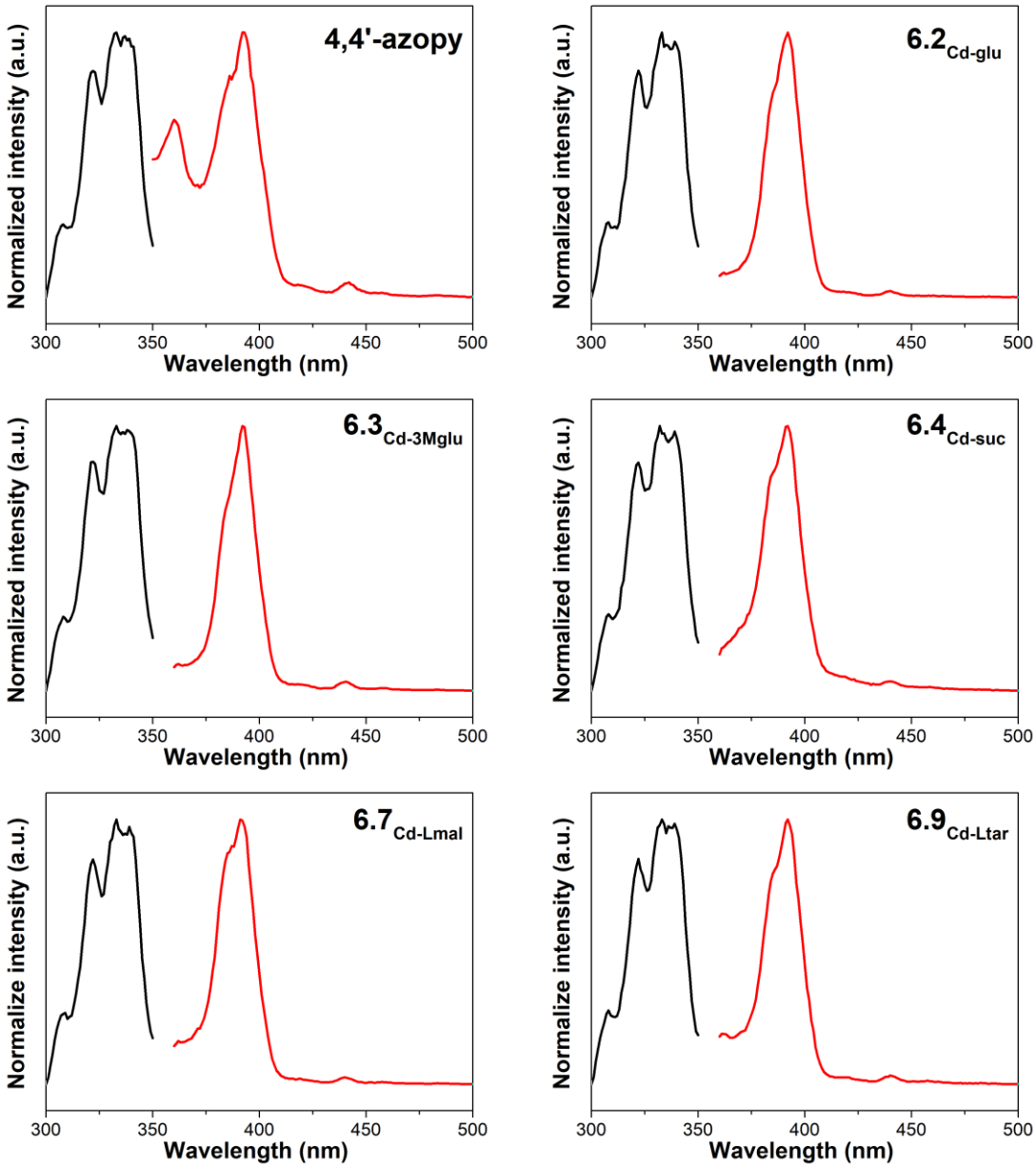

Figure 6.5. Ambient temperature (294 K) excitation spectra (black, $\lambda_{Em.}$ = 394 nm) and emission spectra (red, $\lambda_{Exc.}$ = 325 nm) of 4,4'-azopyridine and compounds **6.2**-**6.4**, **6.7** and **6.9**.

6.7.3 Chiroptical properties

6.7.3.1 Circular dichroism experiments

Given the chiral nature of the synthesised compounds (**6.7**–**6.10**) differential absorption of the right and left circularly polarized light (CD) was investigated as the absolute configuration of homochiral coordination compounds can be confirmed by positive or negative CD signals. Thus, CD spectra of the corresponding water suspensions were recorded for each enantiomeric pair according to the procedure detailed in the 0 section. According to the spectra, the enantiomeric compounds display mirror-symmetric images indicating in all cases the formation of enantiomeric samples.

CD spectra of **6.7**$_{\text{Cd-Lmal}}$ and **6.8**$_{\text{Cd-Dmal}}$ display a set of bands peaking at around 198, 205, 247, 259 and 270 nm with alternating Cotton effects. CD spectra of **6.9**$_{\text{Cd-Ltar}}$ and **6.10**$_{\text{Cd-Dtar}}$ exhibits similar profile with a set of bands with maxima at 190, 196, 209 and 221nm.

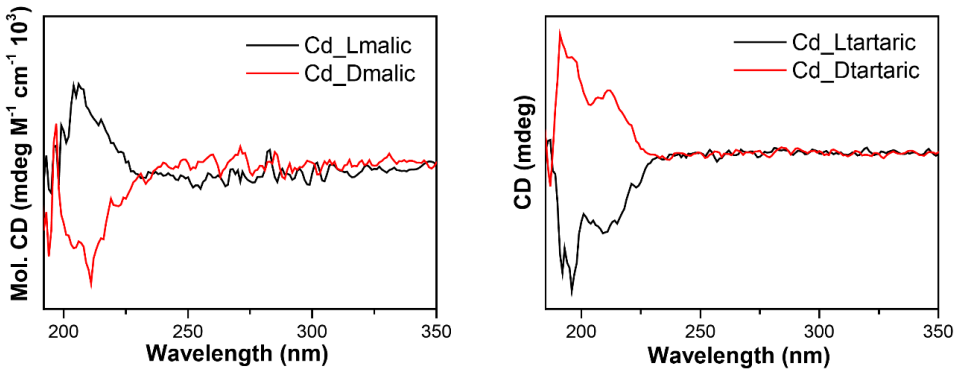

Figure 6.6. Circular dichroism spectra were recorded for compounds **6.7**$_{\text{Cd-Lmal}}$ and **6.8**$_{\text{Cd-Dmal}}$ (left) and **6.9**$_{\text{Cd-Ltar}}$ and **6.10**$_{\text{Cd-Dtar}}$ (right).

Table 6.4. Crystallographic data and structure refinement details of compounds **6.2**-**6.10**.

Compound	**6.2**$_{Cd\text{-}glu}$	**6.3**$_{Cd\text{-}3Mglu}$	**6.4**$_{Cd\text{-}suc}$
Formula	$C_{50}Cd_3H_{60}N_{16}O_{16}$	$C_{16}H_{14}CdN_4O_4$	$C_{15}H_8CdN_4O_4$
Mr	1478.34	438.71	420.6
Crystal system	monoclinic	orthorhombic	orthorhombic
Space group	*C*2/*c*	*Aea*2	*Pbcn*
a(Å)	23.351(6)	15.4288(9)	9.8375(9)
b(Å)	13.682(3)	17.1147(8)	16.3566(14)
c(Å)	20.225(8)	13.5360(8)	10.9203(10)
α(°)	90	90	90
β(°)	115.347(2)	90	90
γ(°)	90	90	90
Volume(Å^3)	5840(3)	3574.3(3)	1757.2(3)
Z	4	8	4
ρ_{calc} g/cm^3	1.681	1.631	1.59
μ/mm^{-1}	1.163	1.249	1.267
F(000)	2976	1744	824
Crystal size/mm^3	0.12 × 0.11 × 0.10	0.14 × 0.12 × 0.09	0.13 × 0.11 × 0.08
Radiation	MoKα (λ = 0.71073)	MoKα (λ = 0.71073)	MoKα (λ = 0.71073)
2Θ range for data collection/°	3.548 to 55.414	4.658 to 57.642	4.832 to 57.642
Index ranges	-30 ≤ h ≤ 30, -17 ≤ k ≤ 17, -25 ≤ l ≤ 26	-20 ≤ h ≤ 20, -23 ≤ k ≤ 23, -18 ≤ l ≤ 18	-13 ≤ h ≤ 13, -22 ≤ k ≤ 22, -14 ≤ l ≤ 14
Reflections collected	23521	49798	80210
Independent reflections	6702 [R_{int} = 0.0445, R_{sigma} = 0.0478]	4653 [R_{int} = 0.0626, R_{sigma} = 0.0314]	2298 [R_{int} = 0.0959, R_{sigma} = 0.0255]
Data/restraints/parameters	6702/455/461	4653/1/228	2298/6/114
Goodness-of-fit on F^2	1.036	1.084	1.754
Final R indexes [I>=2σ (I)]	R_1 = 0.0655, wR_2 = 0.1675	R_1 = 0.0330, wR_2 = 0.0702	R_1 = 0.1172, wR_2 = 0.3754
Final R indexes [all data]	R_1 = 0.0771, wR_2 = 0.1761	R_1 = 0.0434, wR_2 = 0.0742	R_1 = 0.1442, wR_2 = 0.4118
Largest diff. peak/hole / e Å^{-3}	3.21/-1.33	0.84/-0.72	2.97/-2.71
Flack parameter			

Table 6.4. Crystallographic data and structure refinement details of compounds **6.2**-**6.10** (continuation).

Compound	**$6.5_{Zn\text{-}suc}$**	**$6.6_{Zn\text{-}2Msuc}$**	**$6.10_{Cd\text{-}Dtar}$**
Formula	$C_{28}H_{24}N_8O_8Zn_2$	$C_{18}H_8N_4O_4Zn$	$C_{42}H_{24}Cd_3N_{11}O_{22}$
Mr	731.29	220.85	1371.92
Crystal system	monoclinic	orthorhombic	orthorhombic
Space group	*Cc*	*Pbcn*	$P2_12_12$
a(Å)	15.4203(12)	9.846(5)	22.010(5)
b(Å)	12.1049(12)	16.367(5)	24.647(5)
c(Å)	9.4922(7)	10.906(5)	13.624(5)
α(°)	90	90.000(5)	90.000(5)
β(°)	118.211(4)	90.000(5)	90.000(5)
γ(°)	90	90.000(5)	90.000(5)
Volume(Å^3)	1561.4(2)	1757.5(13)	7391(4)
Z	2	4	4
ρ_{calc} g/cm^3	1.555	1.669	1.233
μ/mm^{-1}	1.598	1.454	0.918
F(000)	744	912	2692
Crystal size/mm^3	0.16 × 0.12 × 0.10	0.14 × 0.12 × 0.10	0.15 × 0.13 × 0.07
Radiation	MoKα (λ = 0.71073)	MoKα (λ = 0.71069)	MoKα (λ = 0.71069)
2Θ range for data collection/°	4.506 to 57.45	4.828 to 46.66	4.456 to 46.524
Index ranges	-20 ≤ h ≤ 20, -16 ≤ k ≤ 15, -11 ≤ l ≤ 12	-10 ≤ h ≤ 10, -18 ≤ k ≤ 18, -12 ≤ l ≤ 12	-24 ≤ h ≤ 24, -27 ≤ k ≤ 27, -15 ≤ l ≤ 15
Reflections collected	17781	10362	41397
Independent reflections	3726 [R_{int} = 0.0808, R_{sigma} = 0.0610]	1269 [R_{int} = 0.0487, R_{sigma} = 0.0396]	10483 [R_{int} = 0.1052, R_{sigma} = 0.1129]
Data/restraints/parameters	3726/2/209	1269/0/108	10483/0/704
Goodness-of-fit on F^2	0.934	1.057	1.116
Final R indexes [I>=2σ (I)]	R_1 = 0.0343, wR_2 = 0.0830	R_1 = 0.0626, wR_2 = 0.1605	R_1 = 0.1220, wR_2 = 0.2965
Final R indexes [all data]	R_1 = 0.0391, wR_2 = 0.0865	R_1 = 0.0827, wR_2 = 0.1814	R_1 = 0.1451, wR_2 = 0.3103
Largest diff. peak/hole / e Å^{-3}	0.54/-0.36	1.28/-0.82	1.95/-3.00
Flack parameter	0.900(17)		0.22(14)

6.8 Conclusions

To sum up, in this second annexe, we have demonstrated the infinite possibilities that the combination of two or more ligands presenting different and diverse functionalities, thus, coordination modes offer in the synthesis of novel MOFs. In this sense, we have developed the synthesis and characterization of a family of nine structures based on metals of group 12 (Zn^{2+} and Cd^{2+}) and we have studied the photoluminescent properties of these materials revealing that the emissive properties of the structures are clearly driven by 4,4'-azopyridiene ligand.

ANNEXE 3

6.9 Introduction. A 3D tetrazole-based Zn(II) coordination polymer based on 1-H-tetrazole-5-carboxylic acid ethyl ester ligand: crystal structure, luminescence and modulable adsorption

Over the past few decades, crystal engineering has been one of the more rapidly developing fields within materials science. The successful rational design and controlled synthesis have allow obtaining multifunctional materials[38–41] with unprecedented topologies and importantly, high-performance materials for specific applications.[42–49]

In this sense, the rich variety of coordination modes presented by the 1-H-tetrazole-5-carboxylic acid ethyl ester ligand deriving in a great structural diversity have been the reason to be selected as an ideal candidate for the synthesis of novel coordination polymers of diverse dimensionality and applicability. Several of the aforementioned coordination modes of the tetrazole ring are displayed in Scheme 6.3.

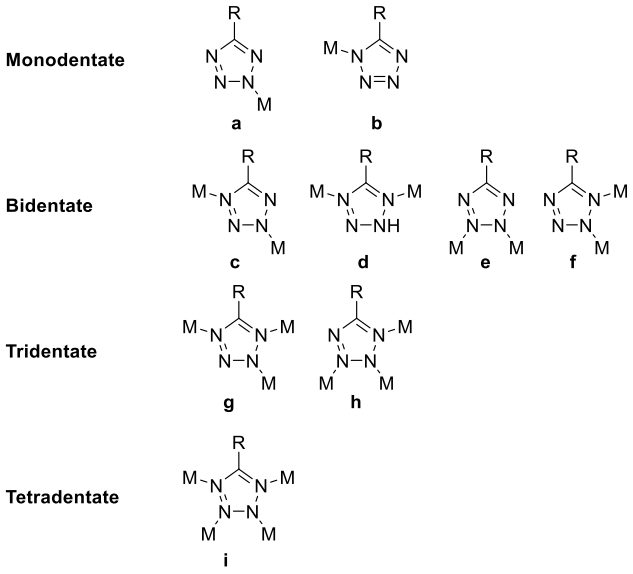

Scheme 6.3. Coordination modes of 5-substituted tetrazoles.

For the reason above discussed, in this work, we present the synthesis and characterization of a new three-dimensional metal-organic framework based on 1-H-tetrazole-5-carboxylic acid ethyl ester ligand and Zn^{2+} for the future analysis of its potential application in photoluminescence and modulable adsorption.

6.10 Materials and methods

6.10.1 Compound synthesis

Synthesis of $[ZnL_2]_n$, namely $\mathbf{6.11_{Zn}}$: 1-H-tetrazole-5-carboxylic acid ethyl ester sodium salt (0.010 g, 0.0610 mmol) was dissolved in 0.5 mL of DMF and 0.5 mL H_2O solvent mixture. In a separated vial, $Zn(OAc)_2{\cdot}2H_2O$ (0.0067 g, 0.0305 mmol) was dissolved in the same solvent mixture employed for ligand solution. After dissolution, the metal solution was added dropwise to the ligand solution while keeping magnetic agitation. Finally, a colourless solution was introduced in a screw-capped vial (6 mL) to the oven at 95°C for 24 hours to yield single crystals.

6.11 Results and discussion

6.11.1 Structural characterization

Single-crystal X-ray crystallographic studies on $[ZnL_2]_n$ where L = 1-H-tetrazole-5-carboxylic acid ethyl ester sodium salt exhibits three dimensional (3D) metal-organic framework that crystallizes in $P2_12_12_1$ orthorhombic space group. The asymmetric unit of $\mathbf{6.11_{Zn}}$ is composed of one Zn^{2+} ion and two deprotonated ligand molecules. Albeit, the ligand is achiral the final structure crystallises as non-enantiogenic space group. This phenomenon is known as accidental chirality and is derived from a spatial rearrangement of a rigid molecule belonging to a point group containing only rotational symmetry elements not containing an inversion centre.[50]

1-H-tetrazole-5-carboxylic acid ethyl ester ligand exhibit coordination to the metallic centre from the nitrogen atoms belonging to the tetrazole group. Each ligand acts as a bidentate bridging linker and binds two Zn atoms through 1,4-nitrogen atoms of the tetrazole group (Scheme 6.3). Precisely, the $[ZnN_4]$ environment is comprised of the coordination of four nitrogen donor atoms belonging to four ligands in such disposition that continuous shape measurements (CShMs)[51] reveal that Zn1 build (Td) tetrahedron polyhedron.

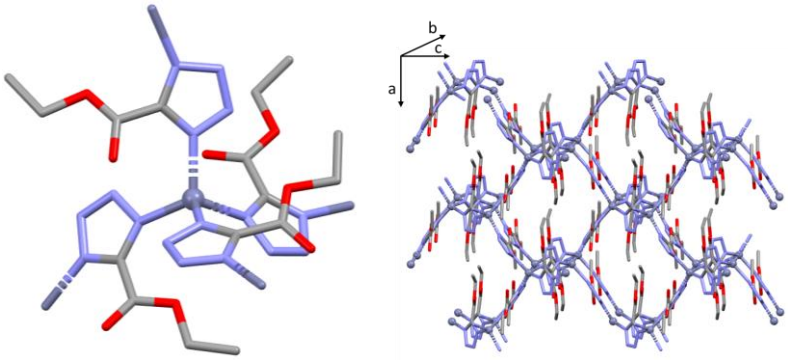

Figure 6.7. Perspective view of the metal coordination environment in **6.11$_{Zn}$** (left) and view of the packed structure where ethyl moiety of 1-H-tetrazole-5-carboxylic acid ethyl ester ligand is pointing out the pore (right). In both figures, hydrogen atoms are omitted for clarity.

Table 6.5. Table of the continuous Shape Measurements for the [ZnN_4] coordination environment.

SP-4	D_{4h}	Square
T-4	T_d	Tetrahedron
SS-4	C_{2v}	Seesaw or sawhorse (cis-divacant octahedron)
vTBPY	C_{3v}	Axially vacant trigonal bipyramid

Complex 6.11$_{Zn}$	**SP-4**	**T-4**	**SS-4**	**vTBPY-4**
Zn1	33.113	**0.034**	90151	3.097

The growth of the structure leaves porous along with the *a* and *b* axis. This cavity is partly occupied by the ethyl moiety of the 1-H-tetrazole-5-carboxylic acid ethyl ester ligand. As it is appreciable in Figure 6.7, the ester group is pointing out the pore and partly occupying solvent accessible volume. The analysis of the topology by means of TOPOS Pro software[32] reveals that **6.11$_{Zn}$** presents a 4- connected diamond-like net, where Zn^{2+} centres are considered as four connected nodes and ligands as bridging linkers.

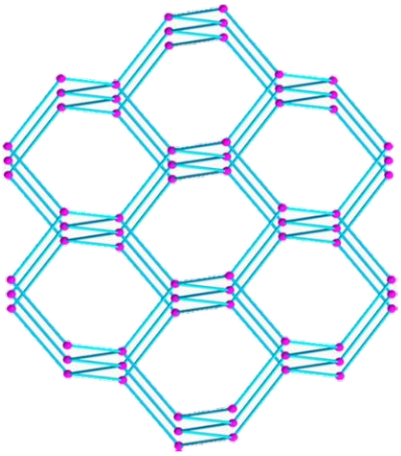

Figure 6.8. A 3D-diamondoid-like net of **6.11$_{Zn}$**. Blue connections represent 1-H-tetrazole-5-carboxylic acid ethyl ester ligand and the pink positions denote Zn^{2+} metal atoms.[52]

Table 6.6. Crystallographic data and structure refinement details of compound **6.11$_{Zn}$**

Compound	**6.11$_{Zn}$**
Formula	$C_8H_{10}N_8O_4Zn$
M_r	347.61
Crystal system	orthorhombic
Space group (no.)	$P2_12_12_1$
a(Å)	9.8740(6)
b(Å)	9.8845(6)
c(Å)	13.7666(9)
α(°)	90
β(°)	90
γ(°)	90
V(Å^3)	1343.61(15)
Z	4
ρ_{calc}g/cm^3	1.718
μ/mm^{-1}	1.859
F(000)	704.0
Crystal size/mm^3	0.13 × 0.12 × 0.1
Radiation	MoKα (λ = 0.71073)
2θ range for data collection/°	5.074 to 52.742
Index ranges	-12 ≤ h ≤ 11, -11 ≤ k ≤ 12, -17 ≤ l ≤ 17
Reflections collected	2593
Independent reflections	2593 [R_{int} = 0.0143, R_{sigma} = 0.0605]
Data/restraints/parameters	2593/52/193
Goodness-of-fit on F^2	1.146
Final R indexes [I>=2σ (I)]	R_1 = 0.0524, wR_2 = 0.1413
Final R indexes [all data]	R_1 = 0.0575, wR_2 = 0.1445
Largest diff. peak/hole / e Å^{-3}	0.96/-0.53
Flack parameter	-0.119(19)

6.12 Conclusions

In this third annexe, the synthesis and preliminary structural characterisation of a diamond like 3D MOF composed by $Zn^{2+}$and 1-H-tetrazole-5-carboxylic acid ethyl ester ligand has been conducted. As future work is expected to perform the analysis of photoluminescent properties and adsorption capacity.

6.13 References

1. Bavykina, A.; Kolobov, N.; Khan, I.S.; Bau, J.A.; Ramirez, A.; Gascon, J. Metal–Organic Frameworks in Heterogeneous Catalysis: Recent Progress, New Trends, and Future Perspectives. *Chem. Rev.* **2020**, *120*, 8468–8535, doi:10.1021/ACS.CHEMREV.9B00685.

2. Yadav, A.; Kanoo, P. Metal-Organic Frameworks as Platform for Lewis-Acid-Catalyzed Organic Transformations. *Chem. - An Asian J.* **2019**, *14*, 3531–3551, doi:10.1002/asia.201900876.

3. Mo, K.; Yang, Y.; Cui, Y. A homochiral metal-organic framework as an effective asymmetric catalyst for cyanohydrin synthesis. *J. Am. Chem. Soc.* **2014**, *136*, 1746–1749, doi:10.1021/ja411887c.

4. Hu, Z.; Zhao, D. Metal–organic frameworks with Lewis acidity: synthesis, characterization, and catalytic applications. *CrystEngComm* **2017**, *19*, 4066–4081, doi:10.1039/C6CE02660E.

5. Dvries, R.F.; Iglesias, M.; Snejko, N.; Gutiérrez-Puebla, E.; Monge, M.A. Lanthanide metal-organic frameworks: Searching for efficient solvent-free catalysts. *Inorg. Chem.* **2012**, *51*, 11349–11355, doi:10.1021/ic300816r.

6. Zhang, Z.; Chen, J.; Bao, Z.; Chang, G.; Xing, H.; Ren, Q. Insight into the catalytic properties and applications of metal-organic frameworks in the cyanosilylation of aldehydes. *RSC Adv.* **2015**, *5*, 79355–79360, doi:10.1039/c5ra13102b.

7. Alzamly, A.; Bakiro, M.; Hussein Ahmed, S.; Alnaqbi, M.A.; Nguyen, H.L. Rare-earth metal–organic frameworks as advanced catalytic platforms for organic synthesis. *Coord. Chem. Rev.* **2020**, *425*, 213543, doi:10.1016/j.ccr.2020.213543.

8. Gawronski, J.; Wascinska, N.; Gajewy, J. Recent Progress in Lewis Base Activation and Control of Stereoselectivity in the Additions of Trimethylsilyl Nucleophiles. *Chem. Rev.* **2008**, *108*, 5227–5252, doi:10.1021/CR800421C.

9. Batista, P.K.; Alves, D.J.M.; Rodrigues, M.O.; De Sá, G.F.; Junior, S.A.; Vale, J.A. Tuning the catalytic activity of lanthanide-organic framework for the cyanosilylation of aldehydes. *J. Mol. Catal. A Chem.* **2013**, *379*, 68–71, doi:10.1016/j.molcata.2013.07.016.

10. Dvries, R.F.; De La Peña-Oshea, V.A.; Snejko, N.; Iglesias, M.; Gutiérrez-Puebla, E.; Monge, M.Á. Insight into the correlation between net topology and ligand coordination mode in new lanthanide MOFs heterogeneous catalysts: A theoretical and experimental approach. *Cryst. Growth Des.* **2012**, *12*, 5535–5545, doi:10.1021/cg301096d.

11. Dvries, R.F.; Snejko, N.; Iglesias, M.; Gutiérrez-Puebla, E.; Monge, M.A. Ln-MOF pseudo-merohedral twinned crystalline family as solvent-free heterogeneous catalysts. *Cryst. Growth Des.* **2014**, *14*, 2516–2521, doi:10.1021/cg5002336.

12. Gomez, G.E.; Kaczmarek, A.M.; Van Deun, R.; Brusau, E. V.; Narda, G.E.; Vega, D.; Iglesias, M.; Gutierrez-Puebla, E.; Monge, M.Á. Photoluminescence, Unconventional-Range Temperature Sensing, and Efficient Catalytic Activities of Lanthanide Metal-Organic Frameworks. *Eur. J. Inorg. Chem.* **2016**, *2016*, 1577–1588, doi:10.1002/ejic.201501402.

13. Gomez, G.E.; Brusau, E. V.; Sacanell, J.; Soler Illia, G.J.A.A.; Narda, G.E. Insight into the Metal Content-Structure-Property Relationship in Lanthanide Metal-Organic Frameworks:

Optical Studies, Magnetism, and Catalytic Performance. *Eur. J. Inorg. Chem.* **2018**, *2018*, 2452–2460, doi:10.1002/ejic.201701474.

14. Gustafsson, M.; Bartoszewicz, A.; Martiín-Matute, B.; Sun, J.; Grins, J.; Zhao, T.; Li, Z.; Zhu, G.; Zou, X. A family of highly stable lanthanide metal-organic frameworks: Structural evolution and catalytic activity. *Chem. Mater.* **2010**, *22*, 3316–3322, doi:10.1021/cm100503q.

15. He, H.; Ma, H.; Sun, D.; Zhang, L.; Wang, R.; Sun, D. Porous lanthanide-organic frameworks: Control over interpenetration, gas adsorption, and catalyst properties. *Cryst. Growth Des.* **2013**, *13*, 3154–3161, doi:10.1021/cg400531j.

16. Karmakar, A.; Rúbio, G.M.D.M.; Paul, A.; Guedes da Silva, M.F.C.; Mahmudov, K.T.; Guseinov, F.I.; Carabineiro, S.A.C.; Pombeiro, A.J.L. Lanthanide metal organic frameworks based on dicarboxyl-functionalized arylhydrazone of barbituric acid: Syntheses, structures, luminescence and catalytic cyanosilylation of aldehydes. *Dalton Trans.* **2017**, *46*, 8649–8657, doi:10.1039/c7dt01056g.

17. Wu, P.; Wang, J.; Li, Y.; He, C.; Xie, Z.; Duan, C. Luminescent Sensing and Catalytic Performances of a Multifunctional Lanthanide-Organic Framework Comprising a Triphenylamine Moiety. *Adv. Funct. Mater.* **2011**, *21*, 2788–2794, doi:10.1002/adfm.201100115.

18. Evans, O.R.; Ngo, H.L.; Lin, W. Chiral porous solids based on lamellar lanthanide phosphonates. *J. Am. Chem. Soc.* **2001**, *123*, 10395–10396, doi:10.1021/ja0163772.

19. Wang, X.; Zhang, L.; Yang, J.; Liu, F.; Dai, F.; Wang, R.; Sun, D. Lanthanide metal-organic frameworks containing a novel flexible ligand for luminescence sensing of small organic molecules and selective adsorption. *J. Mater. Chem. A* **2015**, *3*, 12777–12785, doi:10.1039/c5ta00061k.

20. Liu, X.; Lin, H.; Xiao, Z.; Fan, W.; Huang, A.; Wang, R.; Zhang, L.; Sun, D. Multifunctional lanthanide–organic frameworks for fluorescent sensing, gas separation and catalysis. **2016**, *45*, 3743–3749, doi:10.1039/c5dt04339e.

21. An, H.; Wang, L.; Hu, Y.; Fei, F. Temperature-induced racemic compounds and chiral conglomerates based on polyoxometalates and lanthanides: Syntheses, structures and catalytic properties. *CrystEngComm* **2015**, *17*, 1531–1540, doi:10.1039/c4ce01802h.

22. Fei, F.; An, H.; Meng, C.; Wang, L.; Wang, H. Lanthanide-supported molybdenum-vanadium oxide clusters: syntheses, structures and catalytic properties. **2015**, 18796–18805, doi:10.1039/c4ra16237d.

23. Echenique-Errandonea, E.; Pérez, J.M.; Rojas, S.; Cepeda, J.; Seco, J.M.; Fernández, I.; Rodríguez-Diéguez, A. A novel yttrium-based metal-organic framework for the efficient solvent-free catalytic synthesis of cyanohydrin silyl ethers. *Dalton Trans.* **2021**, *50*, 11720–11724, doi:10.1039/d1dt01953h.

24. Pérez, J.M.; Rojas, S.; García-García, A.; Montes-Andrés, H.; Martínez, C.R.; Romero-Cano, M.S.; Choquesillo-Lazarte, D.; Abdelkader-Fernández, V.K.; Pérez-Mendoza, M.; Cepeda, J.; et al. Catalytic Performance and Electrophoretic Behavior of an Yttrium–Organic Framework Based on a Tricarboxylic Asymmetric Alkyne. *Inorg. Chem.* **2022**, acs.inorgchem.1c02864, doi:10.1021/ACS.INORGCHEM.1C02864.

25. Huang, Z.; Liu, D.; Camacho-Bunquin, J.; Zhang, G.; Yang, D.; López-Encarnación, J.M.; Xu, Y.; Ferrandon, M.S.; Niklas, J.; Poluektov, O.G.; et al. Supported Single-Site Ti(IV) on a Metal-Organic Framework for the Hydroboration of Carbonyl Compounds.

Organometallics **2017**, *36*, 3921–3930, doi:10.1021/acs.organomet.7b00544.

26. Newar, R.; Akhtar, N.; Antil, N.; Kumar, A.; Shukla, S.; Begum, W.; Manna, K. Amino Acid-Functionalized Metal-Organic Frameworks for Asymmetric Base–Metal Catalysis. *Angew. Chemie - Int. Ed.* **2021**, *60*, 10964–10970, doi:10.1002/anie.202100643.

27. Antil, N.; Akhtar, N.; Newar, R.; Begum, W.; Kumar, A.; Chauhan, M.; Manna, K. Chiral Iron(II)-Catalysts within Valinol-Grafted Metal-Organic Frameworks for Enantioselective Reduction of Ketones. *ACS Catal.* **2021**, *11*, 10450–10459, doi:10.1021/acscatal.1c02529.

28. Zhang, T.; Manna, K.; Lin, W. Metal-Organic Frameworks Stabilize Solution-Inaccessible Cobalt Catalysts for Highly Efficient Broad-Scope Organic Transformations. *J. Am. Chem. Soc.* **2016**, *138*, 3241–3249, doi:10.1021/jacs.6b00849.

29. Manna, K.; Ji, P.; Greene, F.X.; Lin, W. Metal-Organic Framework Nodes Support Single-Site Magnesium-Alkyl Catalysts for Hydroboration and Hydroamination Reactions. *J. Am. Chem. Soc.* **2016**, *138*, 7488–7491, doi:10.1021/jacs.6b03689.

30. Manna, K.; Ji, P.; Lin, Z.; Greene, F.X.; Urban, A.; Thacker, N.C.; Lin, W. Chemoselective single-site Earth-abundant metal catalysts at metal-organic framework nodes. *Nat. Commun.* **2016**, *7*, 1–11, doi:10.1038/ncomms12610.

31. Pérez, J.M.; Echenique-Errandonea, E.; Rojas, S.; Choquesillo-Lazarte, D.; Seco, J.M.; Fernández, I. Improved Cyanosilylation Performance on demanding ketones by the play of a Europium-based MOF under RT and Solvent-Free Conditions. *Green Chem.* **2022**, In revision.

32. Blatov, V.A.; Shevchenko, A.P.; Proserpio, D.M. Applied topological analysis of crystal structures with the program package topospro. *Cryst. Growth Des.* **2014**, *14*, 3576–3586, doi:10.1021/cg500498k.

33. Spek, A.L. Structure validation in chemical crystallography. *Acta Crystallogr. Sect. D Biol. Crystallogr.* **2009**, *65*, 148–155, doi:10.1107/S090744490804362X.

34. Gomez, G.E.; Brusau, E. V.; Sacanell, J.; Soler Illia, G.J.A.A.; Narda, G.E. Insight into the Metal Content–Structure–Property Relationship in Lanthanide Metal–Organic Frameworks: Optical Studies, Magnetism, and Catalytic Performance. *Eur. J. Inorg. Chem.* **2018**, *2018*, 2452–2460, doi:10.1002/ejic.201701474.

35. Dhakshinamoorthy, A.; Asiri, A.M.; Garcia, H. Mixed-metal or mixed-linker metal organic frameworks as heterogeneous catalysts. *Catal. Sci. Technol.* **2016**, *6*, 5238–5261, doi:10.1039/C6CY00695G.

36. Firmino, A.D.G.; Mendes, R.F.; Ananias, D.; Figueira, F.; Tomé, J.P.C.; Rocha, J.; Almeida Paz, F.A. Pyrene Tetraphosphonate-Based Metal-Organic Framework: Structure and Photoluminescence. *Eur. J. Inorg. Chem.* **2020**, *2020*, 3565–3572, doi:10.1002/ejic.202000726.

37. Zhu, L.N.; Zhang, L.Z.; Wang, W.Z.; Liao, D.Z.; Cheng, P.; Yan, S.P.; Jiang, Z.H. A novel 4,4′-azopyridine-bridged binuclear zinc complex. *J. Coord. Chem.* **2003**, *56*, 1447–1453, doi:10.1080/00958970310001596773.

38. Desiraju, G.R. The supramolecular concept as a bridge between organic, inorganic and organometallic crystal chemistry. *J. Mol. Struct.* **1996**, *374*, 191–198, doi:10.1016/0022-2860(95)08932-2.

39. O'Keeffe, M.; Yaghi, O.M.; O'Keeffe, M.; Yaghi, O.M.; O'Keeffe, M.; Yaghi, O.M. Deconstructing the Crystal Structures of Metal–Organic Frameworks and Related Materials into Their Underlying Nets. *Chem. Rev.* **2011**, *112*, 675–702, doi:10.1021/CR200205J.

40. Hoskins, B.F.; Robson, R. Infinite Polymeric Frameworks Consisting of Three Dimensionally Linked Rod-like Segments. *J. Am. Chem. Soc.* **1989**, *111*, 5962–5964, doi:10.1021/JA00197A079/SUPPL_FILE/JA00197A079_SI_001.PDF.

41. Li, J.R.; Ma, Y.; McCarthy, M.C.; Sculley, J.; Yu, J.; Jeong, H.K.; Balbuena, P.B.; Zhou, H.C. Carbon dioxide capture-related gas adsorption and separation in metal-organic frameworks. *Coord. Chem. Rev.* **2011**, *255*, 1791–1823, doi:10.1016/J.CCR.2011.02.012.

42. Liu, J.; Chen, L.; Cui, H.; Zhang, J.; Zhang, L.; Su, C.-Y. Applications of metal–organic frameworks in heterogeneous supramolecular catalysis. *Chem. Soc. Rev.* **2014**, *43*, 6011–6061, doi:10.1039/C4CS00094C.

43. Li, J.-R.; Sculley, J.; Zhou, H.-C. Metal–Organic Frameworks for Separations. *Chem. Rev.* **2011**, *112*, 869–932, doi:10.1021/CR200190S.

44. Hu, Z.; Deibert, B.J.; Li, J. Luminescent metal–organic frameworks for chemical sensing and explosive detection. *Chem. Soc. Rev.* **2014**, *43*, 5815–5840, doi:10.1039/C4CS00010B.

45. Kurmoo, M. Magnetic metal–organic frameworks. *Chem. Soc. Rev.* **2009**, *38*, 1353–1379, doi:10.1039/B804757J.

46. Zabala-Lekuona, A.; Seco, J.M.; Colacio, E. Single-Molecule Magnets: From Mn12-ac to dysprosium metallocenes, a travel in time. *Coord. Chem. Rev.* **2021**, *441*, 213984, doi:10.1016/J.CCR.2021.213984.

47. Yi, P.; Huang, H.; Peng, Y.; Liu, D.; Zhong, C. A series of europium-based metal organic frameworks with tuned intrinsic luminescence properties and detection capacities. *RSC Adv.* **2016**, *6*, 111934–111941, doi:10.1039/C6RA23263A.

48. Pérez-Yáñez, S.; Beobide, G.; Bhadbhade, M.; Cepeda, J.; Fröba, M.; Hoffmann, F.; Luque, A.; Román, P.; Castillo, O.; Cepeda, J.; et al. Improving the performance of a poorly adsorbing porous material: template mediated addition of microporosity to a crystalline submicroporous MOF. *Chem. Commun.* **2011**, *48*, 907–909, doi:10.1039/C1CC15589J.

49. Lu, F.; Hu, R.; Wang, S.; Guo, X.; Yang, G. Luminescent properties of benzothiazole derivatives and their application in white light emission. *RSC Adv.* **2017**, *7*, 4196–4202, doi:10.1039/C6RA25369E.

50. Pidcock, E. Achiral molecules in non-centrosymmetric space groups. *Chem. Commun.* **2005**, 3457–3459, doi:10.1039/B505236J.

51. Llunell, M.; Casanova, D.; Cirera, J.; Bofill, J. M.; Alemany, P.; Alvarez, S.; Pinsky, M.; Avnir, D. Program for the Stereochemical Analysis of Molecular Fragments by Means of Continuous Shape Measures and Associated Tools. *SHAPE, v1.1b; Barcelona, Spain* **2005**, 1–35.

52. Chen, Q.Y.; Li, Y.; Zheng, F.K.; Zou, W.Q.; Wu, M.F.; Guo, G.C.; Wu, A.Q.; Huang, J.S. A 3D-diamond-like tetrazole-based Zn(II) coordination polymer: Crystal structure, nonlinear optical effect and luminescent property. *Inorg. Chem. Commun.* **2008**, *11*, 969–971, doi:10.1016/j.inoche.2008.05.009.

Conclusions and Future Perspectives

Conclusions

The general aim of this doctoral thesis has been exploiting the multifunctionality of the novel coordination compounds and metal-organic frameworks prepared in this work derived the combination of transition metals and lanthanides with carboxylate group ligands. The linkers with the aforementioned functionality have proved to be excellent building blocks for the design of novel architectures, both because of the structural diversity structural diversity achieved as well as for the great variety of properties exhibited by these materials.

The interesting crystalline structures obtained have allowed the fine tuning of the application optimally suited to each structural feature. In this sense, some of the applications explored in this work have been magnetism, luminescence, magnetic resonance imaging, adsorption, conductivity, heterogeneous catalysis, antibacterial activity and biological properties.

Regarding the followed synthetic-pathways, solvothermal synthesis and microwave assisted synthetic routes have been followed for the preparation of the materials. The former, has allowed obtaining single-crystals with which structural resolution has been performed. Furthermore, the use of glass vials has facilitated the reaction monitoring. The latter synthetic pathway has allowed to scale up reaction significantly reducing the required reaction time.

In advance, the particular conclusions stemmed for each family of compounds will be described in short.

Chapter 1

- In chapter 1, a family of 3d (Mn^{2+}, Zn^{2+} and Cd^{2+}) metals and tetrazol derivative amino acid based coordination compounds have been *in situ* synthesised for their application in MRI, photoluminescence and chiroptical properties.
- Concretely, relaxativity measurements in compound **1.1**, demonstrated being possibly used in magnetic resonance imaging as a T_2 contrast agent. As future work, additional analysis on cytotoxicity, biodistribution and pharmacokinetics i*n vivo* should be conducted prior to be clinically applied.

- On another level, photoluminescent analysis performed in d^{10} metal derived complexes have demonstrate the emission being ruled by ligand centred π→π* transition.
- Finally, chirality preserved in amino acid precursor's motivated us to study chiroptical properties of compounds **1.6**-**1.9**. Circular dichroism demonstrated in all cases enantiomeric pairs display opposite cotton effects being only Zn_phen enantiomeric pairs able to display circularly polarized luminescence.

Chapter 2

Part 1

- The ligand explored in chapter 2 has allowed extensively exploit the multinationalism derived of 3-amino-4-hydroxybenzoic acid not only by combining to 3d block metals but also to Ln^{3+}.
- To begin with, the combination with Co^{2+} has allowed exploring the magnetic behaviour of the pristine 3D MOF in addition to the magnetically diluted sample with Zn^{2+} which demonstrated a magnetic barrier for the reversal of magnetization of U_{eff} = 6.31 K.
- Additionally, dilution with Zn^{2+} not only resulted in an enhancement in the magnetic properties but also different doping proportions had demonstrating a linear response in the fluorescent intensity decrease with respect to Co^{2+} quencher incorporation.

Part 2

- The combination of the ligand with Ln^{3+} ions have allowed the formation of a family of isostructural 3D MOFs to which magnet behaviour, photoluminescent properties and adsorption capacity have been studied.
- Regarding magnetic properties, compound **2.11$_{Yb}$** showed signal dependency among frequency. Consequently, magnetic dilution strategy was performed in compounds **2.13$_{Y\text{-}Dy}$**, **2.14$_{Y\text{-}Er}$** and **2.15$_{Y\text{-}Yb}$** obtaining successful results in the latter two compounds as the position of the maxima in χ_M'' was shifted towards higher temperatures.
- Photoluminescent analysis conducted in compounds **2.4$_{Eu}$** and **2.6$_{Tb}$** present characteristic emissions of the ions exhibiting a more efficient for the former owing to the low energy gap between their excited states. In

addition, mixed-lanthanide networks have demonstrated compounds **2.17** and **2.18** could find potential application in thermometry.

- From other side, the porous structure allowed us studying CO_2 adsorptive capacity revealing a comparable behaviour to other MOFs containing open-metal sites and relatively high isosteric heat (41.4 kJ/mol).
- Finally, the porous nature and accessibility of external molecules to metallic clusters has permitted compound **2.12$_{Y}$** and **2.19$_{Eu}$** being tested as catalyst in the solvent-free cyanosilylation reaction of a carbonyl substrates demonstrating great ability to heterogeneously catalyse the aforementioned reaction.

Part 3

- To conclude, **2.6$_{Tb}$** material has been shaped and processed into pellets and membranes to further study its emissive properties in membrane immobilized material demonstrating being able to keep emissive properties. Finally, water adsorption studies revealed a promising uptake of 18 % increment in mass; it would be expected good conductivity values nonetheless exhibited proton conductivity was relatively modest.

Chapter 3

- A a novel copper-based 3D MOF is presented based on 3,4-dihydroxybenzoic acid ligand.
- This novel material has been shaped through palletisation and membrane-immobilization processing techniques and exhibited good stability by means of temperature and moisture conditions which simulated possible industrial operation conditions.
- Additionally, microporous structure permitted to collect CO_2 sorption isotherms before and after solvent-exchange procedure showing relatively tripled adsorption capacity with the latter procedure.
- Finally, the well-known antibacterial capacity of Cu^{2+} and 3,4-dihydroxybenzoic acid ligands motivated us performing a preliminary study on the antibacterial activity of compound **3.1$_{Cu}$** and its precursors by disk-diffusion method towards pathogenic *S. aureus* bacteria. Results exhibited that the antibacterial activity of both Cu^{2+} and 3,4-dihydroxybenzoic acid

ligand remain practically unaltered after the formation of the compound. Further analysis should be addressed to determine among others, MIC, MCB in addition to MOFs degradation procedure and mechanism of action.

Chapter 4

- This section proposes the synthesis and characterization of a family of isostructural metalloligand assisted 3D MOFs with the formula $\{[(RuL_3)_2Ln_3]ClO_4\}_n$ for the exploration of photoluminescent properties and use as catalyst in oxidative desulfurization of fuel.
- Several catalytic loadings of compound **4.3$_{Ru\text{-}Eu}$** have been tested in ECODS reaction. However, none of them reached full conversion. In addition, a transformation of the original crystalline phase was appreciated.
- Photoluminescent properties studied in ligand, metalloligand and compounds **4.1$_{Ru\text{-}Nd}$**, **4.3$_{Ru\text{-}Eu}$**, **4.4$_{Ru\text{-}Gd}$**, **4.5$_{Ru\text{-}Tb}$** and **4.7$_{Ru\text{-}Er}$** demonstrated that in compounds **4.4** and **4.5** emission was centred metalloligand emission while only **4.3** exhibited Ln^{3+} intra f transitions. Compounds **4.1** and **4.7** when exciting at ligand maximum absorption displayed typical narrow lines ascribed to each metallic centre ion in the NIR region derived by a energy transfer from the metalloligand to the lanthanide centre.

Chapter 5

- This chapter describes the synthesis of a family of coordination compounds based on diclofenac for the evaluation of magnetic and photoluminescent properties, anti-inflammatory activity and contrast agent behaviour.
- Magnetic properties evaluated in **5.6$_{Dy}$** revealed that it exhibited subtle slow relaxation of the magnetization near the detection limit of the apparatus.
- Emissive properties of prepared materials exhibit good performance of the ligand in sensitizing the emission of lanthanide ions both in the visible and near-infrared region.
- The anti-inflammatory response of the pristine drug and Gd^{3+}-based coordination compounds exhibiting enhanced behaviour in coordination compounds.
- In addition, with the aim of determining whether Gd^{3+} based coordination compound could acta as CA relaxativity studies were conducted exhibiting relatively poor values.

- Liposome encapsulation was set as strategy to enhance encapsulated material concentration and thus relaxativity. We decided to follow this strategy not only for Gd^{3+} based counterpart but also from Eu^{3+} and analogous Fe^{3+} compounds with the aim of determining the best mechanism to produce MRI signal. Although material encapsulation resulted satisfactorily no enhancement of the relaxativity values was obtained due to lack of accessibility and interchangeability of the bulk water with respect to metal-coordinated solvent molecules.

Chapter 6

Annexe 1

- This works follows the one presented in chapter 2, and resumes the synthesis of the first heterobimetallic /Eu-MOF based on 3-amino-4-hydroxybenzoic acid ligand with the objective of searching a synergistical effect in cyanosilylation reaction concerning Y- or Eu-MOFs counterparts.
- The novel material has been not only tested in cyanosilylation reaction of a aldehydic and ketonic substrates of different nature in the solvent free media, but also in hydroboration reaction exhibiting good catalytic efficiency in both scenarios. Comparing to its pristine counterparts the novel material presents reduced recyclability.

Annexe 2

- The present section describes the synthesis and characterization of of a family of nine structures based on Zn^{2+} and Cd^{2+} with the combination of two ligands offering diverse structures and coordination modes.
- Photoluminescent properties studied in prepared compounds suggest that emissive properties in all compounds are dominated by the bands ascribed to 4,4'-azopyridine ligand.

Annexe 3

- To conclude this chapter, the synthesis and preliminary structural characterisation of a novel diamond like 3D MOF composed by Zn^{2+} and 1-H-tetrazole-5-carboxylic acid ethyl ester ligand has been conducted with which photoluminescent properties and adsorptive capacity are expected to explore in a future.

List of publications and CV

Within the scope of this doctoral thesis, the following articles were published in international journals with references:

Related to the introduction,

- **Konposatu metal-organikoen sintesia laborategitik industriako aplikazioetara (review).** Echenique-Errandonea, *E. EKAIA EHUko Zient. eta Teknol. aldizkaria* **2021**, 153–168, doi:10.1387/EKAIA.21710.

Related to Chapter 2,

- **3-amino-4-hydroxybenzoate and 3d metal ion Based Bifunctional Coordination Polymer: Magnetic and Modulated Photoluminescence properties.** Echenique-Errandonea, E.; Rojas, S.; Cepeda, J.; Choquesillo-Lazarte, D.; Seco, J.M.; Rodríguez-Diéguez, A. (*in preparation*).

- **Multifunctional Lanthanide-based Metal-organic Frameworks derived from 3-amino-4-hydroxybenzoate: Single-molecule magnet behaviour, luminescent properties for thermometry and CO_2 adsorptive capacity.** Echenique-Errandonea, E.; Mendes, R.F.; Figueira, F.; Choquesillo-Lazarte, D.; Beobide, G.; Cepeda, J.; Ananias, D.; Rodríguez-Diéguez, A.; Almeida Paz, F.A.; Seco, J.M. *Inorg. Chem*. **2022**, 10.1021/acs.inorgchem.2c00544.

- **A novel yttrium-based metal-organic framework for the efficient solvent-free catalytic synthesis of cyanohydrin silyl ethers.** Echenique-Errandonea, E.; Pérez, J.M.; Rojas, S.; Cepeda, J.; Seco, J.M.; Fernández, I.; Rodríguez-Diéguez, A. *Dalton Trans.* **2021**, 50, 11720–11724, doi:10.1039/d1dt01953h.

- **Improved Cyanosilylation Performance on demanding ketones by the play of a Europium-based MOF under RT and Solvent-Free Conditions.** Pérez, J.M; Echenique-Errandonea, E.; Rojas, S.; Choquesillo-Lazarte, D.; Seco, J.M.; Fernández, I.; Rodríguez-Diéguez, A. (*under review)*.

- **Easy handling and cost-efficient processing-techniques of a three-dimensional Tb^{3+}-MOF. Emissive capacity of the membrane-immobilized material, water adsorption capacity and proton conductivity of the prisitine MOF.** Echenique-Errandonea, E.; Barbosa, P.; Mendes, R.F.; Figueira, F.; Cepeda, J.; Ananias, D.; Seco, J.M.; Almeida Paz, F.A.; Rodríguez-Diéguez, A. (*in preparation*).

Related to Chapter 3,

- **Antibacterial Activity, Adsorptive Capacity and processing techniques for a Novel Copper-MOF based on the 3,4-dihydroxybenzoate ligand.** Echenique-Errandonea, E.; Rojas, S.; Cepeda, J.; Figueira, F.; Karim Abdelkader-Fernández, V.; Pérez-Mendoza, M.; Mendes, R.F.; Ananias, D.; Almeida Paz, F.A.; Barbosa, P.; Delgado-López, J.M.; Seco, J.M.; Rodríguez-Diéguez, A. (*in preparation*).

Related to Chapter 5,

- **Photoluminescence and magnetic analysis of a family of lanthanide(III) complexes based on diclofenac.** Echenique-Errandonea, E.; Oyarzabal, I.; Cepeda, J.; San Sebastian, E.; Rodríguez-Diéguez, A.; Seco, J.M. *New J. Chem*. **2017**, 41, 5467–5475, doi:10.1039/C7NJ00794A.

- **Marked Improvement Anti-inflammatory Properties of a Drug Based on Luminescent Gadolinium Dinuclear Complexes.** Echenique-Errandonea, E.; Fernández, B.; Cepeda, J.; San Sebastián, E.; Oyarzabal, I. Rufino-Palomares, Eva E; Pérez-Jiménez, A.; Lupiáñez, J.A.; Reyes-Zurita, F.J. Rodríguez-Diéguez, A.; Seco, J.M. (*in preparation*)

- Patent Nº: P202230425. **"Complejos metálicos anti-inflamatorios de Gadolinio basados en Diclofenaco"**.

Related to Chapter 6,

- **A Mixed Heterobimetallic Y/Eu-MOF for the Cyanosilylation and Hydroboration of Carbonyls.** Echenique-Errandonea, E.; López-Vargas, M.E.; Pérez, J.M.; Rojas, S.; Choquesillo-Lazarte, D.; Seco, J.M.; Fernández, I.; Rodríguez-Diéguez, A. *Catalysts*, **2022**, doi:10.3390/catal12030299.